PFS Science White Paper

Prepared by the PFS Science Collaborations

Contents

1 Introduction: Rationale for and Capabilities of a Wide-Field Spectrograph for Subaru

Michael Strauss (Princeton), Jim Gunn (Princeton), et al.

1.1 Scientific Rationale

Wide-field surveys of the sky are tremendously powerful and versatile astronomical tools. While they are often designed with very specific scientific goals, their census of the heavens typically has impact in a broad range of astronomical areas. The best example of this is the Sloan Digital Sky Survey (SDSS; York et al. (2000)). It was conceived at a time (the late 1980's) when the nature of the large-scale distribution of galaxies was only hinted at by the largest redshift surveys of the time (de Lapparent et al. 1986; Kirshner et al. 1987) and so it took as its goal a comprehensive redshift survey of a million galaxies over a volume of about $2 \times 10^8\, h^{-3}\mathrm{Mpc}^3$, to characterize the galaxy power spectrum and topology of large-scale structure on the largest scales. The SDSS redshift survey indeed fulfilled this scientific goal (Strauss et al. 2009; Gott et al. 2005; Eisenstein et al. 2005; Percival et al. 2010), but the imaging and spectroscopic data gathered to do so allowed it to make fundamental breakthroughs in many other areas of astrophysics, including asteroid science (Ivezić et al. 2002), the discovery of brown dwarfs (Strauss et al. 1999); the largest sample by far of spectroscopically confirmed white dwarfs (Eisenstein et al. 2006), the kinematics (Bond et al. 2010) and substructure (Belokurov et al. 2006) of the Galactic Halo, the discovery of dwarf companions to the Milky Way, the detailed photometric properties of nearby galaxies (Blanton et al. 2003), the measurement of the Supernova 1a Hubble Diagram (Kessler et al. 2009), the evolution of quasars (Richards et al. 2006), and the reionization of the early universe (Fan et al. 2006), to name but a few. Indeed, there have been over 3500 refereed papers to date that reference SDSS in their title or abstract, and based on the number of highly cited papers, it is considered the most productive telescope facility of the past decade (beating Keck, HST, and others; Madrid & Macchetto (2009)).

Inspired by the SDSS and other wide-field surveys in the ultraviolet (GALEX), near-infrared (2MASS), and radio (Becker et al. 1995), a wide variety of next-generation imaging surveys are on-going or planned, including of course Hyper-SuprimeCam (HSC) on Subaru. However, one of the great strengths of the SDSS is the combination of its imaging and spectroscopic surveys, and while there are wide-field spectroscopic surveys being planned for the next generation (HETDEX on the Hobby-Eberly Telescope, BigBOSS on the Kitt Peak 4-m, the Large Sky Area Multi-Object Fibre Spectroscopic Telescope (LAMOST) in China, and the near-infrared Fiber Multi-Object Spectrograph (FMOS) on Subaru), these are all limited in wavelength coverage, throughput, or

scope of the survey they will carry out. This white paper describes the exciting possibility of building a wide-field fiber-fed spectrograph for the Subaru Telescope, which is unique among 8-meter-class telescopes in having a field of view of 1.5° diameter. The scientific potential for such a facility is vast, and this white paper outlines some of the principal scientific opportunities it would enable.

We make the case that reaching the full scientific potential of the next generation of imaging surveys in general and HSC in particular, from the formation history of the Milky Way halo to the nature of galaxies at the epoch of reionization, requires a massively multiplexed spectrograph with high throughput and resolution and a wavelength coverage from 3800Å to 1.3 microns. This wavelength coverage is driven by the need to obtain emission-line redshifts of galaxies over the full range ($z = 0$ to $z > 10$, with no gaps). The wide-field corrector on the Subaru telescope has limited throughput outside of this spectral range. In addition, the natural atmospheric cutoff between the J and H bands, and the need for a cooled spectrograph at wavelengths beyond 1.3μm, make this a natural cutoff for such a spectrograph. In what follows, we refer to this instrument as the Prime Focus Spectrograph (PFS). Indeed, we imagine four spectrographs, each receiving light from 600 fibers with 1.13″ entrance aperture, and each covering the full spectral range from 3800Å to 1.3 microns.

This white paper is still in its early stages. The various chapters have been largely written independently, and therefore don't make completely uniform assumptions about the capabilities of the spectrograph, including wavelength coverage, resolution, and throughput. Each of the chapters describes one or more surveys that could be carried out to maximize the scientific opportunities of that chapter, but there has not yet been an attempt to combine these overlapping ideas into a single coherent observing program.

In this introductory chapter, we give the past history of the PFS idea (§ 1.2), then outline the principal surveys that it might carry out, which are detailed in the chapters that follow. Chapter 2 describes the detailed design for the spectrograph that Jim Gunn has developed.

1.2 The history of the PFS concept

The Subaru 8.2-meter telescope, operated by the National Astronomical Observatory of Japan (NAOJ), is distinguished for having by far the widest field of view at prime focus of all telescopes of 6-meter aperture and above. As such, it is uniquely positioned to do wide-field science requiring such a large aperture. Hyper-SuprimeCam (HSC) is a wide-field imager to take advantage of this unique capability; it will see first light in late 2011. It is being built by Satoshi Miyazaki and his team at NAOJ, and will have a field of view of 1.77 deg^2 covered by 112 2K × 4K Hamamatsu CCDs. The combination of this enormous focal plane, the size of the Subaru primary, its superb optics, and the excellent seeing on Mauna Kea will make HSC by far the most powerful optical imaging survey instrument in the world, at least until LSST sees first light late in the decade. A collaboration involving the Japanese astronomical community, Princeton University and the astronomical community of Taiwan are planning a Strategic Survey proposal with HSC; as of this writing, we are planning to ask for of order 300 nights of telescope time to carry out a three-tiered survey:

- Of order 1000 deg^2 in *grizy* to a point-source depth ($5\,\sigma$) of $r = 26.5$;
- Of order 40 deg^2 a magnitude deeper, including narrow-band filters to look for Lyman α at redshifts from $z = 3$ to $z = 6.6$.
- Two pointings (3.5 deg^2 total) to go a magnitude deeper yet, again including narrow-band filters.

These imaging surveys will provide the target lists for the various spectroscopic programs described in this white paper.

About eight years ago, Subaru's wide field inspired the Gemini community to propose building a Wide Field Multi-Object Spectrograph (WFMOS) for the Subaru telescope. The so-called Aspen meeting of 2002 saw wide-field spectroscopy as the highest priority new instrumentation for the Gemini community (for all the science reasons we outline in this white paper), but the Gemini optics do not easily accommodate wide-field instrumentation. Thus the Gemini board suggested to mount WFMOS on Subaru and use it to carry out major spectroscopic surveys. In exchange, the Japanese astronomical community would receive a substantial amount of time on the Gemini telescopes, and would of course be able to use WFMOS for their own science.

A call for designs for WFMOS went out, with a set of requirements that included the ability to do both moderate resolution galaxy spectroscopy, and high-resolution ($R \sim 20,000$) stellar spectrum, and a team centered at Caltech/Jet Propulsion Laboratory won the competition. Their design was distinguished, among other things, by an innovative positioning system that uses a pair of rotating elements for each fiber to cover the focal plane.

After many discussions, NAOJ agreed to host WFMOS on Subaru, and the Japanese scientific community became increasingly excited by its scientific potential. However, in 2008, faced with the imminent withdrawal of the UK from the Gemini consortium and mounting costs for WFMOS, the Gemini board made the decision not to build the instrument after all.

The possibility of resurrecting the idea of a wide-field spectrograph for Subaru came a year later. Faced with the global economic downturn, the Japanese government announced a program of stimulus money for scientifically compelling projects. A proposal was submitted by Professor Hitoshi Murayama, Director of the Institute for the Physics and Mathematics of the Universe (IPMU) of the University of Tokyo, which included funds for both HSC and PFS, This joint project has the name, `SUbaru Measurement of Images and REdshifts` ("SUMIRE", the Japanese word for "violet"). The principal scientific goals included dark energy studies via weak lensing (HSC) and baryon oscillations (PFS), together with the galaxy evolution and reionization studies described below.

The proposal was successful. It earmarks 1.5 billion yen (corresponding roughly to $15 million using today's exchange rate) to the PFS. Under Murayama's leadership, we are in the process of putting together an international collaboration to raise funds for the remainder of the roughly $35 million required to build the instrument as described, and to develop all technical aspects of the instrument, fibers, and software system. Among the non-Japanese partners currently involved or in discussion for this project are:

- The California Institution of Technology/Jet Propulsion Laboratory: Richard Ellis and Michael Seiffert led the development of the chosen WFMOS design. The fiber positioner concept they have developed will be used for the PFS.
- Princeton University: Jim Gunn, building upon ideas developed by Eric Prieto and others at Marseille, has a plausible design for the spectrographs themselves, as described in some detail in Chapter 2. Princeton is also very interested in the software pipelines to analyze the spectra (a subject not currently discussed in this white paper).
- Laboratorio Astrophysico Nacional/Universidade de São Paulo, Brazil has expertise in fiber optics technology.
- The University of Edinburgh, which has interest in the software pipelines.

There is also active interest in this project from the Taiwanese astronomical community, and Johns Hopkins University in Baltimore, Maryland.

1.3 Galaxy Redshifts from zero to > 10

The SDSS carried out a comprehensive redshift survey of the low-redshift ($z < 0.2$) universe, and, with its sample of Luminous Red Galaxies (Eisenstein et al. 2001), is extending the measurement of the large-scale distribution of galaxies, albeit sparsely, to $z \sim 0.7$ as part of the Baryon Oscillation Sky Survey, consisting of 1.3 million galaxies over 10,000 deg^2. The largest redshift surveys at $z \sim 1$ (the DEEP2 survey; VIMOS), cover much smaller effective volumes, and redshift surveys at $z \sim 2$ and $z \sim 3$ cover only tiny solid angles in narrow pencil beams; results from these studies tend to be strongly cosmic-variance limited. Studies of the morphologies, spectral energy distributions, and luminosity functions of high-redshift galaxies have indicated that the epoch from redshift 3 to 1 is when modern galaxy assembly took place and galaxies acquired the properties they have today. The details of this process are quite poorly understood, however, in particular because galaxy redshifts are difficult to measure in the infamous "redshift" desert between $z \sim 1.3$ where [OII]λ3727Å drops out of the range of CCDs, and $z \sim 2.2$ where Lyα becomes visible on the blue end of most spectrographs.

One can get around this limitation with a spectrograph covering the range from 3800Å to 1.3μm. With this, one could see Hα to $z = 1$, [OII] from almost $z = 0$ to $z = 2.5$, and Lyman α from $z = 2.2$ to $z = 10$ (if indeed Lyα-emitting galaxies exist at such a redshift). That is, such a spectrograph has no blind spots to emission-line galaxies at all. [OII] in particular is ubiquitous in galaxies of all types (and has the great advantage of being a doublet split at resolutions above 2500, allowing it to be unambiguously identified as such even if it is the only emission feature in the spectrum).

The design is for four spectrographs, each receiving 600 fibers, over an area comparable to that of HSC (1.77 deg^2). As we outline below, we are driven by a variety of science goals to consider surveying a volume comparable to that of the SDSS main galaxy survey in each of a number of redshift slices, requiring covering of order 50 square degrees, in addition to a very large but shallower survey to obtain emission-line redshifts for baryon-oscillation studies.

1.4 Large-Scale Structure, Baryon Oscillations and Weak Lensing

The surveys to be carried out with the HSC (and similarly for other wide-field imaging surveys underway or planned) will be done in five photometric bands (*grizy*), allowing galaxy redshifts to be estimated by fitting model or empirical spectral energy distributions to the photometry (photometric redshifts). These redshifts typically have rms uncertainties $\delta z/(1+z)$ of order 0.03, although they can be plagued with non-Gaussian outliers (catastrophic errors), especially for galaxies in the blue cloud, which tend to have weak spectral breaks. Photometric redshifts are certainly adequate for certain purposes: if suitably characterized and calibrated, they can be used, for example, in weak lensing studies of the large-scale distribution of dark matter. They have been used for measurements of the clustering of galaxies at high redshift, and to identify galaxies at close to the epoch of reionization.

However, an uncertainty of 0.03 corresponds to 10,000 km/s at low redshift, or $100h^{-1}$ Mpc, larger than the largest voids seen in the galaxy distribution. That is, the topology of the galaxy distribution, and the ability to distinguish between overdense and underdense regions, is essentially lost if one has photometric redshifts only. The baryon acoustic oscillation (BAO) signature in the galaxy power spectrum is at a fixed comoving scale, and thus can be used as a standard ruler to constrain cosmological models. With photometric redshifts, one can measure the baryon oscillation scale in the plane of the sky, which gives a measure of angular diameter distances as a function of redshift, thereby giving constraints most directly on the curvature of the Universe (i.e., $\Omega_k \equiv 1-\Omega_m-\Omega_\Lambda$). But photometric redshift errors are comparable to the scale of the BAO signal itself, and thus BAO cannot be measured in the redshift direction at all with photometric redshifts alone. Spectroscopic redshifts, on the other hand, do allow a measurement of the BAO signal along the line of sight, giving a constraint on the dependence of the Hubble constant with redshift (which in turn gives direct constraints on the properties of the dark energy, especially the equation of state, w and its redshift evolution). With existing surveys pushing baryon oscillation studies to $z \sim 0.6$ (BOSS, WiggleZ), the next frontier is to go to higher redshift. There is a degeneracy in the angular diameter distance measured by baryon oscillations between the parameters of dark energy (i.e., the equation of state parameter w) and the curvature of the universe Ω_k that can be broken with a spectroscopic redshift survey to redshifts of 2.

The volume such a survey needs to subtend can be calculated in comparison to the SDSS measurement of baryon oscillations: Eisenstein et al. (2005) used an effective comoving volume of order half a cubic Gigaparsec ($H_0 = 100\,\mathrm{km/s/Mpc}$) to make the first significant detection of BAO at $z \approx 0.35$. To cover a similar volume over a redshift interval of $\Delta z \sim 0.3$ at $z \sim 1.5$ requires a solid angle of about 500 deg^2, or roughly 300 pointings of the spectrograph, assuming a field of view similar to that of HSC.

A redshift survey is no longer shot-noise limited in measurements of the correlation function when the product of the comoving number density of targets n and their power spectrum P satisfy $nP = 1$. Given that the clustering of galaxies of a given type is roughly independent of redshift (because the bias of galaxies increases with redshift), and that the LRGs used by Eisenstein et al. (2005) have a bias of roughly 2 relative to the "normal" emission-line galaxies likely to be selected for a high-z redshift survey, this suggests that we can make a measurement at high redshift with the same volume and four times the number density as was done at low redshift. Scaling from the

total numbers of galaxies of Eisenstein et al, this leads to a survey of 200,000 galaxies[1]. The space density of [OII] emitters (with luminosities above 10^{42} erg/sec; Figure 2.9 and the corresponding discussion shows that such objects will be easy to observe spectroscopically with PFS) at these redshifts (Zhu et al. 2009) exceeds the required space density by a factor of a few, so there are plenty of objects to be observed. This calculation needs to be done more carefully; this number seems quite small, it is more than an order of magnitude smaller than BigBOSS is proposing at the same redshift.

Another exciting frontier in large-scale structure studies is to measure the distortions due to peculiar velocities in the correlation function on large scales. This allows an independent measurement of the ratio $\Omega(z)/b(z)$ as a function of redshift, independent of the cosmological constraints from baryon oscillations.

An important role for this spectrograph will be to calibrate and test the photometric redshifts we derive from the HSC broad-band photometry: we will never be able to get spectra of *all* the galaxies in our imaging data. Accurate photometric redshifts are key for using faint galaxies in weak lensing analyses: it is crucial that one quantify the error distribution (including non-Gaussian outliers, or "catastrophic errors") and biases in the photometric redshifts accurately to get unbiased estimates of cosmological quantities. The broad wavelength coverage, without any redshift desert, is crucial for determining redshifts over the full range that is important for the weak lensing analyses. Following Newman (2008), one can use the cross-correlation between a limited spectroscopic survey, and a much deeper photometric survey, to tightly constrain the true redshift distribution of the latter, as long as the spectroscopic survey adequately samples the relevant redshift range.

These topics are explored in much more detail in Chapter 4.

1.5 Galaxy Evolution Studies

Spectra give far more information than just a redshift. Most fundamentally, a spectrum allows unambiguous identification of an object, and is crucial for identifying unusual and rare objects (consider for example the fact that high-redshift quasars and brown dwarfs, with distances differing by nine orders of magnitude, have essentially indistinguishable optical broad-band colors). Measurements of emission-line properties at all redshifts allow determination of star formation rates, identification of AGN, metallicities, and velocity dispersions. At sufficient signal-to-noise ratio, absorption lines allow further determination of stellar populations, interstellar and intergalactic absorption and outflows, and additional kinematic information. For stars, spectra allow accurate determination of surface temperatures, metallicities, and surface gravities, and identification.

The PFS spectrograph will see Hα to $z \sim 1$, giving the most robust measurements of the star formation rate as a function of redshift to date, and calibrating rest-frame UV star formation rate indicators against Hα. The spectral coverage of more than a factor of three in a single exposure (380-1300 nm) is unprecedented in wide-field spectroscopy, especially at high redshifts. The spectral region around 4000Å can be seen to redshifts from zero to above 2. It is is particularly

[1]The uncertainty in the measurement of the BAO signal scales as the square root of the volume surveyed, or (for a fixed redshift range) as the square root of the area covered.

important, as it includes quite a few diagnostic features: the 4000Å break itself is a measure of the luminosity-weighted age of the stellar population. The Balmer break at 3650Å and Balmer absorption lines quantify the contribution of A stars, and thus star formation in the last Gigayear, to the light of the galaxy. The strength of [OII]3727Å is an alternative measure of star formation rate, and high-order Balmer lines and (somewhat bluer) [NeV] lines at 3347 and 3427Å in emission are indicative of AGN activity. Finally, the abundance of metal lines in this spectral range are diagnostic of the metallicity of the stellar population, and with sufficient signal-to-noise ratio, the width of these lines give a determination of the velocity dispersion of these galaxies.

As emphasized above, the properties of galaxies in the present day appear to be put in place in the epoch between redshifts 3 and 1, corresponding to roughly 2 billion to 6 billion years after the Big Bang. The majority of the star formation in the universe takes place in that interval, as does the merging that assembles massive galaxies. It is known that the assembly and star formation of massive galaxies happens at an earlier epoch than for less massive objects ("cosmic downsizing"). Observations of morphological segregation of galaxies in clusters tells us that this process *must* be a function of environment, but present-day surveys don't cover enough volume to allow a wide range of environments, from voids to the cores of rare rich clusters. Moreover, no such survey has the wavelength coverage necessary to sample the diagnostically rich regions of galaxy spectra over the relevant range of redshifts to be able to measure those galaxy properties whose evolution we wish to explore. Surveying a volume like that covered by the SDSS main galaxy spectroscopic sample (0.04 Gpc^3) in several redshift slices to $z \sim 2$ (requiring a survey of several tens of square degrees) will give excellent statistics over a broad range of environments. SDSS has done a detailed study of the correlations between galaxy properties and their large-scale environments in the present-day Universe; PFS will allow this to be studied as a function of redshift. sort of sampling of the

In the BAO section above, we found ourselves matching the volume subtended by the SDSS LRG sample, which is something like ten times larger. Thus we must consider two different surveys in this context: a shallow sparse survey for redshifts only, focussed on BAO science and covering several hundred square degrees, and a deeper and close to fully-sampled survey with higher S/N spectra over a few tens of square degrees to study galaxy evolution.

These ideas are developed in much more detail in Chapters 6 and 7.

1.6 Spectroscopy of quasars

Spectroscopy of high-redshift quasars with PFS will also be invaluable. A galaxy redshift survey will of course allow active galactic nuclei to be identified spectroscopically at all redshifts. The HSC imaging survey will extend to y band, potentially allowing the identification of quasars to $z = 7$. The unprecedented wavelength coverage of PFS will allow Hβ to be observed to $z = 1.6$ and Mg II to $z = 3.6$. These two lines are both crucial for the measurement of black hole masses (and thus Eddington ratios) of AGN. Current studies of such lines are hampered by the need to measure masses using the far-less-reliable CIV line, which is strongly affected by non-virial motions (outflows due to winds, etc). Mg II in particular tends to give much more accurate redshifts than CIV because of asymmetries in the latter line due to winds and self-absorption. These more accurate redshifts are important for quasar correlation studies, especially on small scales, and in cross-correlation with galaxy populations. The clustering of quasars yields insights into the nature

of the dark matter potential wells in which their host galaxies sit, and the measurement of the clustering over a broad range of black hole masses, quasar luminosities, and redshift is a key test of models of black hole growth.

Quasar spectra also show absorption lines due to outflows from the central engine, the quasar host galaxy, intervening galaxies, and the cosmic web of neutral hydrogen. PFS spectra of a large sample of quasars thus allows probes of everything from the dynamics of gas close to the black hole to the distribution of neutral gas on cosmological scales and the history of the reionization of the universe. These ideas are explored in much more detail in Chapters 9 and 10.

1.7 Spectroscopic Surveys at $z > 5$

At $z > 5$, photometric redshifts (e.g., i-band dropouts) are effective at identifying *candidate* galaxies. But these remain unconvincing without a spectroscopic confirmation (usually the detection of Lyα in emission). This is especially important at redshifts $z > 6.6$, where only a handful of galaxies have been spectroscopically confirmed.

Galaxy and quasar studies to $z > 6$ are now probing the end of the epoch of reionization. Studies of the Gunn-Peterson (Gunn & Peterson 1965) effect with high-redshift SDSS quasars (e.g. Fan et al. 2006; Carilli et al. 2010) have put a lower limit on the mass-weighted neutral fraction of the IGM at $z = 6.4$ of a few percent. The high-redshift Lyman α luminosity function shows evidence of truncation by the damping wing of a neutral IGM, and gives insights into star formation in proto-galaxy fragments only a Gigayear after the Big Bang. But the samples are small, only a few dozen objects. A proper census of these objects, and especially their large-scale distribution would yield insights into the dark-matter clustering and the halos in which these objects are found, and the topology of the reionization process itself (McQuinn et al. 2007). The HSC survey will carry out very deep broad-band and narrow-band imaging over tens of square degrees, allowing Lyα candidates to be selected for very deep spectroscopy to measure their distribution.

It is thought that reionization occurs as a percolation process, as the roughly spherical ionization fronts surrounding star-forming galaxies and quasars due to their output of ultraviolet photons grow and overlap. Understanding the topology of this ionization is a key goal of high-redshift galaxy studies, and detailed models by McQuinn and his collaborators make predictions for the relative distribution of Lyman α emitters and non-emission-line galaxies at the end of reionization. The characteristic scales that need to be measured are of order one degree, i.e., comparable to the field of view of HSC and PFS. Exploring this is one of the principal drivers of the HSC survey, and spectroscopic follow-up of the brighter sources with PFS will be crucial.

We show in § 2.5 that the spectrograph will have the S/N in as little as a one-hour exposure to detect Lyα emission lines at flux levels comparable to the bulk of the Lyα emitting population at redshifts as high as 7 currently being studied by Subaru.

Spectroscopy of substantial numbers of $z \sim 6$ galaxies extending to 1.3 microns will allow direct measurement of features other than Lyα. Of particular interest is to detect the He II emission line at 1640Å (1.1μm at $z = 5.7$ and 1.23μm at $z = 6.5$) which is thought to be a diagnostic tracer of Population III (i.e., first generation, zero metallicity) stars. We would have to be quite lucky to see this line in individual galaxies, but we might be able to detect it in a stack of many spectra.

These ideas are explored in much more detail in Chapter 8.

1.8 Stellar Spectroscopy

Moderate-resolution spectroscopy over a wide wavelength range of large samples of stars is tremendously powerful as a probe of Galactic archeology ("near-field cosmology"). Measurements of the current distribution, kinematics, and composition of stars in the halo are inputs to, and constraints on, models for the formation of our Milky Way. Wide-field imaging surveys have revealed tremendous substructure in the halo, a reflection of the cannibalization of dwarf satellites. Reasonable S/N spectroscopy at $R = 2500-4500$, especially with *simultaneous* spectral coverage around 4000Å (including the CN band at 3800Å) and the Calcium triplet at 9000Å, allows accurate determination of metallicity (at least [Fe/H], and also [α/Fe]) for stars, and radial velocities good to 5 km/s, good enough to resolve the low thermal motions in the stellar streams that make up the halo. The scientifically very valuable extremely low metallicity population can be identified for detailed high-resolution followup. And important rare populations, including many varieties of white dwarfs, brown dwarfs, close white dwarf binaries, carbon stars, K giants, and cataclysmic variables, will be identified in substantial numbers. The near-IR coverage of PFS will be particularly useful for the coolest stars and brown dwarfs, whose spectra rise steeply into the near-infrared.

These topics are explored in much more detail in Chapters 5 and 11.

References

Becker, R. H., White, R. L., & Helfand, D. J., 1995, *ApJ*, 450, 559
Belokurov, V. et al., 2006, *ApJL*, 642, L137
Blanton, M. R. et al., 2003, *ApJ*, 594, 186
Bond, N. A., Strauss, M. A., & Cen, R., 2010, *MNRAS*, 406, 1609
Carilli, C. L. et al., 2010, *ApJ*, 714, 834
Carter, B. D., Ashley, M. C. B., Sun, Y., & Storey, J. W. V., 1992, Proceedings of the Astronomical Society of Australia, 10, 74
de Lapparent, V., Geller, M. J., & Huchra, J. P., 1986, *ApJL*, 302, L1
Eisenstein, D. J. et al., 2001, *AJ*, 122, 2267
—, 2006, *ApJS*, 167, 40
—, 2005, *ApJ*, 633, 560
Fan, X. et al., 2006, *AJ*, 132, 117
Gott, III, J. R., Jurić, M., Schlegel, D., Hoyle, F., Vogeley, M., Tegmark, M., Bahcall, N., & Brinkmann, J., 2005, *ApJ*, 624, 463
Gunn, J. E., & Peterson, B. A., 1965, *ApJ*, 142, 1633
Ivezić, Ž. et al., 2002, *AJ*, 124, 2943
Iye, M. et al., 2006, *Nature*, 443, 186
Kessler, R. et al., 2009, *ApJS*, 185, 32
Kirshner, R. P., Oemler, Jr., A., Schechter, P. L., & Shectman, S. A., 1987, *ApJ*, 314, 493
Madrid, J. P., & Macchetto, D., 2009, ArXiv e-prints, 0901.4552
Maraston, C., 2005, *MNRAS*, 362, 799
McQuinn, M., Lidz, A., Zahn, O., Dutta, S., Hernquist, L., & Zaldarriaga, M., 2007, *MNRAS*, 377, 1043
Newman, J. A., 2008, *ApJ*, 684, 88
Oke, J. B., & Gunn, J. E., 1982, *PASP*, 94, 586
Percival, W. J. et al., 2010, *MNRAS*, 401, 2148

Rhoads, J. E., & Malhotra, S., 2001, *ApJL*, 563, L5
Richards, G. T. et al., 2006, *ApJS*, 166, 470
Strauss, M. A. et al., 1999, *ApJL*, 522, L61
—, 2009, in ArXiv Astrophysics e-prints, Vol. 2010, astro2010: The Astronomy and Astrophysics Decadal Survey, pp. 57P–+
York, D. G. et al., 2000, *AJ*, 120, 1579
Zhu, G., Moustakas, J., & Blanton, M. R., 2009, *ApJ*, 701, 86

2 Spectrograph Design

Jim Gunn (Princeton), Michael Strauss (Princeton), et al.

The proposed spectrograph is a fairly straightforward design, which employs two dichroics and three camera/detector systems to cover the range 3800Å to 1.30μm contiguously, with resolving power which progresses fairly smoothly from about 2000 in the blue to about 5000 in the infrared (Figure 2.4). The resolving power in the red and infrared is high enough that one can work effectively between the OH airglow lines. The beamsize is large enough (250mm) that one can employ vacuum Schmidt-like cameras with the detector in the beam; the camera enclosure is the cryostat. The fiber system, constructed with Polymicro FBP wide-band fiber, will transform the f/2.24 focal ratio at the Subaru prime focus behind the HSC wide-field corrector to f/2.8 by means of small negative lenslets at the entrance to the 128μm fibers for the run to the spectrograph. The fibers in the focal plane subtend 1.13 arcseconds. The collimator is a Schmidt system operating at f/2.5 to accommodate focal ratio degradation (FRD, the scattering due to imperfections in the fiber or its termination) in the incoming fiber. The cameras operate at f/1.05 in the current preliminary design and consist of a thick double-sided aspheric corrector plate which forms the vacuum window, a spherical primary mirror, and a field flattener.

The three channels cover the wavelength ranges 3800-6700Å, 6500A-10000Å, and 9700-13000Å respectively, and are separated by a pair of sputtered dichroics. A schematic drawing of the spectrograph is shown in Figure 2.1, and a three-dimensional rendering can be found in Figure 2.2. The blue and red channels use a pair of Hamamatsu 2K×4K edge-buttable p-channel, fully depleted CCDs to form a 4K×4K array. These devices are identical to the ones used currently in Suprime-Cam on Subaru and will be used in HSC, except for a somewhat more efficient, newly developed antireflection coating. The IR channel will use the new Teledyne 4RG 4K×4K mercury-cadmium-telluride sensor with substrate removed for short-wavelength response and made of 1.7-micron cutoff material. All of the detectors have 15 micron pixels, so the detector geometry is identical in all three channels. The optics and construction of the cameras are essentially identical except for tweaking for the individual wavelength ranges. The cooling is by commercial pulse-tube coolers capable of pumping 20 watts at 100K. A schematic of the instrument, showing the positions of the three cameras, is given in Figure 2.1.

The cameras make images which are of order 25 microns RMS diameter over the field. The fibers project into 57 micron spots in the camera focal plane, corresponding to 50 microns FWHM, three and a bit pixels. Thus the spectrum is very well sampled, which is crucial for accurate sky subtraction.

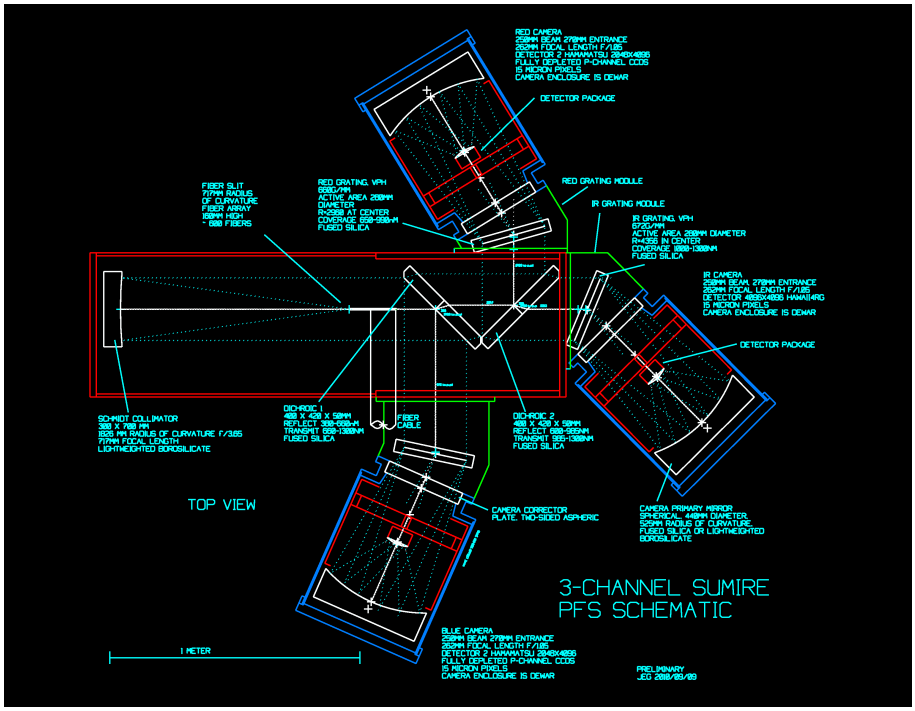

Figure 2.1: A schematic of the proposed design of the spectrograph. The fibers are brought to a slit in the middle of the enclosure. The light travels to the left, reflects off the Schmidt collimator, then passes through two dichroics to be sent to the three cameras. The detector assemblies lie in the center of each camera, and each camera is its own cryostat.

2.1 The Collimator and the Fibers

The choice of a Schmidt for the collimator is almost a no-brainer for any fiber-fed spectrograph. What the collimator should be in detail depends on the fibers and whether and how any f-ratio transformation is handled. Let us discuss the fibers first.

For the red, the best choice would be Polymicro FI ultra-low OH fibers, because they have really excellent throughput longward of about 6000Å. However, with the 50-meter fiber run between the prime focus and the instrument, the losses with this fiber become unacceptably large even at 5000Å and are disastrous at 4000Å. We should instead use the FBP fiber, which has better performance over a broad wavelength coverage: it has a transmission of about 65% at 4000Å, rising to 83% at 5000Å, and is about 90% through the red and IR channel bands.

The focal ratio at prime focus at Subaru with the 1.5-degree HSC corrector, which will be used for this instrument, is f/2.24. Expressed as a numerical aperture (NA, the sine of the maximum angle into which light can enter the fiber), this is 0.22, which is the acceptance specified for both the FI and FBP fibers. One needs for any sizable fiber length to reduce this NA in order not to incur unacceptable losses. In addition, even if we *could* transmit such a fast beam, there is not room for the dichroics in the spectrograph to make a three- channel instrument. However, by slowing the beam down slightly, to f/2.8, we circumvent both difficulties. This can be accomplished easily with microlenses which have quite gentle curvatures at the fiber entrance, so that the fibers *never*

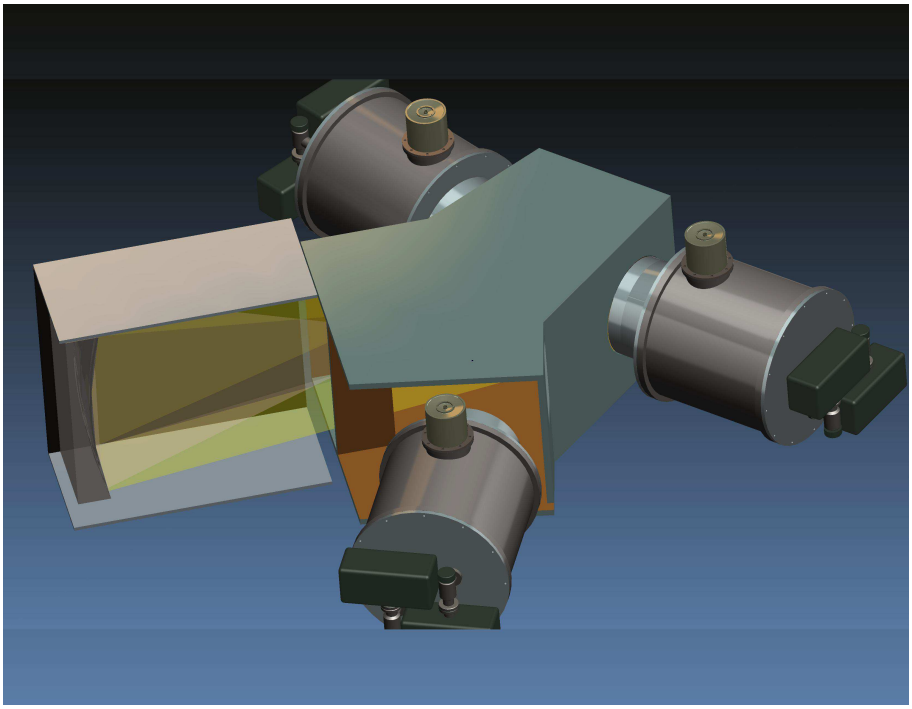

Figure 2.2: A three-dimensional rendering of the spectrograph design, by Mike Carr of Princeton. The collimator is exposed in cut-away, and the three cameras are apparent.

see a beam as fast as their allowable NA, and the usual serious losses associated with field effects in microlens systems can be circumvented by making the microlenses meniscii with a low-index coupling fluid between the lens and the entrance of the fiber. A drawing of what this entrance assenby might look like is shown in Figure 2.3.

The fibers in this schematic design enter the side of the spectrograph in two groups, one for the top half of the slit and one for the bottom, and go to the fiber slit, where they are deployed at the collimator focal surface. This is very similar to the system used in the SDSS spectrographs except for the details of the fiber routing. The minimum radius of curvature of the fibers along this route is 50mm.

The collimator mirrors are quite large, 300 × 560mm, spherical with a radius of curvature of 1350mm; they will be lightweighted Hextek borosilicate mirrors.

2.2 The Gratings

Kaiser Optical has recently commissioned an interferometer for the exposure of large volume-phase holographic (VPH) gratings, and can accommodate single gratings with up to a 280 mm diameter 'ruled' area. Since the gratings are used at an angle (not a very large one in this spectrograph), the illuminated length is larger than the beam, but a 280mm active area is sufficiently larger than our 250mm beam that there is no light lost. This dimension was what really sets the beam size in this design. A larger beam would result in larger, much more expensive optics in any case, and

250mm is big enough to make the detector obscuration in the beam in the cameras (see below) acceptable. The pitches of the three gratings are 786, 642, and 655 lines/mm for the blue, red, and IR, respectively, the Littrow half-angles 12, 15, and 22 degrees, and the central resolving powers 2200, 2900, and 4200. We (SDSS) have recently acquired a very large monolithic *mosaic* grating made on this machine for the APOGEE project, and it is of really excellent quality.

The resolving power increases more-or-less linearly with wavelength both for each camera and from one camera to another (Figure 2.4), resulting in roughly SDSS resolution in the blue to high enough resolution in the red and IR that one can work between the OH lines, as mentioned above. The roughly constant FWHM resolution in wavelength is about 2.5 Å. In the red, this resolution is higher than that needed for galaxy science. The internal velocity dispersion of massive galaxies lies typically in the range of 100-400 km/s, meaning that a resolution of more than 3000 is somewhat overkill. Thus we will find ourselves binning the spectra over a few resolution elements (weighting the errors properly) *after* sky subtraction.

2.3 The Dichroics

There are two dichroics in the system; the first reflects the blue to the first grating and camera and passes 6600-13000Å to the rest of the system. The second reflects the red passband to the second grating and camera shortward of 9850Å and passes the near-IR to the third grating/camera system. These will be probably be made at Asahi's new sputtering facility, which can produce precise coatings with over 100 layers.

2.4 The Cameras

It has been recognized since the beginning that the cameras are the crux of this instrument. They need to be very fast in order to image fibers of reasonable size on the sky with a large telescope onto the ubiquitous 15 micron pixels of advanced sensors available today. The angular scale on the detector depends *only* on the camera focal ratio, and to image a 1 arcsecond fiber onto two 15 micron pixels to obtain Nyquist sampling requires a focal ratio of about 0.75 (in the *absence* of FRD), almost twice as fast as is readily available with modern refracting designs. The constraints are actually not *quite* this severe; the FWHM of a fiber is 0.866 its diameter, and given very faint objects and bright sky lines, one needs to do a bit better than Nyquist for sampling safety. For the proposed 100 micron, 1.13 arcsecond fibers, the FWHM is 0.98 arcseconds, and imaging that onto 3 pixels, 45 microns, one needs an f/ratio of 1.15. FRD losses and reasonable f/ratios for transmission push this faster, to about f/1.05. For this geometry, the FWHM is a bit more than 3 pixels, and the sampling should be excellent; allowing very accurate sinc-shifting and reconstruction for the critical sky subtraction in the red and infrared. It is clear that the success of this spectrograph will depend critically on how well the sky subtraction can be done, and we must be very well-sampled.

One way to get very fast cameras is to use various variants of the basic Schmidt design, making use of the fact that the primary aberrations are already fairly small. For a very fast Schmidt-like camera the detector needs to be in the beam, and so the beam needs to be large enough that the obscuration is acceptable. Beams up to about 250 mm in diameter can be accommodated with

modern, efficient VPH gratings, as we have seen, and a $4K^2$ 15-micron pixel detector in a 250 mm beam obscures 7.7% of the light, surely acceptable... *if* there is no "extra" hardware surrounding the detector. Besides careful treatment of the thermal design and electronics, it surely demands that the detector not be surrounded by a bulky cryostat to cool it. We avoid this problem by making the whole camera the cryostat.

As for the optical design itself, classical Schmidts do not perform adequately with these fast focal ratios and large (18 degree) fields, especially with the necessity to flatten the field for a solid-state detector. The design we have been working on involves a thick (50mm) corrector plate with aspherics on both sides, basically using the Baker-Nunn (e.g. see Carter et al. 1992) idea of using longitudinally displaced plates carrying the derivatives of the off-axis aberrations. A crudely optimized design produces 25 micron rms images over nearly the whole field; we plan to work with our Marseille colleagues to develop a final optimization of this design, which may involve a more complex corrector system at the detector.

2.4.1 Mechanical Issues

The Palomar Double Spectrograph (Oke & Gunn 1982) used the camera mirror as a mechanical element to support the detector assembly via a tripod moored to three flexures bonded to the periphery of the mirror which also served to support the mirror. Given that our spectrographs will be fixed may mean that this simple approach, or a simple variant of it, will be adequate.

For the vacuum container of each camera, we are investigating a vendor which builds drawn and explosive-formed aluminum vacuum vessels to which they can affix stainless steel fittings. They can easily make vessels the size we need, but the techniques are new enough that we need again to prototype the camera.

We will make extensive use of multi-layer insulation (MLI) in these dewars, because we intend to have a large cold structure to getter contaminants and, in the case of the IR detector, to minimize thermal radiation contamination. There will be a conical cold shield which stretches from the front of the primary mirror up to almost the back of the corrector plate, supported by a copper ring which carries heat from the detector package via copper vanes to the cold output of the cooler. Initial tests will be done with an LN_2 reservoir, but we will investigate pulse-tube coolers during the tests; Subaru's policy is to discourage liquid cryogens, but we are hoping that the prospect of dumping the heat from 12 2-5 percent efficient pulse tube coolers each producing of order half to one kilowatt may sway this policy.

2.4.2 The electronics

The initial tests will be done with SDSS-type CCD electronics, which have proven to be exceptionally good and continue to serve very well with BOSS in SDSS-III. The bandwidth, noise, and overall performance is completely satisfactory for this application; the layout and general bulk is not satisfactory for the final configuration here, however, and we will be working on modernizing them. We will certainly use Teledyne's 'Sidecar' controller for the IR channel and will investigate using it for the CCDs as well; there has been some considerable success in such applications. The

initial tests will be done with Hamamatsu CCDs on loan from NAOJ, and we will continue to investigate acquiring an engineering grade IR detector as the production comes on line.

2.4.3 The optics

Final optimization of the optical design will be performed, as well as exploring variants on the original. An effort will be made to reach f/1.0 for the camera, and any tradeoffs at that point between performance and cost/complexity will be made. Since the preliminary design is already almost good enough, we do not anticipate great difficulty in doing this, but performance is greatly enhanced with better images. Finally, a working system with primary mirror, corrector plate, and field-flattener will be produced and tested with a Hamamatsu 2-CCD detector array.

2.5 Spectrograph Performance

We have done a fairly careful analysis of the throughput of the spectrograph as designed, including:

- The quantum efficiency of the Hamamatsu chips with a 2-layer AR coat, and the Teledyne IR chips;
- 28% losses for light from a star that doesn't enter the 1.13 arcsec fiber (assuming 0.7" seeing); perhaps an underestimate for galaxies;
- Losses in 50 meters of Polymicro FBP fiber;
- The measured reflectivity of the Subaru primary;
- Transmission of the corrector (from Satoshi Miyazaki), assuming a mean 90% vignetting;
- 90% throughput of the fiber coupling;
- Camera and collimator throughput, including vignetting;
- Throughput of the dichroics as a function of wavelength;
- Grating transmission (design numbers as supplied by Jim Arns of Kaiser Optical);
- Atmospheric transparency (both continuum scattering and molecular absorption) appropriate for Mauna Kea, based on data from Gemini and CFHT, and assuming a precipitable water column of 1.6 mm (here assuming an airmass of 1.3).

The results are shown in the upper panel of Figure 2.5. These numbers are impressively large; over most of the spectral range, 20% of the photons hitting the top of the atmosphere are detected by the spectrograph. This is comparable to the throughput of the best multi-object spectrographs in the world, including that of the SDSS Baryon Oscillation Sky Survey.

To calculate signal-to-noise ratios for spectra, we need a model for the spectrum of the sky. We used sky models from the ESO and Gemini observatories, corrected for errors in their assumed continua

(too much zodaical light in the IR, too much moonlight in the blue). The spectrum includes the Lorentzian wings to sky lines inherent in grating spectra. Given this sky model, the lower panel of Figure 2.5 shows the predicted signal-to-noise ratio (S/N) for each pixel for the fiducial case of a 1000-sec exposure on a star of AB magnitude 22.5 at all wavelengths. The S/N scales with square root of exposure time, and with the flux. Thus an hour-long exposure, for example, will give the shown S/N for a star of brightness 23.2. One can of course increase the S/N further by binning pixels after sky subtraction (see below).

We have carried out simulations of stellar spectra using stellar population models from Maraston (2005). These are characterized by a star formation rate that goes like $t\exp(-t/t_0)$, where t is the time since the Big Bang. The models are normalized to give an L_* galaxy at the present in the $i^{0.1}$ band (i.e., the SDSS i band as it samples a galaxy at the median redshift of the SDSS sample, $z = 0.1$). Four models are run with different values of t_0; we label them with their color at the present: "blue": $t_0 = 4$ Gyr
"green": $t_0 = 2.8$ Gyr
"red": $t_0 = 1.0$ Gyr
"dead": $t_0 = 0.5$ Gyr

These models do not include the effects of dust or emission lines; see below for an analysis of our sensitivity to emission lines.

These spectra were constructed by using the sensitivities described above, a realistic high-resolution model of the emission from the night sky, and photon noise from the combination of sky and source, though in nearly all cases the sky completely dominates. The proposed spectrograph has high enough resolution that we can work between the OH lines, as described above, but that 'native' resolution is typically much higher than one wishes to work with for faint objects (Finding narrow emission lines is an exception, which we will return to below.) Generally one wishes to work for signal-to-noise reasons at considerably lower resolution, at least to generate spectra to *look at*; such things as fitting for velocity dispersion and redshift can (and should) use the spectra at full resolution if the code is well written. To lower the resolution in a robust way, the full-resolution spectra have been convolved with a gaussian filter at the desired width, but weighting each pixel under the filter by the inverse of its photon-noise variance. This is a minimum-variance estimate of the convolution. In the spectra plotted, the resolving power has been set to 400 in the blue channel, 300 in the red, and 200 in the IR, performed with this inverse-variance-weighting technique. Notice that the resolution in the red and IR is such that individual strong OH lines have little impact on the spectra; they are sufficiently densely distributed and downweighted by the inverse-variance weighting that they are hardly noticeable.

The spectra are plotted in units of "nanomaggies", a unit of flux used by the SDSS, defined such that 1 maggie is the flux from an AB=0 object, 3631 Janskys. Then 1 nanomaggie is equivalent to an apparent AB magnitude of 22.5, or 3631×10^{-9} Jansky, $3.631 \times 10^{-29} ergs/s/cm^2/Hz$.

Figure 2.6 shows these spectra given the throughputs and S/N for galaxies which are $L*$ today at $z = 1.5$ observed with a 5000 second exposure; note the 4000Å break, here redshifted to 1.0μm. These are beautiful spectra, from which very accurate redshifts and SEDs can be determined.

Next is the same exposure time on a galaxy at $z = 2.0$, in Figure 2.7. Lower S/N, but still quite usable spectra; determining redshifts and detailed SEDs is quite easy. At slightly larger redshifts,

the 4000Å break, here at 1.2 microns, moves beyond the wavelength range of the spectrograph, and the job becomes *very* much more difficult:

Figure 2.8 repeats this exercise at $z = 2.5$. For this example, the exposure time has been increased significantly to 30,000 seconds, i.e., over eight hours, to represent a deep exposure with PFS. The spectrum now covers the rest-frame ultraviolet, extending to 3700Å in the rest frame. The UV spectra of galaxies tend to have weak absorption lines, but they are still detectable at this S/N, meaning that redshifts and stellar populations will be discernible from these spectra. Note that 0.1 nanomaggies corresponds to a continuum AB magnitude of 25. While these are usable, note the enormously more difficult task to interpret the spectra once the 4000Å break is beyond the wavelength range of the spectrograph, which it is at z=2.5. We can still see the λ3727 emission if it is present, but absorption redshifts will be very difficult to obtain without very long exposure times.

Finally, as a test of our sensitivity to emission lines, please see Figure 2.9. A model spectrum was made with no continuum and an unresolved emission line (i.e., width set by the resolution of the spectrograph) every 33Å. The flux of each line is indicated in the figure. The flux density corresponds to an emission line with a luminosity of 2×10^{42} erg/sec at redshifts 2.0 (where [OII] would be at 1.11μm), 3.3 (Lyα at 0.52μm), and 4.3 (He II 1640 at 0.87μm), respectively. For comparison, the $z = 6.96$ Lyman α emitter (at 0.97μm) discovered by Iye et al. (2006) with Suprime-Cam has a flux of 2×10^{-17} erg/s/cm^2, and a luminosity of 1×10^{43} erg/s. At the positions of the strong sky lines, the weakest emission lines are undetected, but they are easily detected in this short exposure at all other wavelengths. This exercise indicates that one can detect λ3727 emission for the BAO survey with quite short exposures over the whole accessible wavelength range. Rhoads & Malhotra (2001) have found a surface density of 1 Lyα-emitting galaxy per square arcminute with redshift between 4 and 5; with flux above 2×10^{-17} erg/s/cm^2, so a complete survey of these objects would require two or three pointings of the spectrograph to fully sample these objects.

2.6 The Next Steps

This white paper represents only the first steps in developing the science case and instrument design for PFS. Here we outline briefly the obvious next analyses we hope to do.

2.7 Science and Survey Design

Much more detailed calculations need to be done of the number densities of galaxies as a function of redshift. We have not discussed how the samples of these objects will be selected. We need to make precise calculations of the ability to measure baryon acoustic oscillations as a function of redshift; this will depend on the solid angle covered and the number density of objects for which we measure redshifts. We similarly need to model the extent to which we will be able to recover spectral properties of galaxies (stellar populations, velocity dispersions, parameters of emission lines, AGN diagnostics, etc.) as a function of redshift and signal-to-noise ratio. With these estimates, we can move forward to designs for various surveys to be carried out with the

spectrograph; a survey optimized for BAO will not have the same characteristics as those focused on galaxy evolution at $z = 2$, reionization at $z = 6$, calibration of photometric redshifts, or stellar dynamics in the outer halo of the Milky Way.

More realistic simulations of galaxies, including the effects of merging (early galaxies were lower mass than present-day galaxies), dust, emission lines, and other features, need to be incorporated in the estimates of the spectral quality and what we will be able to measure from these spectra.

2.8 Spectrograph Design

The design presented here, while very promising, should be considered a strawman. More work is needed on all aspects of it. Gunn and Carr are focusing on the optics design and the mechanical design of the cameras, which clearly need work. And of course the project depends on the ability to manufacture tapered fibers, which is under active investigation by the LNA group in São Paulo.

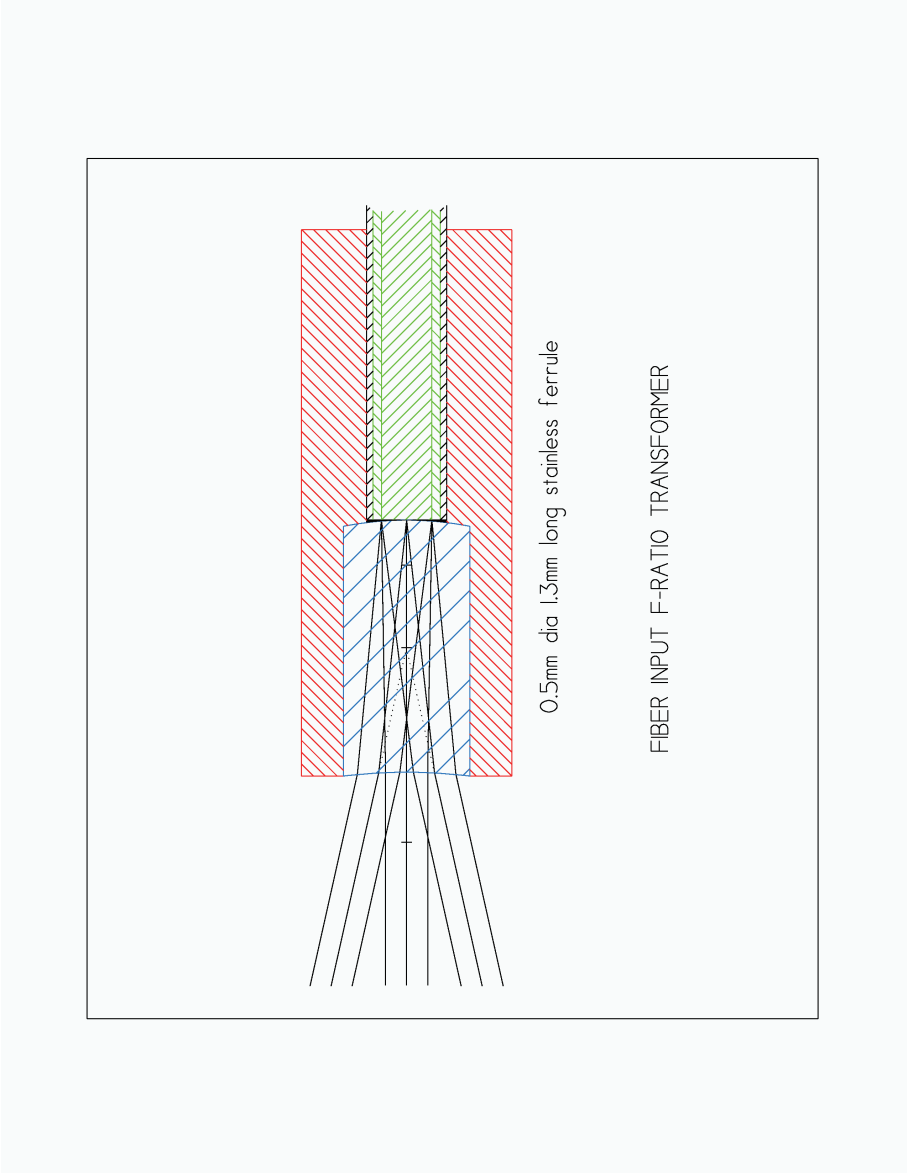

Figure 2.3: The microlens f-ratio converter in an entrance ferrule. The lens is 300 μm in diameter and 600μm long. The index of the glass is 1.69, and the space between the convex rear face of the lens and the flat fiber end is filled with a silicone coupling compound with an index of 1.33. The losses if the front face is coated are less than 2 percent. The input focal ratio is $f/2.24$ and the output is $f/2.8$.

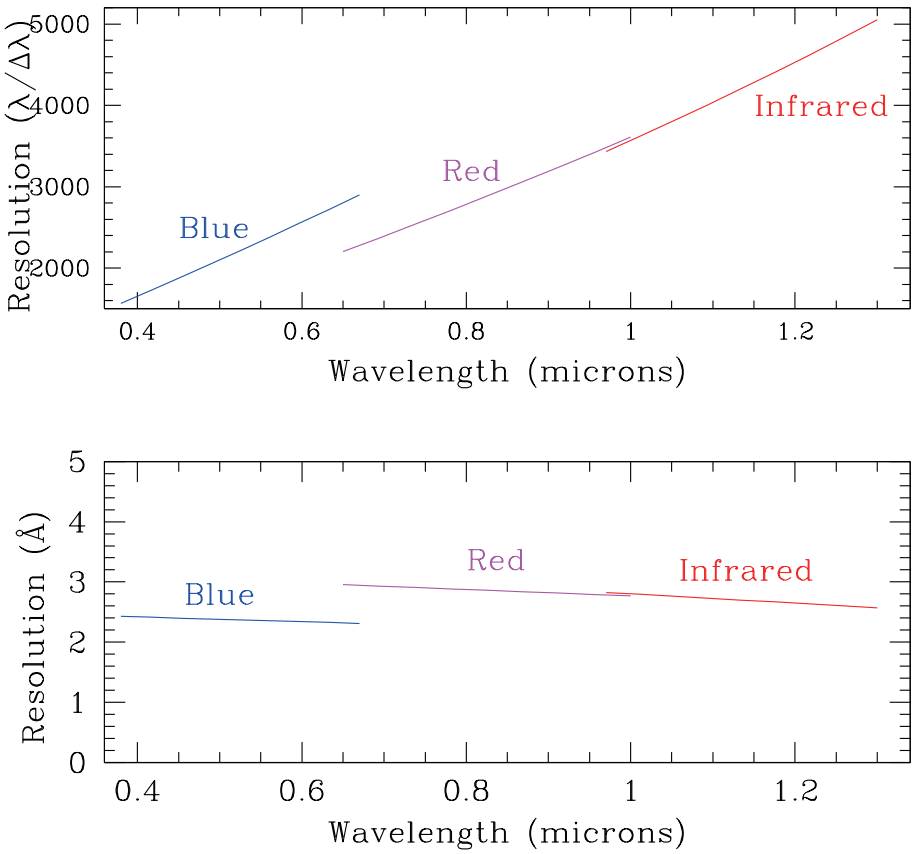

Figure 2.4: Design resolution (expressed as a fraction in the upper panel, and in Ångstroms in the lower panel) for each of the three arms of the spectrograph.

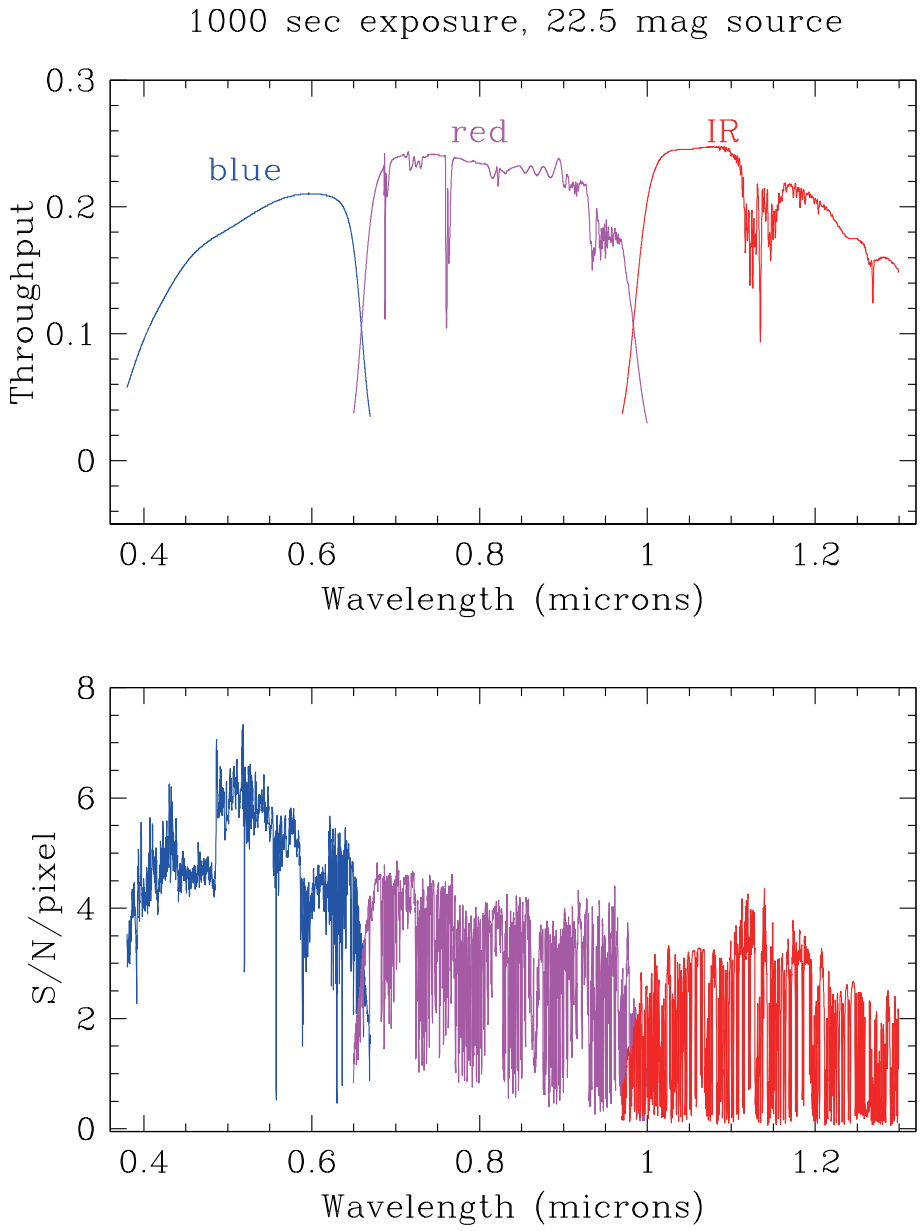

Figure 2.5: Top panel: The computed throughput of the spectrograph for a point source, including losses in the atmosphere, telescope, fibers, instrument optics, gratings, and detectors. Lower panel: The signal-to-noise ratio *per pixel* for a 1000-second exposure on a star with AB magnitude $m = 22.5$ at each wavelength. An airmass of 1.3 is assumed. The discontinuity at 4900Å is an artifact of the sky model assumed.

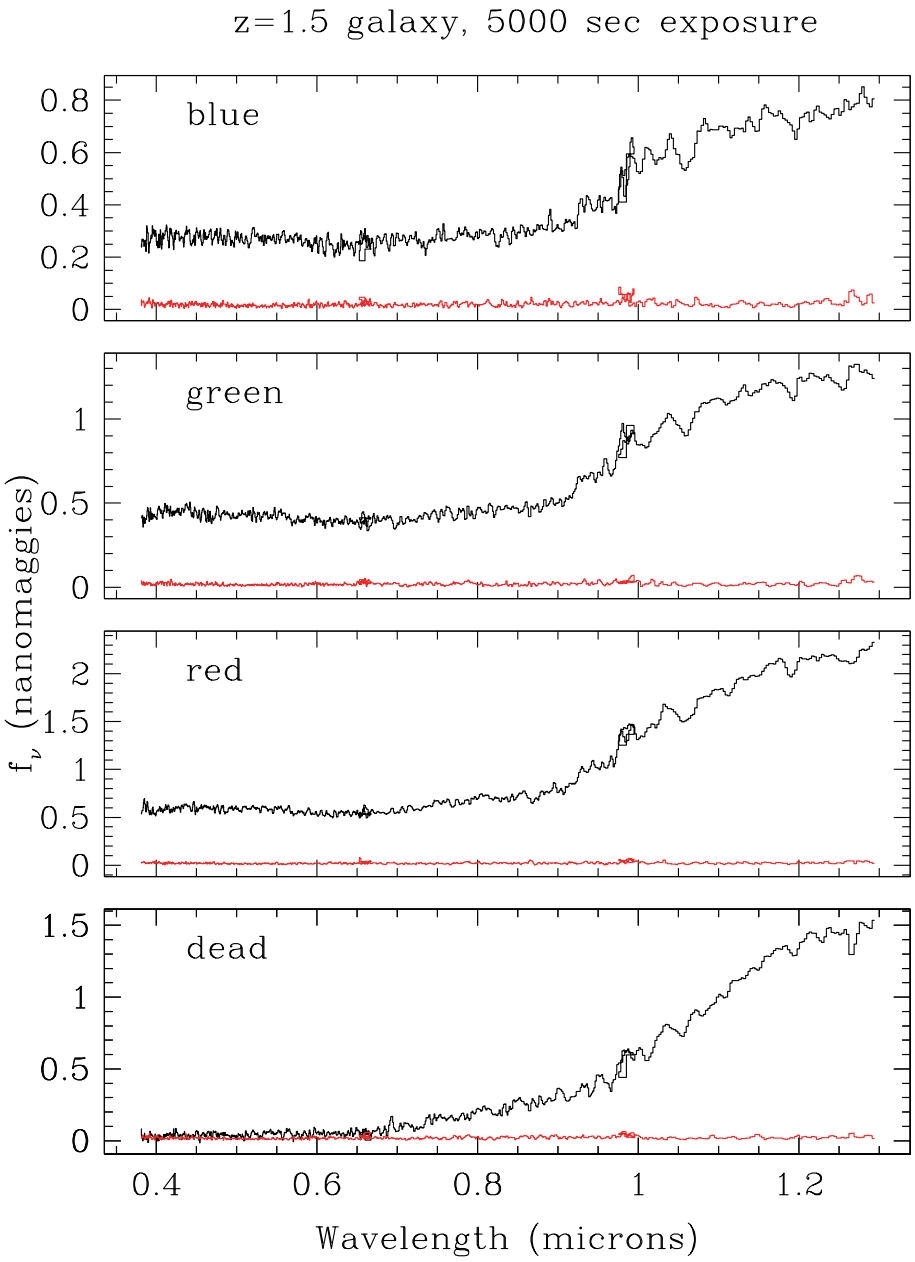

Figure 2.6: Spectra of blue, green, red, and dead galaxies (i.e., with decreasing amounts of current star formation) at $z = 1.5$, all of which will evolve (without mergers) to an L_* galaxy today. A 5000 sec exposure is assumed, and the spectra have been smoothed to a resolution of 400 in the blue, to 200 in the red, to increase S/N. The error per pixel (binned to be critically sampled given the lower resolution) is shown in red in each panel. Note the 4000Å break, here redshifted to 1 micron.

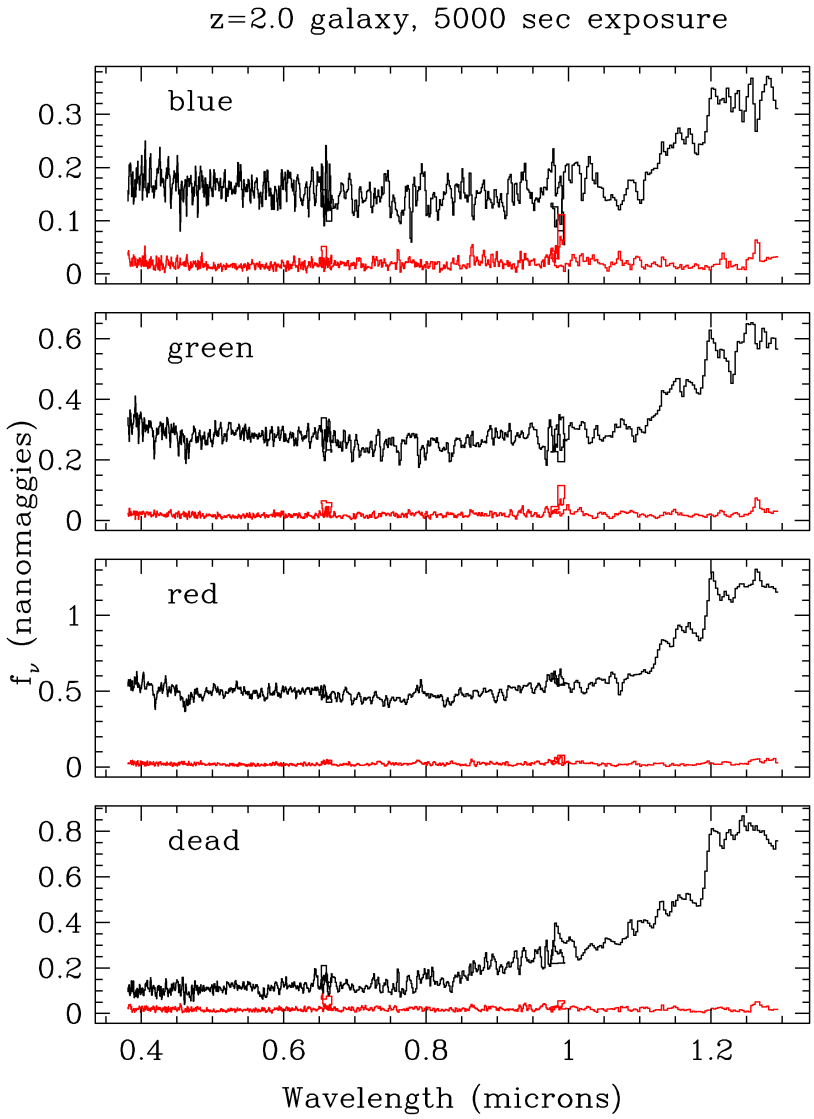

Figure 2.7: Spectra of blue, green, red, and dead galaxies (i.e., with decreasing amounts of current star formation) at $z = 2.0$, all of which will evolve (without mergers) to an L_* galaxy today. A 5000 sec exposure is assumed, and the resolution of the spectra has been reduces as discussed, to increase S/N. The error per pixel (binned to be critically sampled given the lower resolution) is shown in red in each panel. Note the 4000Å break, here redshifted to 1.2 micron. In all cases, even the very difficult blue galaxy, a redshift is easily found and the SED is well measured.

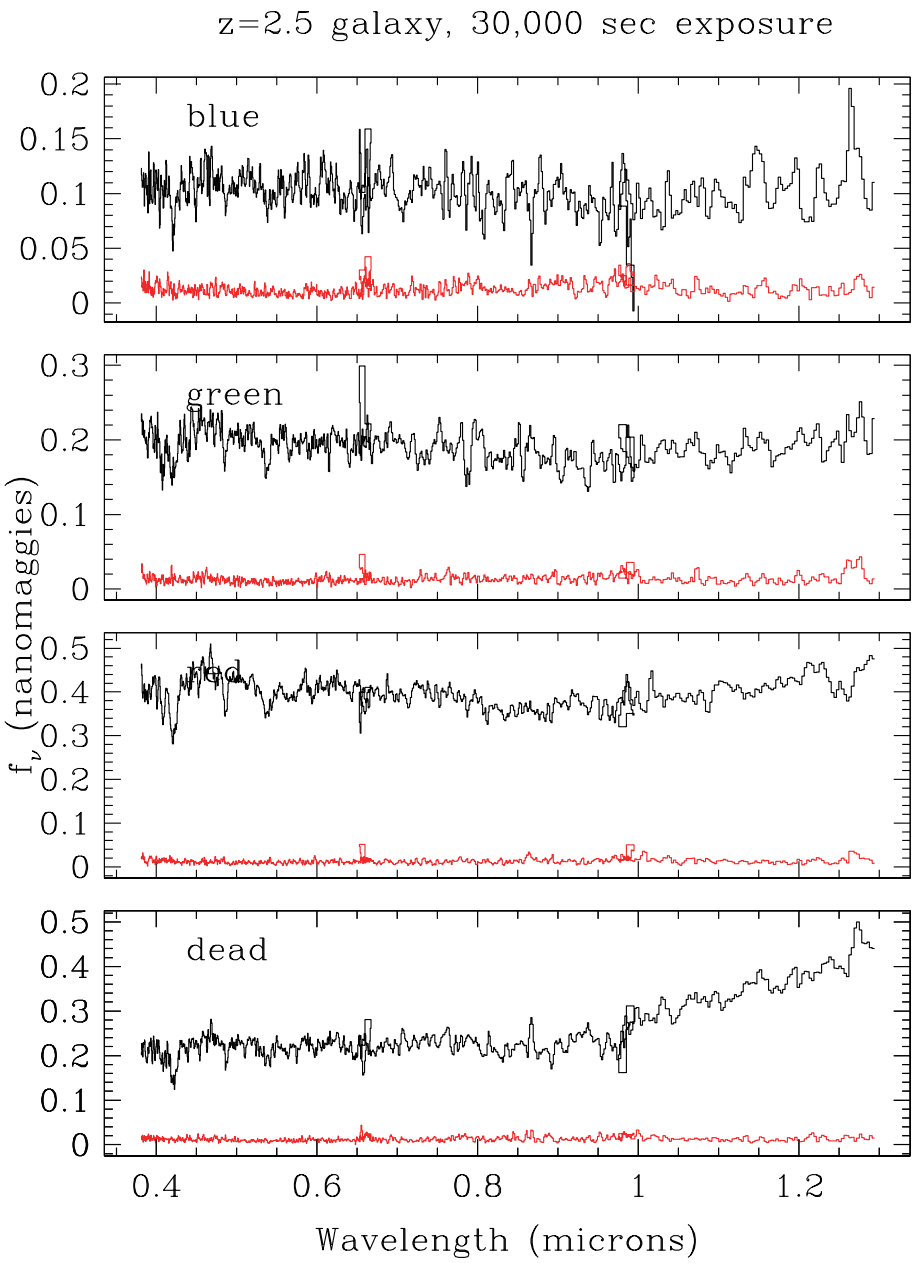

Figure 2.8: As in Figure 2.7, now at redshift 2.5, and assuming a deep exposure of 30,000 seconds. The blue galaxy was far less massive than the red galaxy at high redshift, and the (currently) red galaxy was forming stars at a much higher rate at $z = 2.5$ than the (currently) blue galaxy, which is why the flux in the ultraviolet is considerably stronger.

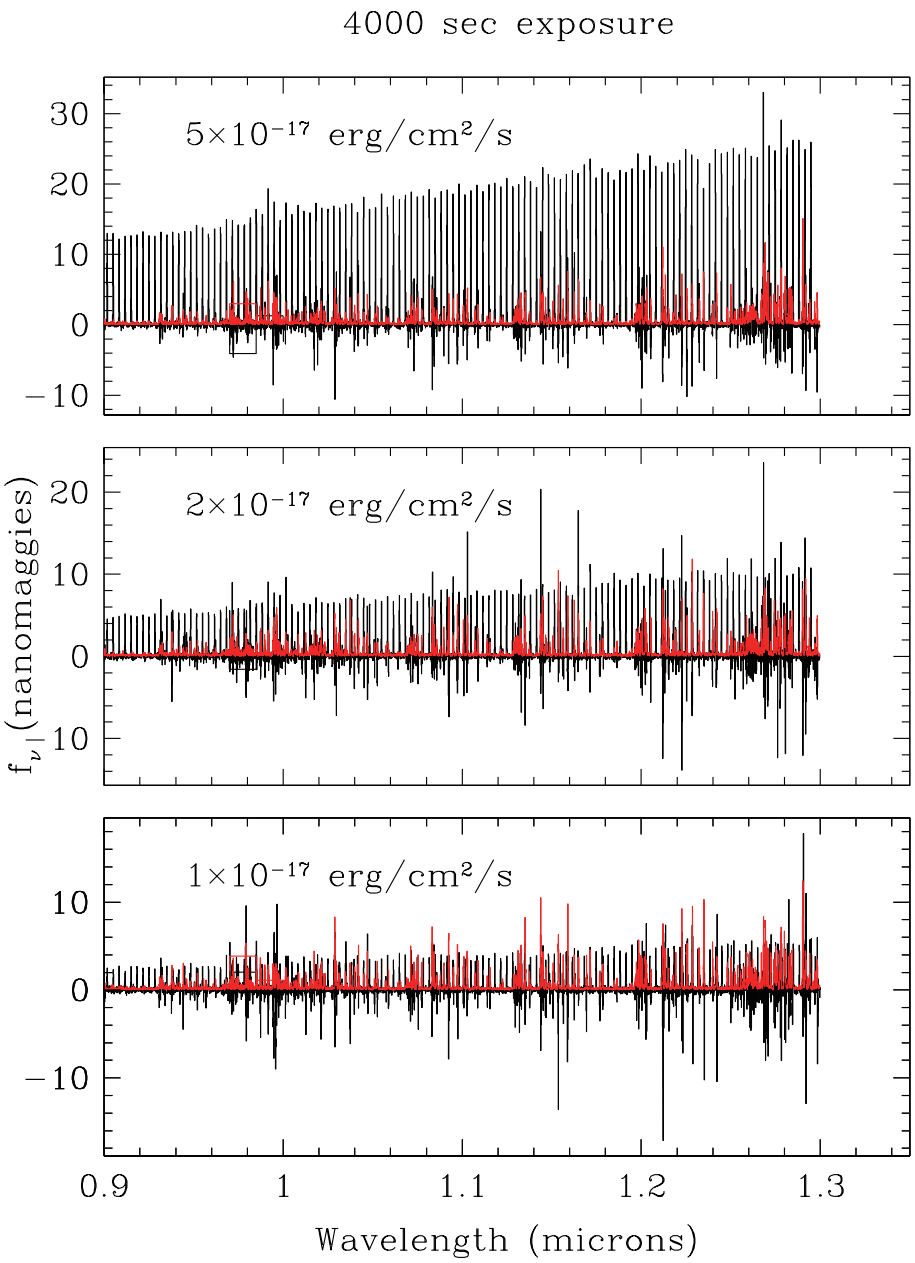

Figure 2.9: A model spectrum consisting of a regular series of unresolved emission lines of flux as given in each panel. The continuum is set to zero. A 1000-second exposure is assumed. The red line shows the estimated error per pixel. Just the red end of the spectrum is shown; in the blue, emission lines of even 1×10^{-17} erg/sec are detected at many sigma at essentially all wavelengths.

3 HSC Survey

The great strengths of the SuMIRe surveys come from the combination of imaging and spectroscopic surveys, which can be indeed done with HSC and PFS (see Chapter 1 for exampled SDSS achievements). In fact the unique depth and image quality of the Subaru Telescope will promise to allow a lot of science cases by having the imaging and spectroscopy surveys. Of course note that, to make this synergy happen, we need to observe the same region(s) of sky with HSC and PFS.

The HSC collaboration which consists of scientists from Japan, Taiwanese institutes and Princeton University is now planning to carry out three surveys with HSC, the HSC-wide, deep and ultra-deep surveys, which are different in the depth and sky coverage. Table 3.1 gives a summary of the HSC surveys, although the final decision on the survey design will be made before the HSC survey will start from the mid of 2012. The HSC-wide, -deep and -ultra-deep surveys are complementary to each other, and having the three survey layers will allow us to cover a broad range of science topics, ranging from solar system to cosmology. The HSC surveys will also offer a synergy with various other surveys: the SDSS-III BOSS survey, the Atacama Cosmology Telescope survey (which has been mainly led by Princeton), the Planck CMB experiment, the Astro-H project, the eROSITA, ALMA, and the Thirty Meter Telescope (TMT). The PFS is not an exception, and the PFS will be an ideal instrument for us to make a follow-up spectroscopic observation of targets that are found by the HSC imaging surveys. In the following chapters we will in detail describe science cases that are possible to carry out with PFS, where the pre-existing HSC survey data are often assumed to find targets for the spectroscopic follow-up.

Table 3.1: A summary of HSC imaging surveys

Survey	Area [sq. deg.]	Depth [AB, 5σ, $2''$]	Key Sciences
Wide	1500-2000	$grizy$ ($i \sim 25.8$)	Cosmology, Clusters, QSOs
Deep	$\sim$30	$grizy$+NBs ($i \simeq 27.2$)	Galaxies, QSO/AGN, Clusters, SNe
Ultra-Deep	$\sim$2 HSC FoVs	$grizy$+NBs ($i \simeq 28$)	high-z galaxies (LAEs, LBGs), SNe

Table 3.2: Survey parameters (passbands, depth, area) and key science cases for the planned HSC-wide, -deep and -ultra-deep surveys (the credit: the HSC collaboration). The final decision on the details of each surveys will be made until the survey will start from the mid of 2012. For all the three surveys the broadband imaging survey ($grizy$) is planned, in different depths, area coverages and cadences. For the HSC-deep and ultra-deep surveys the narrow-band (NB) filter surveys are also planned. It is still under discussion on which narrow band filters (its central wavelength and width) will be used. The HSC survey regions (which are to be determined) will be overlapped with the regions where other data sets are available; e.g. the Atacama Cosmology Telescope survey, the SDSS survey, other spectroscopic surveys, and near infrared data (e.g., VIKING and UKIDSS).

4 Cosmology with SuMIRe HSC/PFS Survey

Masahiro Takada (IPMU), John A. Peacock (Edinburgh), Atsushi Taruya (Tokyo), Kazuhiro Yamamoto (Hiroshima), Richard Ellis (Caltech), John Silverman (IPMU), Jean-Pual Kneib (Marseille), Atsushi Nishizawa (IPMU), Hironao Miyatake (Tokyo), et al.

4.1 Executive Summary

The Subaru Measurement of Images and Redshifts (SuMIRe) is a joint experiment project of wide-field imaging and redshift surveys aimed at exploring the nature of dark energy as well as the growth of structure formation on cosmological scales by combining the *different* methods; weak gravitational lensing, baryonic acoustic oscillation (BAO), cluster counting statistics and probably also Type-Ia supernovae. By fully utilizing the unique capabilities of new prime-focus instruments, Hyper Suprime-Cam (HSC) and Prime-Focus Spectrograph (PFS), with about 1.5 degree diameter field-of-view, we can obtain imaging data of a billion of galaxies and redshifts of a few millions of galaxies (and QSOs). The requirements on the PFS design to maximize scientific outputs from the SuMIRe surveys are: 2000–3000 fibers to target 2200 galaxies per the PFS field-of-view and the spectral resolution $R \simeq 3000$ for wavelength coverage 600–1000nm in order to survey galaxies over redshift range $0.6 \lesssim z \lesssim 1.6$ and to detect absorption/emission lines of each galaxies with high signal-to-noise ratios ($S/N \gtrsim 10$) for an exposure time of 15min per field. Thus the SuMIRe survey offers an exciting opportunity to map the three-dimensional distributions of dark matter, galaxies and clusters over a wide range of redshifts extending out to $z \simeq 1.6$. We will combine the imaging and redshift data sets of the *same* sky region and from the *same* telescope in order to conduct the dark energy experiments and to test gravity on cosmological scales, by minimizing systematic errors inherent in each methods. The unique data sets also enable us to study various additional science cases such as galaxy evolution.

The HSC wide-field, multi-color (*grizy*) survey covering about 2000 square degree area is now being planned to start from 2012 for 5 years and will enable us to measure weak lensing signals of distant galaxy images as a function of angular scales and redshifts as well as to find massive clusters out to $z \simeq 1.5$ based on the available photometric redshift information (its high-redshift sensitivity thanks to the presence of deep y-band data). By maximizing an overlap of the HSC survey region with the survey region of the Sunyaev-Zel'dovich experiment with the Atacama Cosmology Telescope (ACT), the robust cluster experiment becomes available by using the combined mass-proxy relations from all the available optical, lensing and SZ information. Another survey mode, the multi-color, multi-epoch "deep" survey with HSC covering a few tens of square degree field, is also planned, which enables us to find supernovae at high redshifts and then carry out the luminosity distance experiments if the spectroscopic follow-up campaign to obtain their redshifts is properly coordinated.

However, the most damaging systematic errors inherent in the imaging-based experiments arise from photometric redshift errors (e.g. Huterer & Takada 2005; Huterer et al. 2006; Nishizawa et al. 2010). The photometric redshift errors can be robustly calibrated by carrying out a spectroscopic redshift survey with PFS for the HSC survey region delivering spectroscopic redshifts for a few millions of galaxies. More promisingly the PFS redshift survey itself enables us to carry out the BAO experiment using galaxies over a redshift range of $0.6 \lesssim z \lesssim 1.6$, which can have a similar-level constraining power of dark energy with the HSC dark energy experiments and is complementary to the existing/ongoing BAO surveys such as the SDSS and BOSS surveys that cover the range $0 \lesssim z \lesssim 0.65$. The target galaxies for the PFS survey can be delivered from the sufficiently deep HSC data. The redshift distortions due to peculiar velocities of galaxies, if robustly measured, can be used to further improve the cosmological constraints as well as the ability to test gravity on cosmological scales.

Using the model sky spectrum in red wavelengths of interest, we conclude that 15 min exposure is sufficient to detect [OII] emission line of target galaxies for each field. Also, by having about 2400 fibers, we can cover cosmological volumes over redshifts $0.6 \lesssim z \lesssim 1.6$ with sufficient number densities of target galaxies in each redshift slice, allowing us to measure the galaxy power spectrum over the wide range of redshifts with sufficiently high precision. Hence, to cover about 2000 square degrees, fully overlapped with HSC survey, the PFS BAO survey needs ∼50 clear nights (70 nights if including a weather factor of 0.7). When combined with HSC cosmological constraints, the SuMIRe HSC/PFS surveys give the Stage-IV level dark energy constraints. Furthermore, if additional multi-color imaging data are available for other patches of the sky, which is indeed very likely in the PFS era, e.g. from a very shallow survey with HSC, DES and/or LSST the unique PFS multiplicity will enable us to quickly enlarge the surveyed area in order to further improve the cosmological constraints. A more sophisticated arrangement of the PFS observational strategies per target field will be required to maximize other science cases: for example, if the PFS BAO survey includes several fields with much deeper exposures per field such that continuum spectra of target galaxies are detected with good S/N, such a survey will provide us with a unique, homogeneous catalog of galaxy spectra that is not affected by cosmic-variance uncertainties. Such a redshift data set can be used to carry out various galaxy studies and also can be used to calibrate photo-z errors, which are most significant systematic errors for the planned imaging surveys, HSC, DES, Euclid and LSST.

Table 4.5 will summarizes the cosmological powers of HSC, PFS and the SuMIRe HSC/PFS joint experiment for constraining dark energy parameters, neutrino masses and primordial non-Gaussianity parameter.

4.2 Background

4.2.1 The challenge of cosmic acceleration

The most radical conclusion of cosmological research in the late 20th Century was that the expansion of the universe has not decelerated as expected from the gravitational effect of the matter it contains. The most direct evidence for this statement emerged from studies of SNe Ia treated as

standard candles (Riess et al. 1998; Perlmutter et al. 1999). The initial reaction to these observations has been to assume that the universe contains a cosmological constant, Λ, and this is a natural path to follow given that Λ has been a potential feature of cosmological models from the start of the subject. With this addition, the Λ plus cold dark matter (ΛCDM) model of structure formation accounts extremely well for a range of data, and has survived the astonishing advances in Cosmic Microwave Background (CMB) data from the Wilkinson Microwave Anisotropy Probe (WMAP) and other experiments (e.g. Komatsu et al. 2010).

Nevertheless, this is not a satisfactory state of affairs. Following Zel'dovich, modern practice is to place the term on the right hand side of Einstein's field equations and to interpret it as the energy density of the vacuum. Discovering the physical origin of such a density is challenging because the value is extremely small compared to any natural particle physics scale (e.g. see Frieman et al. 2008, for a recent review). As a result, the term "dark energy" is often used to encapsulate our ignorance of the detailed physics that is being probed.

Alternatively, it is possible that the phenomenon of dark energy is entirely illusory. The necessity for this constituent arises from using the Friedmann equation to describe the evolution of the cosmic expansion; if this equation is incorrect, it would require the replacement of Einstein's relativistic theory of gravity with some new alternative (e.g. Jain & Khoury 2010, for a recent review). Either of these alternatives offers an exciting door to new possibilities in physics, and current cosmological research is absorbed with exploring techniques that can play a decisive role.

4.2.2 Dark energy observables

Dark Energy can differ from a classical cosmological constant in being a dynamical phenomenon. Empirically, this means that it is endowed with two thermodynamic properties that astronomers can try to measure: the bulk equation of state and the sound speed. If the sound speed is close to the speed of light, the effect of this property is confined to very large scales, and mainly manifests itself in the large-angle multipoles of the CMB anisotropies (Caldwell et al. 1998; Takada 2006) The equation of state, however, is more readily probed. This is quantified via the equation of state parameter $w \equiv p_{\rm de}/\rho_{\rm de}$ (in the unit of the speed of light $c = 1$), which can in principle be an evolving function of scale factor, $w(a)$.

For adiabatic expansion, we should in general regard as giving the logarithmic rate of change of the dark-energy density, $-3(1+w)d\ln\rho_{\rm de}/\ln a$, so the Friedmann equation describing the Hubble expansion rate is given as

$$H^2(z) = H_0^2\left[\Omega_{\rm m0}(1+z)^3 + \Omega_{\rm r0}(1+z)^4 + \Omega_{\rm de0}e^{\int_1^a da'3[1+w(a)]d\ln a'} - (1-\Omega_{\rm tot})(1+z)^2\right], \quad (4.1)$$

where $1+z = 1/a$, $H_0 = 100h$ km s^{-1} is the Hubble parameter, and $\Omega_{\rm m0}$, $\Omega_{\rm de0}$ and $\Omega_{\rm r0}$ are the present-day energy density parameters of matter, dark energy and radiation in units of the critical density ($\Omega_{\rm tot} \equiv \Omega_{\rm m0} + \Omega_{\rm de0} + \Omega_{\rm r0}$). The last term on the r.h.s. of the equation above is the curvature term as predicted from general relativity. The change in the expansion rate is observed in two ways: via the geometry of the universe and via the growth of density perturbations.

The distance-redshift relation is one of the chief diagnostics of $w(a)$. The general definition of comoving angular diameter distance $D_A(z)$ is

$$D_A(z) = \begin{cases} R_0 \sin \chi(z)/R_0, & \Omega_{\rm tot} > 1 \\ \chi(z), & \Omega_{\rm tot} = 1 \\ R_0 \sinh \chi(z)/R_0, & \Omega_{\rm tot} < 1 \end{cases} \tag{4.2}$$

where $R_0 \equiv 1/(H_0\sqrt{|\Omega_{\rm tot} - 1|})$ and $\chi(z) \equiv \int_0^z dz'/H(z')$. Any standard length in the universe, such as those defined by the pattern of large-scale structure, thus subtends an angle involving $D_A(z)$ if seen transverse to the line of sight, or a redshift increment involving $H(z)$ if seen radially. In detail, these aspects can be separated, although it is frequently convenient to introduce (Eisenstein et al. 2005) to approximate what is measured if we have data sets that average over radial and transverse orientations.

Cosmic structure formation is driven by gravitational instability due to inhomogeneities of matter distribution (mostly dark matter) in the universe. The density fluctuations $\delta \equiv \delta\rho_m/\bar{\rho}_m$ (denoting the fractional density perturbation) grow as a function of scale factor as $\delta \propto a$ at early times, while the universe is matter dominated and curvature can be neglected. But when dark energy becomes important at late times, this growth is reduced, in a way that depends on the amount of dark energy, and also on its equation of state. We incorporate this into a growth suppression factor, $\delta \propto ag(a)$, where $g(a)$ carries the information about the dark sector. Note that in linear regime, where $\delta \ll 1$, all Fourier modes of the density fluctuations grow at the same rate. As we will show, $g(a)$ can be probed in a number of ways, either by estimating the mass fluctuations directly, or by measuring the peculiar velocities associated with their growth. The principal tools for achieving this are galaxy clustering, weak lensing and the counting statistics of galaxy clusters. SuMIRe HSC and PFS surveys allow us to explore all these methods.

The three key quantities $H(z)$, $D_A(z)$ and $g(z)$ are all sensitive to dark energy, but how strongly? Figure 4.1 shows what happens when we perturb these quantities about a fiducial $\Omega_{\rm m0} = 0.24$, $w = -1$ model (assuming a flat universe). In general, the observables respond rather slowly to changes in w, showing a sensitivity multiplier of about 5 (e.g. Peacock et al. 2006), so that a measurement of w to 1% precision requires knowing D_A to 0.2%. Furthermore, there is substantial degeneracy with $\Omega_{\rm m0}$, so that the matter density has to be known well in order to detect the redshift-dependent effect of a change in w on any of the observables. But the good news is that the degree of degeneracy is different for different observables, especially the growth rate. There is therefore a good prospect for attaining a robust measurement of the equation of state of dark energy if all the observable signatures can be accessed.

4.2.3 The evolution of dark energy

Early studies of dark energy tended to treat w as a constant, but physical models for dark energy tend to be dynamical, so the equation of state is almost certain to evolve. Given the lack of a unique model, the simplest non-trivial parametrization is (Chevallier & Polarski 2001; Linder 2003);

$$w(a) = w_0 + w_a(1 - a). \tag{4.3}$$

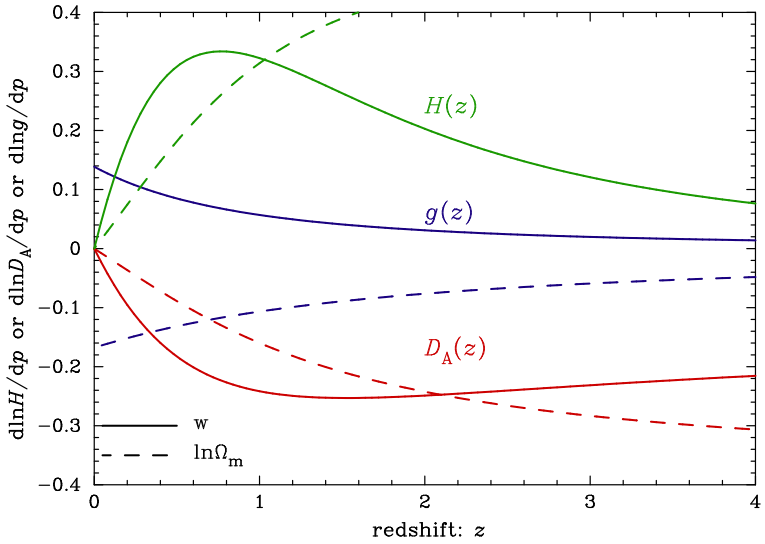

Figure 4.1: Variations in the Hubble expansion rate $H(z)$, the angular diameter distance $D_A(z)$, and the growth rate $g(z)$ against redshift z when the parameters $\Omega_{\rm m0}$ and w are changed by 1 and 10%, respectively, from their fiducial values ($\Omega_{\rm m0} = 0.24$ and $w = -1$; other parameters kept fixed). The growth rate is normalized at $z \simeq 1100$, so as to give the similar CMB anisotropy amplitudes at the redshift. The parameter p refers to either $\ln \Omega_{\rm m0}$ or w: the solid curves show the effect of an increase in w, while the dashed curves show the effect of an increase in $\Omega_{\rm m0}$.

When the evolving model is matched to data, typically a strong correlation is seen between the inferred values of w_0 and w_a. This correlation is readily understandable: the bulk of the sensitivity comes from data at non-zero redshifts, so the $z = 0$ value is an unobserved extrapolation. It is better to assume that we are observing the value at some intermediate pivot redshift:

$$w(a) = w_{\rm pivot} + w_a(a_{\rm pivot} - a). \tag{4.4}$$

The pivot redshift is defined so that $w_{\rm pivot}$ and w_a are uncorrelated; in effect rotating the goodness of fit contours on the w_0-w_a plane.

As will be seen below, the pivot redshift for most experiments tends to be close to $z = 0.6$, reflecting the fact that (1) w manifests itself in an integrated signal that builds up from $z = 0$; (2) if dark energy is close to Λ in its behavior, the contribution becomes sub-dominant and hard to measure for $z \gtrsim 1$. Thus, a first order view of the situation is that different experiments will measure $w(z = 0.6)$ and an uncorrelated estimate of how rapidly it evolves at that time, w_a. The US Dark Energy Task Force (DETF) (Albrecht et al. 2006) advocated a figure of merit, which is the reciprocal product of these two uncertainties, i.e., reciprocal of the area of the error ellipse in the w_0-w_a plane. However, it is not clear that this is the best choice: as long as Λ matches the data, the initial challenge is to rule out this $w = -1$ model, so there could be a case for trying to optimize the accuracy of measuring $w_{\rm pivot}$, independent of evolution. But one could also envisage models that have $w_{\rm pivot} = -1$ and yet show $w_a \neq 0$; it really depends on one's prejudice on how realistic models might occupy the w_0-w_a plane. In practice, the axial ratio of the confidence ellipse is large, so that errors in w_a are around 10 times those in $w_{\rm pivot}$. Thus, if plausible models occupy a small region near $(w_0, w_a) = (-1, 0)$, they are much more likely to be detected via their effect on $w_{\rm pivot}$ than via w_a.

But adopting the assumption that Λ will eventually be rejected, measuring evolution would then be the next goal. For this reason, steps have already been taken to go beyond the simple figure of merit, and the Figure of Merit Science Working Group (FoMSWG) has produced a more elaborate proposal (Albrecht et al. 2009). This concentrates on how many independent modes in $w(a)$ a given experiment can measure, and is certainly an attractive approach once we are sure that a cosmological constant is rejected.

4.2.4 Modified gravity

Current inferences concerning the presence of dark energy rest on the assumption of the Friedmann equation, based on Einstein's gravitational field equations. Independent of this, there has been growing emphasis in the community on the idea of testing Einstein's General Relativity. In fact, we have little idea how to approach cosmology without retaining much of the structure of the standard relativistic treatment.

In four-dimensional space time its metric, which slightly deviates from a homogeneous and isotropic universe, is without loss of generality described in terms of two scalar-mode perturbations (Bertschinger 2006):

$$ds^2 = -(1+2\Phi)dt^2 + a^2(1-2\Psi)d\boldsymbol{x}^2 \tag{4.5}$$

Here, t is cosmological time and $a^2 d\boldsymbol{x}^2$ is the spatial part of the metric; this must still be of the standard Robertson-Walker form, since this is dictated only by symmetry. However, the time evolution of $a(t)$ governs the gravitational field equations that can be different from Einstein's equations if gravity is modified. Observational cosmology survives unchanged, since photon trajectories are still null. The redshift is still such that $1+z$ gives the factor by which the universe has expanded since the light we now see was emitted, and the normal relation between comoving distance and redshift still applies: $\chi(z) = \int_0^z dz' 1/H(z')$. Hence, even if gravity is modified, such a model needs to give the distance-redshift relation that well matches the observed cosmic acceleration.

This exact degeneracy between dark energy and modified gravity can be broken when we consider a perturbed universe and look at the relation between matter and the metric perturbations (e.g. Jain & Zhang 2008; Guzik et al. 2010). This is simplified in Einstein gravity because the perturbations Φ and Ψ are both equal to each other, recognised as the Newtonian potential, which satisfies the Poisson equation (when non-relativistic matter dominates). As a result, the growth law for fractional density fluctuations is rather simple, and can be represented accurately by Peebles' approximation for the logarithmic growth rate: $f_g(a) \equiv d\ln\delta/d\ln a \simeq \Omega_{\rm m}(a)^{0.55}$. Linder (2005) suggested that a similar representation might capture the main behavior in modified gravity models:

$$f_g(a) \equiv \frac{d\ln\delta}{d\ln a} \simeq \Omega_{\rm m}(a)^{\gamma}. \tag{4.6}$$

In Einstein gravity, the approximation $\gamma \simeq 0.55 + 0.05\,[1+w(z=1)]$ works very well, so the growth rate is roughly universal for a given expansion history in conventional gravity theories. But for modified gravity, this need not be so: the number γ emerges as an important additional parameter in testing the consistency of the standard framework.

Within this framework, the freedom to depart from Einstein gravity lies in the relation between matter and space-time curvature. This is described by the field equations that result from adding

a gravitational action to the matter action, and the EinsteinHilbert action is as simple as possible: proportional to the Ricci scalar R. A natural line of attack is then to replace this by something more complicated: e.g., $R \rightarrow R + f(R)$, where $f(R)$ is some function that becomes negligible at large R so that local tests of gravity are not affected (e.g. Hu & Sawicki 2007a). There is enough freedom in this framework to account for any expansion history of the universe without dark energy, simply by choosing an appropriate $f(R)$. This means that there is a modified Friedmann equation; it contains familiar elements such as the density parameter, since $H(z)$ and $\rho(z)$ still define a density parameter in the usual way, but now $\Omega = 1$ is no longer required in order for the universe to be flat.

The most interesting possibilities of this sort to emerge from recent work are modifications motivated by the predictions from string theory of the existence of higher dimensions. The hidden scale associated with these dimensions allows a scale dependence of the strength of gravity, which can mimic cosmic acceleration. For example, in the DGP model (Dvali et al. 2000), we have the relation

$$H^2(z) = H_0^2 \left(\frac{1 - \Omega_{\rm m0}}{2} + \sqrt{\left(\frac{1 - \Omega_{\rm m0}}{2} \right)^2 + \Omega_{\rm m0} a^{-3}} \right)^2 , \tag{4.7}$$

(neglecting radiation), so that the universe tends to a de Sitter model with constant H even without an explicit vacuum energy. This model provides a direct demonstration that an accelerating universe need not require the existence of a physical dark-energy component. The growth of perturbations in the DGP model can be accurately described by Linders model with $\gamma \simeq 0.68$; this is almost 25% larger than the value in a Λ-dominated universe, and we show below that relatively modest surveys using PFS would be capable of detecting this difference. The specific DGP model is probably already ruled out using supernova data (e.g. Song et al. 2007); but it has played an important role in persuading the community that the density growth rate should be treated as a key cosmological diagnostic.

A key requirement arising from our study is the need for PFS to address more advanced models of this general type. Specifically we wish to both improve our understanding of dark energy along the conventional route of measuring w and its possible evolution, as well as to test whether dark energy might arise from inadequacies in General Relativity. In particular, as we will describe below, the SuMIRe HSC and PFS surveys are powerful to constrain the expansion history and the growth rate of cosmic structures separately, by combining weak lensing, galaxy clustering and the counting statistics of galaxy clusters.

4.3 Cosmology with SuMIRe HSC/PFS galaxy surveys

4.3.1 HSC imaging survey

Let us start our discussion with the planned HSC survey which will give an ideal, pre-imaging data set to identify target galaxies for the PFS redshift survey. We are currently planning to carry out three different surveys (wide, deep and ultra-deep) with HSC, and Table 4.1 gives survey parameters of the planned HSC-wide and -deep surveys (although not finalized). The HSC wide survey can achieve new parameter space, deeper by more than one magnitude and greater in surveyed comoving

Table 4.1: HSC imaging survey

	Area [sq. deg.]	Depth [AB, 5σ, $2''$]	Methods	redshifts
HSC-Wide	1500-2000	$g(26), r(25.9), i(25.8), z(25), y(24)$	WL, Cluster	$z \lesssim 1.5$
HSC-Deep	∼30	$grizy$+NBs ($i \simeq 27.2$)	$\sim$ 500SNe	$0.4 \lesssim z \lesssim 1.2$

The magnitudes mentioned are derived assuming a point source for 5σ detection and $2''$ aperture.

Table 4.2: SuMIRe Dark Energy Experiments: Dominant systematic errors of each method and the SuMIRe methods of controlling those errors

Methods	Dominant systematic errors	SuMIRe approaches
Weak lensing	Photo-z errors	PFS data (spectroscopic calibration sample)
	Shape measurements	Subaru image-quality, methods & algorithms
	Small-scale clustering	A suite of high-resolution simulations
Clusters	Mass-observable relations	SZ-optical-lensing cross calibration
	Selection function	PFS spectroscopic calibration of BCGs
BAO	Galaxy biases	Lensing-galaxy cross-correlations
	Nonlinearities	A suite of simulations & refined analytical methods
Type-Ia SNe	Photometric calibration	Calibration strategy, spectroscopic calib.

volume by more than a factor 10 than the existing surveys thanks to the photon collecting power of the 8.2m Subaru Telescope. The HSC-wide survey is also deeper than the planned DES survey by about 1.5 magnitudes in i band. Furthermore, with the advent of the fully depleted CCD chips, the HSC survey can achieve a unique depth in red bands, thereby significantly improving signal-to-noise ratios in imaging red galaxies that are preferentially at higher redshifts.

By having the HSC-wide survey, we can carry out various cosmological experiments. In particular, the unique capabilities of the Subaru Telescope, its photon collecting power and superb image-quality, achieve high-precision measurements of weak lensing distortions of distant galaxy images due to cosmic hierarchical structures. This weak lensing is a powerful way of measuring the dark matter distribution as well as the angular diameter distance combination (Takada & Jain 2004). Furthermore, we will plan to maximize an overlap of the HSC survey region with the ACT SZ survey region (Niemack et al. 2010). The SZ effect is independent of redshift, therefore a very powerful way of finding massive clusters out to high redshifts. The HSC multi-band data can not only determine redshifts of SZ-found clusters out to high redshifts $z \simeq 1.5$ based on the photometric redshifts, especially thanks to the deep y-band data, but also enable us to make lensing-based mass calibration of the clusters in individual and statistical bases. Thus the HSC-ACT data sets can provide us with a unique catalog of massive clusters that extends out to $z \simeq 1.5$. We will use both the weak lensing observables and the cluster counting statistics in order to constrain cosmological parameters (Takada & Bridle 2007; Oguri & Takada 2010).

The primary science driver of the planed HSC-deep survey is to survey type-Ia supernovae (SNe). The depth and wide-field capabilities allows for obtaining light curves of over 500 supernovae.

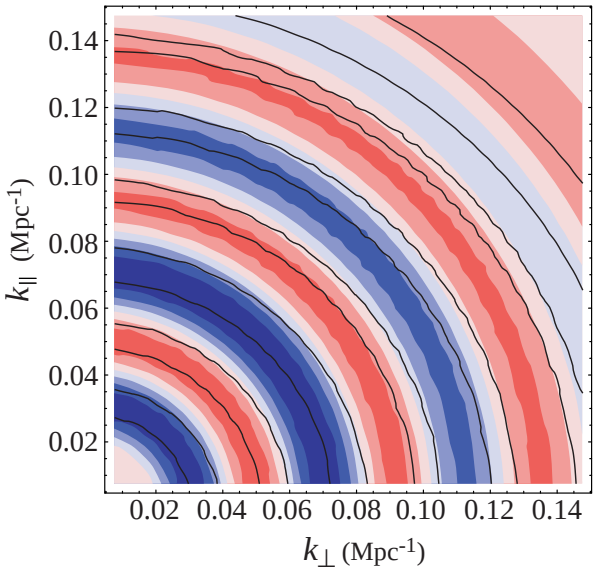

Figure 4.2: An illustration of BAO signatures in galaxy power spectrum (taken from Hu & Haiman (2003)). The shaded contours show BAO rings in two-dimensional power spectrum $P_s(k_\perp, k_\parallel)/\bar{P}_s(k) - 1$ with a smooth component $\bar{P}_s$ removed, in order to highlight the features. The contours are spaced by 0.02. Assuming a cosmological model that differs from the underlying true model causes a distortion in the ring features, as shown by the solid contours. Jaggedness arises from k-cell discretization.

We will thus carry out the luminosity distance measurement with the SNe sample, however, the spectroscopic follow-up campaign needs to be properly coordinated, which is not yet finalized.

The dark energy experiments, weak lensing, cluster counting statistics, and SNe, are summarized in Table 4.2, and the dominant systematic errors inherent in each method are also given.

4.3.2 Cosmology with galaxy redshift survey

BAO standard rulers

The geometrical effect of dark energy can be observed because the pattern of density inhomogeneities in the universe contains preferred lengths. These are related to the horizon lengths at certain key times, i.e., to the distance over which causal influences can propagate. In particular the length scale characterizing the Baryonic Acoustic Oscillations (BAO) in the pattern of cosmic microwave background anisotropies has been now precisely measured (e.g. Komatsu et al. 2010):

$$r_{\rm BAO} \simeq 147 \left(\frac{\Omega_{\rm m0}h^2}{0.13}\right)^{-0.25} \left(\frac{\Omega_{\rm b0}h^2}{0.023}\right)^{-0.08} \ {\rm Mpc}. \tag{4.8}$$

According to the important WMAP results (Komatsu et al. 2010), the BAO scale, more precisely the corresponding angular scale given by the ratio of the BAO length scale above to the angular diameter distance to the last scattering surface, is now determined with a percent level accuracy.

The BAO scale can be extracted from a galaxy redshift survey as follows. Suppose now that we have a redshift survey of galaxies at some redshift. Galaxies are biased tracers of the underlying gravitational field, and the galaxy power spectrum measures how clustering strength of galaxies varies as a function of 3-dimensional wavenumbers, k (or the inverse of 3-dimensional length scales). We do not measure the length scale directly in real space; rather, we measure (1) angular positions of galaxies on the sky, and (2) radial positions of galaxies in redshift space. To convert (1) and (2) to positions in 3-dimensional space, however, one needs to assume a reference cosmological model, which might be different from the true cosmology. An incorrect mapping of observed angular and redshift positions to 3-dimensional positions produces a distortion in the measured power spectrum, known as the "geometrical distortion" (Alcock & Paczynski 1979; Ballinger et al. 1996; Matsubara & Suto 1996). The geometrical distortion can be described as follows. The comoving size of an object at redshift z in radial, $r_{\parallel}$, and transverse, $r_{\perp}$, directions are computed from the extension in redshift, Δz, and the angular size, $\Delta\theta$, respectively, as and the angular size, $\Delta\theta$, respectively, as

$$r_{\parallel} = \frac{\Delta z}{H(z)}, \qquad r_{\perp} = D_A(z)\Delta\theta, \tag{4.9}$$

A tricky part is that $H(z)$ and $D_A(z)$ in Eq. (4.9) depend on cosmological models. It is therefore necessary to assume some reference cosmological model to compute the conversion factors. In the following, quantities in the reference cosmological model are distinguished by the subscript 'fid'. Then, the length scales in Fourier space in radial, $k_{\mathrm{ref}\parallel}$, and transverse, $k_{\mathrm{ref}\perp}$, directions are estimated from the inverse of $r_{\mathrm{ref}\parallel}$ and $r_{\mathrm{ref}\perp}$. These fiducial wavenumbers are related to the true wavenumbers by

$$k_{\perp} = \frac{D_A(z)_{\mathrm{ref}}}{D_A(z)} k_{\mathrm{ref}\perp}, \qquad k_{\parallel} = \frac{H(z)}{H(z)_{\mathrm{ref}}} k_{\mathrm{ref}\parallel}. \tag{4.10}$$

Therefore, any difference between the reference cosmological model and the true model would cause anisotropic distortions in the estimated power spectrum in ($k_{\mathrm{ref}\perp}$, $k_{\mathrm{ref}\parallel}$) space, as demonstrated in Fig. 4.2.

Thus, a prior knowledge on the BAO scale, available from the CMB constraints, allows us to use the measured galaxy clustering pattern to extract information on the angular diameter distance $D_A(z)$ and the Hubble expansion rate $H(z)$ at redshift of the galaxy survey. This method is a pure geometrical test of the cosmological distances; in other words, the obtained constraints are insensitive to the shape and amplitudes of the galaxy power spectrum, which involve uncertainties such as galaxy bias. For this reason, the BAO method is now recognized as a method that is *least affected by astrophysical uncertainties than other methods* (Albrecht et al. 2006).

Promisingly the BAO technique has been already implemented by several groups to actual galaxy surveys such as the SDSS data (Eisenstein et al. 2005) and the 2dF data (Cole et al. 2005), yielding another evidence of the cosmic acceleration when combined with the CMB constraints, but without the SN constraints. The ongoing Planck CMB experiment will further improve to fix the BAO scale with sub-percent precision (Eisenstein & White 2004), and therefore the PFS BAO survey promises to achieve higher precision measurements of the cosmological distance scales.

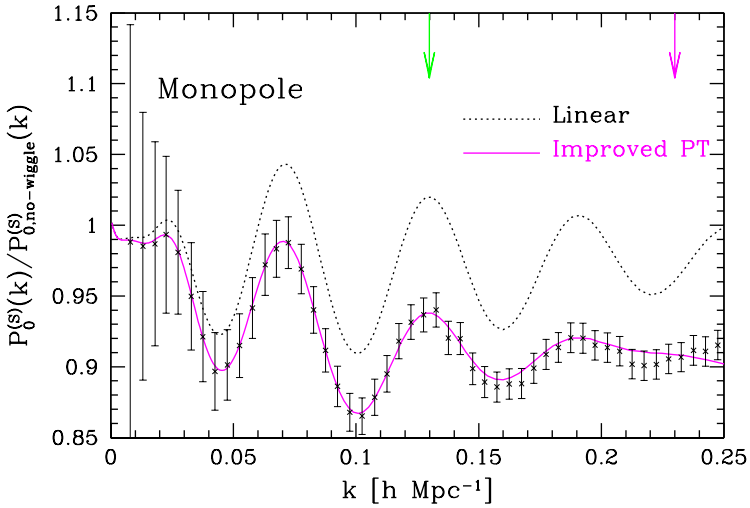

Figure 4.3: An example of the current state-of-art modeling of dark matter power spectrum including the effects of nonlinear clustering and redshift distortion. The solid curve shows the analytical prediction of monopole power spectrum at $z = 1$ (the azimuthal average of redshift-space power spectrum), computed using the refined perturbation theory of nonlinear structure formation (Taruya et al. 2009a). The cross symbols with error bars show the N-body simulation results, where the error bars are the expected 1σ statistical errors of power spectrum measurement at each k's bins assuming the comoving volume surveyed with the PFS BAO survey (see Table 4.3 for details). The perturbation theory prediction is in remarkable agreement with the simulation result on scales up to $k \gtrsim 0.25\,h\mathrm{Mpc}^{-1}$. For comparison, the dashed curve is the linear theory prediction

Beyond BAO: power spectrum amplitudes and redshift distortion

Structure formation, via gravitational instability, also causes peculiar velocity of galaxies. In addition to cosmological distortion we describe above, the peculiar velocities cause a distortion in the shape of galaxy power spectrum along the line-of-sight direction, which is known as "redshift space distortion" (Kaiser 1987). In the linear regime the Fourier coefficients of peculiar velocities, $\tilde{\delta}_s(\boldsymbol{k})$, are modulated in redshift space from the real-space field as

$$\tilde{\delta}_s(\boldsymbol{k}) \simeq \tilde{\delta}(\boldsymbol{k}) + \mu^2\tilde{\theta}(\boldsymbol{k}), \tag{4.11}$$

where μ is the cosine between the wavevector $\boldsymbol{k}$ and the line-of-sight direction, defined as $\mu^2 \equiv k_\parallel^2/k^2 (k^2 \equiv k_\parallel^2 + k_\perp^2)$, and $\theta(\boldsymbol{x})$ denotes the divergence of the peculiar velocity field $\boldsymbol{u}$, $\theta \equiv -\nabla \cdot \boldsymbol{u}$ assuming an irrotational flow of galaxies. As a result the galaxy power spectrum estimated in redshift space, $P_s(k_{\mathrm{ref}\perp}, k_{\mathrm{ref}\parallel})$, is given by the simple form (Seo & Eisenstein 2003):

$$P_s(k_{\mathrm{ref}\perp}, k_{\mathrm{ref}\parallel}) = \frac{D_A(z)_{\mathrm{ref}}^2 H(z)}{D_A(z)^2 H(z)_{\mathrm{ref}}} \left[1 + \beta(z)\mu^2\right]^2 b_1^2 P_m(k, z) + \frac{1}{\bar{n}_g}, \tag{4.12}$$

where b_1 is the linear bias parameter, $\bar{n}_g$ is the mean number density of galaxies, β is the redshift-dependent function that characterizes the peculiar velocity amplitude in the linear regime, and P_m is the linear mass power spectrum. The second term on the r.h.s. denotes the shot noise term arising from a finite-number sampling of the galaxies. If the number conservation holds for galaxies we work on, it can relate the peculiar velocity amplitude to that of the density fluctuation as $\beta = (1/b_1) d\ln\delta/\ln a = f_g/b_1$ (see Eq. [4.6]).

The form (4.12) suggests that the redshift distortion effect gives yet another geometrical probe of cosmological distances, in addition to the BAO peak locations. Adding the redshift effect in the geometrical probe allows a more precise estimation of cosmological distances. Furthermore, if the theoretical prior $\beta = f_g/b_1$ is employed, the measured β can be used to not only test gravity on cosmological scales (see § 4.2.4), but also to break degeneracy between the galaxy bias and the power spectrum amplitude (Takada et al. 2006). In turn the shape and amplitudes of galaxy power spectrum can be used to improve the cosmological constraints. However, in reality there are various uncertainties in this full use of galaxy power spectrum: nonlinear galaxy bias, nonlinear redshift distortion (known as the Finger-of-God effect), and a possible bias of galaxy peculiar velocities. These effects need to be understood for the information beyond the BAO information.

The scales of galaxy clustering we are interested in are anyway on large distance scales of 100Mpc, where lie in the linear regime or at least the weakly nonlinear regime. There has been growing interest in the community on the idea of refining theoretical predictions of galaxy clustering on relevant scales. Most notable attempt is based on the perturbation theory of structure formation, in combination with a suit of N-body simulations (e.g. Jeong & Komatsu 2006a; Crocce & Scoccimarro 2006b; Matsubara 2008; Taruya & Hiramatsu 2008; Saito et al. 2008). Figure 4.3 shows the current status of such theoretical studies, showing that the refined perturbation theory can remarkably well reproduce the BAO features as well as the power spectrum amplitudes up to $k \simeq 0.25\ h\mathrm{Mpc}^{-1}$ at target redshifts $z \sim 1$ for PFS to sufficient accuracies. However, note that the theoretical model shown here is for the dark matter distribution, and does not include the effect of nonlinear galaxy bias. Since our understanding on galaxy formation processes is still lacking, in practice we need to develop a method that is least affected by galaxy bias uncertainties and/or allows the uncertainties to be safely marginalized over a sufficiently broad range of galaxy bias models. There is also an interesting method proposed by Eisenstein et al. (2007); the galaxy distribution measured from a given survey is iteratively used to correct for the effect of nonlinear clustering on the galaxy distribution in order to extract cleaner information on the BAO scales.

Perhaps more interesting attempt, which is recently receiving more attention in the community, is to reconstruct the velocity power spectrum from the galaxy distribution (Eq. [4.11]) in redshift space, rather than a priori assuming the density-velocity relation. The density fluctuation and the peculiar velocity depend on the metric perturbations in a different way, and therefore allow us to constrain the two metric perturbation simultaneously, if the density and velocity power spectra are separately measured. To make this method feasible, we need to properly take into account uncertainties such as the FoG effect when reconstructing the density and power spectra from the observed galaxy distribution in redshift space (Tang et al. 2010).

A striking strength of SuMIRe HSC and PFS surveys is we can *directly* measure the galaxy bias of target galaxies in a given redshift slice by combining the weak lensing measurements and the galaxy distribution. Once the effects of the galaxy bias uncertainty or other nonlinear effects (e.g. FoG effect) are eliminated or reliably marginalized over, we can use the shape and amplitudes of galaxy power spectrum to further improve the cosmological constraints. This is an interesting possibility that is worth pursuing, because it opens up a window for constraining other interesting parameters; neutrino masses, the primordial non-Gaussianity and inflation parameters (Takada et al. 2006; Saito et al. 2008, 2009).

4.3.3 PFS BAO survey parameters

The PFS survey will bring a great synergy with the HSC survey. The deep, multi-color HSC data sets can deliver an ideal catalog to find target galaxies for the PFS redshift survey based on the same telescope. To maximize the synergy of HSC and PFS surveys we can choose, as the target galaxies, red galaxies (BCGs and early-type galaxies) in cluster regions and star-forming blue galaxies. By targeting emission-line [OII] (3726Å, 3729Å) for blue galaxies in high-redshift side, we can probe the three-dimensional galaxy distribution over a wide range of redshifts, $0.6 \lesssim z \lesssim 1.6$, which then becomes complementary to the ongoing BOSS survey with redshift range $0.4 \lesssim z \lesssim 0.65$ and 10000 square degree area (mostly in the northern hemisphere sky). Thus we can use the combined spectroscopic data sets from the BOSS and PFS surveys to calibrate dominant systematic errors in the weak lensing and cluster experiments; photometric redshift errors and cluster selection function (Oguri & Takada 2010).

More importantly the PFS data sets themselves allow us to carry out another dark energy experiment, the baryonic acoustic oscillation (BAO) experiment, from the measured three-dimensional distribution of over a million of galaxies. The BAO method is now recognized as the method "least affected" by systematic uncertainties among the dark energy experiments, as demonstrated in the actual measurements (Eisenstein et al. 2005; Cole et al. 2005). By measuring the BAO length scale imprinted on the galaxy distribution in both the directions along and perpendicular to the line-of-sight direction for the HSC survey region of 2000 square degrees, we can achieve high-precision measurements of the angular diameter distances and the Hubble expansion rates over the redshift range $0.6 \lesssim z \lesssim 1.6$ with precisions of a few percent (see Figure 4.6). Although the most dangerous uncertainty in the BAO experiment arises from nonlinear, scale-dependent galaxy bias, combining the HSC and PFS surveys allows us to observationally disentangle the galaxy bias uncertainties by cross-correlating the galaxy distribution with the total matter (mostly dark matter) distribution reconstructed from the HSC weak lensing measurements. We can then use broad-band shapes of the galaxy power spectrum measured as a function of redshifts, which greatly improves the cosmological constraints and now opens up a window for constraining the growth of structure with the galaxy power spectrum (Takada et al. 2006; Takada 2006; Saito et al. 2008, 2009, 2010). Furthermore, we may be able to use, if robustly measured, redshift distortions in the galaxy distribution caused by the peculiar velocities in order to further improve the cosmological constraints (Tang et al. in preparation)

Thus the SuMIRe (HSC + PFS) survey enables us to carry out both the geometrical measurements (BAO + SNe) and the experiments probing the growth of structure (WL + Cluster + Galaxy Clustering). The combined experiments are very powerful and convincing in several aspects. First, the combined experiments not only provide the precise dark energy experiments, but also allow us to carry out a model-independent test of the metric gravity theory on cosmological length scales as follows. The different structure formation probes are sensitive to different combinations of the metric perturbations, gravitational potential and curvature perturbations, while the Einstein gravity predicts that the two perturbations are equal on all the relevant scales. Therefore, given the expansion history precisely constrained by the geometrical probes, we can now address if all the structure formation probes are consistent with the Einstein gravity predictions as a function of length scales and redshifts (Guzik et al. 2010). Second, by having the different methods, we can cross-check and self-calibrate various systematic uncertainties inherent in the methods in order to

Redshift	V_s $[h^{-3}\mathrm{Gpc}^3]$	N_g (per field)	$\bar{n}_g[h^3\mathrm{Mpc}^{-3}]$	b	$\bar{n}_g P_g @ k = 0.1h\mathrm{Mpc}^{-1}$
$0.6 < z < 0.8$	0.8	212	3×10^{-4}	1.5	1.4
$0.8 < z < 1.0$	1.1	292	3×10^{-4}	1.5	1.2
$1.0 < z < 1.2$	1.4	495	4×10^{-4}	1.5	1.3
$1.2 < z < 1.4$	1.6	565	4×10^{-4}	1.5	1.2
$1.4 < z < 1.6$	1.7	600	4×10^{-4}	1.5	1.0

Table 4.3: PFS survey parameters required for carrying out the BAO experiment, where we assumed 2000 sq. degrees for the sky coverage. The required number of target galaxies in total is 2164 per the SuMIRe PFS field-of-view. We assumed that the linear bias parameters of target galaxies $b = 1.5$ all the redshift slices according to some studies (Coil et al. 2008; Blake et al. 2010; Sumiyoshi et al. 2009), but the actual values are still uncertain. If we can preferentially target early-type galaxies which tend to have greater biases such as $b \simeq 2.3$ for LRGs, it can relax requirements on the number density of target galaxies by up to 50%($\simeq 2.3/1.5$).

derive robust constraints on cosmological parameters. Finally, we can use the combined structure formation probes to explore constraints on a much broader range of variant models: neutrino masses, models of clustered dark energy and primordial non-Gaussianity (Takada 2006; Saito et al. 2008, 2009; Ichiki et al. 2009; Oguri 2009; Oguri & Takada 2010; Saito et al. 2010).

In summary the key science goals for the SuMIRe survey are

- Dark energy (WL, BAO, Galaxy Clustering, Cluster, SNe)
- Growth of structure (WL, Galaxy Clustering, Cluster)
- Neutrino mass (WL, Galaxy Clustering, Cluster)
- Primordial non-Gaussianity (WL, Galaxy Clustering, Cluster)

We now move on to requirements on the PFS specifications in order to achieve the key science goals above. The requirements come mainly from two factors: the number density of target galaxies and the redshift determination accuracy. As described above, the primary target galaxies are (1) brightest central galaxies (BCGs) in HSC-ACT found cluster regions and early-type galaxies and (2) star-forming blue galaxies exhibiting [OII] emission lines. The statistical precision of the BAO scale measurement is determined by the shot noise and the sampling variance. To achieve the nearly sampling variance limited regime for a fixed survey area, we need to sample target galaxies with number densities satisfying $\bar{n}_g P_g \gtrsim 1$ at BAO scales ($k \simeq 0.1h\mathrm{Mpc}^{-1}$), where $\bar{n}_g$ is the mean comoving number density of galaxies and P_g is the galaxy power spectrum amplitude at the BAO scales. Assuming the WMAP 7-year cosmology, we can find that the required total number of galaxies is about 2×10^6 galaxies for a survey with 2000 square degrees assuming the redshift coverage $0.6 \lesssim z \lesssim 1.6$. Or this corresponds to about 2200 galaxies per the PFS field-of-view (about 1.8 square degrees) as given in Table 4.3.

Another important factor we should take into account is the accuracy of redshift determination; the BAO measurement requires redshifts of galaxies to be measured with a percent-level precision in $(1+z)$ (see Fig. 7 in Seo & Eisenstein 2003). Hence the absorption/emission line(s) of each galaxy needs to be detected with a sufficiently high signal-to-noise ratio (greater than $S/N \simeq$ 5-10). In

particular, to cover high redshifts $1.2 \lesssim z \lesssim 1.6$, [OII] emission line (3726Å) needs to be detected in red bands beyond 8000 Å, where there are significant contamination from OH sky lines (see below).

Hence the requirements on the PFS specifications are summarized as

- Enable us to cover redshift range $0.6 \lesssim z \lesssim 1.6$ making the PFS BAO survey complementary to the ongoing BOSS survey that covers $0.4 \lesssim z \lesssim 0.65$
- Enable a multi-object spectroscopic observation of brightest central galaxies (BCGs) in the HSC-ACT found cluster regions, early-type galaxies and [OII] emission-line galaxies ([OII]: 3726Å) in order to maximize its synergy with the HSC survey
- Need to obtain about 2200 spectra per the PFS field-of-view in order to make the BAO experiment be in the sampling variance limited regime, which satisfies $\bar{n}_g P_g \simeq 1$ at BAO scales ($k \simeq 0.1h\mathrm{Mpc}^{-1}$)
- Absorption/emission line(s) of each galaxies needs to be detected with a high signal-to-noise ratio ($S/N \gtrsim 5$–10) in order to have a percent-level determination of galaxy redshifts
- Need to discriminate [OII] emission line from OH sky emission lines in red bands (> 8000 Å)

We will give a detailed study of requirements on exposure time of each field and target selection in § 4.3.6, properly taking into account an adequate level of the sky background contamination that is especially important in red band ($\gtrsim 8000\mathring{A}$).

Expected accuracies of power spectrum measurements

What is the expected precision of measuring galaxy power spectrum with the PFS survey described above? There are two sources of the measurement errors: the sampling variance due to the limited number of wavenumbers sampled for a finite survey volume, and the shot noise the imperfect sampling of fluctuations due to the finite number of galaxies sampled. To be more specific the 1σ statistical error of measuring the galaxy power spectrum at each wavelength bin is estimated in Feldman et al. (1994a) (ignoring effects of survey window function and selection function):

$$\frac{\sigma_P^2}{P^2(k,\mu;z)} = \frac{2}{N(k,\mu;z)}\left[1 + \frac{1}{\bar{n}_g(z)P_s(k,\mu;z)}\right]^2, \tag{4.13}$$

where $N(k,\mu;z)$ is the number of independent Fourier modes with length k, given as

$$N(k,\mu;z) \equiv \frac{2\pi k^2 \Delta k \Delta\mu}{(2\pi)^3/V_s(z)} = \frac{1}{4\pi^2} k^2 \Delta k \Delta\mu V_s(z), \tag{4.14}$$

Δk and $\Delta\mu$ are the bin widths, $V_s(s)$ is the comoving volume of a given survey centered at redshift z, and $\bar{n}_g$ is the mean comoving number density of galaxies. The factor 2 on the r.h.s. of Eq. (4.13) arises from the real condition of the density field: $\tilde{\delta}(\boldsymbol{k}) = \tilde{\delta}^*(-\boldsymbol{k})$. To have better precision we need to either have a larger volume of the surveyed region (up to higher redshifts or over wider area) or reduce the shot noise contamination by having the greater $\bar{n}_g P_s$ (the denser sampling of

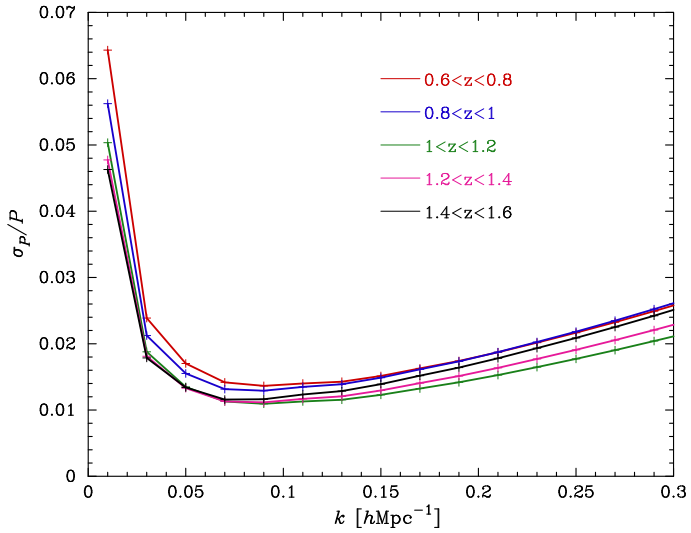

Figure 4.4: Expected fractional uncertainties in galaxy power spectrum measurements for each redshift slice. The survey parameters are given in Table 4.3. We assumed the wavenumber bin width $\Delta k = 0.02h\mathrm{Mpc}^{-1}$, the 5 redshift slices with width $\Delta z = 0.2$ and the linear bias parameter $b = 1.5$ for all the redshifts. The PFS survey achieve a few percent accuracies in $\sigma(P)/P$ at scales $k \gtrsim 0.05h\mathrm{Mpc}^{-1}$ for all the redshift slices.

galaxies or using more biased tracers of galaxies as $P \propto b_1^2$ in the linear regime). The error formula (4.13) assumes the Gaussian fluctuations, which only hold in the linear regime. Takahashi et al. (2009b,a) showed that the non-Gaussian errors, caused by nonlinear clustering, are not important using 5000 realizations of N-body simulations.

Figure 4.4 shows the expected fractional uncertainties in measuring the galaxy power spectrum for each redshift slice, assuming the survey parameters given in Table 4.3.

A direct reconstruction of scale-dependent bias with SuMIRe HSC/PFS

There are a number of scientific merits we can have when combining the HSC imaging data and the PFS spectroscopic data sets, if the two surveys see the same regions of the sky. One example is a *direct* reconstruction of the galaxy bias, which is one of major uncertainties in using galaxy clustering observables for cosmology. To be more specific, for a given spectroscopic sample of galaxies, we can use the deep HSC imaging data to measure the lensing distortion effect on background galaxies due to the spectroscopic, foreground galaxies – the so-called galaxy-galaxy weak lensing or the stacked shear (e.g. Oguri & Takada 2010). The galaxy-galaxy weak lensing probes the average mass distribution around the foreground galaxies; the small-angular-scale signals arise from the mass distribution within one halo that is hosting the foreground galaxies, the so-called one-halo term, while the large-angular-scale signals are from the mass distribution surrounding the halos – the two-halo term. If we select the foreground galaxies in a narrow redshift slice, centered at z, in the cross-correlation measurement, the angular power spectrum of the galaxy-galaxy lensing can be derived in Oguri & Takada (2010) as

$$C_{\gamma g}(l;z) \simeq W_{\mathrm{GL}}(\chi)\Delta\chi\ P_{gm}\left(k=\frac{l}{\chi};z\right), \tag{4.15}$$

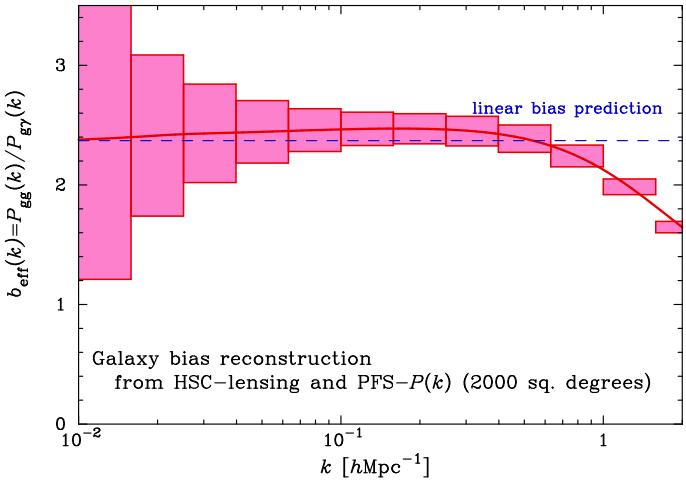

Figure 4.5: A demonstration of the galaxy bias reconstruction, which is feasible by combining the HSC weak lensing observables with the PFS galaxy clustering information (see text for the details). Here we considered, as a working example, LRG-type galaxies in a redshift slice $0.5 \leq z \leq 0.7$ as spectroscopic galaxies and assumed that the LRGs cause lensing distortion effect on background galaxies, which can be probed by the deep HSC data. We used the halo occupation distribution (HOD) in Zheng et al. (2009) to model the galaxy bias, which displays a scale-dependence even at large scales comparable with the BAO scales. The boxes around the solid curve show the $\pm 1\sigma$ statistical uncertainties in reconstructing the galaxy bias at each k-bin's, which are estimated by propagating the measurement errors of the lensing and galaxy power spectra assuming a sky coverage of 2000 sq. degrees with HSC and PFS (see text for the details). The combined HSC and PFS data allows a 5%-level precision of the bias reconstruction at each k-bins in $k \gtrsim 0.1\ h\mathrm{Mpc}^{-1}$.

where $P_{gm}(k)$ is the 3D mass-galaxy power spectrum and $W_{\rm GL}$ is the lensing efficiency function defined as

$$W_{\rm GL}(\chi) \equiv 4\pi G\bar{\rho}_{m0}(1+z)\chi\left[1-\chi\left\langle\frac{1}{\chi_s}\right\rangle\right]. \tag{4.16}$$

In the equations above, $\bar{\rho}_{m0}$ is the present-day mean mass density (mainly dark matter), χ is the comoving angular-diameter distance to the redshift slice of lensing galaxies, $\chi = \chi(z)$, $\Delta\chi$ is the comoving radial distance width of the redshift slice, and $\langle 1/\chi_s\rangle$ is the average of the angular diameter distance over the population of source galaxies. The full-sky formalism for galaxy-galaxy lensing is also developed in de Putter & Takada (2010).

Eq. (4.15) implies that we can infer the galaxy-mass power spectrum, $P_{gm}(k;z)$, from the observed lensing power spectrum, because the prefactors $W_{\rm GL}$ and $\Delta\chi$ are known once a cosmological model is known or specified. One the other hand, the 3D galaxy power spectrum, $P_{gg}(k;z)$, is measurable from the same spectroscopic galaxy sample. Since these spectra at linear scales depend on galaxy bias b and the underlying mass power spectrum P_m as $P_{gg} \propto b^2 P_m$ and $P_{gm} \propto bP_m$, the galaxy bias function in the Fourier space can be directly reconstructed by combining the observed power spectra, $P_{gg}(k;z)$ and $C_{\gamma g}(l;z)$ as

$$b_{\rm eff}(k;z) = W_{\rm GL}(\chi)\Delta\chi\frac{P_{gg}(k;z)}{C_{\gamma g}(l=\chi k;z)} \tag{4.17}$$

Figure 4.5 demonstrates an expected accuracy of the galaxy bias reconstruction method we can achieve with the HSC and PFS data, assuming the area coverage of 2000 sq. degrees (for the

same region of the sky). Here, as a working example, we assumed that LRG-type galaxies in a redshift slice of $0.5 \leq z \leq 0.7$ are available from the PFS survey, and that we can use the HSC data to measure the lensing distortion effect on background galaxies due to the foreground LRG galaxies. To model a galaxy bias for LRG-type galaxies, we employed the halo occupation distribution (HOD) model in Zheng et al. (2009), and also used the method in Zheng et al. (2005) to compute the lensing and galaxy power spectra based on the HOD model. First of all, the galaxy bias shows a scale-dependence at these large scales comparable with the BAO scales. In other words, a scale-independent, linear bias (shown by the dashed line) breaks down, and we cannot use the information in galaxy power spectrum amplitudes for doing cosmology.

The boxes around the solid curve show the expected 1σ statistical errors in reconstructing the bias function. The error bars are estimated by propagating the measurement errors of galaxy power spectra (Oguri & Takada 2010), where we properly took into account the shot noise due to the discrete LRG sampling and the intrinsic shape noise contamination to the lensing measurements. The dominant source of errors arises from the lensing power spectrum errors. The figure shows that the HSC and PFS surveys allow a 5%-level accuracy of the bias reconstruction at each k's bins of $k \gtrsim 0.1h$ Mpc^{-1}. Thus we can then use the measured bias function to extract cosmological information from the measured information in galaxy power spectrum amplitudes. This will open up a new window for constraining the growth rate of mass clustering, e.g. via the power spectrum amplitudes themselves and the redshift distortion effect. We have found that the galaxy bias can be reconstructed out to $z \sim 1.2$ to a similar precision, thanks to the depth of the HSC data (Nishizawa & Takada in preparation).

The galaxy bias for LRG-type galaxies, which are preferentially central galaxies of halos with masses $\gtrsim 10^{13} M_\odot$, is rather relatively well understood in a sense that the bias shows a similar behavior to halo bias with less stocasticity. On the other hand, blue-type galaxies should show a more complicated bias, and therefore the bias reconstruction should be more useful to use.

Furthermore, several works (Pen 2004; Seljak 2009; Hamaus et al. 2010; Gil-Marín et al. 2010) have shown that a weighting method of the galaxy bias estimation, e.g. with halo masses, can reduce the stocasticity as well as the sampling variance fluctuations. These methods, along the HSC and PFS data, should be more carefully explored.

4.3.4 Forecasts of cosmological constraints

PFS BAO precision

In the following we demonstrate the expected power of PFS BAO survey for constraining cosmological parameters, especially focused on dark energy parameters. First of all, we show the forecasts expected from the BAO geometrical test; i.e. a case of using the observed BAO peak locations to constrain cosmological parameters when combined with the CMB information (here assumed the Planck satellite-expected information up to $l = 1500$). Note that the BAO geometrical test thus does not include the power spectrum amplitude information. To do this, we use the Fisher matrix formalism method developed in Seo & Eisenstein (2003); we include the following parameters to

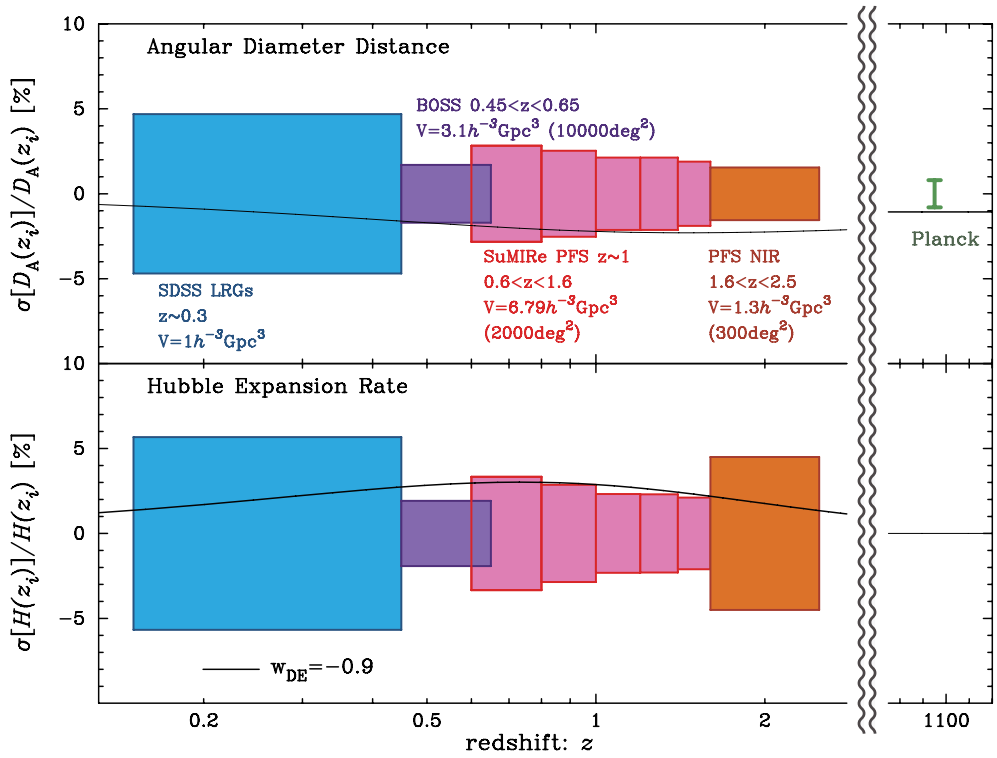

Figure 4.6: Fractional errors in measuring the angular diameter distance and the Hubble expansion rate for each redshift slices for the different BAO surveys, SDSS, BOSS and PFS. For the PFS survey we assumed survey parameters given in Table 4.3. The solid curves in each panel shows the fractional difference of $D_A(z)$ or $H(z)$ when changing the dark energy equation of state w to $w = -0.9$ from $w = -1$ (ΛCDM model).

Data Model	$w_{\rm pivot}$	DE FoM
PFS BAO	0.046	33
HSC WL	0.053	32
PFS BAO+HSC WL	0.032	82
PFS BAO+RSD	0.043	144
PFS BAO+RSD+HSC WL	0.017	345

Table 4.4: Parameter forecasts on dark energy equation of state parameters for different SuMIRe PFS/HSC methods. $\sigma(w_{\rm pivot})$ is the marginalized constraint on the dark energy equation of state at the pivot redshift (see Eq. [4.4]). Here we assumed, as observables, the HSC weak lensing, PFS and the combined measurements. For the observable "PFS BAO+RSD", we assumed that we can use the amplitude and redshift-space distortion information in the galaxy power spectrum (see text for details). The dark energy figure-of-merit (DE FoM) is given as FoM $\equiv 1/\left[\sigma(w_{\rm pivot})\sigma(w_a)\right]$.

model the observed galaxy power spectrum in redshift space (see Eq. [4.12]) for each redshift slice of the assumed PFS survey:

$$\boldsymbol{p} \equiv \left\{\Omega_{\rm m0}, \delta_\zeta^2, n_s, \Omega_{\rm m0}h^2, \Omega_{\rm b0}h^2, H(z_i), D_A(z_i), b(z_i), \beta(z_i), \bar{n}_g(z_i)\right\}, \tag{4.18}$$

where $\Omega_{\rm m0}$, δ_ζ^2, n_s, $\Omega_{\rm m0}h^2$ and $\Omega_{\rm b0}h^2$ are the model parameters that are needed to specify the background cosmological model (assuming a flat universe) and the linear mass power spectrum (its shape and amplitude), z_i is the centering redshift of each redshift slice, and $H(z_i)$ and so on are their quantities in the i-th redshift slice. For the nominal PFS BAO survey in Table 4.3 we have 5 redshift slices over $0.6 \leq z \leq 1.6$, i.e. z_i $(i = 1, 2, \ldots, 5)$. Therefore we include 30 free parameters for the PFS BAO survey.

Figure 4.6 shows the expected accuracies of measuring the angular diameter distances and the Hubble expansion rate for each redshift slices assuming the survey parameters in Table 4.3 for the PFS BAO survey. The errors include marginalization over other parameter uncertainties in Eq. (4.18), and we assumed the ΛCDM model as the fiducial model ($w = -1$) as well as the CMB information expected from the Planck satellite mission on the cosmological parameters. The figure shows that the PFS BAO survey can achieve a few percent accuracies of measuring the angular diameter distances and the Hubble expansion rate at each redshift slices. The figure also shows the expected accuracies for a higher-redshift BAO survey that can be possible to carry out with the PFS near-infrared (NIR) arm spectrograph; here we assumed a BAO survey covering 300 sq. degrees over a redshift range $1.6 \leq z \leq 2.5$ (see below for details). One can clearly find that the PFS BAO survey is quite complementary to the SDSS-I, II and BOSS surveys in their redshift coverage. As a result, by combining the SDSS, BOSS and PFS surveys with the CMB information, we can explore the cosmic expansion history over a wider range of redshifts, $0 \lesssim z \lesssim 1.6$(or 2.5). For comparison, the solid curves in the upper and lower panels show the fractional difference in $D_A(z)$ and $H(z)$ with respect to their fiducial values when changing the dark energy equation of state to $w = -0.9$ from $w = -1$. It clearly shows that the wide redshift coverage easily allows us to discriminate the dark energy effect. In particular a higher-redshift window of the BAO constraints can allow us to test the early dark energy models that have stronger redshift evolutions at higher redshifts than naively expected.

Next we move on to the expected accuracies of PFS BAO survey for constraining dark energy

	BOSS	PFS(+BOSS)	SuMIRe (BOSS+PFS+HSC)
Redshift	$0.2 < z < 0.65$	$0.6 < z < 1.6$	$0 \lesssim z \lesssim 1.6$
Sky Coverage	10000 deg^2	2000 deg^2	2000 deg^2
$\sigma(w_{\rm pivot})$	0.083	0.046	0.017
DE FoM	13	33	345
Growth: $\sigma(\gamma)$	-	-	0.032
$\sigma(\sum m_\nu)$ [eV]	-	-	0.06 eV
$\sigma(f_{\rm NL})$	-	-	$\sim$5

Table 4.5: Summary of parameter forecasts. The Planck CMB prior and SDSS LRGs constraints are assumed for all the surveys. The forecasts for BOSS and PFS are based on the assumed BAO experiments, and we did not include information in the overall shape and amplitudes of galaxy power spectrum. Therefore the dark energy constraints shown are conservative. The forecasts for SuMIRe (PFS+HSC+BOSS) are computed assuming the hypothetical joint experiments of weak lensing, cluster, BAO and galaxy clustering, where we included the overall shape and amplitude information of galaxy power spectrum assuming that galaxy bias uncertainties can be calibrated by comparing the galaxy and lensing-reconstructed matter distributions. However a more careful, realistic forecast needs to be studied (this is in progress).

parameters, especially dark energy equation of state parameters. This can be done by propagating the distance estimation accuracies into the dark energy parameters (see Seo & Eisenstein 2003). Table 4.4 gives the forecasts: the marginalized error on the dark energy equation of state at the pivot redshift, $\sigma(w_{\rm pivot})$ (see Eq. [4.4]), and the dark energy figure-of-merit quantity (DE FoM) defined as DE FoM$\equiv [\sigma(w_{\rm pivot})\sigma(w_a)]^{-1}$ assuming that the dark energy equation of state is parametrized as given in Eq. (4.4). Note that the error such as $\sigma(w_{\rm pivot})$ denotes the expected 1-σ uncertainty on the parameter estimation. For all the forecasts shown in this table, we assumed the Planck CMB priors and the BAO constraints from the SDSS and BOSS. The table shows that the PFS BAO survey can achieve a precision of $\sigma(w_{\rm pivot}) \simeq 0.046$ and DE FoM$\simeq$ 33. For comparison, we also give the dark energy accuracies expected from the HSC survey, which will be carried out before the PFS BAO survey. Here we assumed the dark energy method developed in Oguri & Takada (2010), which is based on weak lensing observables and cluster counting statistics, and included effects of various systematic errors on the parameter forecasts, photometric redshift errors and uncertainties in cluster mass-observable relations. The table shows that the HSC has a similar-level precision of the dark energy parameters with the PFS.

We also comment on the ability of constraining the spatial curvature of the Universe with the PFS BAO survey, which is another prediction of Einstein's general relativity. The previous cosmological data sets are consistent with a spatially flat universe; e.g. the WMAP data put the limit on the curvature parameter as $\Omega_{\rm K} \simeq -0.08^{+0.07}_{-0.09}$(68%C.L.) (Komatsu et al. 2010). If we cannot find any signature on finite curvature value from coming cosmological data, what does this imply? For example, this implies that inflation, what is believed to have happened in the early state of the Universe, had to last for a long enough period in order to make the observable universe sufficiently flat with the observational precision. In addition, the properties of the primordial fluctuations may be modified if inflation have happened in a finite-curvature background. In fact some works have claimed that such a scenario can be a possible solution of the low CMB quadrupole amplitudes, e.g. measured from WMAP (e.g. Efstathiou 2003). Hence it is important to pin down the accuracy

of spatial curvature constraint to a level of $\Omega_{\rm K} = 0.05$ or better. The expected accuracy for the PFS BAO survey can be estimated by simply adding one more parameter, $\Omega_{\rm K}$, in addition to the parameters in Eq. (4.18). We found that the expected constraint is

$$\sigma(\Omega_{\rm K}) = 0.0057. \tag{4.19}$$

Note that the constraint include uncertainties in dark energy parameters. Thus the PFS survey, combined with the Planck information, can achieve a sub-percent precision of the curvature constraint. The Planck information on the angular diameter distance out to the last scattering surface ($s \simeq 1100$) is important in this constraint because it has the tightest precision as indicated in Figure 4.6. Note, however, that the Planck information alone cannot constrain the curvature due to parameter degeneracies with other parameters that also change the distance to the last scattering surface. Hence, the high-precision above can be obtained when combining the PFS BAO constraints with the Planck information.

Synergy with HSC and beyond BAO geometrical constraints

The real strength of the SuMIRe HSC and PFS surveys arises from the joint experiment. There are various improvement expected when combining the HSC imaging data and the PFS spectroscopic data, if the two surveys see the same region of the sky. The joint experiment will allow a more robust calibration of systematic errors inherent in the HSC- and PFS-based experiments, e.g. photometric redshift errors and galaxy bias uncertainty. As a result, it will enable us to improve cosmological constraints. In the following we demonstrate the power of the joint HSC and PFS cosmological experiments.

The column labeled as "PFS BAO+HSC WL" in Table 4.4 gives a minimal synergy of the PFS and HSC surveys, which shows the accuracies expected when combining the PFS BAO constraints with the HSC weak lensing methods. The HSC and PFS methods are complementary, and therefore the dark energy constraints can be improved by combining the two. The dark energy constraints can be further improved if additional information from the supernovae and the PFS Lyman-α forests (see Chapter 10) are combined (if systematic errors in the methods are well under control).

An even more interesting for the joint HSC and PFS experiment is including the amplitude and broad-band shape information of redshift-space galaxy power spectrum. This is feasible because the galaxy bias, the most damaging systematic error in galaxy power spectrum, can be directly calibrated by adding the HSC weak lensing information on the PFS galaxies as we demonstrated around Figure 4.5. To be more explicit we estimate the expected accuracies by including the following parameters to model the redshift-space power spectrum (Eq. [4.12]) as free parameters in the Fisher matrix formalism:

$$\boldsymbol{p} \equiv \left\{\Omega_{\rm m0}, w_0, w_a, \delta_\zeta^2, n_s, \Omega_{\rm m0}h^2, \Omega_{\rm b0}h^2, b(z_i), \bar{n}_g(z_i)\right\}. \tag{4.20}$$

Compared to the set of parameters given in Eq. (4.18), we now assumed that the galaxy power spectrum amplitudes and redshift-distortion effect $\beta(= d\ln\delta/d\ln a)$ in Eq. (4.12) are specified by the parameters above. In other words, we assumed that a possible scale-dependence of the galaxy bias is calibrated by using the HSC weak lensing information, e.g. based on the method

demonstrated around Figure 4.5. A more careful modeling of the redshift-space power spectrum in quasi-nonlinear regime will be demonstrated in § 4.4.

The column labeled as "PFS BAO+RSD" shows the parameter forecasts expected when including the broad-band amplitude and shape of redshift-space power spectrum information in addition to the geometrical BAO constraint. The table shows that this additional information significantly improves the parameter accuracies. Furthermore, when combined with the HSC weak lensing information, a more complete, joint experiment of the HSC and PFS surveys can potentially attain the precisions of $\sigma(w_{\rm pivot}) \simeq 0.017$ and FoM$\simeq 345$, which is comparable with the precision of Stage-IV dark energy experiments discussed in the Dark Energy Task Force report (Albrecht et al. 2006). Thus removing galaxy bias uncertainty is very powerful, and is possible only if we have weak lensing information on galaxies used for the galaxy power spectrum measurements. This is the striking uniqueness of SuMIRe HSC and PFS experiments, compared to other surveys planning either of imaging and redshift surveys alone.

Table 4.5 shows the comparison with the on-going BOSS dark energy experiment as well as forecasts on other interesting cosmological parameters expected for a joint experiment of HSC and PFS surveys (hereafter, simply SuMIRe). As clearly demonstrated in Figure 4.6, the PFS survey can achieve similar-level precisions of the BAO geometrical constraints at each redshift slices that are at higher redshifts and have a wider coverage of redshifts than the BOSS survey has. As a result, adding the PFS BAO geometrical information can improve the dark energy parameters by a factor of 3, compared to the constraints expected from the BOSS BAO alone.

Another interesting direction we can address for the joint PFS and HSC experiments is testing gravity at cosmological scales, motivated by a speculation that a mysterious cosmic acceleration may be a signature of breakdown of Einstein's gravity theory on cosmological scales. Again testing properties of gravity with the PFS survey is possible to carry out *if* we can remove the galaxy bias uncertainty. By having the HSC weak lensing information, which is sensitive to both the expansion history and the growth of structure formation, we can open up a window to discriminate two possibilities between dark energy and modified gravity scenarios. A simple route to this gravity test can be done by constraining the linear growth rate of density perturbations from available cosmological observables. The linear growth rate around the ΛCDM model is parametrized as

$$G(a) \propto \exp\left(\int^a d\ln a' \left[\Omega_{\rm m}^{\gamma}(a') - 1\right]\right), \tag{4.21}$$

where $G(a) \equiv \delta(a)/a$ is the linear growth of density perturbations normalized to Einstein de-Sitter case, γ is a parameter (see below), and $\Omega_{\rm m}(a)$ is the density parameter of total matter relative to the critical density at redshift $z\,[= 1/a - 1]$. The value $\gamma = 0.55$ is shown to closely approximate the exact solution within general relativity for a wide variety of dark energy equation of state models (Linder 2005). Thus, by exploring signatures on $w \neq -1$ and $\gamma \neq 0.55$ from cosmological observables, we can test both dark energy and modified gravity scenarios: dark energy scenarios with Einstein's gravity should give $\gamma \simeq 0.55$, while modified gravity scenarios (presumably without dark energy contribution) can give any γ and generally any w (in this case w is just a parameter to describe the cosmic accelerating expansion, instead for dark energy).

Table 4.5 shows the expected accuracy of constraining the γ parameter to be $\sigma(\gamma) \simeq 0.03$, where the error on γ includes marginalization over other cosmological parameters including the dark energy equation of state parameters w_0 and w_a.

Table 4.6: An assumed PFS NIR BAO survey

Redshift	V_s $[h^{-3}\mathrm{Gpc}^3]$	N_g (per field)	$\bar{n}_g[h^3\mathrm{Mpc}^{-3}]$	b
$1.6 < z < 2.5$	1.34	789	1×10^{-4}	2.5

Furthermore, the growth of structure formation includes information on other interesting cosmological parameters such as the neutrino masses and the primordial non-Gaussianity parameter $f_{\rm NL}$. Table 4.5 shows that the sum of neutrino masses can be constrained with a precision of $\sigma(\sum m_\nu) \simeq 0.06$ eV (also see Saito et al. 2009), meaning that the neutrino masses can be detected at better than a 2σ level if the neutrinos obey the inverted mass hierarchy that predicts the sum of neutrino masses to be $\sum m_\nu \gtrsim 0.11$ eV. The primordial non-Gaussianity can be probed by using the unique catalog of massive clusters available from the SuMIRe survey, because the primordial non-Gaussianity is shown to change the abundance of massive clusters and also induce a characteristic scale-dependence of halo bias. The effect is more significant for more massive halos. The SuMIRe can achieve the accuracy of $\sigma(f_{\rm NL}) \simeq 5$ (Oguri 2009; Oguri & Takada 2010). This precision is similar to that expected from the Planck CMB experiment, however, the SuMIRe can constrain the primordial non-Gaussianities on different length scales and at different redshifts.

4.3.5 Complementarity of PFS NIR BAO survey

The unique capability of PFS is its near-infrared spectrograph. Thanks to the huge multiplicity and high sensitivity addressed in the current design, the PFS NIR arm can offer another BAO survey by further extending redshift measurements of emission-line galaxies out to higher redshifts ([OII] emission lines can be observed up to $z \simeq 2.5$ in the wavelength coverages, 1-1.3μ). The sky emission is brighter in NIR wavelengths than in optical, and the number density of emission-line galaxies to be detected for a given exposure is lower at higher redshifts (see below for details). Hence, it seems impossible to have the full coverage of $0.6 \leq z \leq 2.5$ in red and NIR wavelengths with a *single* survey mode. Here we simply assume a deeper survey covering a smaller sky coverage as given in Table 4.6, motivated by the proposed survey focused on galaxy evolution studies. The numbers in this table need to be more carefully studied. Then we simply address the following questions in order to quantify the complementarity of the PFS NIR BAO survey with the fiducial PFS BAO survey: *The NIR BAO survey can be useful for constraining cosmological parameters? If so, how it can be complementary to the PFS BAO survey in red arm?*

Figure 4.6 shows the expected accuracies of D_A and H measurements at the high redshift window, $1.6 \leq z \leq 2.5$. The D_A estimation can be comparable with the D_A constraints up to $z \simeq 1.6$ from the PFS BAO and BOSS surveys, if the NIR survey of 300 sq. degrees coverage is available. However, the expected constraints on cosmological parameters are only slightly improved by adding the PFS NIR BAO survey, compared to our fiducial red-arm PFS BAO survey alone:

$$\begin{aligned} \sigma(w_{\rm pivot}) = 0.046 \quad &\rightarrow \quad \sigma(w_{\rm pivot}) = 0.045, \\ \mathrm{DE\ FoM} = 33 \quad &\rightarrow \quad \mathrm{DE\ FoM} = 36, \\ \sigma(\Omega_{\rm K}) = 0.057 \quad &\rightarrow \quad \sigma(\Omega_{\rm K}) = 0.054. \end{aligned} \tag{4.22}$$

These improvements do not seem impressive. Therefore, if we want to include the PFS NIR BAO survey, we need to carefully explore an optimal survey design because the NIR BAO survey seems

Table 4.7: Assumed parameters of PFS specifications

Wavelength coverage	$6000 - 10500$Å
Pixel scale	1Å/pixel
Total throughput (including telescope/spectrograph/CCD)	20%
fiber size (diameter)	1.2 arcsec
Spectral resolution (6000-10500Å)	$R \simeq 3000$
gain	2.5-3.5[1]

to require longer exposures per field to obtain the required number densities of target galaxies with sufficiently high signal-to-noise ratios of the [OII] emission lines.

4.3.6 Target selection for PFS redshift survey

The primary science driver of PFS survey is the high-precision measurements of BAO features in the galaxy power spectrum over a range of redshifts $0.6 \lesssim z \lesssim 1.6$. To cover this redshift range we consider early-type galaxies and [OII] emission-line galaxies as target galaxies for the PFS survey. The striking advantage of PFS survey is we can use deep, multi-color HSC imaging data to find target galaxies, *if* we overlap the PFS survey regions with the HSC regions.

For cosmology, what we need to measure for each galaxy is its redshift and angular position, where the angular position is precisely determined from the HSC imaging data. The redshift accuracy we need is a few 10^{-3} in z on average (Seo & Eisenstein 2003), and therefore a spectral resolution of $R \sim 1000$ or higher is required. Hence, the important, practical questions we should resolve for PFS survey are:

- What is the minimum exposure time per pointing to obtain sufficiently accurate redshifts for all the target galaxies?
- What is the minimum total nights to cover the area of sky we require for the BAO survey?
- How can we efficiently select target galaxies? HSC data is enough? Or other data sets, when combined with HSC, can increase the efficiency to have desired number densities of target galaxies?
- To achieve the required redshift survey, what are the requirements on the PFS spectrograph specifications?

For galaxies out to $z \sim 1.2$ it is not hard to obtain the redshifts as the redshift range has been well studied with 8m-class telescopes: various data sets are available such as SDF (Kashikawa et al. 2004), zCOSMOS (Lilly et al. 2007), DEEP2 (Coil et al. 2006), and soon VIPERS[2] surveys. However, this is not the case for higher redshifts or longer wavelengths $\sim$ 8500-10000Å, where sky

[2] http://vipers.inaf.it/

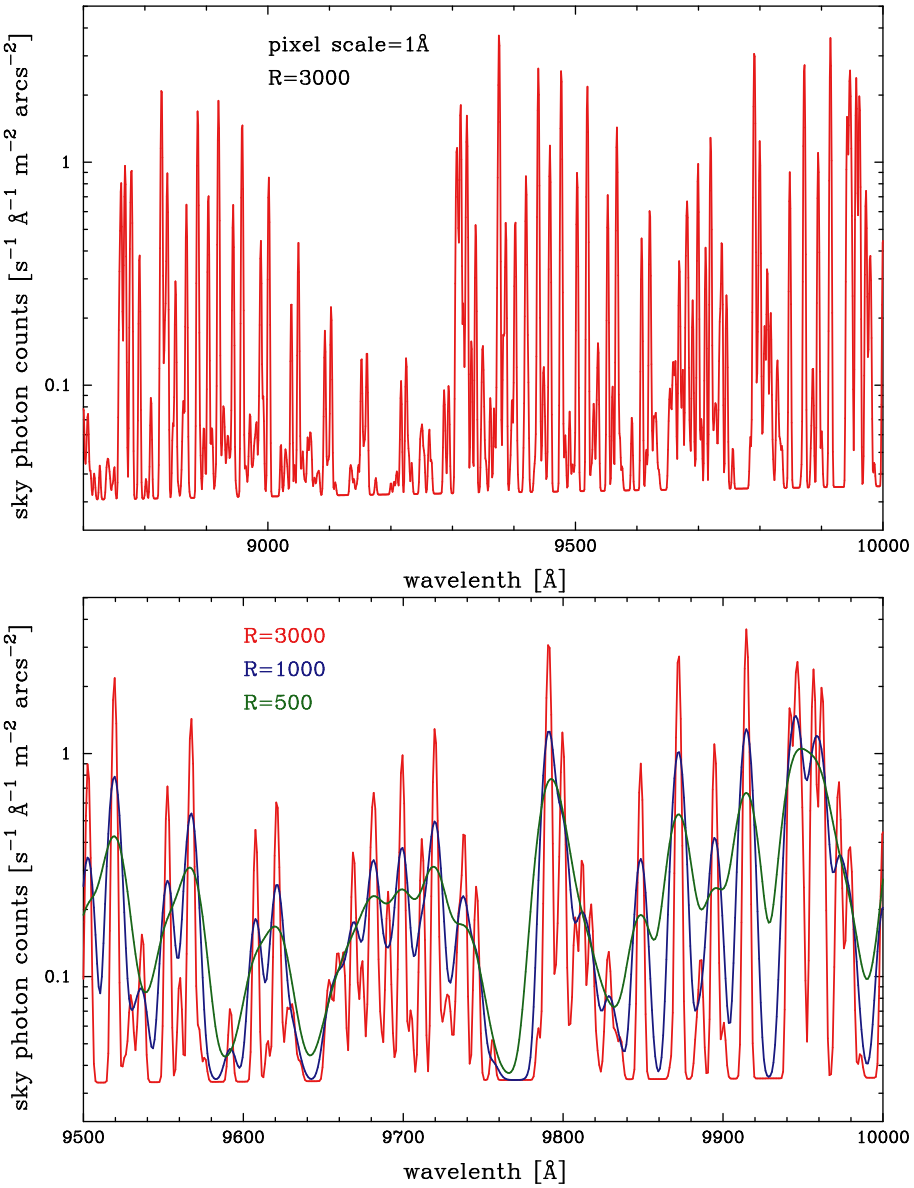

Figure 4.7: *Upper panel*: The model sky spectrum used in the following analysis; the sky model is constructed based on the VLT data of sky emission lines (UVES sky spectrum) plus the continuum flux, where the continuum arises from zodiacal light, and we simply assumed 0.07×10^{-16} erg/s/Å/cm^2 in this wavelength range as suggested in the UVES paper(Hanuschik 2003). Here we included the specification parameters of PFS spectrograph given in Table 4.7: the pixel scale is 1Å/pixel, the spectral resolution $R = 3000$, but didn't include the throughput (that is, shown is the sky flux before the telescope). *Lower panel*: Shown is how different spectral resolving powers change the sky spectrum. Note that the wavelength range shown, 9500-10000Å, is narrower than in the upper panel.

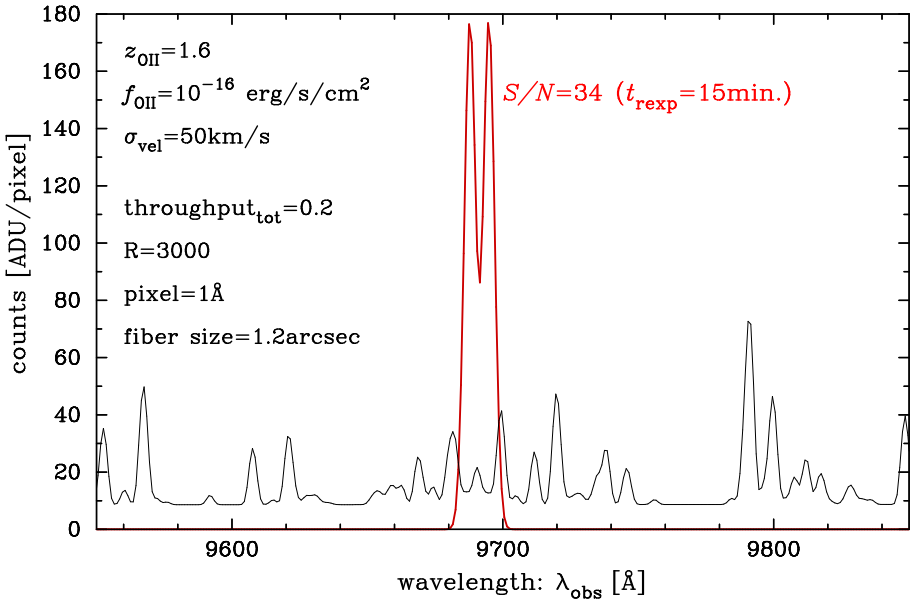

Figure 4.8: A simulated spectrum of [OII] emission line with PFS red arm, assuming 15min exposure, the *observed* line flux, $f_{\rm OII,obs} = 10^{-16}$ erg/s/cm^2, $z_{\rm OII} = 1.6$, and the velocity dispersion $\sigma_{\rm vel} = 50$ km/s. The units in the y-axis is in ADU/pixel, i.e. the expected counts on CCD chips, assuming the PFS specification given in Table 4.7. The black curve shows the expected noise (1σ) assuming the sky spectrum in Figure 4.7 and the Poisson noise. For this OII emission line, the total S/N, integrated over the CCD pixels, is $S/N \simeq 34$.

background is very high and dominates spectral noise in each CCD pixel. A wide-area spectroscopic survey of this wavelength range using 8m-class telescope, using red-sensitive, fully-depleted CCD chips, has not been fully explored. There is a proposed plan (private communication with L. Guzzo) to carry out a large-scale redshift survey with VLT telescope, where the red-sensitive CCD chips were recently installed. If this happens, it will advance our understanding of galaxy redshift survey in the wavelengths.

Hence in the following we focus on the red-wavelength range 8500-10000Å to make the feasibility study of galaxy target selection. Unfortunately, however, there is no sufficiently reliable, accurate model of sky spectrum over this range of wavelengths. In this section, rather than using the model sky spectrum, we use actual data of the sky spectrum, UVES sky emission spectrum, which is taken with VLT in high resolution mode ($R \simeq 40000$) and publicly available from the website[3] (also see Hanuschik 2003).

Figure 4.7 shows the sky spectrum constructed based on the UVES spectrum, and we will use the sky spectrum in the following analysis. The UVES sky spectrum includes only the OH emission lines, where the continuum contribution is subtracted from the original data. There would be some contribution, sub-dominant though, to the sky background arising from zodiacal light, however, this amplitude is not fully understood. We simply added the continuum contribution by assuming the flux $f_{\rm sky,continuum} = 0.07\times10^{-16}$ erg/s/Å/arcsec^2 as suggested in Hanuschik (2003). However, a more careful analysis for refining the sky model is needed, and this is in working progress (Gunn et al. in preparation). To compute the sky model, we included the pixel scale and spectral resolution

[3]http://www.eso.org/observing/dfo/quality/UVES/pipeline/sky_spectrum.html

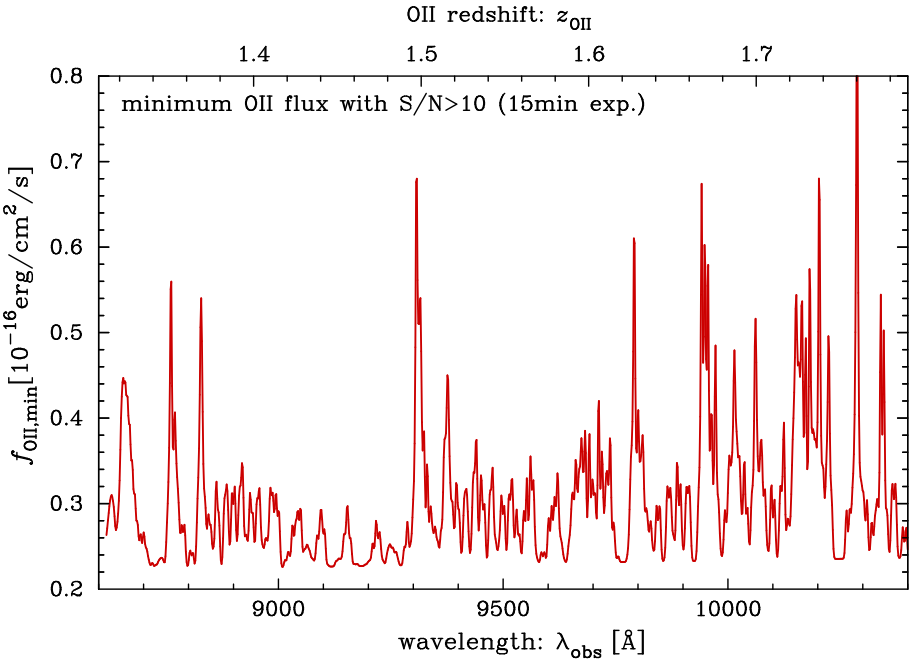

Figure 4.9: Shown is a minimum observed [OII] line flux as a function of emitter redshift such that the emission line at the redshift is detected with total signal-to-noise greater than 10 ($S/N \geq 10$), based on the calculation as in Figure 4.8. We assumed the exposure time of 15min.

of PFS: 1Å/pixel and $R = 3000$, as in Table 4.7. It should be noted that the broadband z'-filter photon counts, computed from this sky spectrum model, gives a photon counts which is consistent with the counts actually observed with the Subaru Suprime-Cam within a factor 2; the sky model above tends to be higher than the counts actually seen. Given the fact that the sky background has large time variabilities, our model is considered as a conservative estimate. In the following we will use this sky model to estimate an expected signal-to-noise ratio for detecting [OII] emission lines for $z \gtrsim 1.4$ galaxies.

The lower panel of Figure 4.7 shows the sky spectrum as a function of the spectral resolution. The higher spectral resolution has an advantage: it gives more windows of wavelengths where the sky emission line contaminations are low. This corresponds to more windows of emitter redshifts for having larger cosmological volumes to cover for a BAO survey.

In Figure 4.8 we show a simulated spectrum of [OII] emission line expected with 15min PFS observation, assuming that the observed [OII] line flux (including dust extinction) $f_{[\mathrm{OII}],\mathrm{obs}} = 10^{-16}$ erg/s/cm^2, redshift $z = 1.6$ and the velocity dispersion $\sigma_{\mathrm{vel}} = 50$ km/s. For the PFS performance we assumed the specification parameters given in Table 4.7. Thanks to the power of Subaru's photon collecting power, such an [OII] emission line is detected at high significance (the total $S/N \simeq 34$), even with such a short exposure time 15min. In addition, a resolution of $R \simeq 3000$ would allow us to resolve [OII] doublets, which would be useful to disentangle from sky emission lines in similar wavelengths, if a velocity dispersion is sufficiently small like $\sigma_{\mathrm{vel}} \lesssim 50$ km/s.

With the model sky spectrum or the simulated spectrum in hand, we can now ask: what is the minimum [OII] flux to be detected by PFS with sufficiently high signal-to-noise ratios for

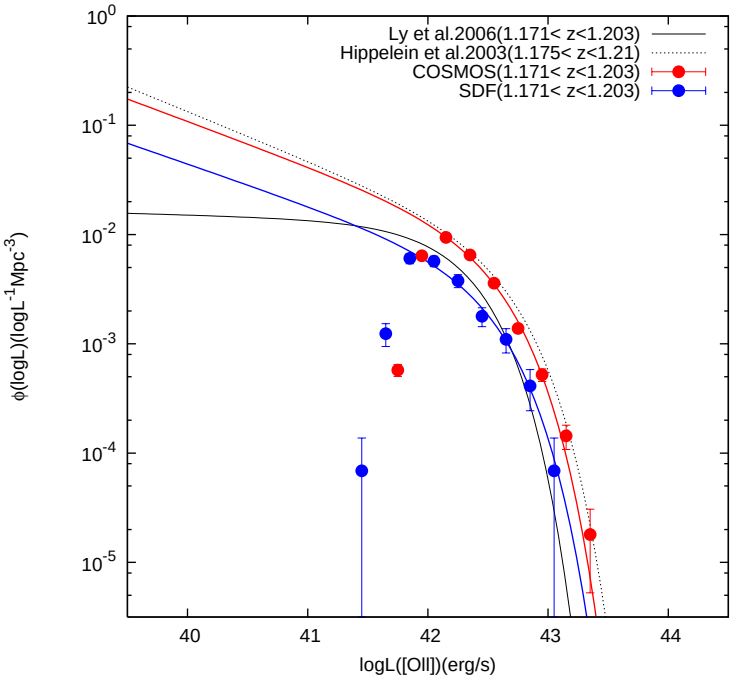

Figure 4.10: Luminosity function (LF) of [OII] emission lines, where dust extinction is corrected (taken from (Takahashi et al. 2007)). Red points are the result obtained combining the multiple narrow-band and broad-band filter data of the COSMOS field, while the blue points are for the narrow- and broad-band imaging data of the SDF field. The error bars denote the Poisson noise, and do not include the cosmic sampling variance arising due to a finite area of the survey. The corresponding red and blue curves are the best-fit Schechter functions, respectively. The black solid and dashed curves are the best-fit models in Hippelein et al. (2003) and Ly et al. (2007).

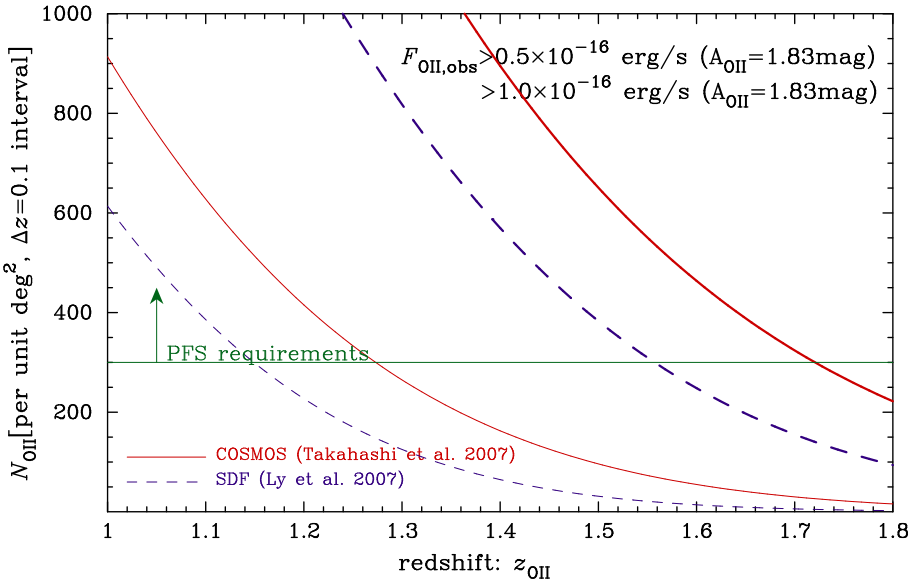

Figure 4.11: Expected number of [OII] emitters per unit sq. degrees and redshift interval $\Delta z = 0.1$ against emitter redshifts, which have *observed* line fluxes greater than 0.5 and 1.0×10^{-16} erg/s/cm^2 with PFS, respectively. Here we assumed the [OII] luminosity functions in Takahashi et al. (2007) (solid curves) and Ly et al. (2007) (dashed), and assumed the dust extinction $A_v = 1.87$ mag to convert the intrinsic flux to the observed flux at PFS. Takahashi et al. (2007)

a fixed exposure time? How does this minimum flux vary as a function of emitter redshift? Figure 4.9 gives an answer to these questions, showing how the minimum [OII] flux with $S/N \geq 10$ varies as a function of emitter redshifts. Here we again assumed the exposure time 15min. The plot clearly shows that OII emitters can be detected with $S/N \geq 10$ if the observed flux $f_{[OII],obs} \gtrsim 0.5 \times 10^{-16}$ erg/s/cm^2, for most range of redshifts we are interested in. For a small portion of redshifts, where the sky background is high, a higher flux threshold is required.

Then, the next important question to be resolved is; are there a sufficient number of [OII] emitters at redshifts to observe with PFS, for a reasonable amount of exposure time? To address this question, we need the intrinsic luminosity function of [OII] emitters. However, a spectroscopic sample of [OII] galaxies at $z \gtrsim 1$ is still lacking, as those galaxies are faint, and the spectroscopic redshift survey is very expensive. Instead we here use the sample of [OII] emitters at such high redshifts constructed based on the narrow-band filter imaging surveys with Subaru Telescope, for the two fields, Subaru Deep Field (SDF; Ly et al. (2007)) and COSMOS (Takahashi et al. (2007)). While the narrow-band imaging survey, in combination with broad-band imaging data, allows a very efficient survey to search for candidates of [OII] emitters thanks to a large field-of-view of the Subaru Suprime-Cam, the sample may still contain contaminations of galaxies at different redshifts due to low spectral resolution that causes a misidentification of emission lines. Figure 4.10 shows the luminosity functions at $z \sim 2$, obtained from the narrow-band filter surveys of SDF and COSMOS fields. Note that the dust extinction was corrected for based on the previous analysis (Hopkins 2004). The results for the different fields show a sizable difference. The difference may be due to the cosmic sampling variance, but hasn't yet resolved.

Figure 4.11 shows the expected number density of [OII] emitters as a function of redshifts, for a

given limiting flux, either $f_{\rm OII,lim} = 1$ or 0.5×10^{-16} erg/s/cm^2, respectively, assuming the [OII] luminosity functions in Figure 4.10 and 15min exposure with PFS. Here we assumed the dust extinction $A_{\rm [OII]} = 1.87$ (Hopkins 2004) to convert the intrinsic flux to the observed flux at the telescope. The horizontal line indicates the requirements for the galaxy number density of [OII] emitters in these redshift range in order to carry out the BAO experiment that is not limited by the shot noise as given in Table 4.3. For both the cases implied from the SDF and COSMOS surveys, if we use the [OII] emitters with observed fluxes $f_{\rm [OII],obs} \gtrsim 0.5 \times 10^{-16}$ erg/s/cm^2 as tracers of large-scale structure, corresponding to the signal-to-noise ratios $S/N \gtrsim 10$ with PFS for 15min exposure as indicated in Figure 4.9, a sufficiently number of [OII] emitters would be available over the whole range of redshifts up to $z \simeq 1.6$.

In summary, thanks to the unique capability of PFS for its multiplicity and sensitivity, just 15min exposure per field is required to sample target galaxies with sufficient number densities in each redshift slice, required to carry out the BAO experiment. Hence, assuming 100% success rate for selecting target emission-line galaxies from multi-color HSC data, **we will just need about 50 clear nights in total to cover 2000 sq. degrees area for the PFS BAO survey** (assuming the PFS FoV of 1.5 degrees in diameter, 8 hours available for observation per night, and 5min overhead per field). However, this is the case if we can select target galaxies from the multi-color HSC imaging survey with 100% success rate, and the required nights would increase if the success rate is degraded, and this issue is discussed below. Anyway the PFS is so powerful instrument to carry out the spectroscopic follow-up survey to carry out a cosmological redshift survey, but this is only the case if a pre-existing imaging survey needed to find target galaxies is needed. In fact, this will very likely happen in the PFS era, because various imaging surveys such Pan-Starrs, DES, LSST and Euclid are currently ongoing or planned. Therefore, the power of PFS for conducting BAO experiments is not rather limited by the number of nights available, but limited by the pre-existing imaging data. Once even a wider-area imaging survey is available, the PFS follow-up survey can achieve its full potential to deliver even higher-precision cosmological constraints.

Selection function

As implied in Figure 4.9, we would have a complicated selection function of [OII] emission-line galaxies in redshift space. For a clustering analysis of the galaxy distribution, we need to properly take into account the observed selection function; otherwise, an incorrect selection function may cause spurious features in the measured galaxy clustering, which would in turn bias parameter estimation. How can we properly take into account the selection function for galaxies measured with PFS? To address this issue we need to use a mock catalog of target galaxies including the effect of sky emission and galaxy clustering. This will be studied carefully.

An efficient target selection with multicolor HSC data

TBD

4.4 Needs for accurately modeling BAO

Since the underlying physics of BAOs is well-understood, and the characteristic scale of BAOs basically lies on the (quasi-)linear regime of the gravitational clustering, the BAOs can be used as a *robust* standard ruler, and utilizing the Alcock-Paczynski effect, a precision measurement of BAO offers the constraints on the angular diameter distance $D_A(z)$ and the Hubble parameter $H(z)$ at given redshift of galaxies. Combining the redshift distortion effect which apparently distorts the galaxy clustering pattern, we can also constrain the growth-rate parameter $f(z)$ of the large-scale structure formation, defined by $f(z) \equiv d\ln D_+/d\ln a$, with the quantities D_+ and a being the linear growth factor and the scale factor of the Universe, respectively.

However, there are several caveats and criticisms against the robustness of the BAOs. In practice, we need an accurate theoretical template for BAOs to correctly determine the acoustic scale and the magnitude of redshift distortion. While the linear theory for BAOs has been fully established and the acoustic structure of BAO can be quantified with a help of the publicly available Boltzmann code, the linear theory prescription is indeed inadequate for the practical measurement of BAOs which include various systematics. Apart from the instrumental systematics, there are at least three known systematics that alter the acoustic structure in the power spectrum and correlation function; non-linear gravitational clustering, non-linear redshift distortion arising from the two competitive effects known as Kaiser and Finger-of-God effects, and finally the galaxy biasing. Figure 4.4 shows the evolution of power spectrum obtained from the N-body simulations, which illustrates the significance of the non-linear gravitational clustering. Although these effects are basically moderate at the relevant scales of BAOs ($k \lesssim 0.3h\,\mathrm{Mpc}^{-1}$), in order to pursue an order-of-magnitude improvement, the accurate modeling of BAOs is observationally demanding.

Indeed, this issue is rather critical when we consider the simultaneous constraints on D_A, H and f. Due to the redshift distortion and Alcock-Paczynski effects, the clustering statistics exhibit some amounts of anisotropies. As a result, the power spectrum is generally described in the two dimension, and is characterized as function of k and μ, i.e., $P(k,\mu)$, where k is the wavenumber and μ is the directional cosine between the line-of-sight direction and the wave vector $\vec{k}$. These distortion effects provide very useful cosmological information, and are the key to simultaneously constrain D_A, H and f. Coupled with the effect of non-linear gravitational clustering, however, both the amplitude and shape of the power spectrum or correlation function are significantly changed, and an accurate modeling of BAOs that ensures a percent-level precision seems non-trivial.

4.5 Modeling BAOs in 2D from perturbation theory

Among various attempts to accurately model the BAOs, the perturbation theory (PT) approach provides a forward modeling technique to model the BAOs in 2D, and is theoretically motivated by the physics of the formation and evolution of large-scale structure. As long as the non-linear systematic effects are relatively mild, PT method gives a reliable and robust theoretical prediction for the power spectrum or correlation function in redshift space.

The formulation of the PT for large-scale structure has been developed long time ago, and based on this, the standard PT treatment has been established (see Bernardeau et al. (2002) for review).

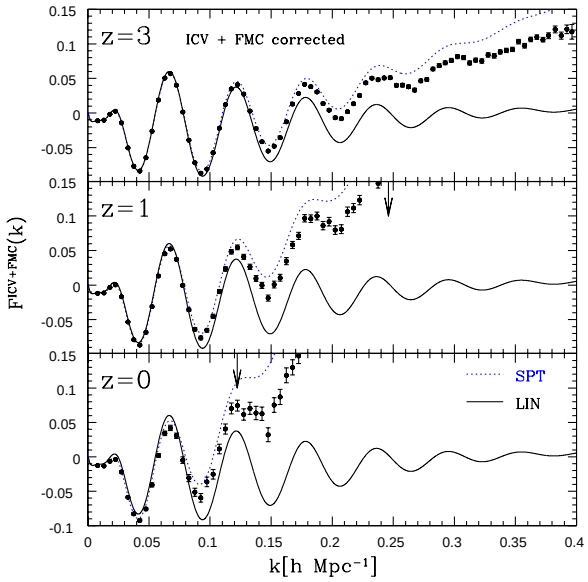

Figure 4.12: Non-linear gravitational evolution of BAOs in N-body simulations at $z = 3$, 1, and 0 (from top to bottom). The matter power spectra obtained from the N-body simulations are divided by the smooth reference power spectra, and are plotted as function of wavenumber. The smooth reference spectrum is calculated from the no-wiggle formula of the linear transfer function in Eisenstein & Hu (1998). By taking the ratio, the effect of linear gravitational growth is canceled, and only the non-linear growth is illuminated in this figure. In each panel, solid line represents the predictions based on linear theory, and the dotted line indicates the leading-order result of standard perturbation theory, referred to as the one-loop SPT. Both of these naive predictions fail to recover the N-body results, and the discrepancy between theory and simulation becomes larger as decreasing the redshift and increasing the wavenumber.

In the framework of PT, we treat the CDM and baryon system as the pressureless and irrotational fluid. Then, the governing equations for the fluid system are reduced to the continuity and Euler equations, in addition to the Poisson equation. Assuming that the field variables of the density and velocity-divergence, denoted as δ and $\theta \equiv -\nabla \boldsymbol{v}/(aH\,f)$, are small perturbed quantities, the solutions for δ and θ are perturbatively obtained. Plugging these solutions into the definition of power spectrum, the corrections for non-linear gravitational evolution can be computed order by order.

The applicability of the standard PT treatment to the theoretical template for BAOs has been carefully examined by several authors (e.g., Jeong & Komatsu (2006b); Nishimichi et al. (2009); Carlson et al. (2009)). A detailed comparison with N-body simulations reveals that the standard PT calculation up to the leading-order correction of non-linear gravity, often quoted as one-loop SPT, is insufficient to describe the non-linear evolution of BAOs at lower redshifts. Figure 4.4 illustrates the example showing that the one-loop SPT fails to reproduce the result of N-body simulations at low-z on small scales. Based on this study, reliable range of the one-loop SPT, within which the prediction reproduces the N-body results quite well with a percent-level precision, is empirically characterized by solving the following equation (Nishimichi et al. 2009):

$$\frac{k_{1\%}^2}{6\pi^2}\int_0^{k_{1\%}} dq P_{\rm lin}(q;z) = C \tag{4.23}$$

with $C = 0.18$ for the one-loop standard PT, where the quantity $P_{\rm lin}$ is the linear matter spectrum.

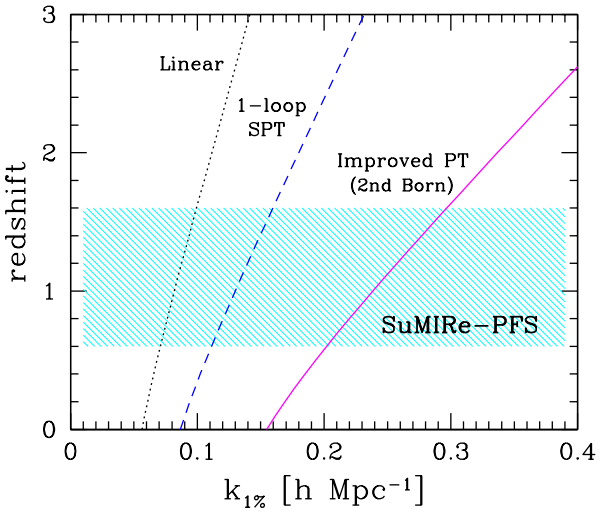

Figure 4.13: Reliable range of power spectrum template for BAOs in wavenumbers, $k_{1\%}$, defined by Eq. (4.23). Dotted, dashed and solid lines represent $k_{1\%}$ for the linear theory, one-loop SPT, and improved PT by Ref. (Taruya et al. 2010). The shaded regions indicates the redshift range planed by the SuMIRe survey.

Figure 4.5 shows the upper limit of the reliable wavenumber $k_{1\%}$ around the relevant redshift of SuMIRe survey (shaded region), for which the reliable range of one-loop SPT depicted as dashed line is estimated as $k \lesssim 0.1 - 0.15h\mathrm{Mpc}^{-1}$.

Recently, however, the situation has changed drastically since several improved treatments of PT were proposed and developed (Crocce & Scoccimarro 2006c,a, 2008; Matarrese & Pietroni 2007; Matsubara 2008; Taruya & Hiramatsu 2008; Taruya et al. 2009b). In contrast to the standard PT calculation, the improved PT is formulated in a non-perturbative way based on the techniques resumming a class of infinite series of higher-order corrections in perturbative calculation. As a result, the applicable range of the PT prediction becomes wider, and the non-linear evolution of BAOs can be accurately described with a percent-level precision. In Figure 4.5, amongst various sophisticated techniques, the results based on the improved PT calculation developed by Taruya et al. (2009b) are compared with N-body simulations. The improved PT predictions coincide with the N-body results beyond the reliable regime of the leading-order calculations (indicated by vertical arrows in right panel), and a sub-percent accuracy can be achieved for the interesting scales of BAOs, where the acoustic signature still remains visible. From this plot, the maximum wavenumber $k_{1\%}$ at each redshift is estimated as those determined from the criterion (4.23) with the constant $C = 0.70$. Figure 4.5 plots the reliable range of improved PT (solid line), which now becomes twice wider than that of the one-loop SPT.

Of course, these successes are just the results in real space, and it cannot be straightforwardly applied to the observed power spectrum in redshift space. Nevertheless, taking a great advantage of the improved PT, modeling non-linear redshift distortion effect becomes even more feasible and tractable. For example, Taruya et al. (2010) presented an improved prescription for the redshift distortion based on improved PT. The full 2D power spectrum of this model is expressed as

$$P(k,\mu) = e^{-(k\mu f\sigma_{\rm v})^2}\left\{P_{\delta\delta}(k) + 2\,f\,\mu^2\,P_{\delta\theta}(k) + f^2\,\mu^4\,P_{\delta\delta}(k) + A(k,\mu;f) + B(k,\mu;f)\right\} \qquad (4.24)$$

with the quantity f being the growth-rate parameter. Here, the power spectra $P_{\delta\delta}$, $P_{\theta\theta}$ and $P_{\delta\theta}$

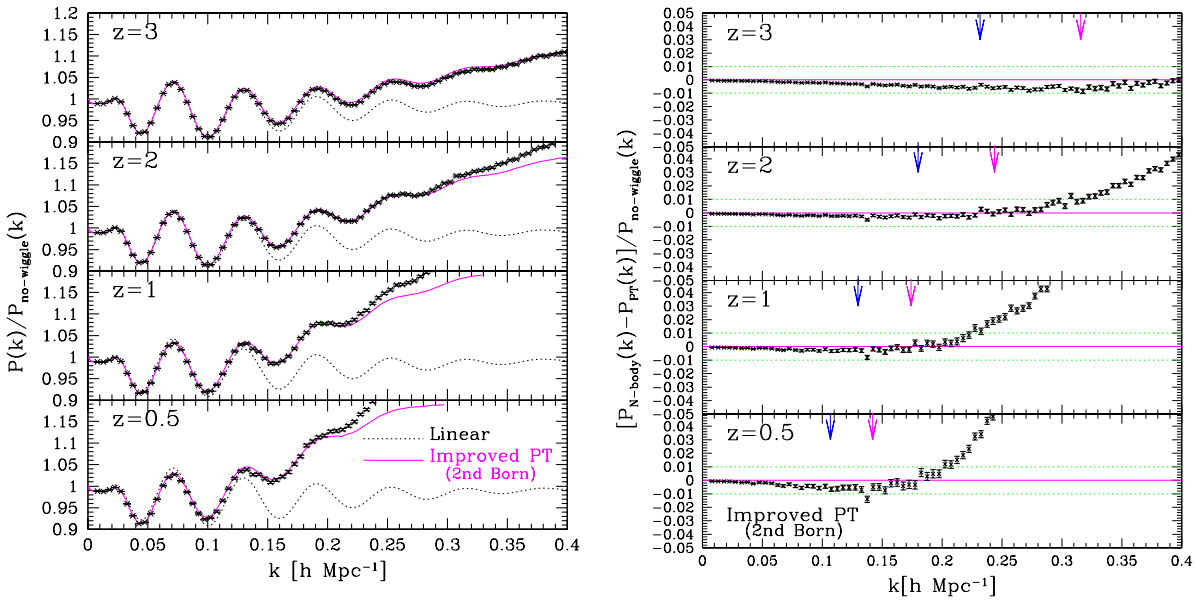

Figure 4.14: Comparison between N-body results and improved PT predictions in real space. The improved PT predictions plotted here are obtained based on the treatment developed by Ref. (Taruya et al. 2009b), which includes the corrections up to the second-order Born approximation of the mode-coupling term. Left: ratio of power spectrum to the smoothed reference spectra, $P(k)/P_{\rm no\text{-}wiggle}(k)$. Solid and dotted lines are improved PT and linear theory predictions, respectively. Right: difference between N-body and improved PT results normalized by the no-wiggle formula, $[P_{\rm N\text{-}body}(k) - P_{\rm PT}(k)]/P_{\rm no\text{-}wiggle}(k)$. In each panel, vertical arrows represent the wavenumber $k_{1\%}$ for the leading-order predictions of standard and improved PT (from left to right).

denote the auto power spectra of density and velocity divergence, and their cross power spectrum, respectively. The quantity $\sigma_{\rm v}$ denotes the one-dimensional velocity dispersion, and the exponential prefactor characterizes the damping behavior by the Finger-of-God effect.

A salient property of the model (4.24) is the terms A and B, which represent the higher-order couplings between velocity and density fields, usually neglected in the phenomenological models of redshift distortion (see Taruya et al. (2010), for more explicit expressions). Figure 4.5 shows the comparison of monopole and quadrupole power spectra between N-body simulations and PT predictions based on the model (4.24). The prediction including the corrections faithfully traces the acoustic feature seen in the N-body simulations, and a percent-level agreement is achieved over the range below the critical wavenumber $k_{1\%}$ (vertical arrows). This is even true for the case adopting the one-loop SPT to compute $P_{\delta\delta}$, $P_{\delta\theta}$ and $P_{\theta\theta}$ (dashed lines). Taruya et al. (2010) have further tested the relevance of the model (4.24), and showed that the parameter estimation using the PT-based template (4.24) correctly recovers the fiducial values of D_A, H and f in a statistically unbiased way.

Although there still remain many aspects for accurately modeling BAOs, and thereby the results mentioned here should be regarded as a partial success, a rapid progress on the PT-based modeling is very encouraging, and the efforts to improve the model are being pursued intensively, taking fully account of galaxy biasing as well.

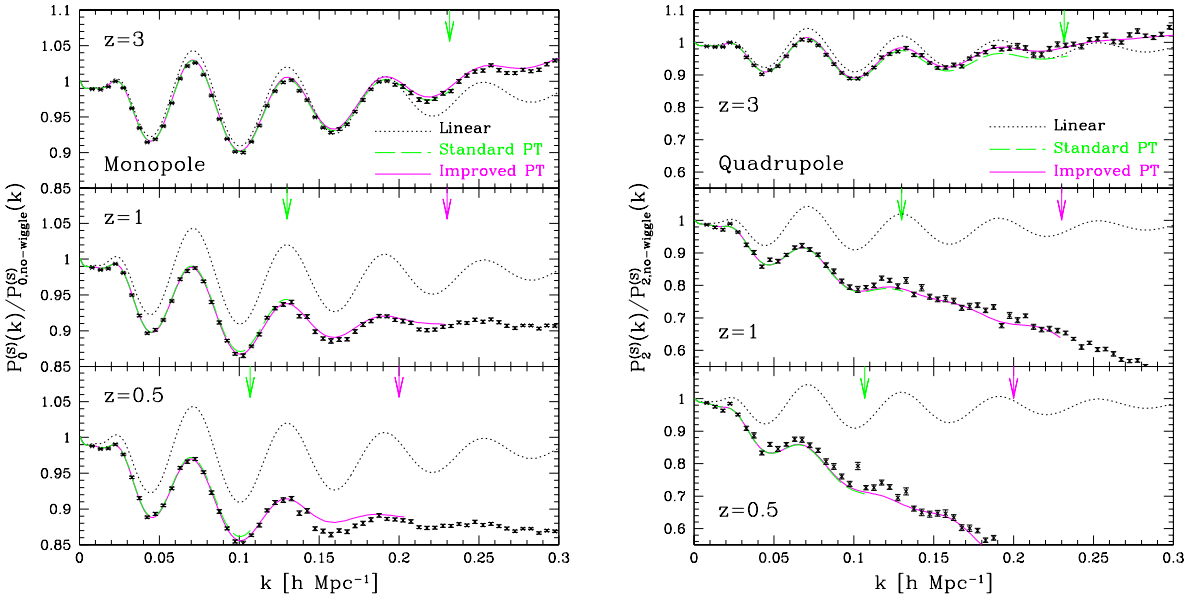

Figure 4.15: Comparison between N-body results and PT predictions in redshift space. Left and right panels respectively show the monopole and quadrupole power spectra, divided by the smooth reference spectrum taking account the linear Kaiser effect, $P^{(S)}_{\ell,\mathrm{no\text{-}wiggle}}$. Solid and dashed lines represent the predictions based on the mode of redshift distortion (4.24), for which the spectra $P_{\delta\delta}$, $P_{\delta\theta}$ and $P_{\theta\theta}$ are obtained from the improved PT and one-loop SPT, respectively. The vertical arrows indicate the maximum wavenumber of the reliable range for one-loop SPT and improved PT calculations, $k_{1\%}$, defined in Eq. (4.23) (from left to right).

4.6 Implications to SuMIRe PFS survey

The SuMIRe PFS survey aims at precisely measuring BAOs around the redshift $z \sim 1$ with the total volume size, $V_s = 6.6\,h^{-3}\mathrm{Gpc}^3$. With the expected number density of galaxies $\overline{n}_g \simeq 3.6 \times 10^{-4} h^3\mathrm{Mpc}^{-3}$ and the bias parameter $b = 1.5$, the SuMIRe PFS survey provides a unprecendented high-precision BAO signal in 2D. Figure 4.5 shows the expected BAO signals for the monopole and quadrupole spectra, with the statistical errors expected from the SuMIRe PFS survey design. Combining the accurate theoretical template, the precision BAO data in 2D can be used for a robust determination of the acoustic scale and redshift distortion.

To illustrate how well we can tightly constrain the cosmic expansion and growth of large-scale structure, Figure 4.17 plots the forecast constraints on D_A, H and f. Here, we consider the specific redshift slice, $1 \le z \le 1.2$, and the range of power spectrum data used in the parameter estimation is assumed to be $k \le k_{\mathrm{max}} = 0.2\,h\mathrm{Mpc}^{-1}$, well within the reliable range of the improved PT. Figure indicates that the monopole spectrum alone (labeled as P_0 only) cannot separately constrain D_A, H and f. This is because the acoustic-scale information obtained from the monopole spectrum is only sensitive to the combination D_A^2/H through the Alcock-Paczynski effect (e.g., Padmanabhan & White (2008)). On the other hand, combination of the monopole and quadrupole spectra or using the full 2D spectrum greatly improves the constraints (indicated by blue, outer shaded region) not only on D_A and H, but also on the growth-rate parameter f. The basic reason for this is simply explained by the fact that the degeneracies between the parameters D_A and H constrained by the monopole is broken by adding the different information from the quadrupole or higher multipoles. Further, the growth-rate parameter is proportional to the strength of redshift

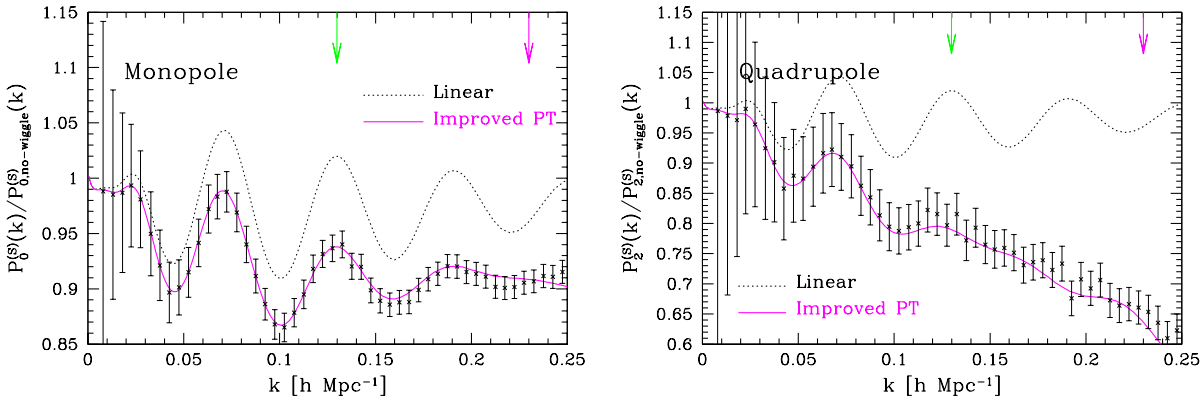

Figure 4.16: Expected BAO signals in the monopole and quadrupole power spectra from SuMIRe PFS survey. The errorbar is estimated from the primary survey design of SuMIRe PFS, combining all the redshift slices at $0.6 < z < 1.6$. The vertical arrows indicate the wavenumber $k_{1\%}$ one-loop SPT and improved PT (from left to right).

distortion, and can be separately determined by combining the monopole and higher multipoles. Although the measurement of the galaxy power spectrum alone merely gives a constraint on $\beta = f/b$, provided the accurate CMB measurement for power spectrum normalization, we can separately determine the growth-rate parameter.

The forecast result in Figure 4.17 is a clear manifestation of the fact that using the information in the anisotropies of the power spectrum is crucial to efficiently extract the cosmological information from the BAOs. Since this can be only achieved with an accurate modeling of BAO in 2D, the PT-based template for power spectrum would play an important role to greatly enchance the scientific outcome of SuMIRe PFS survey. As a consequence, using all the available redshift slices at $0.6 < z < 1.6$, the dark energy equation-of-state parameter w_0 and w_a, and the redshift dependence of the growth-rate parameter $f(z)$ will be tightly constrained, as illustrated in Figure 4.5.

Finally, the accurate modeling of BAO also enables us to find a tiny cosmological signal that is usually neglected. For instance, massive neutrinos imprint a characteristic suppression in the clustering of galaxies at scales below the free-streaming scale of neutrinos. In particular, for neutrino masses of $\sim$ 0.1eV inferred from terrestrial experiments, the free-streeaming scale is incidentally close to the BAO scales. With the accurate theoretical template taking account of the effect of massive neutrinos, a precision BAO measurement can offer an exciting possibility to detect the non-zero neutrino mass, and SuMIRe PFS survey will give a tight constraint on the total neutrino mass, $m_\nu \lesssim 0.1$eV. In this respect, a great synergy of the scienctific outcome would be expected, and a role of accurate BAO template is significant.

4.7 Testing gravity with multipole power spectrum

Testing modified gravity models is one of the important science cases of the SuMIRe PFS survey. Modifying gravity affects both the expansion history of the universe and the growth of the cosmic structures (e.g., (Yamamoto et al. 2007, 2008; Guzik et al. 2010)). The galaxy catalogue from the SuMIRe PFS survey will constrain not only the expansion history but also the growth history by

measuring the BAO signature and the redshift-space distortions. Especially, the growth history plays a key role to distinguish between the dark energy model and the modified gravity models. The multipole power spectrum analysis is useful to quantify the redshift-space distortions to constrain the growth history. The quadrupole power spectrum, which gives the leading anisotropies due to the redshift-space distortion, is demonstrated to be useful in constraining the modified gravity models (Yamamoto et al. 2008, 2010; Kimura & Yamamoto 2010). Techniques to measure the multipole power spectrum are also developed (Yamamoto et al. 2006; Sato et al. 2010).

4.7.1 Models of modified gravity

In general, constructing a consistent theory of modified gravity is challenging. This is because a modification of the gravity theory generally introduces new degree of freedoms, which causes problems. Any theory must pass the stringent solar system tests, which have proved the correctness of the general relativity on those scales. However, the evidence of the accelerated expansion of the universe stimulates the interest in modified gravity models, though successful model is not so many. There are two approaches to the modified gravity model. First approach is the phenomenological one, which introduces general parametrization, in modifying the cosmological perturbation equations. γ-parameter, with which the growth rate is written as $\Omega_{\rm m}^{\gamma}(a)$, is such a simple parametrization of this approach. The second approach is the first-principle approach starting from a Lagrangian. Here, we focus on the $f(R)$ model and the galileon cosmological model or the kinetic gravity braiding model of the second approach.

The galileon model is constructed by respecting the Galilean shift symmetry (Nicolis et al. 2009), $\phi \rightarrow \phi + b_\mu x^\mu + c$, with b_μ and c constant, motivated from an effective theory in the so-called decoupling limit of the Dvali-Gabadadze-Porrati (DGP) model in the brane world scenario. The covariant version of the galileon model does not have the Galileon symmetry, but possesses the original interesting properties such that the galileon field equation of motion is the second-order differential equation, even though the action contains second-order derivatives acting on this field, and that the self-accelerating solution exists (Deffayet et al. 2009). A remarkable property of the galileon model is the Vainshtein mechanism, which enables the galileon theory to recover general relativity on small scales. These properties suggest a possible existence of a viable modified gravity model as an alternative to the simple dark energy model, which stimulates the investigation of the cosmological consequences of the galileon model (Silva & Koyama 2009; Kobayashi et al. 2010; Deffayet et al. 2010).

In a recent paper (Kimura & Yamamoto 2010), an extended model of the galileon model is proposed. The extended galileon model, also called the kinetic gravity braiding model, is characterised by a parameter n, which corresponds to the original galileon cosmological model for $n = 1$. The background expansion of the universe of the kinetic braiding model is the same as the Dvali-Turner's model (Dvali & Turner 2003), and the model approaches the Λ CDM model in the limit of large n. Evolution of the linear density perturbation as well as the spherical collapse in the nonlinear regime of the density perturbations are investigated, which are important in order to distinguish between the kinetic braiding model and the cold dark matter (CDM) model or the dark energy model. The left panel of Fig. 4.19 compares the evolution of the linear growth factor divided by the scale factor, $D_1(a)/a$. The linear growth factor of the kinetic braiding model is larger than that of the ΛCDM model throughout its growth history. In the right panel of Fig. 4.19,

the linear growth rate $f = d\ln D_1(a)/d\ln a$ is plotted. In reference (Kimura & Yamamoto 2010), it is also demonstrated that the SuMIRe PFS survey is useful to test this model by measuring the multiple power spectrum.

On the other hand, the $f(R)$ model introduces some function of the Ricci scalar $f(R)$, adding to the Einstein Hilbert action (Starobinsky 2007; Hu & Sawicki 2007b). For the viable model consistent with observations, the function $f(R)$ must satisfy some conditions. The alternation of the action can be regarded as an introduction of the scalar field f_R, where we defined $f_R = \partial f(R)/\partial R$. The $f(R)$ model can evade the solar system tests because of the chameleon mechanism, which hides the scalar degree of freedom in the region with high density. On the scales of cosmology, the mass of the scalar field is approximately given by $m^2 = 1/3f_{RR}$, where $f_{RR} = \partial^2 f(R)/\partial R^2$. This scalar field mediates an attractive force, and modifies the effective gravity in the range determined by the Compton wavelength scale, $1/m$. Thus, on the scales smaller than the Compton length scales, the growth structure is modified (e.g., (Narikawa & Yamamoto 2010)). The SuMIRe PFS survey is useful to constrain the Compton length scale by measuring the redshift-space distortions with the multipole power spectrum (Yamamoto et al. 2010).

4.7.2 Multipole power spectrum measurement

In order to test the growth history using the redshift-space distortion, the multipole power spectrum analysis is useful. To measure the monopole power spectrum, the method by Feldman, Kaiser and Peacock (FKP (Feldman et al. 1994b; Yamamoto 2003)) is familiar. An estimator to measure the quadrupole power spectrum was developed (Yamamoto et al. 2006). Recently, a noble method to measure the multipole power spectrum has been developed (Sato et al. 2010). This method gives us the multipole power spectrum deconvolved from the window effect, which is essential for the precise measurement. Figure 4.20 demonstrates how the deconvolution recovers the original power spectrum properly (For details, see (Sato et al. 2010)). This method is compatible with the use of the fast Fourier transform (FFT) algorithm, and is time-saving. The result is applied for testing modified gravity models (Kimura & Yamamoto 2010).

4.7.3 BAO damping

Due to the nonlinearity of the density perturbations and the velocity field, the BAO signature damps. If one could measure this damping precisely, we can obtain a constraint on the cosmological parameters. Especially, this damping is sensitive to the amplitude of the matter density perturbations (Nomura et al. 2008). In references (Nomura et al. 2009), the damping of the BAO signature is detected, and a constraint on the amplitude of the matter density perturbations is obtained from a measurement of the BAO signature from the luminous red galaxy sample of the sloan digital sky survey. This method will give a useful constraint when the galaxy power spectrum is measured with the SuMIRe PFS survey (Nakamura et al. 2009).

References

Albrecht, A. et al., 2009, ArXiv e-prints, 0901.0721

—, 2006, ArXiv Astrophysics e-prints, arXiv:astro-ph/0609591
Alcock, C., & Paczynski, B., 1979, *Nature*, 281, 358
Ballinger, W. E., Peacock, J. A., & Heavens, A. F., 1996, *MNRAS*, 282, 877
Bernardeau, F., Colombi, S., Gaztañaga, E., & Scoccimarro, R., 2002, *Phys. Rep.*, 367, 1
Bertschinger, E., 2006, *ApJ*, 648, 797
Blake, C. et al., 2010, *MNRAS*, 406, 803
Caldwell, R. R., Dave, R., & Steinhardt, P. J., 1998, Physical Review Letters, 80, 1582
Carlson, J., White, M., & Padmanabhan, N., 2009, *Phys. Rev. D*, 80, 043531
Chevallier, M., & Polarski, D., 2001, Int. J. Mod. Phys., D10, 213
Coil, A. L., Newman, J. A., Cooper, M. C., Davis, M., Faber, S. M., Koo, D. C., & Willmer, C. N. A., 2006, *ApJ*, 644, 671
Coil, A. L. et al., 2008, *ApJ*, 672, 153
Cole, S. et al., 2005, *MNRAS*, 362, 505
Crocce, M., & Scoccimarro, R., 2006a, *Phys. Rev. D*, 73, 063520
—, 2006b, *Phys. Rev. D*, 73, 063519
—, 2006c, *Phys. Rev. D*, 73, 063519
—, 2008, *Phys. Rev. D*, 77, 023533
de Putter, R., & Takada, M., 2010, *Phys. Rev. D*, 82, 103522
Deffayet, C., Esposito-Farèse, G., & Vikman, A., 2009, *Phys. Rev. D*, 79, 084003
Deffayet, C., Pujolàs, O., Sawicki, I., & Vikman, A., 2010, *JCAP*, 10, 26
Dvali, G., Gabadadze, G., & Porrati, M., 2000, Physics Letters B, 485, 208
Dvali, G., & Turner, M. S., 2003, ArXiv Astrophysics e-prints, arXiv:astro-ph/0301510
Efstathiou, G., 2003, *MNRAS*, 343, L95
Eisenstein, D., & White, M., 2004, *Phys. Rev. D*, 70, 103523
Eisenstein, D. J., & Hu, W., 1998, *ApJ*, 496, 605
Eisenstein, D. J., Seo, H., Sirko, E., & Spergel, D. N., 2007, *ApJ*, 664, 675
Eisenstein, D. J. et al., 2005, *ApJ*, 633, 560
Feldman, H. A., Kaiser, N., & Peacock, J. A., 1994a, *ApJ*, 426, 23
—, 1994b, *ApJ*, 426, 23
Frieman, J. A., Turner, M. S., & Huterer, D., 2008, *ARAA*, 46, 385
Gil-Marín, H., Wagner, C., Verde, L., Jimenez, R., & Heavens, A. F., 2010, *MNRAS*, 407, 772
Guzik, J., Jain, B., & Takada, M., 2010, *Phys. Rev. D*, 81, 023503
Hamaus, N., Seljak, U., Desjacques, V., Smith, R. E., & Baldauf, T., 2010, *Phys. Rev. D*, 82, 043515
Hanuschik, R. W., 2003, *A&A*, 407, 1157
Hippelein, H. et al., 2003, *A&A*, 402, 65
Hopkins, A. M., 2004, *ApJ*, 615, 209
Hu, W., & Haiman, Z., 2003, *Phys. Rev. D*, 68, 063004
Hu, W., & Sawicki, I., 2007a, *Phys. Rev. D*, 76, 064004
—, 2007b, *Phys. Rev. D*, 76, 064004
Huterer, D., & Takada, M., 2005, Astroparticle Physics, 23, 369
Huterer, D., Takada, M., Bernstein, G., & Jain, B., 2006, *MNRAS*, 366, 101
Ichiki, K., Takada, M., & Takahashi, T., 2009, *Phys. Rev. D*, 79, 023520
Jain, B., & Khoury, J., 2010, Annals of Physics, 325, 1479
Jain, B., & Zhang, P., 2008, *Phys. Rev. D*, 78, 063503
Jeong, D., & Komatsu, E., 2006a, *ApJ*, 651, 619
—, 2006b, *ApJ*, 651, 619
Kaiser, N., 1987, *MNRAS*, 227, 1
Kashikawa, N. et al., 2004, *PASJ*, 56, 1011
Kimura, R., & Yamamoto, K., 2010, ArXiv e-prints, 1011.2006
Kobayashi, T., Tashiro, H., & Suzuki, D., 2010, *Phys. Rev. D*, 81, 063513
Komatsu, E. et al., 2010, ArXiv e-prints, 1001.4538
Lilly, S. J. et al., 2007, *ApJS*, 172, 70
Linder, E. V., 2003, Physical Review Letters, 90, 091301
—, 2005, *Phys. Rev. D*, 72, 043529
Ly, C. et al., 2007, *ApJ*, 657, 738
Matarrese, S., & Pietroni, M., 2007, *JCAP*, 6, 26

Matsubara, T., 2008, *Phys. Rev. D*, 77, 063530
Matsubara, T., & Suto, Y., 1996, *ApJL*, 470, L1+
Nakamura, G., Hütsi, G., Sato, T., & Yamamoto, K., 2009, *Phys. Rev. D*, 80, 123524
Narikawa, T., & Yamamoto, K., 2010, *Phys. Rev. D*, 81, 043528
Nicolis, A., Rattazzi, R., & Trincherini, E., 2009, *Phys. Rev. D*, 79, 064036
Niemack, M. D. et al., 2010, in Society of Photo-Optical Instrumentation Engineers (SPIE) Conference Series, Vol. 7741, Society of Photo-Optical Instrumentation Engineers (SPIE) Conference Series
Nishimichi, T. et al., 2009, *PASJ*, 61, 321
Nishizawa, A. J., Takada, M., Hamana, T., & Furusawa, H., 2010, *ApJ*, 718, 1252
Nomura, H., Yamamoto, K., Hütsi, G., & Nishimichi, T., 2009, *Phys. Rev. D*, 79, 063512
Nomura, H., Yamamoto, K., & Nishimichi, T., 2008, *JCAP*, 10, 31
Oguri, M., 2009, Physical Review Letters, 102, 211301
Oguri, M., & Takada, M., 2010, ArXiv e-prints, 1010.0744
Padmanabhan, N., & White, M., 2008, *Phys. Rev. D*, 77, 123540
Peacock, J. A., Schneider, P., Efstathiou, G., Ellis, J. R., Leibundgut, B., Lilly, S. J., & Mellier, Y., 2006, ESA-ESO Working Group on "Fundamental Cosmology". Tech. rep.
Pen, U., 2004, *MNRAS*, 350, 1445
Perlmutter, S. et al., 1999, *ApJ*, 517, 565
Riess, A. G. et al., 1998, *AJ*, 116, 1009
Saito, S., Takada, M., & Taruya, A., 2008, Physical Review Letters, 100, 191301
—, 2009, *Phys. Rev. D*, 80, 083528
—, 2010, ArXiv e-prints, 1006.4845
Sato, T., Huetsi, G., & Yamamoto, K., 2010, ArXiv e-prints, 1010.0289
Seljak, U., 2009, Physical Review Letters, 102, 021302
Seo, H., & Eisenstein, D. J., 2003, *ApJ*, 598, 720
Silva, F. P., & Koyama, K., 2009, *Phys. Rev. D*, 80, 121301
Song, Y., Sawicki, I., & Hu, W., 2007, *Phys. Rev. D*, 75, 064003
Starobinsky, A. A., 2007, Soviet Journal of Experimental and Theoretical Physics Letters, 86, 157
Sumiyoshi, M. et al., 2009, ArXiv e-prints, 0902.2064
Takada, M., 2006, *Phys. Rev. D*, 74, 043505
Takada, M., & Bridle, S., 2007, New Journal of Physics, 9, 446
Takada, M., & Jain, B., 2004, *MNRAS*, 348, 897
Takada, M., Komatsu, E., & Futamase, T., 2006, *Phys. Rev. D*, 73, 083520
Takahashi, M. I. et al., 2007, *ApJS*, 172, 456
Takahashi, R. et al., 2009a, ArXiv e-prints, 0912.1381
—, 2009b, *ApJ*, 700, 479
Tang, J., Kayo, I., & Takada, M., 2010, in preparation
Taruya, A., & Hiramatsu, T., 2008, *ApJ*, 674, 617
Taruya, A., Nishimichi, T., & Saito, S., 2010, *Phys. Rev. D*, 82, 063522
Taruya, A., Nishimichi, T., Saito, S., & Hiramatsu, T., 2009a, *Phys. Rev. D*, 80, 123503
—, 2009b, *Phys. Rev. D*, 80, 123503
Yamamoto, K., 2003, *ApJ*, 595, 577
Yamamoto, K., Nakamichi, M., Kamino, A., Bassett, B. A., & Nishioka, H., 2006, *PASJ*, 58, 93
Yamamoto, K., Nakamura, G., Hütsi, G., Narikawa, T., & Sato, T., 2010, *Phys. Rev. D*, 81, 103517
Yamamoto, K., Parkinson, D., Hamana, T., Nichol, R. C., & Suto, Y., 2007, *Phys. Rev. D*, 76, 023504
Yamamoto, K., Sato, T., & Hütsi, G., 2008, Progress of Theoretical Physics, 120, 609
Zheng, Z. et al., 2005, *ApJ*, 633, 791
Zheng, Z., Zehavi, I., Eisenstein, D. J., Weinberg, D. H., & Jing, Y. P., 2009, *ApJ*, 707, 554

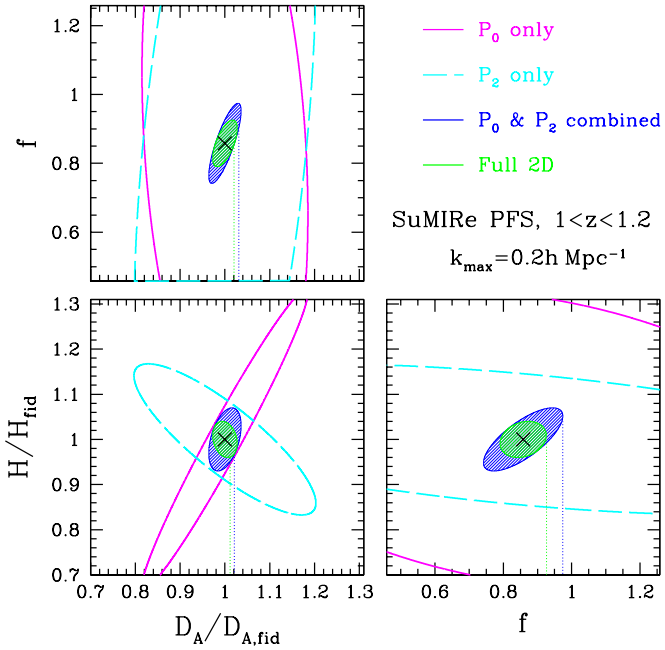

Figure 4.17: Forecast constraints on D_A, H, and f obtained from the redshift slice of $1 \leq z \leq 1.2$. Contours and shades represent the 1-σ errors (68% C.L.) on two-dimensional parameter space. The range of power spectrum data used in the parameter estimation is assumed to be $k \leq k_{\rm max} = 0.2\,h{\rm Mpc}^{-1}$.

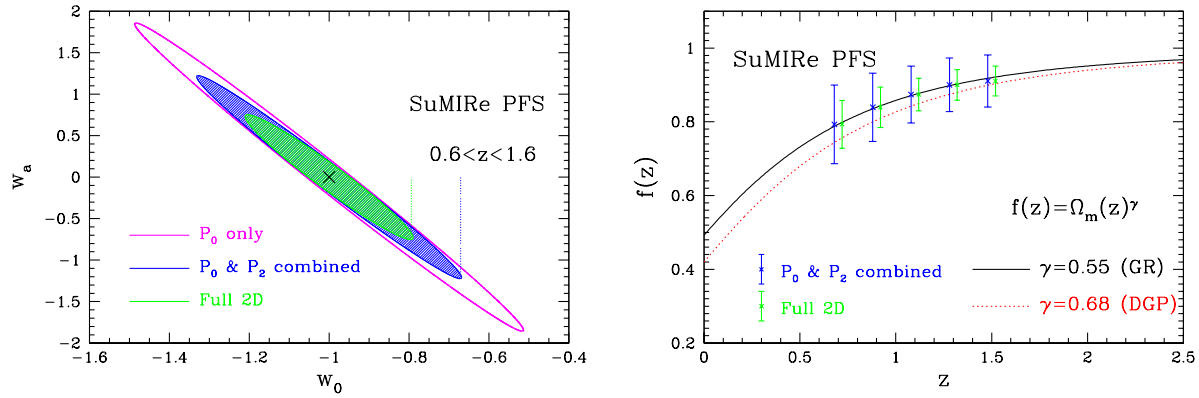

Figure 4.18: Forecast constraints on dark energy equation-of-state parameters, w_0 and w_a (left), and redshift evolution of growth-rate parameter $f(z)$ (right), obtained from all the redshift slices at $0.6 \leq z \leq 1.6$.

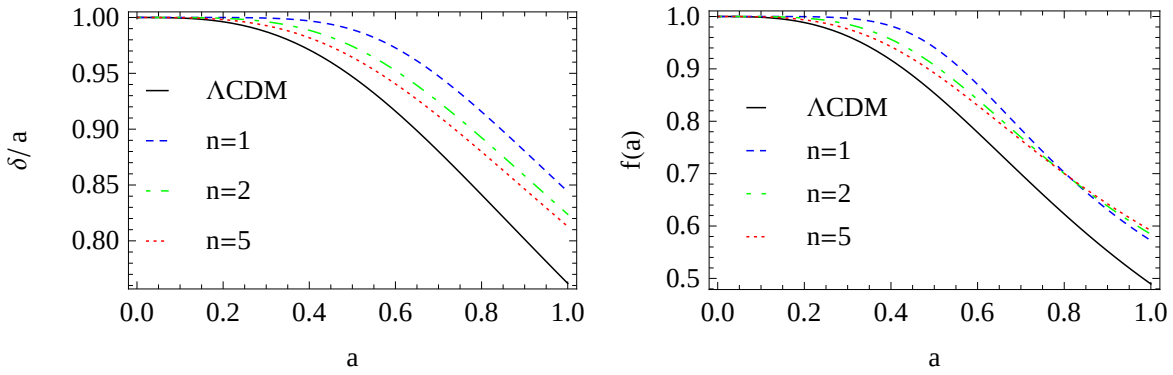

Figure 4.19: Left panel shows the linear growth factor divided by scale factor as a function of scale factor for the ΛCDM model (solid curve) and the kinetic braiding model $n = 1$ (dashed curve), $n = 2$ (dash-dotted curve), and $n = 5$ (dotted curve), respectively. Right panel is the linear growth rate as a function of scale factor. (Kimura & Yamamoto 2010)

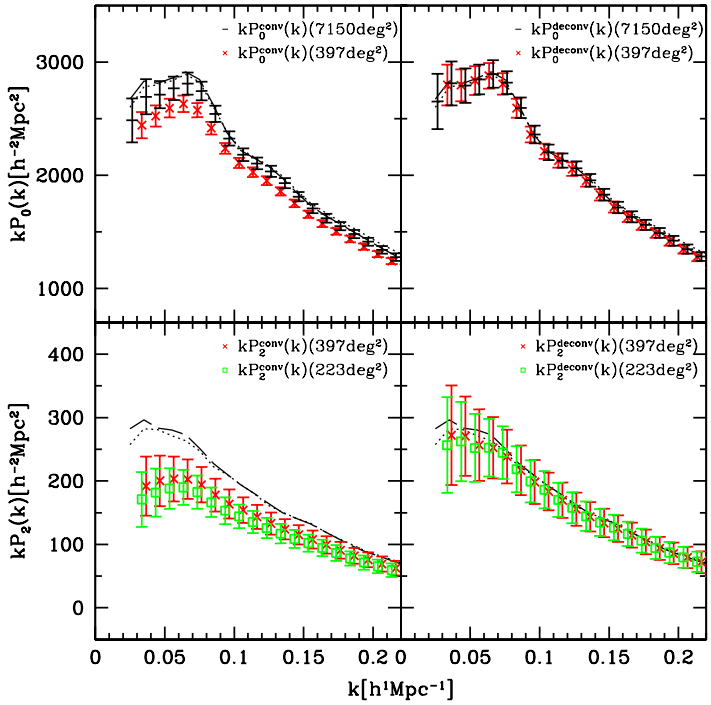

Figure 4.20: Comparison of the convolved $kP_\ell^{\rm conv}(k)$ (left panel) and deconvolved power spectra $kP_\ell(k)$ (right panel), using the average from 1000 mock catalogues with the same survey window of the SDSS LRG sample. The upper panels plot the monopole $\ell = 0$, while the lower ones the quadrupole $\ell = 2$. For the monopole power spectrum, the two cases are presented: One is the case when the full sample is divided into 18 subsamples and the other is the case without division of the full sample. For the quadrupole spectrum, the two different cases of the division of the full sample are presented, in which the mean survey areas are 397 square degrees and 223 square degrees, respectively. In each panel, the solid curve and the dotted curve are the deconvolved spectrum and the convolved spectrum from the ideal catalogue with large volume. The good agreement of all the spectra in the right panels indicates that our deconvolution recovers the original power spectrum properly. This figure is from reference (Sato et al. 2010).

5 Galactic Archaeology with SuMIRe PFS Survey

Masashi Chiba (Tohoku U.), Wako Aoki (NAOJ), Judith G. Cohen (Caltech), Miho Ishigaki (NAOJ), Mikito Tanaka (Tohoku U.), Narae Hwang (NAOJ), and Daisuke Kawata (UCL)

Summary

We propose a PFS survey of resolved ancient stars in the Milky Way, M31, and their satellite galaxies, to unravel the formation history of bright galaxies like our own and also determine their dark-halo density profiles, in light of hierarchical clustering scenarios of Cold Dark Matter. The survey is aiming at measuring radial velocities and metallicities of the numerous sample stars in synergy with both HSC and Gaia. It is also the extension of SDSS/SEGUE in its survey depth. The targets consist of (1) ancient Galactic stars belonging to the stellar halo and thick disk, (2) bright red giant branch stars in the M31 halo, and (3) stars bound to satellite galaxies of the Milky Way and M31. The primary observing mode in this survey is low-resolution spectroscopy with R of $\sim 2,000$ to $3,000$ for 2,000-3,000 fibers per a PFS field, for which calibration methods developed by SDSS/SEGUE can be effectively utilized. We also propose to have a high-resolution mode with $R = 35,000$ and ~ 200 fibers for the purpose of tagging detailed chemical abundance patterns to each of the kinematically independent substructures in the Milky Way halo and thick disk.

5.1 Background

Unraveling how galaxies like the Milky Way and M31 formed in the expanding Universe is our ultimate science goal in near-field cosmology (Freeman & Bland-Hawthorn 2002), because such nearby galaxies offer us most detailed views of galactic structure and evolution through their resolved stars. In particular, ancient galactic components such as extended thick disks and stellar halos provide invaluable information on early chemo-dynamical evolution of disk galaxies more than 10 billion years ago, i.e., well before luminous thin disk components appeared. For instance, stars spread over the vast reaches of the Milky Way halo are characterized by low metal abundance and high velocity dispersion. This extreme nature of halo stars compared to disk ones reflects the dynamical and chemical evolution of the Galaxy at early epochs when its appearance differed significantly from what we see today. In particular, recent growing observational evidence as provided by the Sloan Digital Sky Survey (SDSS) suggests that the halo may have formed, in part, from an assembly process of many subsystems, such as dwarf galaxies. Indeed, the idea of an assembly process for halo formation is in perfect accord with the modern theory of galaxy formation based on hierarchical clustering of sub-galactic building-block systems in the Cold Dark

Matter (CDM) model. Thus, detailed studies of ancient stellar populations in the Milky Way and nearby galaxies provide us with important clues to understanding galaxy formation.

5.2 Key Science Goals

Our primary science goal with the PFS survey is to clarify the formation history of each Galactic component in light of the hierarchical merging scenario of CDM. As mentioned above, resolved ancient stars in Local Group galaxies including the Milky Way are ideal targets for this study, because such stars hold fossil records of galaxy formation through their kinematics and metallicities. Kinematics of stars reflect past galaxy collapse and/or merging events, as their relaxation time via two-body stellar encounters is quite long compared to galaxy life, so that their distribution in phase space (as defined by integrals of motion such as angular momentum) remains basically unchanged. Metallicities of stars reflect star-formation history and chemical evolution over past years, possibly in association with dynamical state of proto-galactic clouds such as their collision and merging. Also, all of these processes are controlled by hierarchical clustering of CDM via self-gravity in galaxy scales. Thus, to assess what the CDM model predicts, it is of great importance to unravel the spatial profile of dark-matter halos in the Galaxy and its satellite galaxies as well. In this respect, stars are ideal tracers of the background gravitational field, provided that their full space motions are available, combined with precise measurements of proper motions by Gaia. All of these requirements are indeed feasible with the planned PFS.

Thus, our science goals are summarized as follows.

1. Formation of Galactic structures

- What is the merging history of the Milky Way?
- What is the formation of old Galactic components (thick disk and stellar halo)?
- What is the star-formation history of dwarf satellites and its relation to the formation of the Milky Way?
- The formation of M31: what is different from that of the Milky Way?

2. The nature of dark matter in galactic and sub-galactic scales

- How is dark matter distributed in the Milky Way?
- The structure of dark-matter dominated dwarf satellites: is CDM correct?

We describe below detailed explanations for each of these science goals.

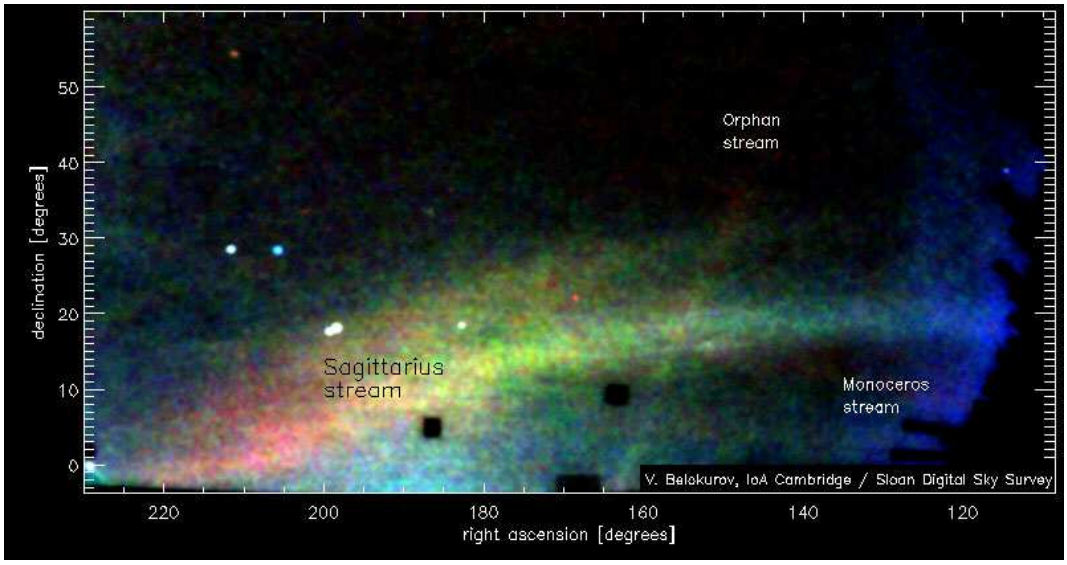

Figure 5.1: Several stellar substructures in the form of stellar streams revealed in the SDSS imaging data (taken from Belokurov et al. 2006). These are remnants of past merging events of dwarf satellites.

5.2.1 Formation of Galactic structures

What is the merging history of the Milky Way?

Our fundamental question is how each of the building blocks of the Milky Way, which possibly consist of mini halos and baryons, is assembled into the current structure of the Galaxy through hierarchical clustering. Actually a couple of lines of evidence for past and current merging events have been revealed as, (i) spatial substructures of stars in the form of stellar streams, which are tidally elongated structures of accreted dwarf satellites (e.g., Ibata et al. 1994; Belokurov et al. 2006) (Figure 5.1), and (ii) a clumpy phase-space distribution of stars in the solar neighborhood, which corresponds to a yet un-relaxed remnant of a past merging event (Helmi et al. 1999; Chiba & Beers 2000) (Left panel of Figure 5.2).

Kinematics and chemistry of these substructures thus tell us the assembly history of dwarf galaxies in the formation of the Milky Way: Those showing yet un-relaxed spatial substructures of stellar distribution in the sky correspond to recent merging events and/or those occurred in the outer halo, because substructures arisen from recent events are still dynamically young and/or the dynamical time in the outer halo is generally as long as 1 Gyr. Instead, even if substructures are spread over and homogenized in the sky after merging, their distribution in a phase space as defined by integrals of motion remains conserved for many dynamical times (Helmi & de Zeeuw 2000, See Figure 5.2). The latter properties of substructures, i.e., their long relaxation time in a phase space, will be of great importance in tracing the assembly history in the Gaia era. Indeed, prior to Gaia, Hipparcos data with precision of ~ 1 mas and ~ 1 mas yr^{-1} for trigonometric parallaxes and proper motions, respectively, have been most accurate and reliable ones for the stars with $V < 12$ mag. However, as shown in the left panel of Figure 5.2, even Hipparcos is not precise enough to identify possibly numerous substructures within the main body of the halo star distribution (except for an apparent clumping feature located at $L_z \simeq 1000$ km s^{-1} kpc and $L_\perp \simeq 2300$ km s^{-1} kpc). The right

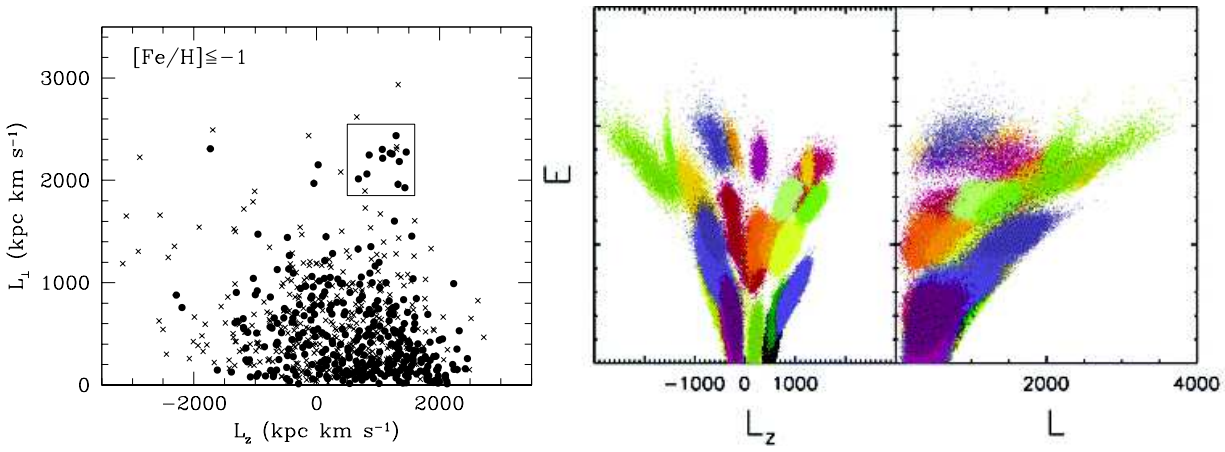

Figure 5.2: Left: Distribution of nearby metal-poor ([Fe/H]≤ -1) stars in the angular momentum space L_z vs. $L_\perp = \sqrt{L_x^2 + L_y^2}$, where astrometric data for many of these stars are taken from Hipparcos Catalog (from Chiba & Beers 2000). Filled circles and crosses denote stars with distance from the Sun of $D < 1.0$ kpc and $1.0 \leq D < 2.5$ kpc, respectively. Note that the stars inside the box form a clumpy substructure, which is possibly associated with a past merging event of a dwarf galaxy. Right: Model distribution of nearby stars in the integrals of motion space, i.e., E vs. L_z and E vs. L, based on numerical simulations of falling satellites into the Milky Way (from Helmi & de Zeeuw 2000). The different colors represent different satellites. Shown is the final distribution of stars after 12 Gyr within about 6 kpc from the Sun, after convolution with the errors expected for Gaia.

panel of Figure 5.2 suggests that Gaia's data will be precise enough to allow us to identify each of substructures in a phase space, provided that we have complementary data of radial velocities and metal abundances for stars as faint as $V = 20$ mag, i.e., to the limiting magnitude of Gaia's astrometry observations.

The identification of merger debris in a phase space is further strengthen by the use of orbital frequencies of stars in a specified gravitational potential, which are straightforwardly estimated from available three dimensional motions and positions. In particular, mean separations of patchy features in frequency space provide a measure of the elapsed time after a merging event of a satellite galaxy (McMillan & Binney 2008). Figure 5.3 shows simulation results demonstrating the power of using orbital frequencies (Gómez et al. 2010). Three different substructures identified in the space defined by the integrals of motion are shown in the space of orbital frequencies $\Omega_r - \Omega_\phi$ vs. Ω_ϕ, where Ω_r and Ω_ϕ are orbital frequencies in radial and azimuthal directions. Tidal debris taken inside a sphere of 2.5 kpc radius at the supposed solar position (8 kpc) from the galactic center show a patchy particle (star) distribution, and the peak of the power spectra of the stellar distribution in the ϕ direction, $P(k_\phi)$, provide us with the accretion time of the satellites.

It is worth noting that all of these merging histories are memorized in three-dimensional positions and space motions of stars. Thus, a coordinated spectroscopic survey of numerous stars belonging to each Galactic component, combined with extensive accurate and uniform quality astrometric data provided by Gaia, will enable us to derive the merging history of the Milky Way.

What is the formation of old Galactic components (thick disk and stellar halo)?

Thick disk:

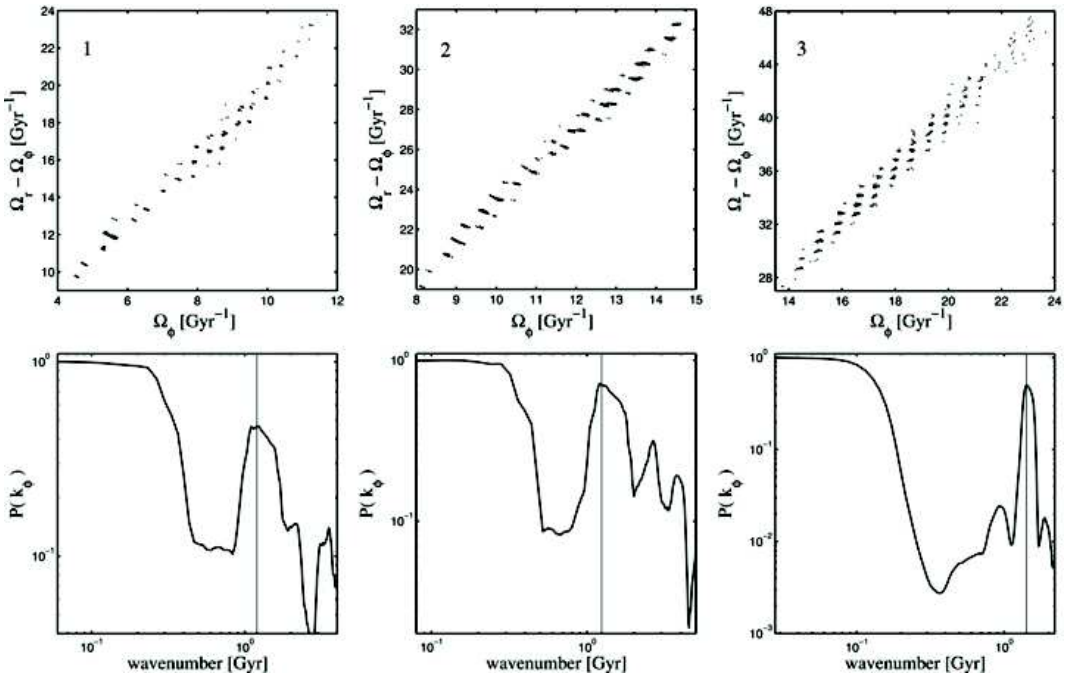

Figure 5.3: The top panels show the distributions of three different tidal debris associated with three different satellites in orbital frequency space ($\Omega_r - \Omega_\phi$ vs. Ω_ϕ), inside a sphere of 2.5 kpc radius at the supposed solar position (8 kpc) from the galactic center, whereas the bottom panels show the 1D normalized power spectra, $P(k_\phi)$, along the $k_r = 0$ direction (taken from Gómez et al. 2010). The wavenumber of the dominant peak (from left to right: 1.24, 1.41 and 1.21 Gyr, respectively) is used to estimate the time since accretion of the satellite (7.8, 8.9 and 7.6 Gyr, respectively). Other peaks in the spectra are associated to either the harmonics of this wavenumber or to the global shape of the particle's distribution in frequency space.

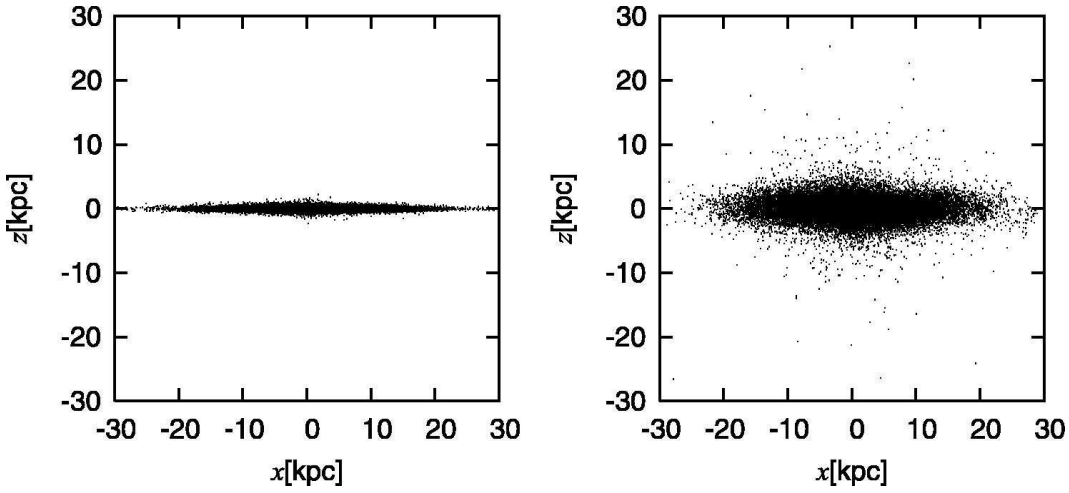

Figure 5.4: Numerical simulation for dynamical heating of a pre-existing thin disk (left panel) to a thick disk with large velocity dispersion (right panel) caused by infalling lumpy CDM subhalos (taken from Hayashi & Chiba 2006). Kinematical properties of this model disk will be directly compared with those of Galactic thick disk provided by the combination of PFS and Gaia.

Since the discovery of the thick-disk component in both external (edge-on) disk galaxies and the Milky Way (Burstein 1979; Yoshii 1982; Gilmore & Reid 1983), its origin has yet remained enigmatic. Several models for the formation of thick disks have been proposed, as summarized into the following five different scenarios: (i) Dissipative collapse of a disk (Burkert et al. 1992), (ii) Multiple dissipative mergers of building blocks (Brook et al. 2004), (iii) Tidal debris of shredded satellites (Abadi et al. 2003), (iv) Disk heating triggered by merging of luminous satellites (Quinn et al. 1993) or CDM subhalos (Hayashi & Chiba 2006), (v) Radial migration of disk stars due to transient spiral arms (Schönrich & Binney 2009).

While each of these scenarios reproduces some properties of the observed thick disk in the Milky Way, a comprehensive understanding of its formation process has not yet been achieved, mostly because of the incomplete observational information on this ancient disk component. Key physical characteristics of the thick disk, which may distinguish different formation scenarios, include: (1) the metallicity distribution and its spatial dependence, (2) the mean rotational velocity and its dependence on the height above/below the galactic plane, (3) the presence or lack of asymmetry in velocity distributions, (4) the distribution of orbital eccentricities and its spatial dependence, and so on (Hayashi & Chiba 2006; Sales et al. 2009). The reasons for the importance of these characteristics are summarized as follows: (1) If energy dissipation of baryonic component is essential in the collapse or merging of a disk, like the scenarios (i) and (ii) mentioned above, a finite metallicity gradient will be prevalent in the thick disk stars, whereas dissipationless process of a stellar system, like (iii) and (iv) in the above, would smear out any metallicity gradients. Also, deriving the detailed metallicity distribution of the thick disk, especially the metal-weak part, and the comparison with the stars in dwarf satellites will tell us the relation between disk formation and satellite galaxies. (2) Merging of visible or dark satellites onto a pre-existing thin disk makes a disk hotter in both R and z direction, in such a way that stars located at higher $|z|$ after heating are originally at smaller R. This results in the systematic decrease of a mean rotational velocity of a thick disk with increasing $|z|$. (3) A finite number of merging processes in the scenarios like

(iii) and (iv), would leave a finite asymmetric distribution of line-of-sight velocities in both R and $|z|$ directions. (4) Each of disk formation scenarios provides a characteristic distribution of orbital eccentricities of thick-disk stars and its spatial dependence (See Figure 5.5).

However, since the currently available data of the thick disk are limited only to samples of less than 1000 stars in the solar neighborhood (Bensby & Feltzing 2010), the intrinsic kinematical and chemical nature of the thick disk is yet largely unknown. To distinguish the above scenarios of the disk formation, especially for the scenario (v), in which radial migration of thin-disk stars from other disk positions is essential, we require the data of both thin-disk and thick-disk stars at different locations far from the Sun. Thus, a systematic survey of disk stars with PFS will be most useful to set important limits on the formation scenario of this enigmatic thick-disk component.

Stellar halo:

In contrast to the thick disk, most parts of the stellar halo may have formed from direct accretion and merging of smaller subsystems, like the satellite galaxies of the Milky Way, as first envisaged by Searle & Zinn (1978) following and advanced from the picture of the seminal paper, Eggen et al. (1962). This merging picture is indeed in agreement with a currently standard scenario of galaxy formation in CDM models, so observational approaches to extracting past merging histories of the stellar halo as already argued in the previous subsection will be essential. Moreover, recent studies of the stellar halo mostly provided by SDSS/SEGUE suggest that its global structure appears to have multiple components, namely 'inner halo' and 'outer halo', which show different kinematical and chemical distributions (e.g., Carollo et al. 2007): An analysis of nearby stars but labeled with their full orbital motions in Galactic space has revealed that inner halo stars confined at the galactocentric distance r less than 15-20 kpc show a flattened density distribution in vertical direction and that azimuthal velocities of the stars are distributed both in positive and negative with nearly zero mean. On the other hand, stars belonging to the outer halo seem to show a spherical density distribution and its mean rotational velocity is retrograde relative to the rotational direction of the disk components. Also, the outer halo contains more metal-poor stars than the inner halo.

However, the current understanding of a multi-component halo is to be more refined and extended by assembling the data of *in situ.* stars, i.e., stars in the outer halo, which are too faint to be accessible with SDSS/SEGUE. Indeed, whether the division between these two halos is distinct or continuous in both kinematics and chemistry of member stars should be clarified by a deeper spectroscopic survey. Also, the spectroscopic sample in the SDSS/SEGUE is only sparsely selected with spatial separation between fields of $\sim$ 20 deg, so detection of smaller substructures may be biased against in sampling. Thus, the use of a larger aperture telescope and more densely selected targets in our Subaru/PFS survey based on 2,000 to 3,000 fibers within a large FOV will be most essential to clarify the complete picture for the formation of the halo and its substructures.

What is the star-formation history of dwarf satellites and its relation to the formation of the Milky Way?

Dwarf satellites in the Milky Way and M31 provide us with most useful information on galaxy formation process through their resolved stars (e.g., Aoki et al. 2009; Cohen & Huang 2010), since

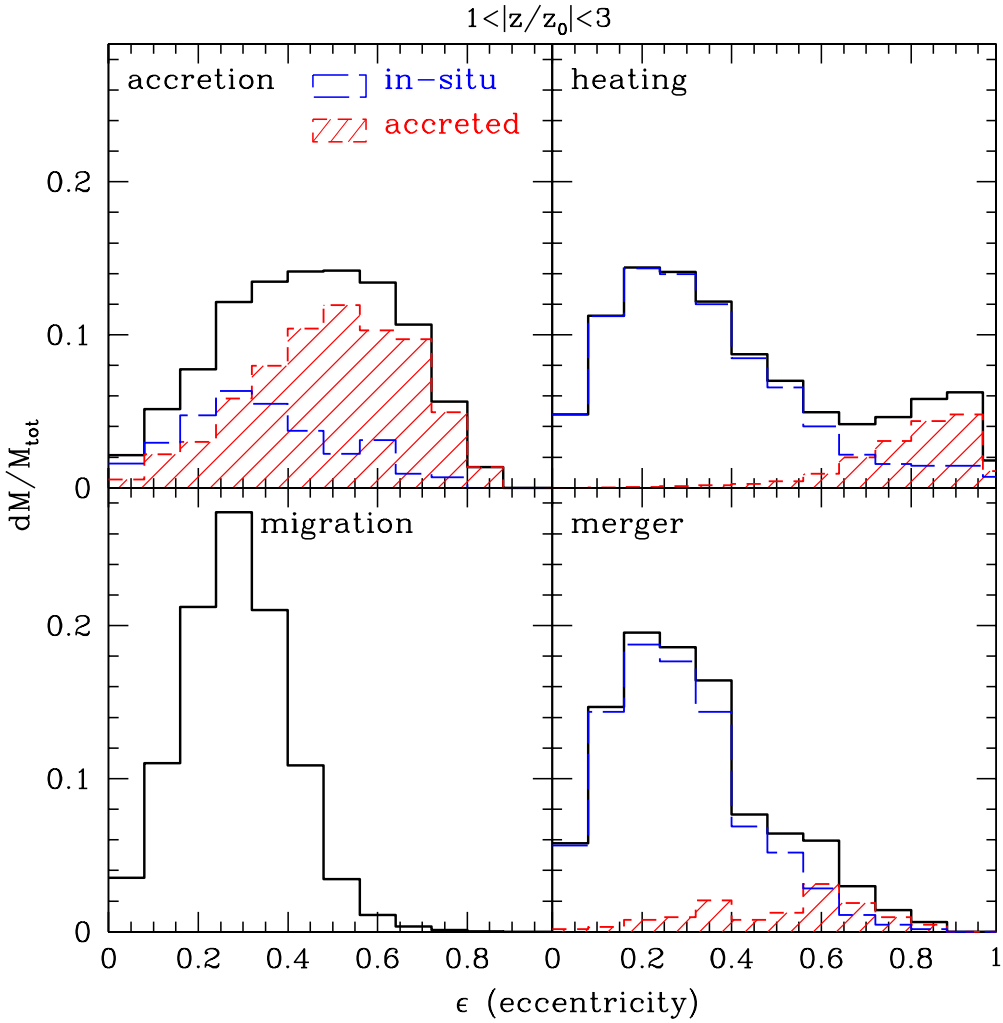

Figure 5.5: Comparison of the eccentricity distributions of each thick disk formation model (accretion, heating, migration, and merger) for stars in the range of 1-3 thick-disk scale-heights and cylindrical distance of 2 to 3 scale radii (taken from Sales et al. 2009). The combination of Gaia and PFS will provide orbital properties of many thick-disk stars to be compared with these theoretical predictions.

such small galaxies may act as building blocks of bright galaxies like the Milky Way in the context of hierarchical clustering scenario of CDM models. Resolving each of stars in nearby satellites is especially advantageous: the star formation history of galaxies can be deduced from a color-magnitude diagram (CMD) of stellar populations, based on the distribution of stars in both turn-off region and giant branches in comparison with theoretical isochrones. However, since ages and metallicities of stars are coupled in a CMD, especially those of bright RGB stars, which are main targets in the observations of satellites because of their brightness, it is essential to obtain independent information from spectroscopic observations, namely metallicities of stars. Thus, the combination of stellar distribution in a CMD with its frequency distribution of metallicities as provided by the PFS survey will enable us to derive star-formation and chemical evolution histories of satellites in both the Milky Way and M31. In particular, while some or many of dwarf satellites seem to hold internal variation of stellar populations as a function of distance from the center, e.g., as judged from horizontal branch morphology, only a limited number of bright stellar spectra in each satellite have been observed (see e.g., Kirby et al. 2010 for recent studies) so that the spatial variation of metallicity distribution of stars is yet unclear. Thus, also for the purpose of increasing statistical significance of derived metallicity distributions, it is of great importance to conduct a coordinated spectroscopic observation of many stars in each of satellites, using the low resolution mode of PFS.

Once the properties of stellar populations in satellites are deduced, a further question is whether the assembly of such stars explains the current populations of the Milky Way halo, taking into account that the halo itself may be comprised of multiple components (inner and outer halos, Carollo et al. 2007). For instance, chemical abundance patterns of dwarf-satellite stars may resemble more to those of the outer halo (Ishigaki et al. 2010) than the inner halo, suggesting that dwarf galaxies are, at least in their outer parts, building blocks of metal-weak halos of bright galaxies. Further, more advanced insight on this issue will be obtained with a large spectroscopic survey of dwarf-satellite stars with PFS.

The formation of M31: what is different from that of the Milky Way?

Besides our own Galaxy, exploring diffuse stellar halos in external galaxies is needed to accomplish our understanding of their generic nature and formation history in different disk galaxies. Model investigations (e.g., Kauffmann et al. 1996) predict that each disk galaxy has been developed through a different formation and evolutionary path: the collapse epoch, star formation history, and assembly rate of small subsystems are not identical and each stellar halo is expected to hold a different morphology, as other, much brighter components (bulge and disk) differ along the Hubble sequence. In this regard, the Andromeda galaxy (M31) is an excellent test-bed for galaxy formation models: it provides an external perspective of the nearest large galaxy similar to our own and yet is close enough for individual halo stars to be studied in great detail.

The most significant discovery in the M31 halo is probably its complex substructures such as the giant southern stream (GSS) (e.g., Ferguson et al. 2002) and other stellar steams (Ibata et al. 2007; Tanaka et al. 2010). The Andromeda GSS contains a high concentration of metal-rich stars (Tanaka et al. 2010) and is located behind M31 with a significant degree of elongation along the line of sight (Figure 5.6). The GSS and other stellar streams have attracted particular attention, as they reveal an ongoing hierarchical formation process of M31 and thus place invaluable constraints

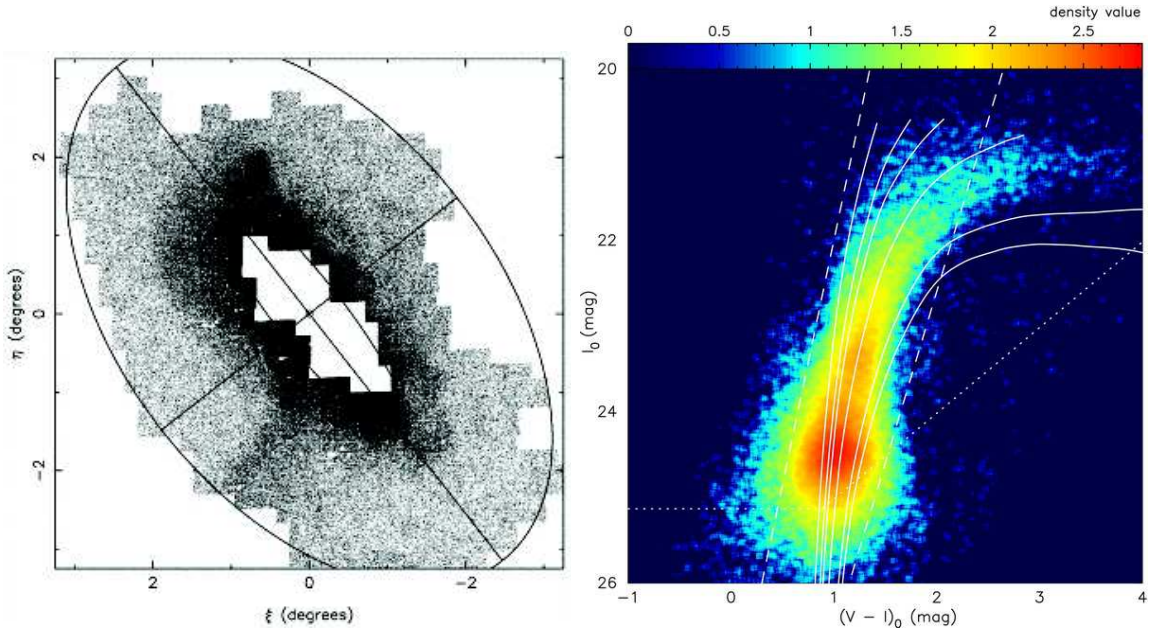

Figure 5.6: Left: Surface density of RGB stars in the M31 halo derived with the INT (taken from Ferguson et al. 2002). Right: Log-scaled CMD for Giant Southern Stream derived from Subaru/Suprime-Cam observations, where solid lines are theoretical isochrones (VandenBerg et al. 2006) of age 12 Gyr spanning the metallicity range [Fe/H]= −2.14, −1.41, −1.14, −0.71, −0.20, and 0.00 (taken from Tanaka et al. 2010).

on galaxy formation models. To get further important insight into such models, spectroscopic data of kinematics and metallicities for stars as faint as V= 21.5 mag (i.e., stars around the tip of RGB) will be most useful to constrain chemo-dynamical formation processes of the M31 halo in the course of hierarchical merging of CDM-based building blocks. In particular, as photometric metallicities are uncertain because of age-metallicity degeneracy, measuring spectroscopic metallicities for a large number of halo stars will allow us to derive the metallicity distribution (MD) and its spatial dependence for a mean halo field as well as the MD for each of halo substructures. Spectroscopic information is also useful to distinguish the M31 stars alone from foreground Galactic stars through the comparison of line-of-sight velocities. For instance, based on such spectroscopic studies, Guhathakurta et al. (2005) succeeded to uncover the presence of an extended halo component in M31 up to the projected distance of $\sim$ 165 kpc, namely resembling the extension of the Milky Way halo (e.g., Sakamoto et al. 2003).

Similarly, dwarf satellites in M31 as well as another nearby late-type galaxy, M33, which is possibly interacted with M31 provide us, through their resolved stars, with a clue to understanding the assembly process since these may play a role as building blocks of brighter galaxies or surviving remnants of hierarchical merging. For instance, for some number of stars in M31's dwarf satellites, Keck/DEIMOS observations have revealed the presence of metal-poor stars (See Figure 5.7 taken from Kalirai et al. 2010). A much larger data set for those galaxies will be available from PFS with a larger FOV, thereby enabling us to obtain the MDs for Andromeda satellites and to compare them with the MDs of Galactic satellites.

A fundamental question on such dwarf satellites is if their formation process is indeed understood in the frame work of CDM models; if all CDM subhalos are successful in forming stars inside

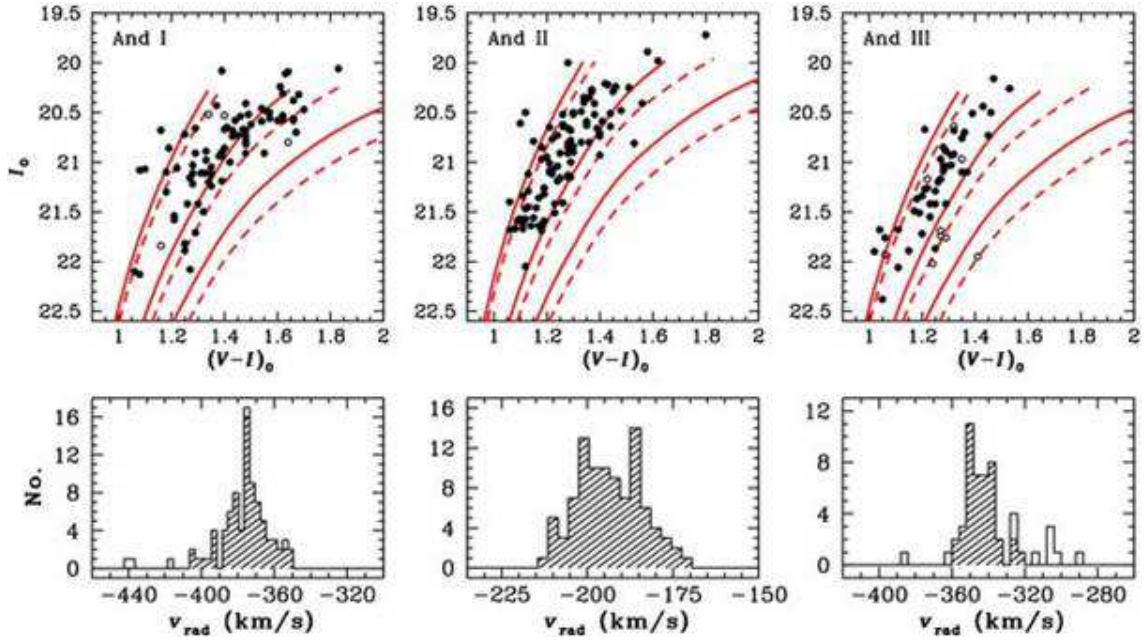

Figure 5.7: CMD (top) and radial velocity histograms (bottom) for three satellite galaxies of M31: And I (80 stars), And II (95 stars), and And III (43 stars) samples of RGB members (taken from Kalirai et al. 2010). The three sets of isochrones shown in each panel of the CMDs (VandenBerg et al. 2006), for an age of 12 Gyr and metallicities of [Fe/H]= −2.31 (left), −1.31 (middle), and −0.83 (right). The models for [α/Fe] = 0.0 are shown as solid curves and those for [α/Fe] = +0.3 are shown as dashed curves.

them, models are suffering from so-called 'the Missing Satellites Problem', i.e., while CDM models predict hundreds of subhalos (with masses of $10^{7-9}M_{\odot}$) around a dark halo like the Milky Way and M31 (with $10^{12}M_{\odot}$), only a few tens of visible satellites are observed in each of these galaxies (Klypin et al. 1999; Moore et al. 1999). Therefore, deriving star formation histories of visible dwarf satellites will offer us important clues to understanding how such galaxies form in the context of CDM scenario.

5.2.2 The nature of dark matter in galactic and sub-galactic scales

How is dark matter distributed in the Milky Way?

The CDM model for structure formation in the Universe has been quite successful to explain a wide variety of observational results on the spatial scales larger than about 1 Mpc (Tegmark et al. 2004). However, the recent advent of high-resolution N-body simulations on CDM-based structure formation has highlighted various important issues on the spatial scales smaller than 1 Mpc, i.e., galactic and sub-galactic scales.

One of the unsolved issues is that while the CDM model predicts largely tri-axial density distribution of dark halos in dynamical equilibrium (e.g., Jing & Suto 2000), observational results as deduced from spatial and kinematical properties of the Sagittarius Stream suggest a rather round or only slightly tri-axial shape of Galactic gravitational potential over the radius of 15 to 60 kpc

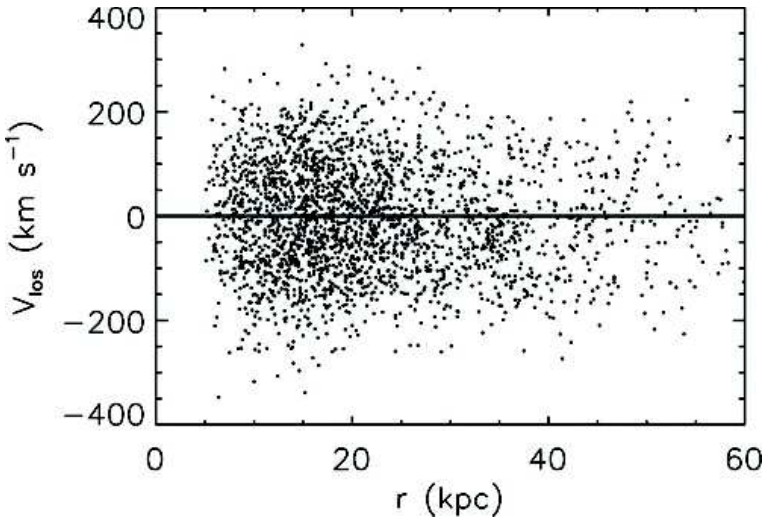

Figure 5.8: Distribution of line-of-sight velocities (corrected for the Local Standard of Rest and solar motions) as a function of galactocentric distance for the sample of 2401 halo BHB stars selected from SDSS DR6 (taken from Xue et al. 2008). Subaru/PFS will collect much larger number of stars at larger galactocentric distance.

(e.g., Johnston et al. 2005). Although some baryonic process, such as back reaction of dark halo to gas cooling, may make CDM halos rounder (Kazantzidis et al. 2004), a more fundamental problem is yet the lack of our knowledge on the accurate shape and form of Galactic gravitational potential, since the Sagittarius Stream is seen only in a plane crossing Galactic poles and in a limited range of radii. In this respect, halo stars, such as blue-horizontal-branch (BHB) stars and other bright red-giant-branch (RGB) stars, are excellent tracers of a background gravitational potential, as they can travel up to the outer reaches of the Galaxy and can be seen even at such a remote position (Figure 5.8). For this purpose, what we require is accurate distances and full spatial motions of halo stars: distances are straightforwardly available from their positions in a color-magnitude diagram and/or trigonometric parallaxes measured by the Gaia astrometry satellite. Full spatial motions are then derived from radial velocities measured by the currently proposed PFS survey, combined with proper motions from the Gaia survey. Thus, both PFS and Gaia will provide us with accurate kinematical information of numerous halo stars, thereby allowing us to estimate the three-dimensional distribution of Galactic potential, namely including dark halo in the Galaxy.

Further insight into the form of Galactic potential in light of CDM models can be elucidated from the careful inspection of phase-space structure of stellar streams. As mentioned earlier, CDM models predict hundreds of subhalos in a Milky Way sized dark halo, whereas the darkness of subhalos makes it difficult to identify them. However, their presence can be unveiled through their gravitational effects on surroundings. One of ideal cases is the interaction with the tidal tails of ancient globular clusters (Ibata et al. 2002): the structure of such tidal tails is sensitive to heating by repeated close encounters with massive dark subhalos, and the resultant effect is readily noticeable in a phase space defined by the integrals of motion, provided accurate kinematical information is available from Gaia and PFS (See Figure 5.9).

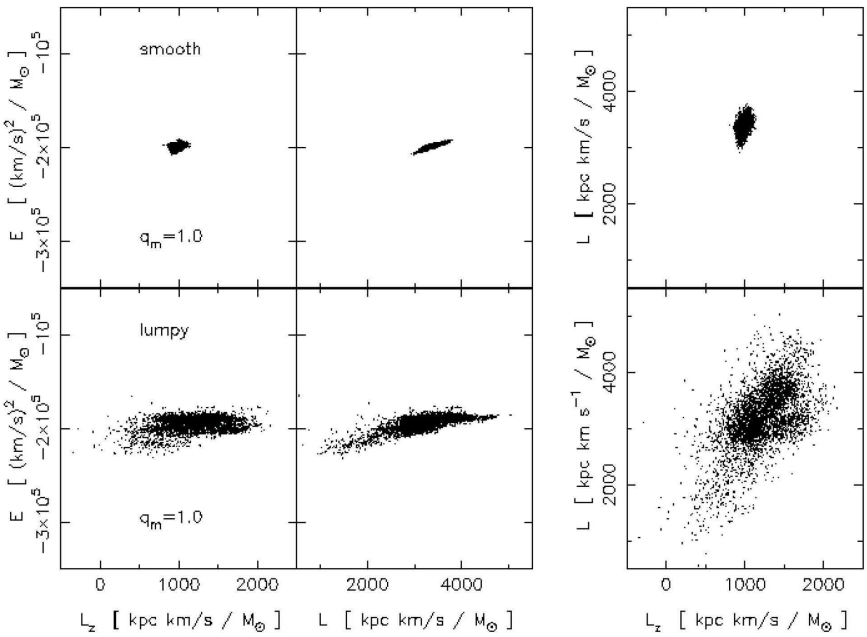

Figure 5.9: Phase-space distribution of a simulated stellar stream associated with a globular-cluster sized system ($10^6 M_\odot$) in a smooth Galactic potential (top panel) and in a potential having lumpy CDM subhalos (bottom panel) (taken from Ibata et al. 2002). It is clear that the interaction with CDM subhalos has smeared out the phase-space distribution of the stream and that this dynamical effect of subhalos can be deduced from the combination of Gaia and PFS.

The structure of dark-matter dominated dwarf satellites: is CDM correct?

Another important issue related to CDM is that the models predict a cuspy density profile at central parts of virialized dark halos, often phrased as NFW profile or more recently Einasto profile (Navarro et al. 1997, 2010), whereas rotation curves of low surface brightness (LSB) galaxies and stellar kinematics of dwarf spheroidal (dSph) galaxies, where both are known as dark-matter dominated, seem not to support a cuspy density profile (Hayashi et al. 2004; Walker et al. 2009) (See Figure 5.10). However, the interpretation of observational results is yet ambiguous, mainly because of limitation and inaccuracies of currently available observational data as well as the incomplete method of data analysis. For instance, in the analysis of stellar kinematics in Galactic satellites, the number of sample stars available in each radial bin is small, so the ambiguities in both the profiles of line-of-sight velocity dispersions and surface density of stars make it difficult to derive the density profile of dark matter in an accurate manner. The situation is even worse for recently found ultra-faint dwarf galaxies (UFDs) with V-band absolute magnitudes fainter than about -5 mag, for which only a small number of stars are detected and analyzed. To overcome this ambiguous situation including the missing satellites problem, it is necessary to target a large number of stars in each of the Galactic satellites and measure their kinematics (and metallicities as well) to set important limits on density profile and shape of dark matter halos in dwarf galaxy scales. PFS/Subaru will allow us to achieve this science goal.

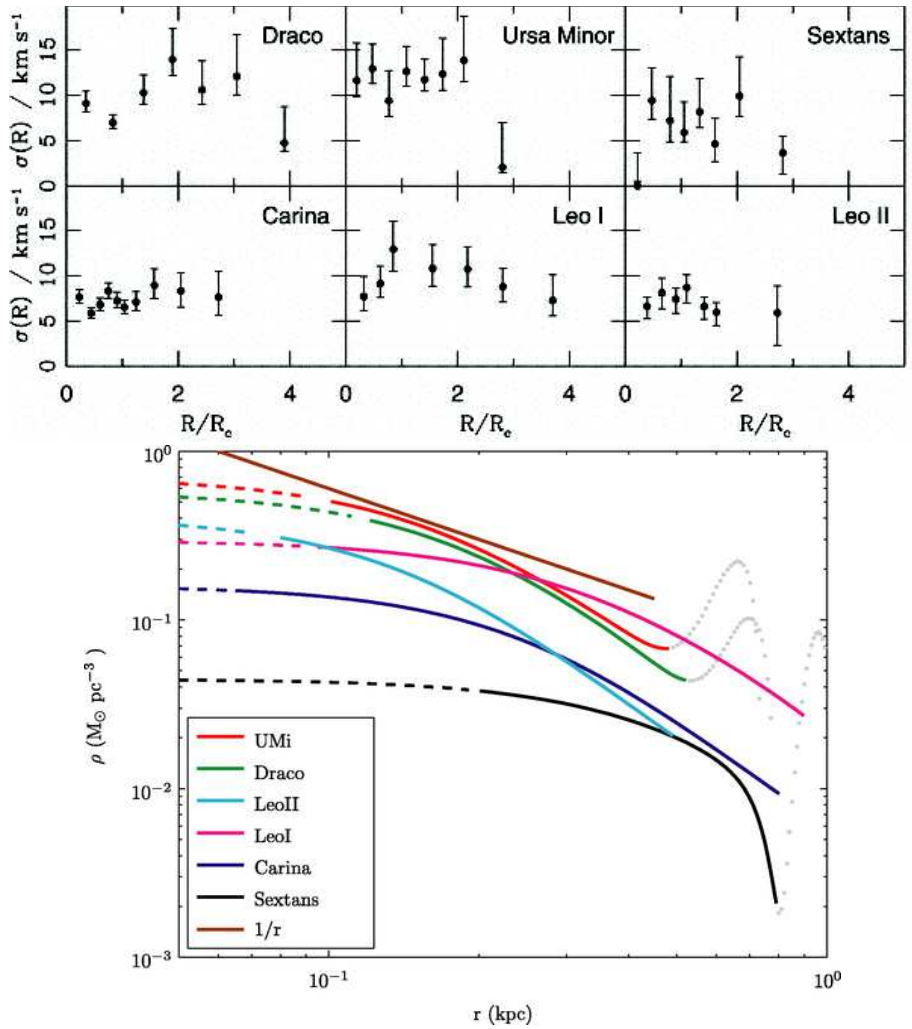

Figure 5.10: Top panels: observed line-of-sight velocity dispersions for six Galactic dSphs. Bottom panel: derived inner mass distributions of these galaxies based on isotropic Jeans equation analyses, in comparison with an NFW-like density profile of r^{-1} (taken from Gilmore et al. 2007).

5.2.3 Other Science Issues

Kinematics of Planetary Nebulae in External Galaxies

Planetary nebulae (PNe) are an ideal dynamical tracer of the stellar population in galaxies, as their spectra consist of strong isolated emission lines of [O III] at $\lambda = 5007$ Å and very weak optical continuum so that PNe are quite easily identified. Recent development of efficient PNe search using a narrow-band filter (~ 35 Å wide) centered on the emission line and the subsequent insertion of a grism as dispersing elements have provided a large number of candidate PNe and their radial velocities (e.g., Merrett et al. 2006; Shih & Méndez 2010). For instance, 2615 PNe have been found in the disk and halo of M31 by a survey to a magnitude limit of $m_{5007} \sim 23.75$ mag with WHT (Merrett et al. 2006) and the same survey identified a significant number of PNe in M31's satellite galaxies. Deeper images and grism slitless spectra of NGC 891 using Subaru/FOCAS (Shih & Méndez 2010) have found 125 PNe in this edge-on galaxy.

Slitless observations provide radial velocities of PNe with an accuracy not larger than 20 km s^{-1}. Better accuracies of radial velocities for numerous PNe will enable us to distinguish stream-like features in a halo through kinematics of PNe (Merrett et al. 2003). Subaru/PFS will be most useful in this respect: a likely flux limit of 0.5×10^{-16} erg s^{-1} cm^{-2} for [O III] suggests $m_{5007} \sim 27.0$ mag, thereby allowing us to determine the PN kinematics in nearby groups of galaxies and even in the Virgo Cluster (Arnaboldi et al. 2004). We would then be able to determine a global mass distribution of each galaxy as well as dynamical substructures in both a disk and halo.

Stellar Populations of Globular Clusters in Nearby Galaxies

Globular clusters (GCs) are also one of the best tracers of overall galaxy evolution as well as the kinematical and chemical properties of various galactic components (e.g., Hwang & Lee 2010). In the Milky Way, about 160 GCs have been identified, and their metallicity distribution and other characteristics (positions, kinematics and ages) suggest multiple components of GC systems: bulge/disk GCs, old halo GCs, and young halo GCs (e.g., Mackey & Gilmore 2004). While each of member stars in Galactic GCs is easily resolved, thereby enabling to distinguish GCs from other star clusters, identifying GCs in external galaxies is not straightforward. For instance, 600 to 1000 GCs are listed in M31, i.e., much larger number of GCs than in the Milky Way, even though many morphological similarities exist between these two neighboring galaxies. However, the estimated number of GCs varies depending on the studies (e.g., Kim et al. 2007), and the M31 GC catalogs in the literature are often found to include young clusters and asterisms in addition to genuine GCs (e.g., Cohen et al. 2005; Caldwell et al. 2009).

This ambiguity of identifying GCs in external galaxies emphasizes the importance of spectroscopic campaign with homogeneous high data quality to confirm and to investigate the physical properties of GCs in M31, M33, and other nearby galaxies. A wide FOV of Subaru/PFS is especially advantageous in studying M31's GCs, because with its huge dimension of M31, an incomplete survey of GCs has sometimes led to inconsistent scenarios on M31's disk formation (e.g., Morrison et al. 2004). With the proposed PFS survey combined with HSC observation, we will be able to obtain all the spectra of M31's GCs with homogeneous data quality. GCs are mostly smaller than 6 pc in diameter (e.g., Hwang & Lee 2008) so that M31's GCs are not usually resolved into member

stars with Subaru observation but they are still more extended than point sources. Therefore, the PFS fiber with diameter of 1.2 arcsec, corresponding to about 4.7 pc (assuming a distance of $\sim$ 800 kpc), is expected to collect more than 60% of total flux of M31's GCs when placed at their center. This would not pose any sensitivity problem for PFS observation since GCs are much brighter than individual stars (usually $14.5 < V < 20.0$ mag for M31's GCs).

As described in the previous subsection, the discoveries of many halo substructures in M31 have led to suggest that M31 should have undergone multiple events of dynamical evolutions that may have left major impact on the star formation history. Recent wide field surveys of M31's GCs report that many halo substructures in M31 are likely to be spatially correlated with newly found halo GCs, which suggests that many halo GCs in M31 may be assembled as a result of accretion along with associated stellar streams (Mackey et al. 2010). This reinforces the importance of spectroscopic observations of halo GCs as well as halo stellar streams to compare their kinematical and chemical properties, which would reveal the overall accretion history of M31. For example, a study of one extended star cluster (ESC) by Collins et al. (2009) shows that the EC4 bears similar velocity and metallicity to those of a stellar stream, revealing the association of a star cluster with a specific stellar stream for the first time. Subaru/PFS will play an essential role in the progress of this research area.

5.2.4 HSC imaging survey

Motivated by the same scientific background and also being complementary to PFS spectroscopic survey as detailed below, we are preparing for the plan of a HSC imaging survey of Galactic and Andromeda stars (PI: M. Chiba) in the frame of the HSC/Subaru strategic proposal to be undertaken in 2012-2016. Our proposed HSC survey will be two-fold:

1. The Milky Way halo survey (led by S. Okamoto): searching new faint dwarf satellites and halo substructures in the outer part of the Galactic halo over 1,500 to 2,000 sq. degree of the sky with (g, r, i) down to $\sim$ 26 mag, i.e., 3 mag fainter than SDSS. This survey fully utilizes the wide-field survey data of HSC dedicated to the weak-lensing science case.

2. The M31 halo survey (led by M. Chiba): mapping Andromeda's stellar halo over $\sim$ 230 sq. degree (Figure 5.11), based on the separation of bright red giants with (g, r, i) of < 22.5 mag from foreground Galactic dwarfs using a narrow-band filter NB515.

Our primary aim of the survey 1 is to discover new faint dwarf satellites in the outer part of the Milky Way halo by identifying their main-sequence turn-off (MSTO) stars and also new halo stellar streams based on MSTO and brighter red giant branch (RGB) stars. We note that the known Galactic satellites are located at radii from 30 kpc (Ursa Major II) to 250 kpc (Leo I), thus we expect the MSTO stars of new satellites in the range of $g = 21.0 \sim 25.5$ mag. An exquisite image quality of HSC will thus enable us to identify yet missing, $\sim$ 20 or more faint satellites as well as some 3 to 4 new large stellar streams and additional $\sim$ 10 faint streams associated with tidal debris of Galactic globular clusters over the proposed survey area of 1,500 to 2,000 sq. degree. Also, this imaging survey provides us with basic photometric data including $g - r$ colors for PFS follow-up observations as described below.

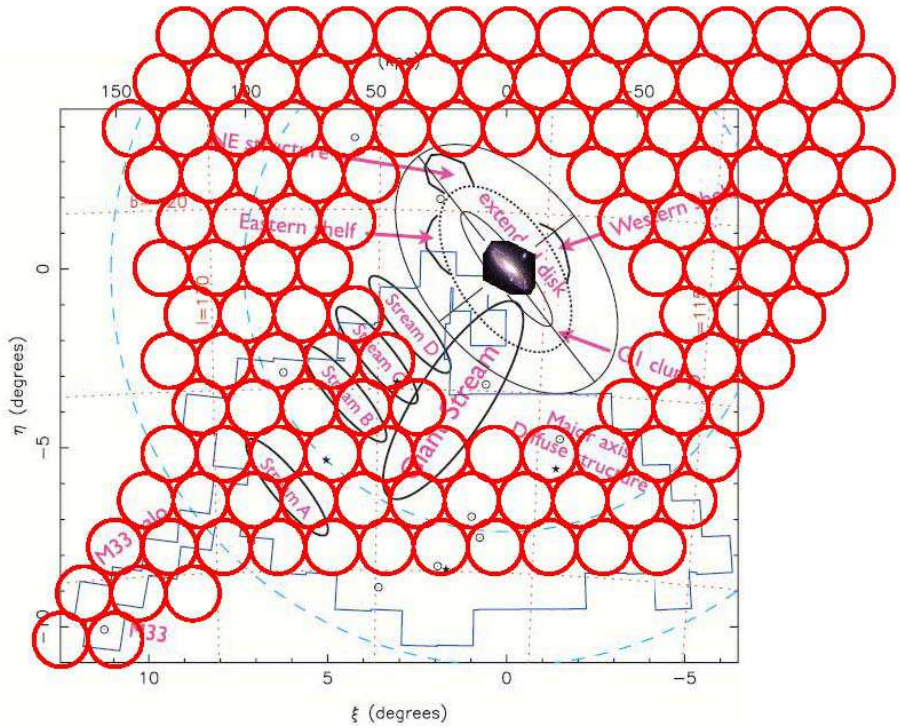

Figure 5.11: Proposed HSC pointings in M31's outer halo over ∼ 230 sq. degree (∼ 130 pointings).

The survey 2 is dedicated to mapping bright RGB stars in the M31 halo, by developing and using a newly designed narrow-band filter (NB515 filter with CW = 5145 Å and BW = 80 Å). This NB515 filter covers a series of magnesium hydride absorption lines which are sensitive to surface gravity; these lines are strong in dwarfs and weak in giants, thus enabling us efficiently to remove the Galactic dwarfs in the foreground and to derive the intrinsic halo structures of M31. Thus, these imaging samples will become an important source of targets in our PFS survey.

5.3 Proposed Survey and its Requirements

5.3.1 Proposed survey with PFS

Our primary goal with the PFS survey is to measure radial velocities and chemical abundances for millions of stars in the Milky Way, M31, and their satellite dSphs, for the purpose of unraveling the formation history of these galaxies and the spatial distribution of their dark-matter halos. The survey consists of the following three parts depending on the targets and is summarized in Table 5.1.

1. The Milky Way survey:

Primary targets in this survey are those in the old stellar components of the Milky Way. PFS will measure spectra of ∼ 1 million stars at $b > 20$ deg with $18 < V < 21.5$ mag and $B - V < 1.0$

mag. This magnitude range is complementary to Gaia, in which astrometric observations will be made for billion stars with precision of 12-25 μas for $V < 15$ and 300 μas for $V < 20$, whereas radial velocities and metal abundances will be measured, with the Gaia Spectrometer, only for bright stars with $V < 17$ and $V < 12$, respectively. Thus, this PFS survey is primarily aiming at obtaining radial velocities and metal abundances for (i) *the Gaia sample* with $V < 20$ mag. In addition to this Gaia sample, PFS will target (ii) *the faint sample*, which is fainter than this Gaia astrometry limit, i.e., with $V > 20$ and as faint as $V = 21.5$, and the sample stars are taken from stars associated with halo substructures in the form of stellar streams (e.g., Sagittarius Stream, Orphan Stream and Monoceros Stream as shown in Figure 5.1) and also field stars located in the outer-most part of halo with $60 < r < 200$ kpc (i.e., corresponding to $V > 20$ for a giant star with $M_V = 1$ mag and $V < 21.5$ for a BHB or RR Lyr with $M_V = 0$ mag). Measurements of radial velocities and metal abundances of these halo stars will set important constraints on chemo-dynamical properties of both each of halo substructures and *in situ.* stars in the outer halo component. The multi-color imaging required for target selection will be coming from the planned wide-field imaging survey with HSC/Subaru (depth: $gri \sim 26$, $z \sim 25$, $y \sim 24$), which is mainly dedicated to weak lensing survey over the contiguous fields of 1,500 to 2,000 sq. degree, but the imaging data will also be utilized for the Milky Way science case. The target catalog is also supplemented by SDSS imaging survey with *ugriz* coverage and by Pan-STARRS as well. The plan of this survey is thus summarized as follows.

- Total number of stars: we request about one million stars for the Gaia sample (i) for the reason described in what follows. Suppose that stellar masses of building blocks for the halo and/or thick disk range from 10^3 to 10^7 $M_\odot$, as deduced from the luminosities of Galactic satellites including Classical dSphs and UFDs (e.g., Strigari et al. 2008) and assuming that stellar mass-to-luminosity ratio is an order of 1. Then, the stellar halo or thick disk with total stellar mass of $\sim 10^9$ $M_\odot$ is comprised of about 10^4 building blocks if their mass function has a power-law form of an index $-1.8 \sim -1.5$ (i.e., $n(M)dM \propto M^{-1.8 \sim -1.5} dM$). Provided that the observation of at least 100 stars in each building block is needed for characterizing its metallicity and velocity distribution, we require the observation of ~ 1 million stars in total. On the other hand, for the faint sample (ii), we request at least five PFS pointings for each of some 8 to 9 stellar streams discovered by SDSS survey to obtain chemo-dynamical characteristics of each stream. Also, to deduce the metallicity and velocity distributions of outer-halo stars (located up to $r \sim 30$ kpc with MSTO stars and $r \sim 130$ kpc with RGB stars), at least several 10^4 sample stars are required, corresponding to about 10^5 stars in the magnitude range of $18 < V < 21.5$. Among this total sample (i) + (ii) selected at $b > 20$ deg and $18 < V < 21.5$, ~ 55 %, ~ 40 % and ~ 5 % belong to the halo, thick disk and thin disk, respectively.

- Total area surveyed: for the Gaia sample (i), the total area of at least $\sim 1,000$ sq. degree (~ 560 pointings) at high b is required to assemble ~ 1 million stars belonging mainly to the halo and thick disk. For the faint sample (ii), at least five PFS pointings for each of the stellar streams discovered by SDSS survey (i.e., ~ 80 sq. degree) and further 10^5 targets for sampling the outer halo down to $V = 21.5$ (i.e., ~ 100 sq. degree) correspond to the total area of ~ 180 sq. degree (~ 100 pointings) for this sample.

- Survey time: as detailed in the later subsection, we require at least S/N$>$ 30 per resolution element spectra at $\lambda = 5000$ Å for reasonable estimation of metal abundances and radial

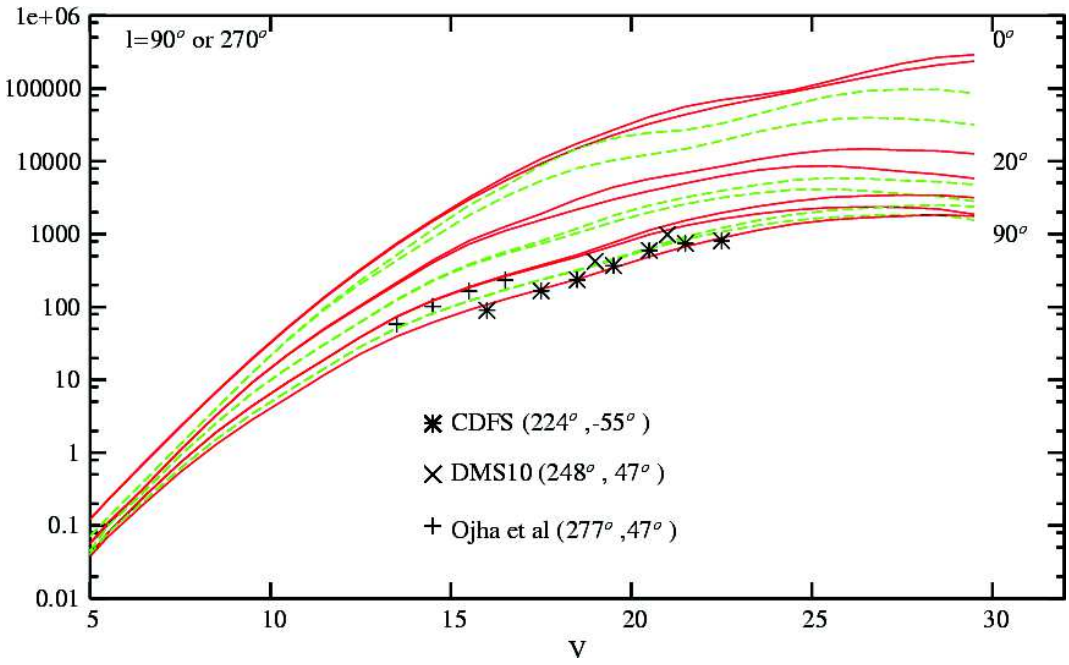

Figure 5.12: Star count predictions (stars per magnitude and per sq. degree) from the Besancon model of the Milky Way (Robin et al. 2003) in the V band at $l = 90°$ or 270°, for latitudes 10° to 90° from top to bottom (0°, 20°, 45° and 90° with solid lines, 10°, 30° and 60° with dashed lines). For each latitude the bifurcation is due to the warp, the highest part being for $l = 90°$, $b > 0$ or $l = 270°$, $b < 0$.

velocities. Thus, for stars with $V = 20$ mag, we require 1800 sec of exposure, whereas 7200 sec of exposure (1800 sec × 4) is needed for stars with $V = 21.5$ mag. Then, provided that 20 fields per night are observed for the Gaia sample (i) with $V < 20$, we require ~ 30 nights for the area of $\sim 1,000$ sq. degree (~ 560 pointings). For the faint sample (ii) of halo substructures and outer-halo stars as faint as $V = 21.5$ mag, if 5 fields per night are observed for the total of ~ 180 sq. degree (~ 100 pointings), we require ~ 20 nights. Thus, in total ~ 50 nights will be dedicated for the Milky Way survey.

- Measurement accuracy: Δ [Fe/H] ~ 0.2 dex and $\Delta\ V_{rad} \sim$ a few km s^{-1}

2. The M31 halo survey:

Primary targets in this survey are bright red giants with $V \simeq 21.5$ mag, i.e., stars around the tip of RGB, in the outer part of the M31 halo, where pre-imaging observations and selection of the targets will be provided by HSC survey (Figure 5.11). PFS will measure radial velocities and metal abundances for M31's halo stars to set important constraints on their chemo-dynamical properties.

- Total area surveyed: maximum area is ~ 230 sq. degree (~ 130 pointings) planned to be imaged with HSC in its strategic Subaru program (Figure 5.11).
- Survey time: in order to obtain at least S/N> 30 per resolution element spectra at $\lambda = 5000$ Å, we require 7200 sec of exposure (1800 sec × 4) for stars with $V = 21.5$ mag. Thus, maximum nights required for observing the above whole targeted area would be ~ 30 nights

Table 5.1: Summary of Galactic Archaeology Survey

Survey	Magnitude range (mag)	Exposure time (hrs)	Area (deg^2)	Survey Time (nights)	Comments
1. The Milky Way	$18 < V < 20$	0.5	1000	30	Gaia sample
	$18 < V < 21.5$	2.0	180	20	Faint sample
2. M31 halo	$18 < V < 21.5$	2.0	230	30	
3. Dwarf galaxy	$18 < V < 21.5$	2.0	53	8	Dwarf satellites
Total				88	

if 2 hr exposure per pointing is made. Parts of this M31 halo survey may be conducted in several PI-led short programs, where each of the programs would target specific halo substructures and/or globular clusters in M31.

- Measurement accuracy: Δ [Fe/H] $\sim$ 0.2 dex and $\Delta V_{rad} \sim$ a few km s^{-1}

3. Dwarf galaxy survey:

Primary targets in this survey are bright red giants with $V < 21.5$ mag in the satellite galaxies of both the Milky Way (Ursa Minor, Draco, Sextans, Sculptor, Fornax, Leo I, Leo II and several ultra-faint dwarf galaxies) and M31 (And I - X, M32, NGC 205, NGC 147 and NGC 185). Target selection will be made by HSC observations. Then, PFS measurements of velocity and metallicity distributions for each of these galaxies will provide important insight into the formation and dynamics of dwarf galaxies.

- Survey time: for each PFS field, we require 7200 sec of exposure (1800 sec $\times$ 4) to obtain S/N> 30 spectra for stars with $V = 21.5$ mag. We thus require at least 8 nights for some 30 satellites. Although parts of this survey can be conducted in some PI-led short programs, a coordinated program will be worth undertaking to efficiently obtain the whole data set.
- Measurement accuracy: Δ [Fe/H] $\sim$ 0.2 dex and $\Delta V_{rad} \sim$ a few km s^{-1}

5.3.2 PFS requirements

- Spectral resolution and signal-to-noise ratio

  We require at least S/N> 30 per resolution element spectra for a broad range of wavelength covering Ca II lines in both the blue (3933 Å) and red (8400-8700 Å), to determine metallicities better than $\sim$ 0.2 dex and radial velocities better than $\sim$ 10 km s^{-1}. It is also important to cover a 5150 Å region, which includes Mg Ib and MgH features providing enhanced sensitivity to estimate surface gravity of stars: these lines are strong in dwarfs and weak in giants. The PFS survey targets stars brighter than $V = 21.5$ mag, namely reaching bright red giant

stars in M31 and its satellite galaxies. This magnitude limit is also complementary to the upcoming Gaia astrometry all-sky survey.

Although a higher resolving power R of spectrograph is generally favorable in distinguishing many metallic lines especially in a blue wavelength range, estimation of metallicities [Fe/H] with reasonable accuracy as well as other stellar parameters (surface gravity $\log g$ and effective temperature $T_{\rm eff}$) can be made possible, even with relatively low R, by considering and combining multiple techniques for calibrating such parameters based on several key lines and/or fitting to synthetic spectra over a broad wavelength coverage. As detailed below, the SEGUE (Sloan Extension for Galactic Understanding and Exploration) survey as a part of SDSS has developed a pipeline software to calibrate its $R = 2,000$ spectra, with which one can achieve reasonable estimation of stellar atmospheric parameter as long as the wavelength coverage extends sufficiently to include 3800 Å (to include Ca II HK), 5200 Å (to include Mg features), and 8400-8700 Å (to include Ca triplet lines) (Lee et al. 2008; Allende Prieto et al. 2008). Thus, even R is as low as 2,000 like spectra in SDSS/SEGUE, a sufficient wavelength coverage in the PFS spectrograph will enable us to obtain, for our sample of million stars, metallicities [Fe/H] as good as 0.2 dex as well as reasonable estimation for $T_{\rm eff}$ and $\log g$, based on the use of multiple techniques as detailed in the next subsection.

It is also noted that in order to determine radial velocities with accuracy of a few km s^{-1}, a higher resolving power as large as $R = 3,000$ is required with a wide wavelength coverage, in particular for the red region where highest S/N ratios are expected.

- The number of fibers

  We require to observe many target stars per a PFS field in order to assemble a statistically meaningful number of stellar data. Based on a standard star-count model (e.g., Robin et al. 2003), there exist $\sim 2,300$ stars of $V = 17$ mag at Galactic latitude $b = 30$ deg per a PFS field and a comparable number of stars is expected at fainter magnitudes and/or higher Galactic latitudes (Figure 5.12). Thus, the number of fibers with 2,000 to 3,000 is sufficient for the studies of Galactic stars. Also with this setup, it is possible to target a sufficient number of red giant stars in the halo of M31, since the stellar density of the M31 halo with $V = 22.5$ mag at projected distance of 30 kpc from the M31 center is estimated as $\sim 5,000$ stars /sq. deg and decreases to ~ 100 stars/sq. deg at 165 kpc, the currently known limiting radius of the M31 halo (Guhathakurta et al. 2005).

- Fiber size

  Angular size of fiber ~ 1.2 arcsec is sufficient to resolve stars in the Milky Way, M31, and their satellite galaxies, although it is insufficient to resolve stars in dense star clusters like globular clusters.

- The impact of throughput from 20 % to 10 %

  Since we do not want to decrease the S/N ratio for the PFS Survey spectra, if the throughput of the system as built is reduced from 20 % to 10 %, we will decrease the number of fields to be observed (i.e. the size of the stellar sample) and increase the exposure time for each field by at most 50 %. We will thus maintain the high quality of the PFS spectra and the depth of the survey, which are the unique components of the PFS high spectral resolution survey. (This assumes that the total observing time that can be allocated to the PFS survey cannot be doubled given the constraints on the Subaru observing schedule.)

5.3.3 Analysis of PFS spectra

Estimation of stellar atmospheric parameters from LR spectra

A number of techniques for the estimation of metallicity [Fe/H] and other stellar atmospheric parameters (effective temperature $T_{\rm eff}$ and surface gravity $\log g$) are available from low-resolution spectral data taken from PFS, combined with photometric data provided by, e.g., SDSS and HSC. Well established techniques include, e.g., fitting observed spectra with grids of synthetic ones for obtaining the most likely set of ([Fe/H], $T_{\rm eff}$, $\log g$) (e.g., Wilhelm et al. 1999; Allende Prieto et al. 2006; Re Fiorentin et al. 2007), using the Ca II K line, auto-correlation analysis of a stellar spectrum, and Ca II triplet lines for obtaining [Fe/H] (Beers et al. 1999; Starkenburg et al. 2010), and using gravity-sensitive Ca I line and Mg features for obtaining $\log g$ (Morrison et al. 2003). Each of the methods is usually optimal over restricted ranges of color $g-r$, metallicity [Fe/H], and signal-to-noise ratio S/N. A great advantage of PFS in this respect is that PFS stellar spectra are designed to cover a broad wavelength range from the blue ($\sim$ 3900 Å) to red ($\sim$ 10,000 Å) continuously, so that it is possible to apply various calibration methods and arrive at the robust set of stellar parameters ([Fe/H], $T_{\rm eff}$, $\log g$).

Based on such existing multiple techniques for the estimation of stellar parameters, the SEGUE Stellar-Parameter Pipeline (SSPP) has been developed and utilized in the SDSS/SEGUE survey (Lee et al. 2008; Allende Prieto et al. 2008). Also, recent papers (e.g., Li et al. 2010) successfully demonstrate that the SSPP can provide reasonable estimation of stellar atmospheric parameters for even non-SEGUE data with similar R (as low as $R = 1,000 \sim 2,000$), as long as the wavelength coverage extends from 3800 Å (to include Ca II HK) to 5200 Å (to include Mg features at 5150 Å which are sensitive to surface gravity)[1]. Thus, the implementation of the SSPP for the calibration pipeline of PFS spectra will enable us to obtain, for our sample of million stars, metallicities [Fe/H] as good as 0.2 dex as well as reasonable estimation for $T_{\rm eff}$ and $\log g$. Furthermore, with this pipeline, the abundance ratios to distinguish Type II or Ia SNe, [α/Fe], are also available (Lee et al. 2010).

The methods used in the SSPP are briefly summarized as follows (See Table 5.2) and more detailed descriptions are given in Lee et al. (2008) and Allende Prieto et al. (2008).

- Spectral fitting with the $k24$ and $ki13$ grids (Allende Prieto et al. 2006):

  A grid of fluxes from synthetic spectra based on the Kurucz (1993) model atmospheres are compared with observed ones in the range of 4400-5500 Å, in order to obtain best-fitted model stellar parameters ([Fe/H], $T_{\rm eff}$, $\log g$). The $k24$ grid includes a predicted broadband color index $g-r$, whereas for the $ki13$ no photometry is considered. These methods perform best in $0.0 \leq g-r \leq 0.8$.

- Spectral fitting using the Wilhelm et al. (1999) procedures (WBG):

  The stellar parameter determinations make use of comparisons with theoretical ugr colors and line parameters from synthetic spectra generated from ATLAS9 model atmospheres (Kurucz 1993). In this procedure, two temperature ranges divided at $g-r = 0.25$ are considered for

[1] We are grateful to Prof. T. C. Beers (MSU) for his many useful comments and suggestions on the SSPP and its applications.

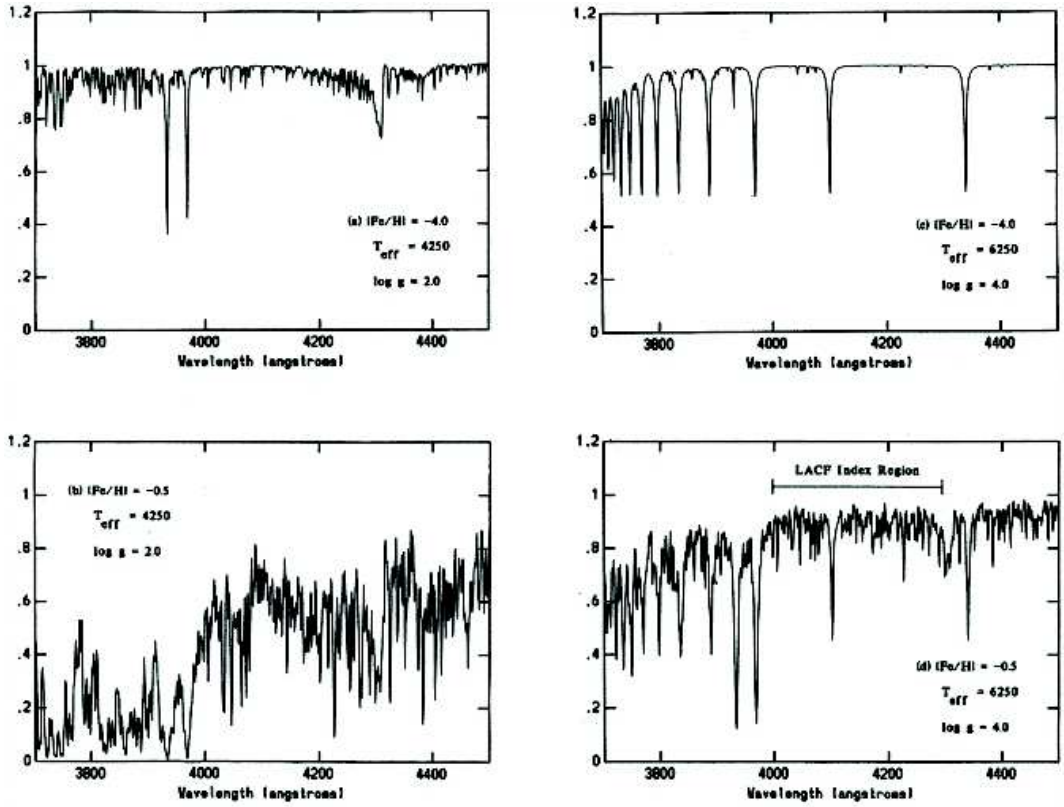

Figure 5.13: Sample synthetic spectra for the calibration of the Ca II K-line index as an indicator of stellar metallicity (taken from Beers et al. 1999).

optimization. For the hotter stars, the equivalent widths and $D_{0.2}$ (the line width at 20% below the local pseudo-continuum level) of the Balmer lines, combined with $u-g$ and $g-r$ colors are used to establish initial $T_{\rm eff}$ and $\log g$ estimates. For the cooler stars, only the $g-r$ color is used for an initial estimate of $T_{\rm eff}$, whereas the estimate of $\log g$ is from $u-g$ for stars as cool as $T_{\rm eff} = 5,750$ K and the use of MgH strength for those cooler than this limit. The metal abundance is determined by the Ca II K line and other metallic lines.

- Spectral fitting using the Neural Network Approaches ($ANNRR$ and $ANNSR$) (Re Fiorentin et al. 2007):

  Neural Network Approaches are used for a global nonlinear mapping between a set of inputs (the stellar spectrum) and a set of outputs (the stellar atmospheric parameters). The regression models are based on the model of real spectra ($ANNRR$ performed well for $-0.3 \leq g-r \leq 1.2$) or that of synthetic ones ($ANNSR$ for $-0.3 \leq g-r \leq 0.8$).

- Spectral fitting using the χ^2 minimization technique ($NGS1$ and $NGS2$) (Lee et al. 2008):

  This makes use of Kurucz's NEWODF models (Castelli & Kurucz 2003) with the use of solar relative abundances from Grevesse & Sauval (1998) to generate a grid of synthetic spectra, one employing appropriate alpha-element enhancements ($NGS1$) and one without employing them ($NGS2$).

- Metallicity from the Ca II K line and auto-correlation function methods ($CaIIK2$, $CaIIK3$, and ACF) (Beers et al. 1999, See Figure 5.13)

  The equivalent width of the Ca II K line (3933 Å) is a function of [Fe/H] and broadband $B-V$ color (as obtained from the observed color $CaIIK2$ or the synthetic one $CaIIK3$), as predicted from spectrum synthesis and model atmosphere calculations. Thus, this line is used for [Fe/H] estimation for both dwarfs and RGBs over the metallicity range of $-4.0 <$ [Fe/H] < -1.0 and the color range of $0.1 \leq g-r \leq 0.8$. The method is degraded above [Fe/H]$= -1.0$ and cooler stars below $T_{\rm eff} = 5,000$ K.

  The auto-correlation function method works well at higher [Fe/H], where the Ca II K line-index techniques are limited by saturation. This method relies on an auto-correlation of a given stellar spectrum, which generates a correlation peak whose strength is proportional to the frequency and strength of weak metallic lines in a given spectrum. The range of color for the application of this method is $0.1 \leq g-r \leq 0.9$.

- Metallicity and Gravity from 3850-4250 Å ($CaIIK1$ and $CaI1$) (Lee et al. 2008):

  The method makes use of the $NGS1$ grid but over a different wavelength range of 3850-4250 Å, where the Ca II KH lines and the gravity sensitive Ca I (4226 Å) line are available. The color range for this application is $-0.3 \leq g-r \leq 0.8$).

- Metallicity from Ca II triplet lines (e.g., Starkenburg et al. 2010, See Figure 5.14)

  The equivalent width of these triplet lines, which fall in the range of 8400-8700 Å, is also a good [Fe/H] indicator for RGBs over $-3.0 <$ [Fe/H] < -0.5.

- Surface gravity from the Ca I line ($CaI2$) and Mg features (MgH) (Morrison et al. 2003):

  The Ca I line at 4227 Å and Mg features (Mg I b and MgH) at 5150 Å are sensitive to surface gravity and thus good indicators to calibrate $\log g$, over the color range of $0.4 \leq g-r \leq 0.9$.

- Estimation of $T_{\rm eff}$

  Effective temperatures are estimated from the observed $g-r$ color, strength of the Balmer lines, or comparisons with theoretical models as stated above.

Estimation of radial velocities

We have conducted several simulations for radial velocity measurements from the wavelength coverage of 5000-6000 Å, which includes $\sim 10,000$ spectral lines for a metal-poor giant. Template spectra are calculated for the parameter set ($T_{\rm eff} = 4,800$ K, $\log g = 2.2$, [Fe/H]$= -1.0$) assuming $R = 3,000$ and 5,000, and S/N$= 50$. Synthetic spectra are calculated for a slightly different parameter set ($T_{\rm eff} = 5,000$ K, $\log g = 2.5$, [Fe/H]$= -1.0$) and S/N$= 10$, 20, and 50. Radial velocity is measured by cross-correlation between the template and synthetic spectra. The results are given in Table 5.3. The accuracy of the radial velocity measurement is better in the case of $R = 5,000$ by more than a factor of two than that of $R = 3,000$. However, in the calculation, the sampling is also changed corresponding to the spectral resolution. That is, a higher S/N is achieved in the lower resolution spectra for the same exposure time. Moreover, the wavelength coverage is fixed in this simulation. If a wider coverage is assumed in spectra with a lower resolution, the

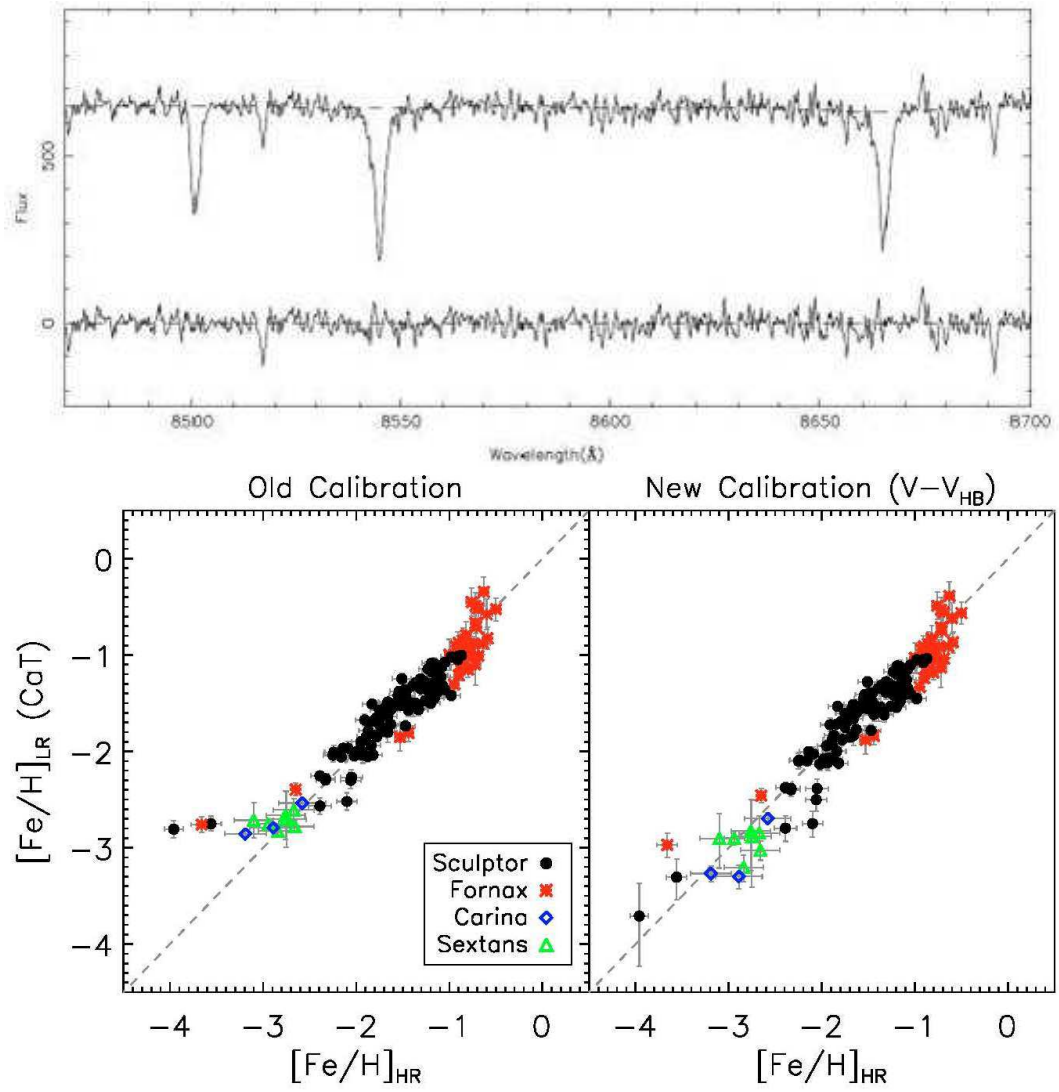

Figure 5.14: Top: CaT region for a K-giant in the Sculptor dSph (taken from Battaglia et al. 2008). Bottom: Comparison between [Fe/H] from CaT and that from high-resolution measurements, where old and new CaT calibrations are shown (Starkenburg et al. 2010).

Table 5.2: Valid Ranges of $g - r$ and S/N for Individual Methods in the SSPP (Lee et al. 2008)

$T_{\rm eff}$			$\log g$			[Fe/H]			
Name	Method	$g-r$	Name	Method	$g-r$	Name	Method	$g-r$	S/N
T1	ki13	$0.0-0.8$	G1	ki13	$0.0-0.8$	M1	ki13	$0.0-0.8$	≥ 15
T2	k24	$0.0-0.8$	G2	k24	$0.0-0.8$	M2	k24	$0.0-0.8$	≥ 15
T3	WBG	$-0.3-0.8$	G3	WBG	$-0.3-0.8$	M3	WBG	$-0.3-0.8$	≥ 10
T4	ANNSR	$-0.3-0.8$	G4	ANNSR	$-0.3-0.8$	M4	ANNSR	$-0.3-0.8$	≥ 20
T5	ANNRR	$-0.3-1.2$	G5	ANNRR	$-0.3-1.2$	M5	ANNRR	$-0.3-1.2$	≥ 10
T6	NGS1	$-0.3-1.3$	G6	NGS1	$-0.3-1.3$	M6	NGS1	$-0.3-1.3$	≥ 15
...	...	...	G7	NGS2	$0.0-1.3$	M7	NGS2	$0.0-1.3$	≥ 20
...	...	...	G8	CaI1	$-0.3-0.8$	M8	CaIIK1	$-0.3-0.8$	≥ 10
...	...	...	...	...	$0.4-0.9$	M9	CaIIK2	$0.1-0.8$	≥ 10
...	...	...	...	...	$0.4-0.9$	M10	CaIIK3	$0.1-0.8$	≥ 10
...	...	...	...	...	...	M11	ACF	$0.1-0.9$	≥ 15
...	...	...	...	...	...	M12	CaIIT	$0.1-0.7$	≥ 20
...	...	...	G9	CaI2	$0.4-0.9$	...	...	...	≥ 10
...	...	...	G10	MgH	$0.4-0.9$	...	...	...	≥ 10
T7	HA24	$0.0-0.8$	...	...	...	...	...	...	≥ 10
T8	HD24	$0.0-0.6$	...	...	...	...	...	...	≥ 10
T9	T_K	$-0.3-1.3$	...	...	...	...	...	...	N/A
T10	T_G	$-0.3-1.3$	...	...	...	...	...	...	N/A
T11	T_I	$-0.3-1.3$	...	...	...	...	...	...	N/A

Table 5.3: Accuracy of radial velocity measurement

	$R = 3,000$	$R = 5,000$
S/N= 10	4.2 km s^{-1}	1.7 km s^{-1}
S/N= 20	2.2 km s^{-1}	1.0 km s^{-1}
S/N= 50	1.0 km s^{-1}	0.4 km s^{-1}

accuracy of velocity measurements increases. If these assumptions in the simulation are taken into consideration, the difference of the accuracy between the two assumed spectral resolutions should be smaller than a factor of two.

A similar result is obtained by an independent estimate for the measurements from the wavelength range around the Ca H-K lines.

We note that the above estimates ignore the errors in the measurements due to the limitation of wavelength calibration and stability of the instrument. If the sampling of a spectrum is 30 km s^{-1} per pixel (3 pixel sampling for $R \sim 3,000$), an error of 0.1 pix corresponds to the 3 km s^{-1}, which could be larger than the errors obtained above. Hence, an accurate wavelength calibration and stability of the instrument are essential to achieve the required accuracy.

5.3.4 High Resolution (HR) spectroscopy with PFS

Necessity of HR follow-up survey: chemical tagging of each building block

Overall metallicity of a star to be measured with the above PFS LR survey reflects just an integration of star formation and chemical evolution over past years, resulting in the present luminosity distribution of the Milky Way halo and thick disk. While such photometric properties of old Galactic components in the present day are dominated by those of low-mass stars having long life time, detailed spectroscopic properties of the stars, which provide chemical abundance patterns synthesized inside them, reflect differential star-formation rate and rate of chemical enrichment (through mass loss and supernovae explosion) as a function of stellar masses. Unraveling this detailed Galactic past is what Galactic Archaeology should ultimately pursue and is thus our science goal based on a coordinated observation of high-resolution stellar spectra (Freeman & Bland-Hawthorn 2002).

Massive stars with $> 8\ M_\odot$ end their lives as Type II Supernovae (SNe), ejecting elements synthesized by the addition of successive helium nuclei or so called α elements. Thus stars enriched by Type II SNe show a high [α/Fe] ratio, where enrichment occurs on timescales of 10^7 years, a typical life time of massive stars. Less massive stars with $< 8\ M_\odot$ end their lives as Type Ia SNe and eject a plenty of iron on timescale of 10^8 to 10^9 years. The r-process elements are synthesized in the environments of being affected by high neutron flux, i.e., associated with Type II SNe, whereas the s-process elements are synthesized only slowly in evolved low-mass stars, i.e., Asymptotic Giant Branch stars. Thus elemental abundance ratios tell us the fraction of newly formed massive stars at each epoch, relative to the timescale of star formation in the system.

If stars form in individual aggregates of 10^5 to 10^6 $M_\odot$ and each of aggregates is chemically homogeneous as shown in De Silva et al. (2007), it would be possible to distinguish each of aggregates by obtaining high-resolution spectra of, say, million stars with a precision of ~ 0.05 dex and tagging each with specific abundance ratios like DNA. Namely, based on this "chemical tagging" method, it would be possible to trace back a past individual star-forming region from where stars originated (Freeman & Bland-Hawthorn 2002). However, this chemical tagging method requires a very ambitious observing program with Subaru: we require very accurate derived abundances for a million stars (to distinguish stars chemically in a statistically significant manner), for which more than two hundred Subaru nights must be allocated to this observing program even if $\sim 1,000$ fibers are utilized for HR mode. This scope looks rather unrealistic now at the time of writing this document.

Instead, taking into account the current and future boundary conditions for the design of PFS, it seems to us more realistic and practical to pursue a mode of measuring follow-up high-resolution spectra for some 100 to 200 stars per a PFS field. The scientific reasoning for this request is that a LR PFS survey combined with Gaia astrometry data will provide six-dimensional phase-space information, with which it is possible to identify individual progenitors as building blocks of the Milky Way, in the form of kinematically distinct clumps in phase space (Helmi & de Zeeuw 2000). Recent merging events and/or those occurred in the outer halo (where dynamical time is sufficiently long) leave yet un-disrupted substructures or stellar streams. Then, a natural next step is to determine chemical abundance pattern of each kinematic or spatial substructure seen in either of phase space or space coordinates, thereby setting limits on star formation and chemical evolution history in each building block of the Milky Way. Thus, based on the kinematical and chemical information of the substructures in the thick disk and halo, all of which are available from the PFS survey, we would be able to arrive at a unique picture of the Galaxy formation.

Requested requirements for the HR mode in PFS

In order to achieve the above scientific goal with the HR mode, we confine ourselves to measuring bright stars at $V < 17$ with S/N ~ 100, for which very precise astrometry data will be available from Gaia. Our request for the HR mode of PFS is summarized as follows.

- Resolution: $R = 35,000$
- Wavelength: any of the following interesting wavelength ranges can be adopted to measure abundances of chemical elements:
  - $\lambda = 4112 - 4322$ Å: Fe-group and neutron-capture (r-process and s-process) elements (incl. Eu II 4129 Å), CH lines, alpha elements
  - $\lambda = 5015 - 5268$ Å: Fe-group and s-process elements, alpha elements, (no Eu)
  - $\lambda = 6280 - 6593$ Å: Fe-group (incl. Zn) and s-process elements, alpha elements, CN lines, (no light odd-Z elements)
  - $\lambda = 6456 - 6779$ Å: light odd-Z elements (Al), Fe-group, s-process, and r-process elements (incl. Eu II 6645 Å), alpha elements, Li lines, (no Zn)
  - $\lambda = 8380 - 8804$ Å: light odd-Z elements (Na, Al), alpha elements, Fe-group elements, CN lines, (no r-process elements)
- The number of fibers: ~ 200

5.3.5 Uniqueness of this survey with PFS

Several other existing and/or planned facilities are being used for the purpose of Galactic Archaeology surveys in 2010-2020. A summary of each in comparison with the PFS survey is given below. In brief, the PFS survey is unique and complementary to other surveys over the next decade.

RAVE : based on 1.2-m UK Schmidt telescope in Australia, spectra of bright Galactic stars with $9 < I < 12$ mag have been and will be taken with $R = 8,500$ and 150-fiber spectroscopic surveys in the southern hemisphere. This survey is, in depth and area, complementary to the PFS survey ($18 < V < 21.5$).

Gaia : astrometry survey for billion stars with precision of $12 - 25$ μas for $V < 15$ and 300 μas for $V < 20$ over the whole sky. Radial velocity (RV) measurements will be made for 150 million stars at $V < 17$ with precision of ~ 15 km s^{-1} ($R = 11,500$ in λ of 8450-8750 Å). Metallicities will also be measured for 2 million stars at $V < 12$. Thus, the PFS survey would provide, being complementary to Gaia, RVs for $V > 17$ and metallicities for $V > 12$ stars.

AAT/HERMES : a proposed survey using 392-fiber $R = 28,000$ spectrograph on the 3.9-m AAT, for the purpose of chemical tagging of southern stars with $10 < V < 14$.

SDSS/SEGUE I-II : spectroscopic survey using the 2.5-m Sloan Foundation Telescope with $R = 2,000$ and magnitude limit of $r \sim 19.5$ for spatially sparse sampling of $\sim 200,000$(?) stars. PFS will observe a much larger number of stars and reach and 2 mag fainter taking advantage of the larger telescope aperture of Subaru (8.2 m).

SDSS/APOGEE : a proposed 300-fiber $R = 24,000$ near-infrared (H-band) spectrographic survey for 100,000 bright red giant stars with limit $H = 12.5$ mag. APOGEE is aiming at measuring high-resolution spectra of bright Galactic stars at near-infrared band and is thus complementary to the PFS survey.

LAMOST : spectroscopic survey using 4,000-fiber $R = 1,800$ spectrograph attached on a 4 m Schmidt telescope with 20 sq. degree FOV. Many of the LAMOST targets would be bright stars, whereas PFS will see fainter targets. Thus, it may be worth exploring the collaboration of a LAMOST survey in a manner that bright and faint targets are observed with LAMOST and Subaru/PFS, respectively, to save mutual observing time.

CFHT/GYES : a wide-field multi-object spectrograph at the prime focus of CFHT (3.6 m) with $R = 20,000$, 500 fibers, FOV ~ 0.9 deg (diameter), and the wavelength coverage of 3900-4500 Å and 5880-6700 Å. The main objective is chemical tagging of Galactic stars with $V < 18$. Phase A has begun from the beginning of 2010.

WHT/WEAVE : a new wide-field MOS of WHT (4.2 m) with dual-beam spectrograph of $R = 5,000$ and $20,000$, 1,000 fibers, FOV = 2 deg (diameter), and the wavelength coverage of 3700-10000 Å. Measuring radial velocity of stars with $V < 20$ to complement Gaia is a primary design driver of WEAVE, to be on-sky in 2016.

GO-IRS : a new optical multi-object spectrograph proposed for the 10.4-m GTC (Gran Telescopio Canarias), with $R = 20,000$, 1,000 fibers, FOV = 15.1 arcmin, and the wavelength coverage of 3700-10000 Å.

References

Abadi, M. G., Navarro, J. F., Steinmetz, M., & Eke, V. R., 2003, *ApJ*, 597, 21

Allende Prieto, C., Beers, T. C., Wilhelm, R., Newberg, H. J., Rockosi, C. M., Yanny, B., & Lee, Y. S., 2006, *ApJ*, 636, 804

Allende Prieto, C. et al., 2008, *AJ*, 136, 2070

Aoki, W. et al., 2009, *A&A*, 502, 569

Arnaboldi, M., Gerhard, O., Aguerri, J. A. L., Freeman, K. C., Napolitano, N. R., Okamura, S., & Yasuda, N., 2004, *ApJL*, 614, L33

Battaglia, G., Helmi, A., Tolstoy, E., Irwin, M., Hill, V., & Jablonka, P., 2008, *ApJL*, 681, L13

Beers, T. C., Rossi, S., Norris, J. E., Ryan, S. G., & Shefler, T., 1999, *AJ*, 117, 981

Belokurov, V. et al., 2006, *ApJL*, 642, L137

Bensby, T., & Feltzing, S., 2010, in IAU Symposium, Vol. 265, IAU Symposium, K. Cunha, M. Spite, & B. Barbuy, ed., pp. 300–303

Brook, C. B., Kawata, D., Gibson, B. K., & Freeman, K. C., 2004, *ApJ*, 612, 894

Burkert, A., Truran, J. W., & Hensler, G., 1992, *ApJ*, 391, 651

Burstein, D., 1979, *ApJ*, 234, 829

Caldwell, N., Harding, P., Morrison, H., Rose, J. A., Schiavon, R., & Kriessler, J., 2009, *AJ*, 137, 94

Carollo, D. et al., 2007, *Nature*, 450, 1020

Castelli, F., & Kurucz, R. L., 2003, in IAU Symposium, Vol. 210, Modelling of Stellar Atmospheres, N. Piskunov, W. W. Weiss, & D. F. Gray, ed., pp. 20P–+

Chiba, M., & Beers, T. C., 2000, *AJ*, 119, 2843

Cohen, J. G., & Huang, W., 2010, *ApJ*, 719, 931

Cohen, J. G., Matthews, K., & Cameron, P. B., 2005, *ApJL*, 634, L45

Collins, M. L. M. et al., 2009, *MNRAS*, 396, 1619

De Silva, G. M., Freeman, K. C., Asplund, M., Bland-Hawthorn, J., Bessell, M. S., & Collet, R., 2007, *AJ*, 133, 1161

Eggen, O. J., Lynden-Bell, D., & Sandage, A. R., 1962, *ApJ*, 136, 748

Ferguson, A. M. N., Irwin, M. J., Ibata, R. A., Lewis, G. F., & Tanvir, N. R., 2002, *AJ*, 124, 1452

Freeman, K., & Bland-Hawthorn, J., 2002, *ARAA*, 40, 487

Gilmore, G., & Reid, N., 1983, *MNRAS*, 202, 1025

Gilmore, G., Wilkinson, M. I., Wyse, R. F. G., Kleyna, J. T., Koch, A., Evans, N. W., & Grebel, E. K., 2007, *ApJ*, 663, 948

Gómez, F. A., Helmi, A., Brown, A. G. A., & Li, Y., 2010, *MNRAS*, 408, 935

Guhathakurta, P., Ostheimer, J. C., Gilbert, K. M., Rich, R. M., Majewski, S. R., Kalirai, J. S., Reitzel, D. B., & Patterson, R. J., 2005, ArXiv Astrophysics e-prints, arXiv:astro-ph/0502366

Hayashi, E. et al., 2004, *MNRAS*, 355, 794

Hayashi, H., & Chiba, M., 2006, *PASJ*, 58, 835

Helmi, A., & de Zeeuw, P. T., 2000, *MNRAS*, 319, 657

Helmi, A., White, S. D. M., de Zeeuw, P. T., & Zhao, H., 1999, *Nature*, 402, 53

Hwang, N., & Lee, M. G., 2008, *AJ*, 135, 1567

—, 2010, *ApJ*, 709, 411

Ibata, R., Martin, N. F., Irwin, M., Chapman, S., Ferguson, A. M. N., Lewis, G. F., & McConnachie, A. W., 2007, *ApJ*, 671, 1591

Ibata, R. A., Gilmore, G., & Irwin, M. J., 1994, *Nature*, 370, 194

Ibata, R. A., Lewis, G. F., Irwin, M. J., & Quinn, T., 2002, *MNRAS*, 332, 915

Ishigaki, M., Chiba, M., & Aoki, W., 2010, *PASJ*, 62, 143

Jing, Y. P., & Suto, Y., 2000, *ApJL*, 529, L69

Johnston, K. V., Law, D. R., & Majewski, S. R., 2005, *ApJ*, 619, 800

Kalirai, J. S. et al., 2010, *ApJ*, 711, 671

Kauffmann, G., Charlot, S., & White, S. D. M., 1996, *MNRAS*, 283, L117

Kazantzidis, S., Kravtsov, A. V., Zentner, A. R., Allgood, B., Nagai, D., & Moore, B., 2004, *ApJL*, 611, L73

Kim, S. C. et al., 2007, *AJ*, 134, 706

Kirby, E. N., Lanfranchi, G. A., Simon, J. D., Cohen, J. G., & Guhathakurta, P., 2010, ArXiv e-prints, 1011.4937

Klypin, A., Kravtsov, A. V., Valenzuela, O., & Prada, F., 1999, *ApJ*, 522, 82

Lee, Y. S. et al., 2010, ArXiv e-prints, 1010.2934

—, 2008, *AJ*, 136, 2022

Li, H. N. et al., 2010, *A&A*, 521, A10+
Mackey, A. D., & Gilmore, G. F., 2004, *MNRAS*, 355, 504
Mackey, A. D. et al., 2010, *ApJL*, 717, L11
McMillan, P. J., & Binney, J. J., 2008, *MNRAS*, 390, 429
Merrett, H. R. et al., 2003, *MNRAS*, 346, L62
—, 2006, *MNRAS*, 369, 120
Moore, B., Ghigna, S., Governato, F., Lake, G., Quinn, T., Stadel, J., & Tozzi, P., 1999, *ApJL*, 524, L19
Morrison, H. L., Harding, P., Perrett, K., & Hurley-Keller, D., 2004, *ApJ*, 603, 87
Morrison, H. L. et al., 2003, *AJ*, 125, 2502
Navarro, J. F., Frenk, C. S., & White, S. D. M., 1997, *ApJ*, 490, 493
Navarro, J. F. et al., 2010, *MNRAS*, 402, 21
Quinn, P. J., Hernquist, L., & Fullagar, D. P., 1993, *ApJ*, 403, 74
Re Fiorentin, P., Bailer-Jones, C. A. L., Lee, Y. S., Beers, T. C., Sivarani, T., Wilhelm, R., Allende Prieto, C., & Norris, J. E., 2007, *A&A*, 467, 1373
Robin, A. C., Reylé, C., Derrière, S., & Picaud, S., 2003, *A&A*, 409, 523
Sakamoto, T., Chiba, M., & Beers, T. C., 2003, *A&A*, 397, 899
Sales, L. V. et al., 2009, *MNRAS*, 400, L61
Schönrich, R., & Binney, J., 2009, *MNRAS*, 396, 203
Searle, L., & Zinn, R., 1978, *ApJ*, 225, 357
Shih, H., & Méndez, R. H., 2010, *ApJL*, 725, L97
Starkenburg, E. et al., 2010, *A&A*, 513, A34+
Strigari, L. E., Bullock, J. S., Kaplinghat, M., Simon, J. D., Geha, M., Willman, B., & Walker, M. G., 2008, *Nature*, 454, 1096
Tanaka, M., Chiba, M., Komiyama, Y., Guhathakurta, P., Kalirai, J. S., & Iye, M., 2010, *ApJ*, 708, 1168
Tegmark, M. et al., 2004, *ApJ*, 606, 702
VandenBerg, D. A., Bergbusch, P. A., & Dowler, P. D., 2006, *ApJS*, 162, 375
Walker, M. G., Mateo, M., Olszewski, E. W., Peñarrubia, J., Wyn Evans, N., & Gilmore, G., 2009, *ApJ*, 704, 1274
Wilhelm, R., Beers, T. C., & Gray, R. O., 1999, *AJ*, 117, 2308
Xue, X. X. et al., 2008, *ApJ*, 684, 1143
Yoshii, Y., 1982, *PASJ*, 34, 365

6 Galaxy and AGN evolution with SuMIRe PFS Survey

(PFS galaxy working group in alphabetical order) C. M. de Oliveira, R. Cid Fernandes, J. Gunn, M. Imanishi, L. Lin, Y.-T. Lin, B. Menard, M. Ouchi, J. D. Silverman, L. Sodre Jr, T. Storchi-Bergmann, M. Strauss, M. Takada, N. Tamura, M. Tanaka

6.1 Introduction: Reaching the epoch ($z \sim 2$) of massive galaxy formation and black hole growth

As previously mentioned, the original aim of the SDSS was to measure the galaxy power spectrum thus providing an accurate trace of large-scale structure out to $z \sim 0.5$. While such initiatives established the geometry or 'cosmic scaffolding' of our Universe, detailed studies of the visible constituents (i.e., galaxies, quasars) with SDSS have resulted in equivalent leaps in our understanding of our Universe. With the PFS BAO survey, as clearly demonstrated in the previous chapter, pushing the cosmological model out $z \sim 1.7$, studies of the galaxy and AGN population are likely to result in advances of similar magnitude.

Further progress in our understanding of galaxy evolution up to $z \sim 1$ has been made from spectroscopic surveys such as zCOSMOS (Lilly et al. 2009), VVDS (Le Fevre 2005) and DEEP2 (Cooper et al. 2006) to just name a few. A picture is emerging where the mass buildup is dependent on environment with star formation being truncated not only by such environmental factors (e.g., Thomas et al. 2010) but quenched by a mechanism that is not yet understood (Peng et al. 2010). Likely candidates include feedback from supernova and Active Galactic Nuclei possibly triggered in major mergers of galaxies (e.g., Hopkins et al. 2008).

While current surveys are now providing large sample of galaxies up to redshifts of 1, they do not cover a sufficient area, at a required depth, to probe the progenitors of today's massive clusters beyond $z \sim 1$ (See Knobel et al. 2009). Furthermore, a wider area survey (see Figure 6.1) is required to overcome the effects of cosmic variance that is present even in the two-square degree COSMOS survey (e.g., Meneux et al. 2009). As well, the numbers of massive galaxies ($M > 10^{11}$) are not of sufficient size to accurately tie down the high end of the mass function (Bolzonella et al. 2009, Ilbert et al. 2010) when split into those that are still actively forming stars or those of a more quiescent nature. With AGNs more prevalent in the massive galaxies (Kauffmann et al. 2003; Silverman et al. 2009), a full understanding of the relation between galaxies and their supermassive black holes requires samples comparable to SDSS but out to $z \sim 2$, an epoch of maximal growth rates.

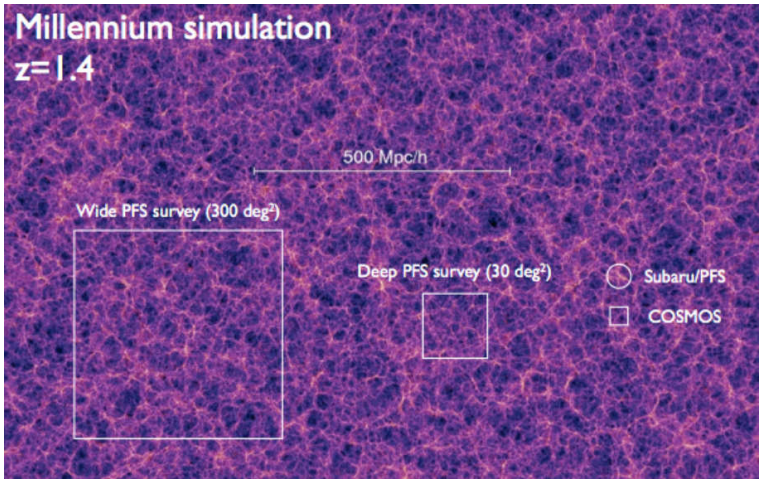

Figure 6.1: Image slice from the Millenium simulation (Springel et al. 2005) at z=1.4. Regions are overlaid that exhibit the sampling of large-scale structure for a deep area survey with PFS and a possible future wider area survey that can identify the rare objects such as QSOs at high-redshift ($z > 4$) and the most massive clusters between $1 < z < 2$. For comparison, the field size of the COSMOS survey and one PFS footprint are shown.

A wide-field spectrograph mounted on an 8-m class telescope (i.e., Subaru) with a high multiplex design is unique in its capability to provide spectroscopic redshifts for galaxies one magnitude fainter than current surveys and over an area more than 10X larger. A spectrograph with versatile capabilities in terms of wavelength coverage and spectral resolution will enable a broad range of scientific investigations pertaining to galaxy and AGN evolution as fully outlined below. Specifically, a wavelength range of $\sim 3800 - 13000$ Å is ideal to acquire spectroscopic redshift for galaxies up to $z \sim 2$. Moderate-resolution spectra ($R \sim 3000$) will provide stellar velocity dispersions with an instrumental velocity resolution of ~ 50 km s^{-1}, star formation rates (e.g., [OII]), stellar ages (e.g., Dn4000, HδA), metallicities, and diagnostics for identifying AGN activity (Kewley et al. 2006). With ~ 2300 apertures/fibers per configuration, it is possible to complete a spectroscopic survey covering a large area of tens of square degrees with a high sampling rate ($\sim 70\%$). The primary scientific drivers for galaxy evolution studies with Subaru/PFS are aimed to answer the following fundamental questions:

- At what epoch, were the today's massive galaxies put in place?
- In what environments are galaxies actively forming stars at high redshift ($z > 1$)?
- Are galaxies and their supermassive black holes co-evolving since $z \sim 2$?

6.2 Unique spectral capabilities for galaxy surveys with PFS

In addition to the multiplex capabilities, we highlight how the design of PFS offers remarkable new capabilities given its moderate-level spectral resolution ($R \sim 3000$) over a wide wavelength range that extends into the near-infrared (0.4-1.3μ). In Figure 6.2, we illustrate the redshift range for which PFS is capable of measuring stellar mass, star formation rates, AGN content and gas

Table 6.1: Primary and secondary spectroscopic features.

	primary features	secondary features
Redshift measurements	[OII], CaII H+K, G-band, Hβ, MgI, [OIII], Hα	—
SFR measurements	Hα+Hβ, or Hα	Hβ or [OII]
Stellar mass measurements	Hδ and D_{4000} or spec-z and broad-band colors	
AGN identification	Hβ, [OIII], Hα and [NII]	either Hβ+[OIII] or Hα+[NII]
Gas-phase metallicity	[OII], [OIII], Hβ, Hα, [NII]	either [OII]+[OIII]+Hβ or Hα+[NII]
Stellar metallicity	Mg, Hβ, and Fe	—

metallicity. As detailed in Section 6.4, an accurate assessment of these quantities over a broad range of redshift is central to the PFS science program. The wide wavelength coverage provides the ability to track spectral features (i.e., emission or absorption lines) from the optical to the infrared.

There are well-established spectral indicators that are used to measure the quantities mentioned above and will be fully exploited in PFS surveys . In Table 6.1, we list these spectral features and label them as either 'primary' and 'secondary' depending of their reliability. Primary spectral features are those that provide well-calibrated measurements or allow for further corrections due to dust extinction. For example, the availability of both Hα and Hβ in emission allows one to measure star formation rates (SFRs) corrected for dust extinction. With PFS, these lines will be available for galaxies up to $z \sim 1$. At higher redshifts, the [OII]λ3727 emission line enables a determination of star formation rate up to $z \sim 1.7$. The analysis of galaxy spectra with spectral synthesis models (Cid Fernandes et al. 2005) is also a powerful method to retrieve SFRs, stellar masses and other parameters useful to characterize the stellar populations of a galaxy.

6.3 A wide area survey for galaxy and AGN studies

The design for a wide-area extragalactic survey must take into consideration an interrelated suite of science goals that will provide a clear picture of the buildup of galaxies at the redshifts under consideration. Even so, there are primary drivers that will lend more weight than others. For instance, there is much incentive to make use of the superb deep imaging available from the HSC deep imaging survey that will cover just under 30 sq. degrees and enable studies of galaxy morphology. For example, we can accurately measure the size evolution of elliptical galaxies as long as the imaging is of sufficient depth to measure the light profile with high significance. In other cases, a high sampling rate is desirable for a number of reasons such as (1) an accurate characterization of the environment (i.e., galaxy overdensity, group/cluster identification), (2) detection of galaxy pairs, in projection, for absorption-line studies, and (3) building samples of physical kinematic pairs for galaxy evolution studies. Futhermore, high signal-to-noise spectra provide the ability to accurately model the stellar populations in galaxies and measure stellar velocity dispersions for studies such as the fundamental plane at high redshift.

To provide an initial estimate of the magnitude of a PFS survey in terms of area coverage and depth, we have carried out a simplified approach based on a few assumptions and constraints. Initially, we focus on the study of galaxies at $1 < z < 2$ and their large-scale environments. This is

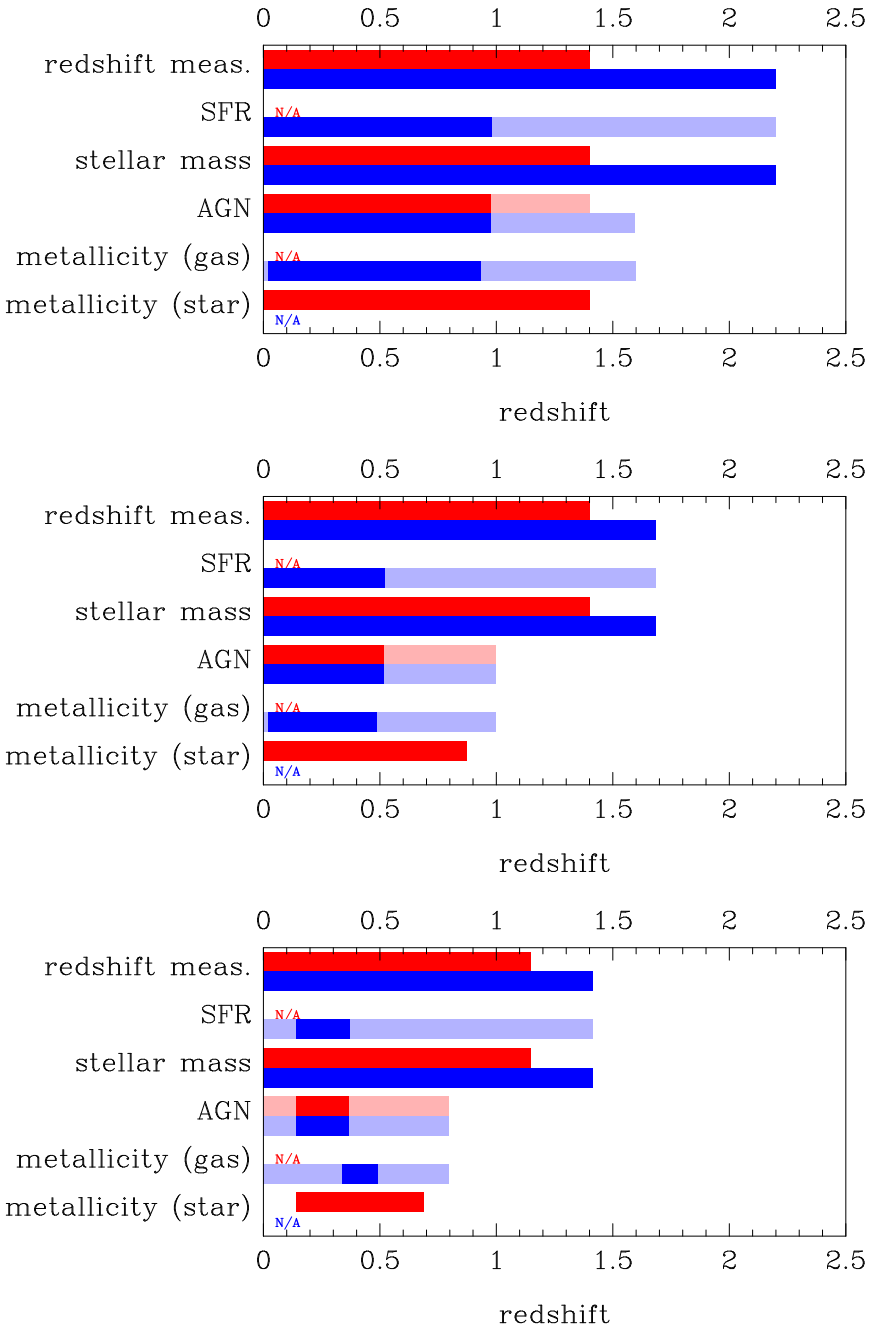

Figure 6.2: Redshift range over which various spectroscopic properties of galaxies can be tracked. The top panel demonstrates the capabilities of PFS with the full wavelength coverage (optical+NIR) while the middle panel is based on only the optical band. The bottom panel shows the equivalent for the zCOSMOS redshift survey (Lilly et al. 2007): a flux-limited survey down to $i = 22.5$. The dark and light areas show the redshift regime where a primary and secondary set of spectral features will be available for galaxies with masses above a characteristic value (m^*). Passive and star forming galaxies are marked in red and blue.

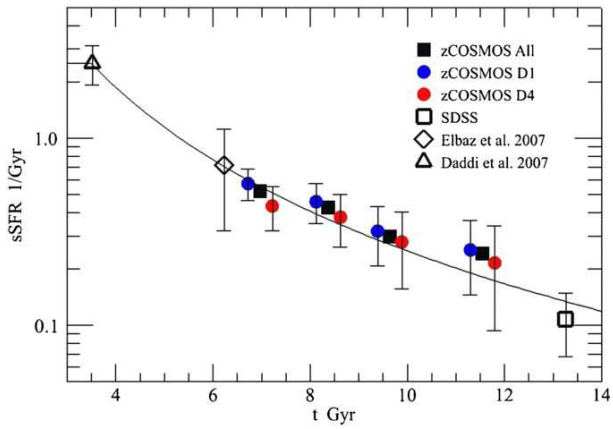

Figure 6.3: Specific star formation rate as a function of the age of the Universe (Peng et al. 2010). A clear gap in the coverage of available data exists between $1 < z < 2$ that will be filled in with a PFS survey.

a redshift regime for which (1) galaxy evolution studies are still in their infancy, as exemplified by our lack of knowledge in their growth rates (see Figure 6.3), and (2) adequate samples of galaxy groups and clusters are not yet available for such environmental studies. We aim to determine a survey area and depth capable of probing a wide dynamic range in galaxy overdensity at high redshift $z > 1$.

Our procedure is simply to determine how many dark matter halos, based on simulations, of a given mass are likely to be present in a given survey area for a given depth in terms of limiting optical magnitude. We utilize the lightcone N-body simulation presented in Sehgal et al. (2010) to determine the number of halos per square degree of a given mass and redshift. The simulation adopts the WMAP5 cosmology, with $\sigma_8 = 0.8$. We then implement a halo occupation model, which provides a good fit to the clustering of K-band selected galaxies at $z = 1 - 2$ (Tinker & Wetzel 2010), to determine which halos have at least five members above a given limiting magnitude. We choose the HSC z-band magnitude that requires a correction to K-band for which the HOD models are based upon. The exposure time is then determined for PFS assuming the current instrument characteristics and a minimum signal-to-noise in the continuum of 3. Such a procedure takes into account of field-to-field variation in halo number counts. We also set the following initial observing constraints: (1) 100 nights of observing time on Subaru, (2) six hours of science time per night, and (3) no overlap between each PFS pointing.

We find that for a survey of ~ 30 square degrees that has a limiting magnitude $z_{AB}^{lim} \sim 22.5$ there will be ~ 260 halos with $M > 5 \times 10^{13} M_{\odot}$ over the redshift range $1 < z < 2$. Such a combination of depth and area is optimal for the following reasons. (1) Based on the dark matter halo mass growth history, the progenitors of a present-day typical cluster ($M \sim 1 - 2 \times 10^{14} M_{\odot}$) will on average have masses $\sim 5 \times 10^{13} M_{\odot}$. Thus, the large spectroscopically confirmed group sample will allow us to trace the progenitors of today's massive cluster elliptical galaxies out to $z \sim 2$. (2) Such a survey will provide a sizeable sample (~ 100) of more massive (1×10^{14} M$_{\odot}$) galaxy clusters at $1 < z < 2$. Recent observations (Tran et al. 2010; Tanaka et al. 2010; Hilton et al. 2010) provide the first hint of elevated star formation activity toward cluster cores at $z \sim 1.6$. (3) For $M \geq 10^{14} M_{\odot}$ clusters, we find that reaching to $z^{\rm lim} = 23.5$ does not gain us much in terms of halo redshift distribution, while reducing the depth to $z^{\rm lim} = 22.0$ will cause a significant loss of $z \geq 1.5$

clusters.

In addition, the wide area and depth of our survey will deliver the first large spectroscopically confirmed *cluster* sample at $0.1 < z < 1$, an equivalent to the SDSS C4 (Miller et al. 2005) and friends-of-friends (Berlind et al. 2006) catalogs. Such a group and cluster sample will be invaluable in many areas of cluster study, such as mass/velocity dispersion function (requiring stacking of clusters), rotation of dark matter halos, density profile of clusters, environmental effects on galaxy formation and evolution (AGN, star formation activity). In combination with external cluster samples such as that from ACT or eROSITA, or using radio data from LOFAR and/or TIFR GMRT Sky Survey (TGSS), we would be able to investigate in detail the cluster physics related to the intracluster medium, including the scaling relations, fraction of cool core systems, and AGN heating.

6.3.1 Target selection: one million galaxies up to $z \sim 2$

We aim to carry out a two-fold approach to constructing a target catalog for PFS. There will be a flux-limited sample of galaxies based on HSC imaging in 5 bands (grizy) that should be sufficient to identify galaxies up to $z \sim 1.3$. Beyond this, a color selection criteria will be utilized that incorporates wide area near-infrared imaging from surveys such as VIKING that will enable the identification of cluster members and field galaxies at $1.3 < z < 2.0$. Surveys like J-PAS (Benitez et al. 2009), which will cover 8,000 sq. degrees on the sky from a new observatory in Spain, will provide low resolution spectra ($R \sim 60$) up to $z_{mag} \sim 22$, being a good pathfinder for target selection for redshifts below $z \sim 1$.

We crudely estimate the number of galaxies that can be targeted in a 30 square degree survey that reaches depths of $z_{AB} = 22.5$. Given a total exposure per PFS pointing of 3 hours, we can reach a signal-to-noise of 3 in the continuum thus such spectra are likely to provide a secure spectroscopic redshift, based on the known success rate ($S/N > 2$ per pixel) in the SDSS-III BOSS survey. The three hours of total integration time will be split into 30 minute individual exposures. The number of frames that a particular source has an assigned fiber is magnitude dependent. For example, a bright galaxy at $z_{AB} = 21$ will only be observed in one exposure while the fiber will be reassigned to another target in the next exposure. A galaxy with a magnitude at the limit of the survey will be observed for the full exposure of 3 hours of on-source integration time. Each PFS footprint will then be revisited 10 times in order to acquire spectra for a large fraction (70-100%) of the galaxies. This will enable us to acquire spectra for $\sim$ 60000 galaxies per PFS footprint thus bringing the total sample to roughly over one million galaxies. In Figure 6.4, we show how PFS-wide compares with large spectroscopic surveys to date. It is clear that a PFS survey falls in a region of the area versus depth plane offset in both parameters from other surveys thus, under this scheme, a PFS survey will effectively cover a volume similar to SDSS at $z \sim 1$ and become a high-redshift benchmark for survey science for a decade to come.

6.4 Science

We provide a brief description of the science topics for which PFS will make extraordinary leaps in our understanding of how galaxies and their supermassive black holes grow with time.

Table 6.2: Targets for a PFS galaxy evolution survey

Redshift range	Magnitude limit	Selection	Sample size size	Targets
$0.1 < z < 2$	$z_{AB} < 22.5$	Random	$\sim 1 \times 10^6$	Galaxies
$0.5 < z < 7.0$	$z_{AB} < 23.5$	Photometric	~ 5000	QSOs (See Section X)
$1.0 < z < 2.0$	TBD	Photometric	$\sim 3 - 5 \times 10^3$	Cluster members
$0.5 < z < 2.0$	TBD	Multi-wavelength	TBD	X-ray, SZ clusters
$0.5 < z < 7.0$	$z_{AB} < 23.5$	Multi-wavelength	TBD	AGN (X-ray, radio)

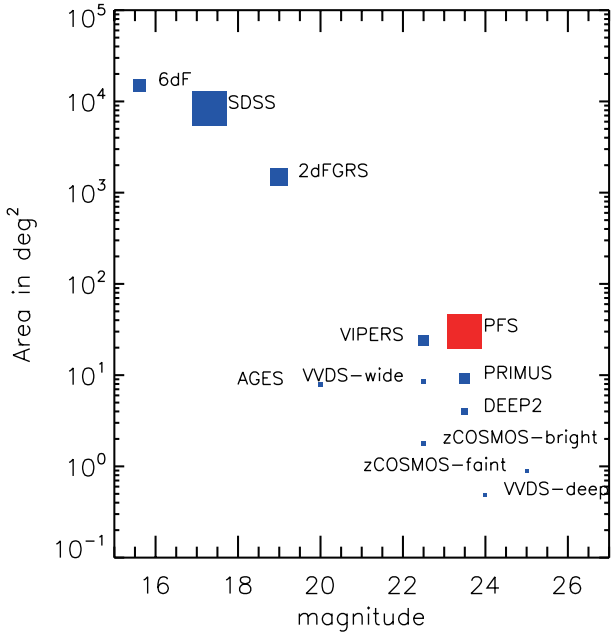

Figure 6.4: Area coverage versus limiting magnitude for various large extragalactic surveys. The point size represent the number of spectra; the SDSS symbol size corresponds to one million spectra. Clearly, a PFS survey occupies a unique position in this parameter space. The BigBoss survey is arbitrarily placed at 23rd magnitude since the continuum will not be detected in most galaxies.

6.4.1 Star formation history

One of the main science driver for PFS will be tracing the evolution of star formation in galaxies up to $z \sim 2$. Cold gas in galaxies gravitationally collapses with time and eventually becomes dense enough to initiate star formation. Continuing gas infall from the intergalactic medium, and both major and minor mergers are other channels by which star formation is triggered in galaxies. Fig. 6.4.2 shows the observed rise and fall of star formation activity of galaxies as a function of cosmic time, as inferred by a variety of star formation indicators in galaxies. The cosmic star formation rate increases from the dawn of the universe to $z \sim 1-3$, and then dramatically declines. If one integrates this function (recognizing the logarithmic y-axis and the very non-linear time axis), the majority of stars in the universe formed between redshifts of 1 and 3 (this is also the epoch when galaxies obtain their basic morphologies: at $z = 3$, HST images show most galaxies to be amorphous, while by $z = 1$, most massive galaxies fall into the familiar elliptical or spiral categories).

However, measurements of the cosmic star formation rate at high redshift suffer from large errors, due to two fundamental problems:

- Cosmic variance. What we wish to measure is the star formation rate, averaged over a volume which encompasses a statistically sigificant number of all types of structures in the universe. Existing surveys simply have not sampled a large enough volume to do this adequately.
- Astronomers use a variety of star formation rate indicators in different wavebands at different redshifts, each subject to its own uncertainties and systematics, and difficult to calibrate against the others.

PFS will greatly improve our ability to make progress on both these issues. The large volume it will survey allows it to minimize cosmic variance, and its very large wavelength coverage means that star formation indicators that are well-calibrated at low redshift can be used to much higher redshift than before.

In particular, PFS probes a period of active star formation at $1 < z < 2$ that includes the redshift desert ($1.5 < z < 2$), where no prominent spectral features of galaxies are available in the optical, and thus existing surveys have been unable to study. Little is known about galaxy evolution with sufficient statistical accuracy at these redshifts, but PFS with its very wide wavelength coverage will have no holes in its redshift coverage. It thus has the ability to cultivate the desert and allow us to perform a statistical study of galaxy populations at these epochs for the first time. The [OII] emission line can be studied with PFS from the local universe to $z > 2$; it allows us to estimate rough SFRs and identify galaxy populations undergoing intense star formation. In the local universe, the most massive galaxies are passively evolving and most of the star formation activities are found in low-mass galaxies. With PFS, we can identify the stellar mass of galaxies where most the active star formation is happening as a function of cosmic time. Cowie et al. (1996) showed that the characteristic luminosity of galaxies hosting active star formation is higher at higher redshifts. This trend is often called down-sizing. Cowie et al. (1996) used only 400 galaxies, but we can easily surpass the previous studies with improved statistical and measurement accuracies over a wider redshift range. With our excellent imaging from HSC, we can then ask whether intense star formation is triggered by galaxy-galaxy interactions or if it is just self-regulated. We have HST

images in some of our fields to obtain morphological information, and we expect to be able to measure Sersic indices (a proxy for morphology) for galaxies at $z \sim 1$ from the HSC data. Thus with star formation rates and stellar masses from our spectra, morphologies from the imaging, and environmental information from the redshift survey, we can explore the dependence of star formation rate on all these quantities, all as a function of cosmic time.

PFS also will allow us to refine the star formation histories of galaxies at $z < 1$. We can observe the Hα line from galaxies, which is one of the most robust star formation indicators, only up to $z \sim 0.4$ with an optical spectrograph. But the wide wavelength coverage of PFS allows us to observe Hα go up to $z \sim 1$ (Fig. 6.2). To date, the redshift range between 0.5 and 1 has been explored mainly using [OII] emission, which provides a less precise measurements of SFRs because it is prone to dust extinction and metallicity variations. By measuring SFRs using Hα/Hβ, we will be able to make the most precise measurements of SFRs ever achieved at $0.5 < z < 1$. At lower redshifts, one needs to survey a wide area of the sky to probe a sufficient volume. Recently surveys on 8m telescopes are too small to statistically study galaxies $z \lesssim 0.5$. SDSS surveyed a quarter of the sky, but it did not go deep enough to observe typical galaxies at $z \gtrsim 0.2$. PFS will dramatically improve the statistics by a large factor.

6.4.2 Metal enrichment history

Massive stars that formed in star-forming regions explode at the end of their life and eject a large amount of metals to the surrounding interstellar space. The ejected materials eventually mix with the interstellar medium and may gravitationally contract again to initiate another cycle of star formation. The metallicity of galaxies increase in this way, and the metal enrichment history is another essential aspect of galaxy evolution. The story may be made more complicated by the infall of chemically pristine gas from the intergalactic medium (IGM), or the blowout of metal-rich gas given enough kinetic energy to escape into the IGM.

The most precise measurement of gas-phase metallicity for a large sample of galaxies was made by Tremonti et al. (2004) using the data from the SDSS as shown in Fig. 6.4.2. Metallicity has strong dependence on the stellar mass of galaxies. We would like to measure the mass-metallicity relation out to high redshifts to unveil the metallicity evolution of galaxies. With PFS, we can precisely measure the gas-phase metallicity up to $z \sim 1$. So far, precise measurements of metallicity have been made for large samples of galaxies only to $z \sim 0.5$, limited by the coverage of the Hα and [NII] lines in optical spectrographs. PFS will allow us to extend such analyses to $z \sim 1$, when the universe was 50% of its current age, and measure precise metal enrichment histories for a large sample of galaxies in the latter half of universe's life for the first time.

We can go up to even higher redshifts ($z \sim 1.3$) using the O_{23} method (based on the ratio of the Hβ and [OIII] lines, but emission lines from AGNs will cause us to underestimate the metallicity measured from O_{23}, and thereby bias our results. With Hα, this is not a problem, as AGNs can be recognized and removed using line ratios (Baldwin et al. 1981). At higher redshift, we can use multi-wavelength data available in a part of our survey fields to identify and remove AGNs (e.g., by using X-rays) and study the mass-metallicity relation with unprecedented statistical accuracy.

The gas-phase metallicity can be measured by the emission line indicators described above, but with absorption features that passive galaxies show, we can also measure metallicity of stars and

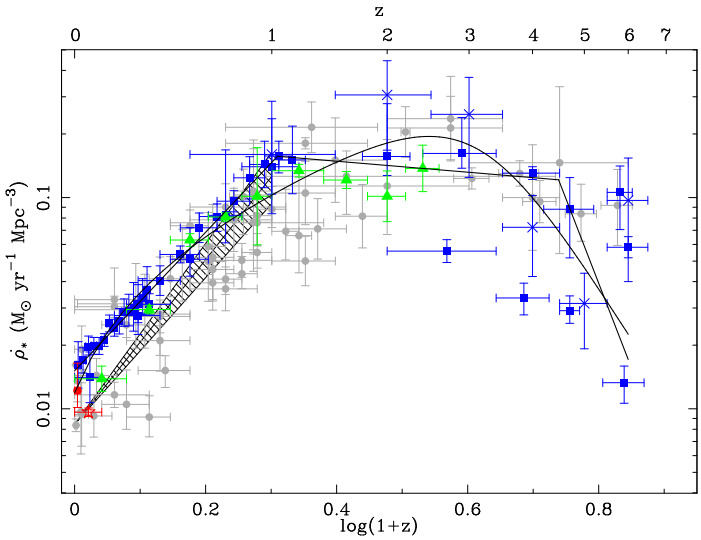

Figure 6.5: Rise and fall of star formation activity of galaxies (Hopkins & Beacom 2006). Different symbols show measurements made at different wavelengths. The solid lines show parametric fits to the data (refer to Hopkins & Beacom 2006 for details).

look into the formation of galaxies. Fig. 6.2 shows that we can measure stellar metallicities of typical galaxies up to $z \sim 1.2$. We may not have sufficient S/N ratio to measure absorption features securely in individual galaxies, but we can stack a large number of spectra to make a very high S/N composite spectrum to measure absorption features. Of particular interest will be to measure $[\alpha/Fe]$ of galaxies. This is sensitive to the star formation time scale of galaxies — α elements are produced mainly by type-II supernovae, while Fe mainly comes from type-Ia supernovae. These types of supernovae occur on different time scales, thus $[\alpha/Fe]$ gives an constraint on the star formation time scales of galaxies. Thomas et al. (2005) showed that more massive galaxies formed earlier on a shorter time scale using galaxies in the local universe (Fig. 6.4.2). PFS allows us to perform this analysis at $z > 1$, an epoch much close to their formation than the present, to put a stronger constraint on the formation time scale of galaxies.

6.4.3 External influences on galaxy evolution

The distribution of galaxies in the universe is far from uniform. Galaxies are arrayed in filamentary structures, and massive concentrations of galaxies, which we call clusters of galaxies, are often located at knots of those filaments. While there were hints from earlier data, the filamentary nature of the galaxy distribution first became obvious in the maps from the CfA redshift survey (Geller & Huchra 1989) and the recently completed Sloan Digital Sky Survey mapped out the prominent cosmic structure in the local universe (York et al. 2000).

Galaxies of course live in a wide variety of environments within this cosmic web. Some galaxies live in dense clusters, while others lie along filaments or in low-density regions such as voids. Dressler (1980) performed the first quantitative analysis of the dependence of galaxy morphology on environment; he found that the fraction of early-type galaxies increases at higher density environment with a proportional decrease of late-type galaxies. Since that pioneering work, there has been

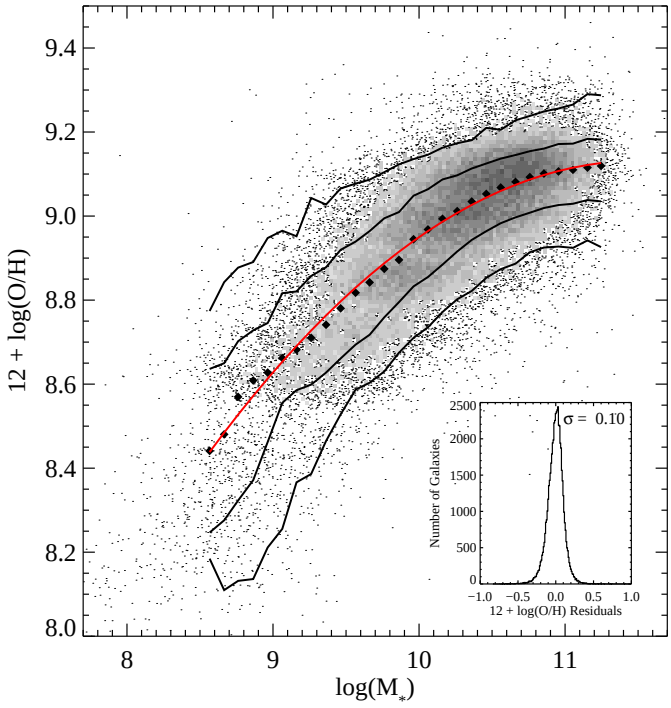

Figure 6.6: Stellar mass-gas metallicity relation for galaxies in the local universe (Tremonti et al. 2004).

an enormous amount of evidence that galaxies in clusters and those in the low-density field have different properties in the local universe. For example, similar to morphology, star formation rates (SFRs) also depend on galaxy densities in the sense that galaxies in higher density environments have lower SFRs (e.g., Lewis et al. 2002; Gómez et al. 2003). Blanton et al. (2005) summarized galaxy properties and correlations between them and environment in the local universe.

Recent large optical spectroscopic surveys with 8m telescopes have extended the relationship between galaxy properties and environment at redshifts up to $z \sim 1$ (e.g., Smith et al. 2005; Postman et al. 2005; Cucciati et al. 2006; Elbaz et al. 2007; Cooper et al. 2008). However, none of these surveys was made with a sufficiently wide wavelength coverage with sufficient spectral resolution, well-defined target selection to reduce selection biases, high sampling rate, and covering a large enough volume to fully sample all relevant environments. There are unsettled issues left in the literature as we discuss below. A large spectroscopic survey with PFS based on imaging data from the HSC would surpass the previous surveys in all these respects. Note that items listed below are just a short list of the unsettled issues and PFS will surely do an excellent job in many other areas.

- **Galaxy clusters at high redshifts**

  Existing spectroscopic surveys such as SDSS, zCOSMOS and DEEP2, are limited either in redshift range or volume, and thus can't study clusters of a wide range of both mass and cosmic time. This is due either to lack of sufficient depth (e.g., SDSS reaches only up to

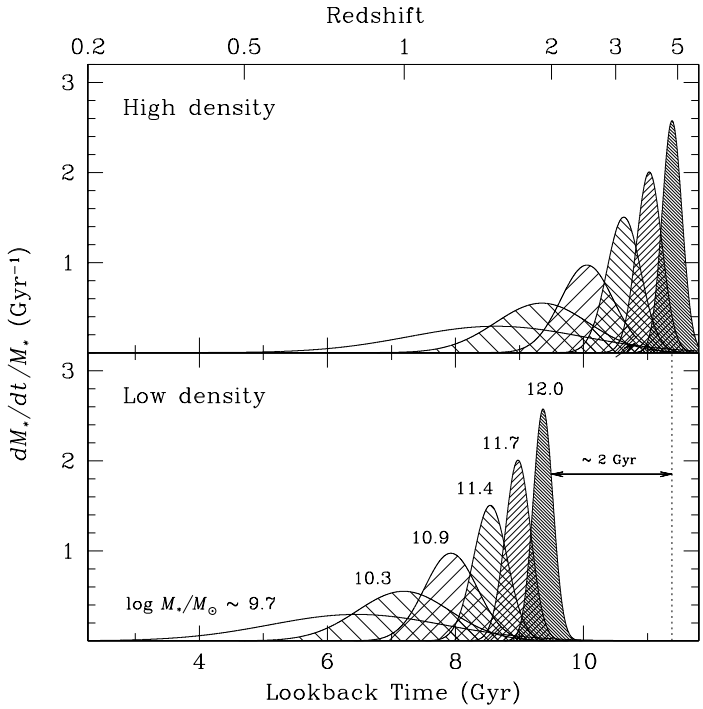

Figure 6.7: Average star formation histories of galaxies with different masses in clusters (top) and field (bottom) (Thomas et al. 2005).

$z \sim 0.3$ or so) or to small field coverage (e.g., zCOSMOS probes only 1 square degree). There is clear observational evidence that galaxy evolution depends on mass of groups and clusters in the sense that galaxies in more massive systems are more evolved (Tanaka et al. 2005; Koyama et al. 2007). It is therefore essential to observe galaxies in a wide range of cluster masses over a wide redshift range to quantify effects of environment on galaxy evolution. A wide and deep spectroscopic survey of PFS will be the first survey to do this job at high redshifts.

A statistical sample of distant clusters will be the sample we would like to make. So far, only $\sim$ 30 clusters (although the number is growing fast) are known to date at $z > 1$ (Stanford et al. 1997, 2002; Rosati et al. 2004; Stanford et al. 2005; Tanaka et al. 2010 for the most intensively studied clusters.), all of which are massive clusters ($> 10^{14} M_{\odot}$). Our PFS survey will improve the statistics by more than 2 orders of magnitude and will discover an even larger number of poor groups. The low-mass end of the cluster mass spectrum has not yet been extensively studied, but high-z low-mass groups are likely the site where blue galaxies are being transformed into red passive galaxies (Tanaka et al. 2007, 2008), as we discuss below.

- **Color(SFR)-density relation**

  Using the wide range of environment over a wide redshift range probed by PFS, we will study the color-density or SFR-density relation. In the local universe, high-density environments are filled with red passive galaxies. But recent results seem to suggest that star formation may be as active in cluster cores at $z \gtrsim 1.5$ is it is in field galaxies (Hilton et al. 2010; Hayashi et al. 2010; but see also Bauer et al. 2010), i.e., the SFR-density relation may be flat or potentially even reversed at high redshift. These results indicate that galaxies in clusters strongly evolve above $z \sim 1$. However, the physical processes driving this evolution (mergers? Gas infall? Feedback?) has yet to be identified. The massive redshift survey that PFS will do will give the spectral diagnostics (stellar populations, stellar mass, star formation rate, metallicity) and environmental information necessary to study this.

  As shown in Fig. 6.2, zCOSMOS cannot reach the important redshift regime of $z > 1$ for this question, but PFS will have an excellent sample of both red and blue galaxies up to $z \sim 1.2$, and will observe the most luminous galaxies up to ~ 1.6. It will be essential to sample a wide density range because the survey areas of the existing surveys at high redshifts are too small to find massive galaxy clusters and they cannot probe the highest density environments. We will be able to securely conclude if there is a reversal of the color (or SFR)-density relation at $z > 1$ based on our unique sample.

  Galaxy properties are strongly dependent not only on environment, but also on stellar mass. In the present-day universe, massive galaxies tend to be red, while low-mass galaxies tend to be blue. Mass and environment are the key parameters to characterize galaxy star formation (Fig. 6.4.3). PFS will allow us to study galaxies of typical mass at $z \sim 1.2$ and more luminous galaxies up to higher redshifts and quantify the role of environment as a function of stellar mass. A number of physical processes affecting star formation are likely to depend on stellar mass, and thus studying trends with stellar mass will be crucial in understanding the physics governing the evolution of the galaxies. For example, ram-pressure stripping (Gunn & Gott 1972) is more effective in lower mass galaxies as their potential wells are shallower. PFS will allow us to explore the cosmic down-sizing as a function of environment at $z > 1$ for the first

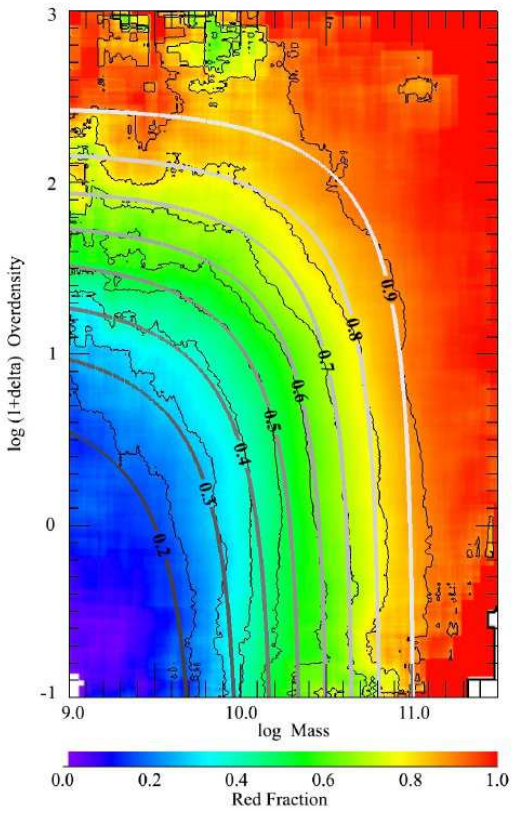

Figure 6.8: Fraction of red galaxies as functions of stellar mass and environment (Peng et al. 2010).

time and put constraints on physical drivers of the environment-dependent galaxy evolution.

- **Morphology-density relation**

  Morphology is another essential property of galaxies. Following the pioneering work by Dressler (1980), Postman & Geller (1984) extended the relation between morphology and galaxy density to group environments, showing that the relation exists over a wide range of galaxy density. At higher redshifts, high resolution HST imaging becomes necessarily. Dressler et al. (1997) presented the evolution of the relation up to $z \sim 0.5$. While their study was limited to the cores of clusters, Treu et al. (2003) probed the relation out to large cluster centric radii at $z = 0.4$. There are only a few studies of the morphologies of galaxies in clusters at $z \sim 1$ (Smith et al. 2005; Postman et al. 2005), and they are limited in the dynamic range of densities they explore.

  PFS provides us with a unique opportunity to probe the morphology-density relation at $z > 1$, particularly in at low and intermediate densities. This will require morphological information from HST imaging. Our target fields include "deep fields" such as SXDF and we will be able to use public HST data available in those fields. For example, CANDLES will observe SXDF with WFC3 in the J and H bands, which probe the rest-frame optical at $z > 1$. The solid angle covered by HST imaging is not wide enough to probe a wade range of environmental densities. As mentioned above, we will be able to measure Sersic indices for these galaxies from sufficiently high S/N HSC images, which is a rough proxy for

morphology, thus extending the HST data we'll have. We expect to confirm several groups down to $5\times10^{13}M_{\odot}$ at $z > 1$ within SXDF, which will be a good first sample to study the low-medium density region of the morphology-density relation. Here, redshift information from PFS will be essential to quantify the density field at such low-densities. Without redshifts, Fore/background contamination is an overwhelming source of noise; without spectroscopic redshifts, groups are essentially impossible to identify. PFS will give us the first data set that allows us to statistically study the morphology-density relation at $z > 1$.

- **Build-up of the red sequence**

  Passive red galaxies in clusters form a tight sequence on a color-magnitude diagram, called the red sequence (Baum 1959; Sandage 1972; Bower et al. 1992). The red sequence is a ubiquitous feature of galaxy clusters. A clear signature of the build-up of the red sequence has been observed in $z > 0.5$ clusters (e.g.,Tanaka et al. 2005). This build-up has important implications for galaxy evolution. As long as galaxies are forming stars, we do not observe a red sequence; galaxies are blue, without a strong correlation between color and luminosity (the blue cloud). Blue galaxies start to become red as their star formation rates decrease, and gradually move to the red sequence. The build-up of the red sequence as a function of environment and redshift tells us *when* and *where* galaxies stop forming stars. Recent observations seem to show that high redshift groups show a deficit of faint red galaxies, suggesting that the faint end of the red sequence is being formed there (Fig. 6.4.3; Tanaka et al. 2007, 2008). Therefore, high redshift groups probed by PFS will be a unique sample to identify when and where the galaxy transformation occurs.

  We can also try to address the remaining question of *how* star formation turns off in galaxies. The physical mechanisms by which star formation turns off are not understood at all, and is one of the key questions of galaxy evolution. One of the key pieces of information to identify the physical process(es) responsible for galaxy quenching is a time scale of that quenching. Some physical processes such as strangulation (Larson et al. 1980), which is effective in groups and clusters, take of order 1 Gyr to quench galaxies. On the other hand, other processes such as starbursts triggered by mergers (Mihos & Hernquist 1996) end on a shorter time scale. A way to constrain the quenching time scale observationally is to use spectral diagnostics, such as the strength of the 4000Å break (D_{4000}) and the equivalent width of the Hδ absorption line. As shown in Fig 6.4.3, the two spectral indices evolve differently with time: D_{4000} monotonically increases with time as a stellar population ages, while Hδ shows a maximum at $0.1 - 1$ Gyr, as A stars dominate the blue light of the galaxies. Therefore, outliers on a D_{4000} vs. Hδ diagram (i.e., Hδ is too strong for its D_{4000} for normal star forming galaxies) can be identified as post-starburst galaxies, in which star formation has been quenched on a very short timescale (Fig. 6.4.3). We therefore need a good statistics to study the quenching time scale. PFS will deliver a large number of galaxies over a wide range of redshift and environment for constructing significant samples of those in a post-starburst phase. Galaxies at higher redshifts are more active and we expect to observe more transient galaxies than at low redshifts. The broad spectral coverage of PFS will allow these objects to be recognized to redshift 2, which is completely impossible using optical spectrographs. By studying the build-up of the red sequence and the spectral features of dying galaxies, we will be able to constrain physical processes responsible for the galaxy quenching.

- **Galaxy mass assembly as a function of environment**

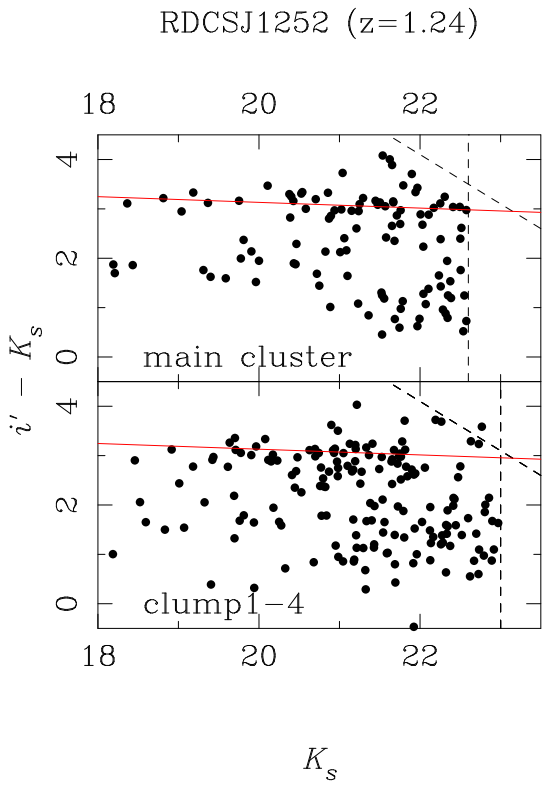

Figure 6.9: $i-K$ color plotted against K color for galaxies in different environments(Tanaka et al. 2007). The top and bottom panels show a rich cluster and a composite of poor groups at $z = 1.2$. Note the clear truncation of the red sequence at $K > 22$ in groups.

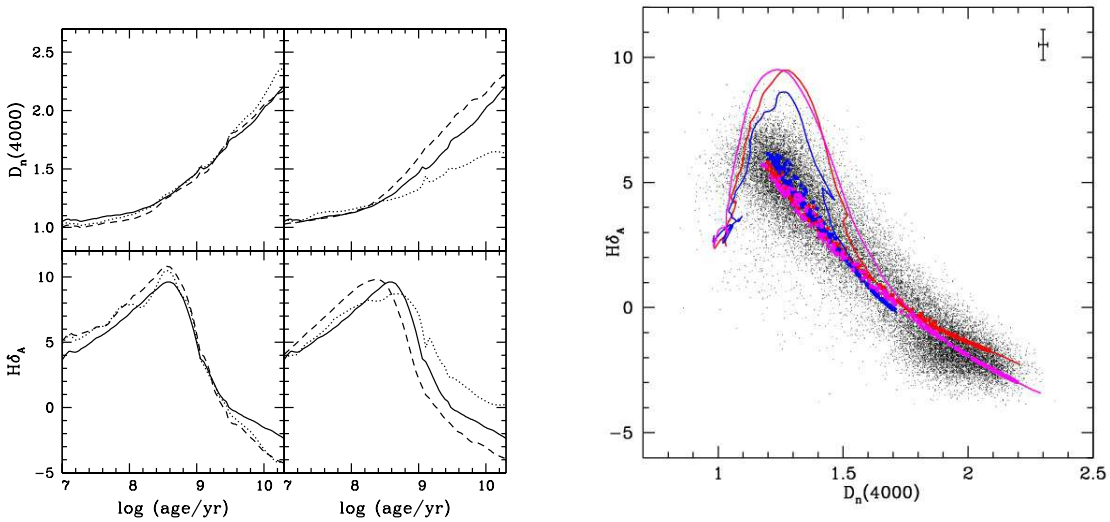

Figure 6.10: **Left:** Evolution of D_{4000} and Hδ spectral indices of a single burst model (Kauffmann et al. 2003). The different line styles show different stellar libraries. The behaviors of the indices are the same in all the models. **Right:** Hδ plotted against D_{4000} (Kauffmann et al. 2003). Different colors represent models with different metallicities. Post-starburst galaxies can be identified as relatively blue (i.e., small D_{4000}) galaxies with strong Hδ absorptions.

The stellar mass function is one of the most fundamental measures of the properties of galaxies. The stellar mass functions of field galaxies have been extensively studied based on both photometric and spectroscopic data (Ilbert et al. 2010 for the latest result). The stellar mass function in high density clusters has also been the subject of many studies (e.g., Strazzullo et al. 2010). These two extreme environments are relatively easy to study because precise determination of the density field is not required. Cluster stellar mass functions can be derived statistically even without photometric/spectroscopic redshifts; the overdensity is strong enough that foreground-background contamination are weak (Strazzullo et al. 2006). Intermediate density regions (i.e., groups) are the most difficult environment to study because one needs spectroscopic redshifts to define the group membership, but this is the environment where morphologies (and presumably the stellar mass function) go through the most dramatic transition.

Based on the zCOSMOS data, Bolzonella et al. (2009) compiled stellar mass functions as a function of environment at $0 < z < 1$. PFS would allow us to extend their work out to $z \sim 1.6$. We will have a large enough number of groups and clusters to construct stellar mass functions in fine redshift and environment bins. Also, we will divide the galaxies into passive and quiescent galaxies using spectral signatures such as the ratio of Hβ to [OII]. A clear red sequence and apparently non-evolving stellar mass function is observed in rich clusters (Toft et al. 2004; Strazzullo et al. 2006; Tanaka et al. 2008; Strazzullo et al. 2010), which is in stark contrast to field where the stellar mass function shows a strong evolution (Ilbert et al. 2010). Little work has been done on stellar mass functions of poor groups at $z > 1$, and PFS will fill this gap. Stellar mass functions of quiescent/star forming galaxies are an excellent tool to quantify how blue galaxies migrate to the red sequence and are complimentary to the discussions above.

6.4.4 Galaxy mergers

According to models of hierarchical structure formation, galaxy merging is a fundamental process to build up massive galaxies. Galaxy mergers not only assemble the galaxy mass, but may also induce starburst, transform the galaxy morphology, trigger AGN activity, as well as quench the star formation. Quantifying galaxy merger rates and characterizing the effects of mergers are keys to understand the mass assembly history and the evolution of galaxies.

Conventionally there are two approaches to identify merger candidates: one is by selecting close galaxy pairs (Patton et al. 2002; Lin et al. 2004, 2008; de Ravel et al 2009) and the second is to select morphologically disturbed galaxies (Conselice et al. 2003; Lotz et al. 2004). The advantage of using close pairs to study mergers is that they are still in the stage before their nuclei have coalesced and hence allow ones to characterize the properties of the merger progenitors (e.g., mass/luminosity ratio, colors, gas content, etc). In order to properly exclude the interlopers from both foreground and background contaminations, it is required to have sufficient spectral resolutions ($R > 2000$) to pick up kinematic close pairs. The wide-field, large number of fibers, moderate spectral resolutions ($R = 2500-4500$), and the wide spectral coverage (0.38 - 1.3 micron) of PFS will have an unique position to detect a large sample of close galaxy pairs up $z \sim 7$ and even beyond if they exist, thereby enabling us to address the following key issues regarding galaxy mergers:

Evolution of galaxy merger rate: Recent merger studies based upon existing spectroscopic surveys have revealed that the evolution of galaxy merger rates depends on merger type, galaxy luminosity, and local environment (Lin et al. 2008; Patton et al. 2008; Bundy et al. 2009; Lin et al. 2010). While the relative abundance of gas-poor (dry merger) and mixed mergers gradually increases toward low redshifts, the gas-rich mergers (wet merger) dominated the merger events at $z \sim 1$, (see Figure 6.11). Extending the merger studies to greater redshifts is of great interest since it provides direct constraints on how galaxies are assembled at earlier time and whether gas-rich mergers are responsible for the peak of the star formation and AGN activity at $z \sim 2-3$. Estimating merger rates beyond $z \sim 1$, however, have been hampered owing to the difficulty in obtaining a large number of spectroscopic samples at greater redshifts. With PFS, one can extend the search of kinematic pairs to ~ 2.5 via [OII], and identify pairs of Lyα emitters at $z = 2-7$, allowing for the full understanding on the merger histories.

Trigger star formation and AGN activity in galaxy mergers: It is known that the most extreme starbursting systems such as ULIRGS and Submillimetre galaxies are often associated with the galaxy mergers (Borne et al. 1999; Engel 2010), which is consistent with the predictions from theoretical works based on hydrodynamic simulations (Mihos & Hernquist 1996; Barnes 2004). It is thus expected that galaxy merging provides an efficient way to consume all the gas within galaxies, serving as a key mechanism to transform blue galaxies into the red sequence. Previous studies nevertheless have found that the level of SF enhancement seen in very close pairs and late-stage mergers is no greater than a factor of 2 compared to wide-separated pairs and isolated samples (Barton et al. 2000; Lambas et al. 2003; Nikolic, Cullen, & Alexander 2004; Lin et al. 2007) over the redshift range of $0 < z < 1$, although with limited statistics for samples at $z > 0.3$. Such results suggest that additional processes such as AGN feedback are required to explain the cease of the star formation after the merger process is completed. With PFS, we aim to address the interplay among galaxy mergers, star formation, and AGN by quantifying the star formation rate and the AGN activity as a function of galaxy properties of kinematic close pairs.

Environment of galaxy mergers The formation and evolution of the most massive galaxies remain open questions nowadays. There is clear evidence that the most massive evolved galaxies tend to reside in overdense regions such as the cores of clusters of galaxies. Yet which mechanism operating in dense environment drives the galaxy evolution is unclear. Galaxy merging, preferentially occurs in high-density regions, can potentially be the key process transforming the properties of galaxies as well as building up the red-sequence in galaxy clusters. Based on the DEEP2 redshift survey, Lin et al. (2010) probes the relation between mergers and environment (see Figure b). They conclude that at $z \sim 1$, the wet merger rate is not sensitive to the local density, while the dry merger rate is a strong function of environment, suggesting a crucial role of dry mergers in assembling the massive cluster galaxies since $z \sim 1$. However, the above results are only based on measurement of local environment rather than the physical environment, since the small survey size of DEEP2 does not allow for identification of massive groups and clusters. PFS will be able to sample a variety of environment from field, groups, to clusters, and thereby has the ability to pin down the role of mergers in all kinds of environment.

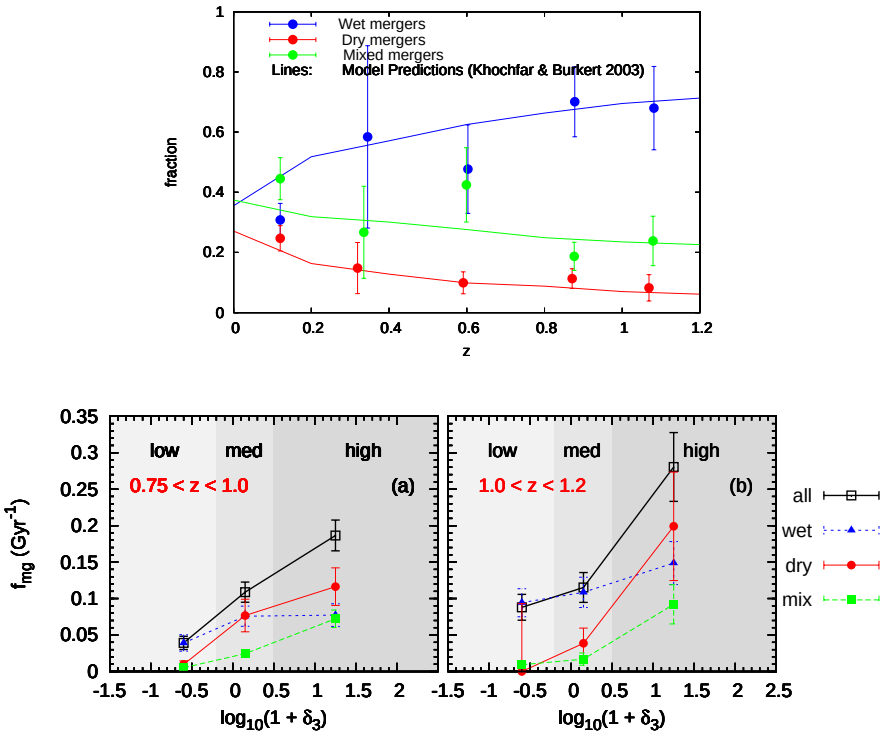

Figure 6.11: *top* Merger fractions as a function of redshift. *bottom* Merger fraction as a function of environment in two redshift bins.

6.4.5 Active Galactic Nuclei

It is now well understood that almost every massive galaxy in the local Universe hosts a supermassive black hole (SMBH) at its center. There is much ongoing effort to determine how these SMBHs are put in place. Our ability to study the mass buildup of SMBHs beyond those in our local vicinity requires an investigation of those in an active phase that have a broad characterization typically given as "Active Galactic Nuclei" with the more luminous of these known as the quasars. Given the steeply increasing numbers of quasars with decreasing luminosity, the lower luminosity AGN represent the bulk of the population of SMBHs undergoing accretion thus our understanding of this population must be incorporated into any coherent picture of black hole growth. Furthermore, the majority of the AGN at lower luminosities enable us to easily discern the properties of their host galaxies thus providing important clues to their formation. To date, studies of such systems have either been restricted to low redshifts or to limted samples in deep survey fields. A wide and deep survey of galaxies out to $z \sim 2$, an epoch of maximal galaxy and black hole growth, will enable us to address fundamental questions that remain unanswered to date: *What physical mechanisms are primarily responsible for the growth of SMBHs? Is there a causal connection between mass accretion onto SMBHs and star formation? How do galaxies and their SMBHs align themselves on the local black hole - bulge relations? Does most black hole growth occur in an obscured state possibly triggered by major mergers of galaxies?*

Characterizing the nature of the accretion flow: In the present day Universe (z 0), most of the mass accretion to SMBHs occur via "radiatively inefficient accretion flows" (RIAFs, Narayan et al. 1998, Storchi-Bergmann 2006), at mass accretion rates smaller than 10^{-3} Eddington (Nemmen et al. 2006). The class of nuclear activity characterized by accretion rates this low is the "Low Ionization Nuclear Emitting Region" (LINER) class, the dominant one in the present day Universe. On the other hand, at z 2, the scenario is quite distinct, as at these redshifts we see the "peak" of QSO activity (the "quasar/QSOs era"), characterized by much higher accretion rates and Eddington ratios, and "radiative efficient" accretion flows, giving origin to geometrically thin and optically thick accretion disks. The transition between these two epochs (z=2 and z=0) is very sparsely probed due to the "redshift desert" resulting from the spectral coverage of present instrumentation, mentioned previously in this document. When/how did the transition between the dominance of high and low mass accretion rates to SMBHs in the Universe occur? This question can only be answered by observing and characterizing the nuclear activity between z=1 and z=2. With the wavelength coverage of the PFS, we will be able to obtain the AGN powers/accretion rates using the emission lines of [OIII]5007A ($0 < z < 1.6$), [NeIII]3869A ($0 < z < 2.3$) and [NeV]3427 ($0 < z < 2.8$). These emission lines will allow us to quantify of the evolution of AGN power from z=0 to z=2.5.

Obscured accretion and host galaxy relations

In the present day Universe ($z < 0.3$) there is a relation between the age of stellar population in the inner kiloparsecs and nuclear activity in galaxies: active galaxies have an excess of young to intermediate age stellar population when compared to non-active galaxies (e.g. Storchi-Bergmann et al. 2000, 2005; Cid Fernandes et al. 2005, 2007, Kauffmann et al. 2003). This relation supports an AGN-Starburst connection, in which the birth of new stars in the nuclear region of the galaxies is associated to the growth of the SMBH. This connection is probably what drives (at least partially) the M-sigma relation (Ferrarese & Merrit 2000; Gebhardt et al. 2000): the observed correlation

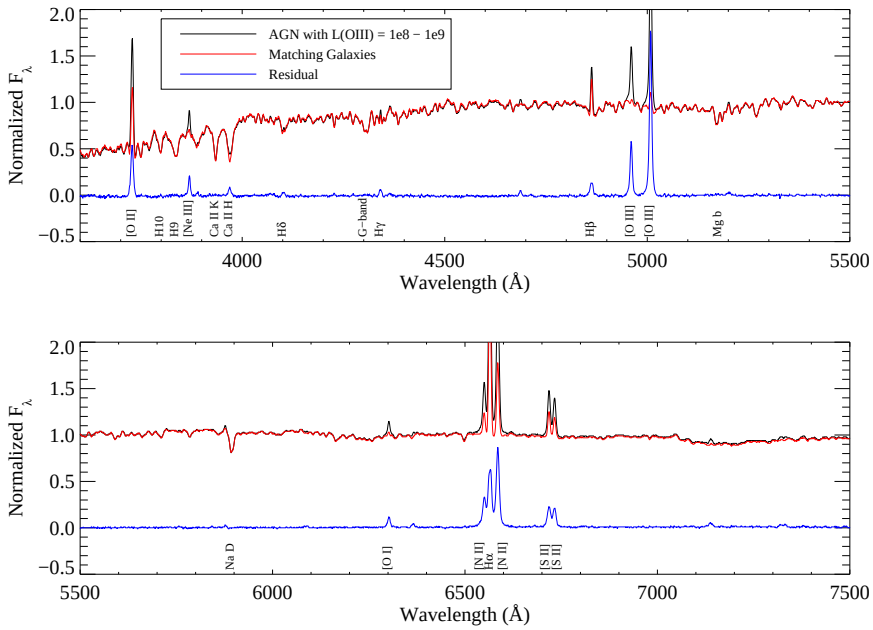

Figure 6.12: Representative SDSS spectra of a narrow-line AGN with host galaxy template modeled and removed (Kauffmann et al. 2003).

between the mass of the SMBH and the stellar dispersion of the bulge (a proxy for its mass). Is this connection between the stellar population and nuclear activity also valid for the more distant Universe? Is there an evolution in the age of the stellar population of AGN hosts? This answer is also to be looked for in the spectra of active galaxies at higher z's, using spectral synthesis of the stellar population (Cid Fernandes et al. 2004) or indexes (Kauffmann & Heckmann 2003).

AGNs for such studies are typically selected by their strong emission lines indicative of a non-thermal source producing prodiguos numbers of UV photons capable of ionizing gas on scales reaching a few kpc. The observed emission lines are produced from ionized gas either in the vicinity of the SMBH with line widths, in terms of velocity, greater than 1200 km s^{-1} (usually called a "type 1" or broad-line AGN), or farther out thus having smaller velocity widths ("type 2" or narrow-line AGN). The lack of broad emission lines in many AGNs is attributed to the presence of a dusty torus effectively hiding the broad-line region. It is these narrow-line AGN that have an intrinsic screen (i.e., nature's coronagraph) that enables us to study the host galaxies (e.g., Kauffmann et al. 2003; Kewley et al. 2006; Wild et al. 2007) for even those with high luminosities (e.g., Zakamska et al. 2003; Liu et al. 2009).

While the SDSS has made remarkabe progress in our understanding of obscured AGN (e.g., Kauffmann et al. 2003), these galaxies tend to harbor low luminosity AGN at $z < 0.3$ that have much of their mass in place. With PFS, we can identify type 2 AGN out to $z \sim 1.6$, an epoch of maximal black hole growth (i.e., the quasar heyday), that can be identified by their strong [OIII]λ5007 emission line. It remains to be confirmed whether the ratio of obscured-to-unobscured AGN increases with redshift that can be addressed with a PFS surveys. Furthermore, at $0.1 < z < 1.0$, the full suite of emission lines (Hα,[NII], Hβ,[OIII]) will be available for not only identification but

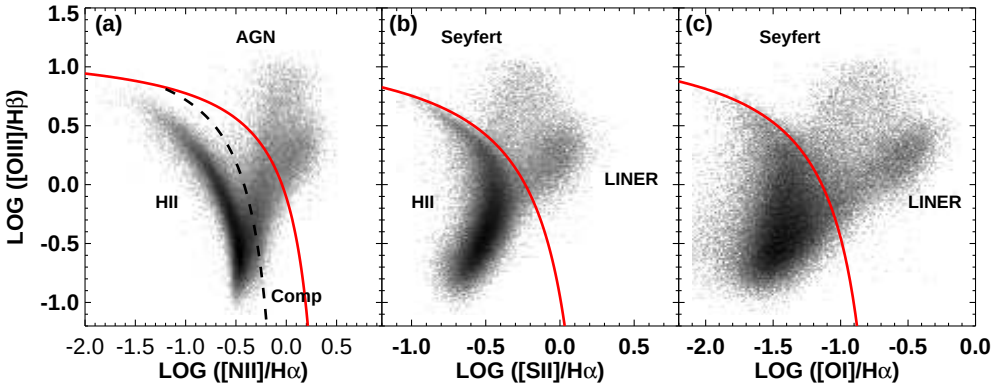

Figure 6.13: Classification scheme for narrow emission-line galaxies (Kewley et al. 2006).

extinction estimates.

Here we list a few key projects from a large list of topics pertaining to type 2 AGN science with PFS:

- Distribution function of black hole mass and accretion rate (Greene & Ho 2007; Kauffmann & Heckman 2009)
- Host galaxy properties: stellar masses or velocity dispersion (Greene & Ho 2006; Schawinski et al. 2007), age ($H\delta_A$, D_n4000; Greene et al. (2009)), star formation rates based on [OII]λ3727 (see Figure 6.14; Silverman et al. (2009a))
- Space density and properties of luminous type 2 QSOs (Zakamska et al. 2003)
- Physics of photoionization, narrow-line emitting gas (Stasińska et al. 2006) and nuclear obscuration

Low luminosity accretion: broad line AGNs

AGNs, identified within a primarily, galaxy-targeted survey that have evidence for broad (FWHM $>$ 2000 km s^{-1}) emission lines, offer a remarkable opportunity to both measure the black hole and host galaxy mass. The masses of the SMBHs, powering these AGNs, can be obtained via scaling relations (e.g. Peterson et al. 2004, 2010) and from observations of Hβ in the broad-lined AGN (as a probe of the kinematics of the BLR) up to z=1.6, Hα up to $z \sim 1$, and to higher redshifts ($z \sim 3.6$) with the MgII 2800A emission line.The high signal-to-noise spectra of such galaxies in SDSS have opened new opportunities to study populations of SMBHs at low mass and those accreting with sub-Eddington rates. Preliminary studies show signs of evolution in their mass ratios thus indicating a possible migratory path onto the local mass relations but such studies may still suffer from inherent biases. A deeper spectroscopic survey with PFS will provide a firmer lever arm in order to control systematic effects. Furthermore, the deep imaging data from the HSC survey will be exploited to measure the morphology and structural parameters of their host galaxies at $z < 1$. In addition, the low luminosity of these broad-line AGNs, as done with the

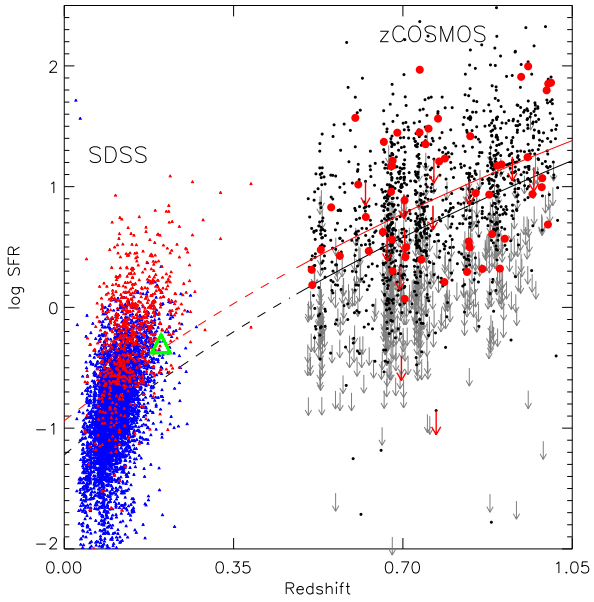

Figure 6.14: Star formation rates in galaxies hosting AGN from SDSS to zCOSMOS (Silverman et al. 2009b).

narrow-line AGNs, permits an assessment of the level of star formation. Here, we list a few of key investigations that push SDSS studies of broad-line AGN out to higher redshifts.

- M_{BH} vs. σ_* (Figure 6.15; Greene & Ho (2006))
- Star formation rates in type 1 AGN (Kim et al. 2006)
- Powering and launching of synchrotron-emitting jets (Kauffmann et al. 2008)

Environments of AGNs from galaxy mergers to massive clusters

The local environment of galaxies harboring AGNs and QSOs has long been thought to play a potential role in triggering mass accretion onto SMBHs. With many of the properties of galaxies (e.g., morphology, color, star formation rate) clearly dependent on environment and the possibility of a common history of mass assembly for SMBHs and their host bulges, we expect that AGNs may prefer to reside in specific environments most nuturing for their growth. Identifying environmental factors might allow us to determine the physical mechanism(s) responsible for supplying gas for accretion such as major mergers of galaxies that has been demonstrated through numerical simulations (Barnes & Hernquist 1992) to be able to remove angular momentum from rotationally-supported gas thus transferring mass to the nuclear regions (further detailed below). For example, there is evidence that AGNs reside in dark matter halos with masses $M_{halo} \sim 10^{13} M_{sun}$, a mass regime comparable to the group-scale environments thought to be fertile ground for galaxies to coalesce. As well, high density regions such as massive clusters of galaxies are expected to be inhospitable environments for AGN given the strong empirical association between AGN activity and concurrent star formation.

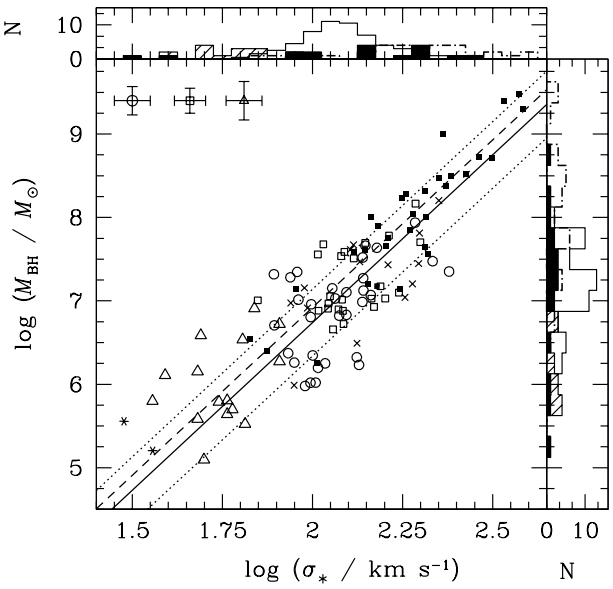

Figure 6.15: Extending black hole - host galaxy relations at the lower end with SDSS type 1 AGNs (see Greene & Ho 2006, for details)

The triggering of nuclear activity in galaxies requires a flow of matter from galactic to nuclear scales, which have only recently become to be actually mapped (Fathi et al. 2006; Storchi-Bergmann et al. 2007; Riffel et al. 2008; Schnorr-Muller et al. 2010; Riffel & Storchi-Bergmann 2010). The observation of a younger stellar population in active galaxies as compared with non-active galaxies, as discussed above, suggest a common triggering mechanism for recent star formation and the nuclear activity. One possibility is galaxy encounters with nearby companions, which could produce a flow of gas towards the centers of galaxies, giving birth to new stars and also feeding the SMBH. Nevertheless, no excess of companions has been found around active galaxies relative to non-active galaxies (e.g. Schmitt 2001; Li et al. 2006), in spite of the fact that such an excess is found around star-forming galaxies (Li et al. 2008). As there is an excess of young/intermediate age stellar population in active galaxies, one possibility to explain this dichotomy is a delay between the star-formation episode(s) and the triggering of nuclear activity (Storchi-Bergmann et al. 2001). Actually, companions to active galaxies are only found when the stellar population is very young, in which case both the starburst and AGN are very luminous (Storchi-Bergmann et al. 2001). If there is an evolution in AGN luminosity with z (brighter AGN for higher z) we may find more companions to active galaxies at higher redshift (Silverman et al. in preparation), allowing the testing of this possible evolutionary scenario. With a spectroscopic survey using PFS that samples a wide dynamic range in galaxy density from the fields to rich clusters, we can determine such environments most nurturing for black hole growth up to the QSO epoch ($z \sim 2$).

A census of binary supermassive black hole mergers Using the double-peaked OIII emission lines in their spectra, Liu et al. (2010) have identified a sample of binary AGNs. As massive galaxies are believed to harbor SMBHs in their center, and that galaxies are built up hierarchically (through mergers and/or accretion), binary SMBH mergers are naturally expected. The PFS survey will provide a prime opportunity to conduct a census of such merger candidates; with follow up imaging and spectroscopy, we would be able to constrain on the merger process of SMBHs.

Multiwavelength studies

The wide area coverage and high multiplexing of PFS enable fibers to placed on special targets of interest especially those identified in other wavebands (i.e., X-ray, radio, far-infrared, submillimeter). Future wide area X-ray surveys with eROSITA are likely to identify high redshift ($z > 6$) quasars too faint optically to be identified in shallow surveys such as the SDSS. The *Chandra* and XMM-*Newton* archives also contain many targets of interest for a fair number of studies of AGNs.

Much spectroscopic followup is also required to identify the radio source population. In the local Universe, RGs are found to inhabit in massive halos ($M > 10^{13} M_{\odot}$; Mandelbaum et al. 2009; Lin et al. 2010). The origin of the radio-loud phase is still unclear; the trigger of the gas accretion onto the central SMBH may be the cooling instability at the centers of groups/clusters, the galaxy interaction within massive halos, or simply from the recycled gas from the aged stellar population. As PFS survey fields may overlap with the LOFAR radio survey, we would be able to study the RG population up to $z \sim 2$. The high sampling rate of the survey allows us to measure the environments of RGs, and thus could help us differentiate the true origin of the radio activity.

References

Baldwin, J. A., Phillips, M. M., & Terlevich, R., 1981, *PASP*, 93, 5
Bauer, A. E., Grutzbauch, R., Jorgensen, I., Varela, J., & Bergmann, M., 2010, ArXiv e-prints, 1010.1238
Baum, W. A., 1959, *PASP*, 71, 106
Blanton, M. R., Eisenstein, D., Hogg, D. W., Schlegel, D. J., & Brinkmann, J., 2005, *ApJ*, 629, 143
Bolzonella, M. et al., 2009, ArXiv e-prints, 0907.0013
Bower, R. G., Lucey, J. R., & Ellis, R. S., 1992, *MNRAS*, 254, 601
Cooper, M. C. et al., 2008, *MNRAS*, 383, 1058
Cowie, L. L., Songaila, A., Hu, E. M., & Cohen, J. G., 1996, *AJ*, 112, 839
Cucciati, O. et al., 2006, *A&A*, 458, 39
Dressler, A., 1980, *ApJ*, 236, 351
Dressler, A. et al., 1997, *ApJ*, 490, 577
Elbaz, D. et al., 2007, *A&A*, 468, 33
Geller, M. J., & Huchra, J. P., 1989, Science, 246, 897
Gómez, P. L. et al., 2003, *ApJ*, 584, 210
Greene, J. E., & Ho, L. C., 2006, *ApJL*, 641, L21
—, 2007, *ApJ*, 667, 131
Greene, J. E., Zakamska, N. L., Liu, X., Barth, A. J., & Ho, L. C., 2009, *ApJ*, 702, 441
Gunn, J. E., & Gott, III, J. R., 1972, *ApJ*, 176, 1
Hayashi, M., Kodama, T., Koyama, Y., Tanaka, I., Shimasaku, K., & Okamura, S., 2010, *MNRAS*, 402, 1980
Hilton, M. et al., 2010, *ApJ*, 718, 133
Hopkins, A. M., & Beacom, J. F., 2006, *ApJ*, 651, 142
Ilbert, O. et al., 2010, *ApJ*, 709, 644
Kauffmann, G., & Heckman, T. M., 2009, *MNRAS*, 397, 135
Kauffmann, G., Heckman, T. M., & Best, P. N., 2008, *MNRAS*, 384, 953
Kauffmann, G. et al., 2003, *MNRAS*, 341, 33
Kewley, L. J., Groves, B., Kauffmann, G., & Heckman, T., 2006, *MNRAS*, 372, 961
Kim, M., Ho, L. C., & Im, M., 2006, *ApJ*, 642, 702
Koyama, Y., Kodama, T., Tanaka, M., Shimasaku, K., & Okamura, S., 2007, *MNRAS*, 382, 1719
Larson, R. B., Tinsley, B. M., & Caldwell, C. N., 1980, *ApJ*, 237, 692
Lewis, I. et al., 2002, *MNRAS*, 334, 673
Lilly, S. J. et al., 2007, *ApJS*, 172, 70
Lin, Y., Shen, Y., Strauss, M. A., Richards, G. T., & Lunnan, R., 2010, *ApJ*, 723, 1119
Liu, X., Shen, Y., Strauss, M. A., & Greene, J. E., 2010, *ApJ*, 708, 427

Liu, X., Zakamska, N. L., Greene, J. E., Strauss, M. A., Krolik, J. H., & Heckman, T. M., 2009, *ApJ*, 702, 1098
Mandelbaum, R., Li, C., Kauffmann, G., & White, S. D. M., 2009, *MNRAS*, 393, 377
Mihos, J. C., & Hernquist, L., 1996, *ApJ*, 464, 641
Peng, Y. et al., 2010, *ApJ*, 721, 193
Postman, M. et al., 2005, *ApJ*, 623, 721
Postman, M., & Geller, M. J., 1984, *ApJ*, 281, 95
Rosati, P. et al., 2004, *AJ*, 127, 230
Sandage, A., 1972, *ApJ*, 173, 485
Schawinski, K., Thomas, D., Sarzi, M., Maraston, C., Kaviraj, S., Joo, S., Yi, S. K., & Silk, J., 2007, *MNRAS*, 382, 1415
Silverman, J. D. et al., 2009a, *ApJ*, 695, 171
—, 2009b, *ApJ*, 696, 396
Smith, G. P., Treu, T., Ellis, R. S., Moran, S. M., & Dressler, A., 2005, *ApJ*, 620, 78
Stanford, S. A. et al., 2005, *ApJL*, 634, L129
Stanford, S. A., Elston, R., Eisenhardt, P. R., Spinrad, H., Stern, D., & Dey, A., 1997, *AJ*, 114, 2232
Stanford, S. A., Holden, B., Rosati, P., Eisenhardt, P. R., Stern, D., Squires, G., & Spinrad, H., 2002, *AJ*, 123, 619
Stasińska, G., Cid Fernandes, R., Mateus, A., Sodré, L., & Asari, N. V., 2006, *MNRAS*, 371, 972
Strazzullo, V. et al., 2010, ArXiv e-prints, 1009.1423
—, 2006, *A&A*, 450, 909
Tanaka, M. et al., 2008, *A&A*, 489, 571
Tanaka, M., Finoguenov, A., & Ueda, Y., 2010, *ApJL*, 716, L152
Tanaka, M., Kodama, T., Arimoto, N., Okamura, S., Umetsu, K., Shimasaku, K., Tanaka, I., & Yamada, T., 2005, *MNRAS*, 362, 268
Tanaka, M., Kodama, T., Kajisawa, M., Bower, R., Demarco, R., Finoguenov, A., Lidman, C., & Rosati, P., 2007, *MNRAS*, 377, 1206
Thomas, D., Maraston, C., Bender, R., & Mendes de Oliveira, C., 2005, *ApJ*, 621, 673
Toft, S., Mainieri, V., Rosati, P., Lidman, C., Demarco, R., Nonino, M., & Stanford, S. A., 2004, *A&A*, 422, 29
Tremonti, C. A. et al., 2004, *ApJ*, 613, 898
Treu, T., Ellis, R. S., Kneib, J., Dressler, A., Smail, I., Czoske, O., Oemler, A., & Natarajan, P., 2003, *ApJ*, 591, 53
Wild, V., Kauffmann, G., Heckman, T., Charlot, S., Lemson, G., Brinchmann, J., Reichard, T., & Pasquali, A., 2007, *MNRAS*, 381, 543
York, D. G. et al., 2000, *AJ*, 120, 1579
Zakamska, N. L. et al., 2003, *AJ*, 126, 2125

7 Dust-shrouded Star Formation and Black Hole Accretion

Hideo Matsuhara, Stephen Serjeant, Tomotsugu Goto, Youichi Ohyama, Matt Malkan, Toshinobu Takagi

7.1 Background

The past decade has seen revolutionary developments in hierarchical (i.e. "top-down") models of galaxy evolution. A new population of high-redshift violent starbursts was discovered using SCUBA (Smail et al. 1997; Hughes et al. 1998). These extreme submm galaxies (SMGs) were not anticipated by previous semi-analytic hierarchical models, and accounting for them has in part driven the new "downsizing" paradigm in galaxy evolution, in which present-day massive galaxies formed the bulk of their stars counter-intuitively at early cosmic epochs: at the very least, fine-tuning of feedback processes or the Initial Mass Function (IMF) seem to be required. This is not the first time that unexpected extreme populations have challenged prevailing descriptions of galaxy evolution (Rowan-Robinson et al. 1991); important new constraints often follow from exploration of new parts of the observational parameter space (see e.g. Serjeant arXiv:1002.3053 for a brief review). Spectroscopic follow-up of overwhelmingly large number of dusty galaxies with Subaru/PFS is a unique opportunity to discover a new population that may derive a new paradigm in galaxy evolution.

In this Chapter, we first introduce how the dust-shrouded star formation and black hole accretion has been revealed with mainly space infrared telescopes. It is now common understanding that the focusing on $z = 1 - 2$ era (the 'violent epoch') is the critically important to find a clue to understand why the "downsizing" paradigm works, and to understand the stellar mass assembly and the black hole growth history over cosmic time. Then we describe the key sciences of PFS spectroscopic survey of Herschel-ATLAS galaxy sample, observing strategy, and synergy to SPICA, the next-generation space infrared telescope.

7.1.1 Luminosity Density Evolution in the Violent Epoch of the Universe

To understand the cosmic history of star formation and AGN (active galactic nuclei), it is vital to understand infrared (IR) emission; the more intense star formation, the more deeply it is embedded in the dust, hence, such star formation is not visible in UV but in the infrared. AGN evolutionary scenarios predict that AGN are heavily obscured at their youngest, Compton-thick stage (Treister et al. 2009). For example, at z=1, Goto et al. (2010) estimated 90% of star formation

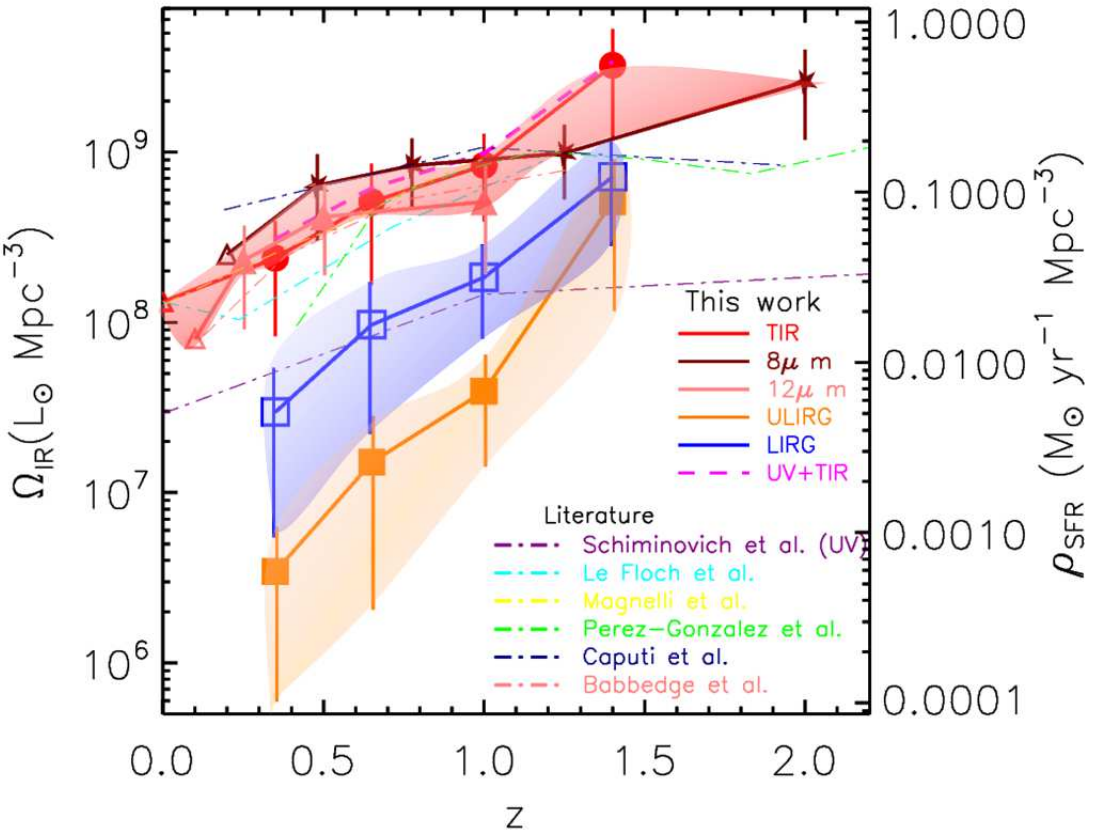

Figure 7.1: Evolution of TIR luminosity density based on TIR LFs (red circles), 8μm LFs (stars), and 12μm LFs (filled triangles). The blue open squares and orange filled squares are for only LIRG and ULIRGs, also based on our L_{TIR} LFs. Overplotted dot-dashed lines are estimates from the literature: Le Floc'h et al. (2005), Magnelli et al. (2009), Pérez-González et al. (2005), Caputi et al. (2007), and Babbedge et al. (2006) are in cyan, yellow, green, navy, and pink, respectively. The purple dash-dotted line shows UV estimate by Schiminovich et al. (2005). The pink dashed line shows the total estimate of IR (TIR LF) and UV (Schiminovich et al. 2005).

activity is hidden by dust. Studies of the extragalactic background suggest at least half the luminous energy generated by stars has been reprocessed into the infrared (IR) by dust (Lagache et al. 1999; Puget et al. 1996; Franceschini et al. 2008), suggesting that dust-obscured star formation was much greater at higher redshifts than today.

The Spitzer and AKARI satellites revealed large amounts of infrared emission in the high-redshift Universe, showing strong evolution in the infrared luminosity density (Le Floc'h et al. 2005; Pérez-González et al. 2005; Babbedge et al. 2006; Caputi et al. 2007; Magnelli et al. 2009) toward a higher redshift.f Fig.7.1 shows cosmic star formation history revealed by the AKARI (Goto et al. 2010). By taking advantage of its continuous mid-infrared bands, the AKARI has revealed cosmic star formation history without relying on extrapolation based on an assumed SED.

However, both Spitzer and AKARI suffered from poorer sensitivity in far-IR wavelengths to measure emission from cold dust directly, and thus, had to rely on in-direct mid-IR detections to estimate total dust emission at high redshift Universe. Since the rest-frame IR SEDs of star-

forming galaxies and AGN peak at 60-200μm, we need to observe in far-infrared to accurately measure the bolometric luminosity, and its evolution. Even with the deepest Spitzer 70μm data, only $z \sim$1 could be reached in the far-infrared (Magnelli et al. 2009). Ground-based observations in the mm/sub-mm range probing the evolution of the most distant ($z >$2) and luminous dusty galaxies, have so far been limited to the identification of sources at the very bright end of the luminosity function (Chapman et al. 2005b). A number of studies found cold dust that cannot be detected in the mid-IR. For example, Dunne & Eales (2001) detected such cold dust with $T \sim$ 20K using SCUBA 450,850 μm observation. Symeonidis et al. (2009) detected cold galaxies with SED peaks at longer wavelengths using Spitzer/MIPS. Therefore, to fully understand cosmic evolution of infrared luminosity density, it is essential to directly observe in far-IR, where dust emission peaks.

Herschel is currently changing the view: (Gruppioni et al. 2010) measured rest-frame 60 and 90μm IR LFs up to z$\sim$3. In the following we will desribe the *Herschel* ATLAS galaxy sample. which, we propose, is a precious candidate for Subaru/PFS spectroscopic study.

7.1.2 The *Herschel* ATLAS key project

The *Herschel* Astrophysical Terahertz Large Area Survey (Eales et al. 2010), or ATLAS, is the largest Open Time Key Project on *Herschel*. This legacy survey is covering 550 deg^2, an order of magnitude larger than all other Herschel extragalactic surveys combined, and will provide more extragalactic sources than all other *Herschel* surveys combined. It has already made its first public data release, from the first 16 deg^2. *Herschel* ATLAS builds on the pioneering *AKARI* All-Sky Survey and has six primary science themes: (a) the local galaxy luminosity function and dust mass function down to $10^{4.5} M_{\odot}$; (b) a submm-selected survey of $\sim$ 300 strong gravitational lenses; (c) the star formation rates in active galaxies and the co-evolution of black hole and stellar mass assembly; (d) the large-scale structure of the submm galaxy population and the star formation density field; (e) protostars, debris discs and galactic dust; (f) the synergy with Planck.

The ATLAS fields are shown in Fig.7.2. There are five fields:

- NGP block: a rectangular block 15° × 10° centred on α = 199.5°, δ = 29° and rotated by $\simeq$ 8° clockwise.
- Three fields from the Galaxy And Mass Assembly (GAMA) project centred on 9^h, 12^h and 14.5^h. Each field covers about 12° in α and 3° in δ.
- SGP block (not shown in Fig.7.2): consists of two concatenated rectangular blocks. One has dimensions of 26.7° (i.e. 31.5° cos(δ)) by 6°. The other has dimensions of 17.0° (i.e. 20° cos(δ)) by 6°.

The advantage of targetting the GAMA fields is the availability of redshifts over 144 deg^2, but no redshifts are available for the NGP 150 deg^2 ATLAS field.

Fig.7.3 shows the SDSS r(AB) magnitudes of the 250 μm-selected (black crosses) and 500 μm-selected (red circles) galaxies in the first 16 deg^2 of *Herschel* ATLAS. Only galaxies with ID reliabilities $>$ 0.8 are plotted. These, in turn, represent only 36% of the full sample of 6576 galaxies

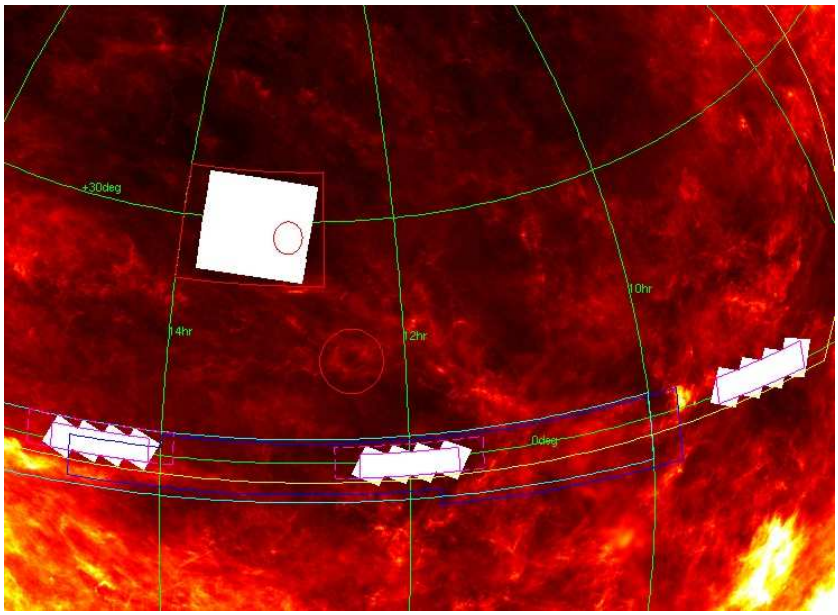

Figure 7.2: The Northern and Equatorial fields of the *Herschel* ATLAS key project, superimposed on an *IRAS* 60 μm map. The large white rectangle is the *Herschel* NGP field. Scan constraints determine the angle. The GAMA fields are shown in magenta: the solid lines are the 1 year "guaranteed areas", while the dashed lines are the eventual goals. The blue line shows the approximate 2dF outline. Cyan is the KIDSS area and yellow shows the SDSS. The two red circles are Coma and Virgo. The large red area surrounding the NGP field is the UKIDSS coverage in YJHK. The solid green lines are RA and Dec, while the dotted green lines are Ecliptic Latitude and Longitude.

detected at $> 5\sigma$ at 250 μm, and only 23% of the 307 galaxies at $> 5\sigma$ at 500 μm. (NB the ID statistics for the HerMES *Herschel* survey presented in Vaccari et al. (2010) are for a 24 μm pre-selected local galaxy sample and do not represent the statistics of the HerMES sample as a whole.) The expectation is therefore that ATLAS will detect around 22,000 galaxies with robust IDs in the NGP ATLAS field at 250 μm, and around 700 at 500 μm. Around half of the 500 μm sample will be identified with blazars and local galaxies, while the remainder are likely to be strong gravitational lenses (see below). Of the 250 μm galaxies with redshifts, the galaxies lie at $z \leq 1$ (median $z \simeq 0.3$, Dye et al. (2010)), but source count models predict the ATLAS population as a whole to have a median redshift of $z \simeq 1$. In total, the NGP ATLAS field will contain $\sim 70,000$ galaxies (about 1/3 of ATLAS) with a median redshift of $z \simeq 1$.

7.2 Key Science Goals

7.2.1 The evolution and environment-dependence of star formation in galaxies

How did galaxy environment regulate or otherwise affect the stellar mass assemblies of galaxies? In the local Universe, optical studies have shown that star-forming galaxies avoid richer environments (e.g. Kauffmann et al. 2004; Balogh et al. 2004). However, mid-infrared studies in small fields at $z < 1$ have already demonstrated that this relationship is reversed at earlier epochs, to an extent which already challenges semi-analytic models (e.g. Elbaz et al. 2007). There are ~ 60 clusters of

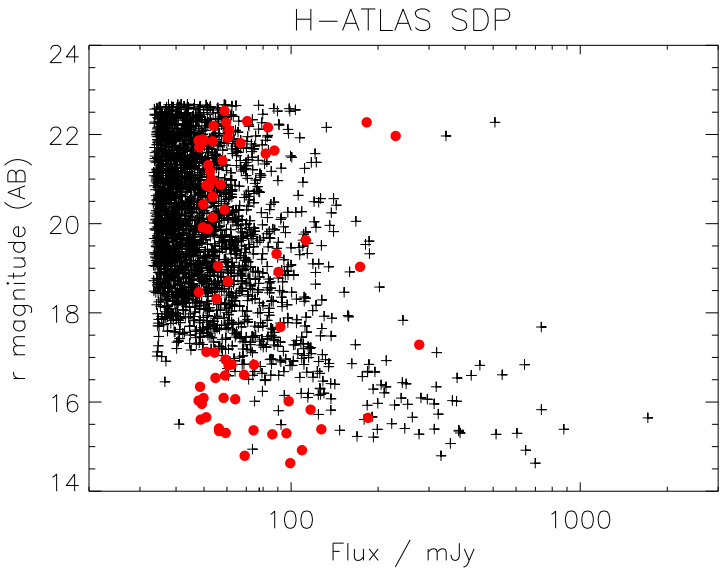

Figure 7.3: SDSS optical identifications of the first 16 deg^2 of the *Herschel* ATLAS key project. Black crosses show the 5σ 250 μm catalogue, while red circles show the 5σ 500 μm catalogue. Only identifications with reliabilities of > 0.8 are plotted, though these represent only 36% (23%) of the population at 250 μm (500 μm).

Abell class 1 or greater in the ATLAS fields, enabling a robust local benchmark for the relationship between dust-shrouded star formation and galaxy density (i.e., comparing the local *star formation* density field with the galaxy *number* density field). Comparison of ATLAS star-forming galaxies with galaxy surveys (see elsewhere in this white paper) will enable corresponding investigations of this relationship at $z < 1$.

ATLAS will also be the only survey to trace the large-scale structure of the star-forming galaxy population up to the $\simeq$ 1000 Mpc scale. This will allow estimates of the masses of dark matter halos and will provide clear discrimination between competing galaxy evolution models (e.g. van Kampen et al. (2005); see also Eales et al. (2010)).

How has the dust content of the Universe and dust-shrouded star formation rate evolved over the past three billion years? The spectrum of the extragalactic background light, on its own, implies that half of the electromagnetic energy emitted by galaxies was absorbed by dust and re-radiated as thermal emission. However, there are very few direct measurements of the evolution of the galaxy bolometric luminosity function, with many studies relying instead on mid-infrared proxies for the bolometric output of star formation. By covering the peak of the far-infrared SEDs of star-forming galaxies, *Herschel* is making the best possible direct measurement of the dust-shrouded star formation rates, since the far-infrared emission is directly tracing the reprocessed emission from young massive stars. By mapping such a large area, the overall volume-averaged statistical properties of the infrared star-forming galaxy population will be essentially immune to cosmic variance effects. This is a key diagnostic test of downsizing models of galaxy evolution.

7.2.2 The link between black hole accretion and stellar mass assembly

The cosmic star formation history (e.g. Madau et al. 1996, et seq.) has a curious similarity to the evolving luminosity density of quasars (QSOs) at most redshifts (e.g. Boyle & Terlevich 1998; Franceschini et al. 1999), suggesting some physical links between black hole growth and stellar mass assembly. Moreover, mid-infrared spectra (e.g. Genzel et al. 1998; Spoon et al. 2007) and radiative transfer modelling (e.g. Farrah et al. 2002) require that the AGN contribution to bolometric luminosity increases for higher luminosity starbursts. The tight K-band Hubble diagram of far-infrared-selected hyperluminous starbursts is also strikingly similar to the $K-z$ relation of radiogalaxies (e.g. Serjeant et al. 2003), though see Smail et al. (2004) for the submm-selected counterparts).

A close relationship between black hole growth and stellar mass assembly is also required the strong correlations betwen spheroid properties and supermassive black hole masses (e.g. Magorrian et al. 1998; Merritt & Ferrarese 2001). The strength of these relationships are surprising given the enormous differences in mass scale and spatial scale. These correlations can be reproduced by by galaxy evolution models with kinetic and/or radiative energy outputs from the AGN regulating star formation in the host galaxies (Granato et al. 2006), but such feedback models have many adjustable parameters. Feedback is arguably the largest uncertainty in semi-analytic models of galaxy evolution and the most pressing case for better observational constraints. One of the few observational techniques available for constraining feedback models is to measure the star formation rates in QSO host galaxies.

There are ~ 400 AGN candidates in SDSS per square degree to $i < 23$ (median $i \simeq 21$) much deeper than the spectroscopic SDSS QSO catalogue (see e.g. Abraham et al. 2010 arXiv1011.2173), i.e. approximately $60,000$ in the NGP field. By conducting a Subaru spectroscopic AGN survey (see AGN/QSO chapter this white paper) in fields with *Herschel* coverage, it will be possible to measure the star formation rates in the QSO host galaxies (via the far-infrared and submm photometry), the black hole matter accretion rates (via the optical continuum luminosities), the black hole masses and Eddington ratios (via equivalent widths of broad Balmer lines and other lines), gas outflows from the central engine (via broad absorption lines), line of sight obscuration to the central engines for type-1 AGN (via Balmer decrements), and a large suite of other major spectroscopic diagnostics of central engine activity. Moreover, extending the AGN sample to the radio-loud population (around 10% of the total AGN population) will provide a large sample of radio-loud type-2 AGN and measure the differential stellar mass assembly in the radio-loud and radio-quiet populations. In total, this is perhaps the best opportunity to study AGN feedback process on star formation in a large statistical sample. As most AGN will not be detected directly by *Herschel* the high-z constraints will proceed via stacking analyses. *Herschel*'s large $110-500\,\mu$m photometric coverage will test for luminosity and redshift dependences of the mean SED.

As a taster for what the full AGN sample will reveal, Fig.7.4 shows the cosmic star formation history of *quasar host* galaxies, as determined from stacking analyses of QSOs from the first $16\,\mathrm{deg}^2$ of the *Herschel* ATLAS key project, assuming a single common SED (Serjeant et al. 2010). The evolution rate at high luminosities is astonishingly strong, e.g. $(1+z)^{10\pm1}$ at $-26 < I_{\mathrm{AB}} < -28$. The correlation between star formation rate and black hole accretion rate is also found to vary significantly with redshift, a property which has not yet been reproduced by models of AGN feedback.

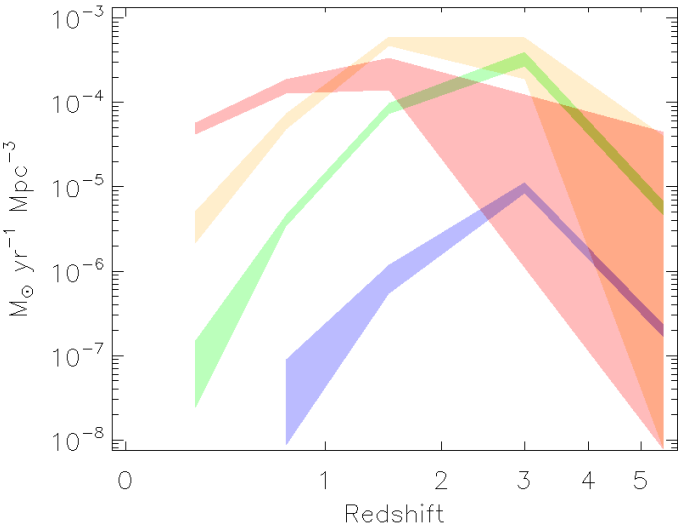

Figure 7.4: The cosmic star formation history of quasar host galaxies, as inferred from 100 μm rest-frame luminosities. Quasars are plotted with $-22 < I_{\rm AB} < -24$ (red), $-24 < I_{\rm AB} < -26$ (orange), $-26 < I_{\rm AB} < -28$ (green), $-28 < I_{\rm AB}$ (blue). Figure from Serjeant et al. (2010).

7.2.3 Discovery of Overwhelmingly Luminous IR Galaxies

Which are the most luminous galaxies in the Hubble Volume? By surveying $\sim 1\%$ of the sky and thanks to the favourable submm K-corrections, the statistical expectation is that the ATLAS key project will detect galaxies among the ~ 100 most luminous in the $z < 6$ observable Universe. Taken in conjunction with the fainter *Herschel* surveys (e.g. HerMES) and the de-magnified lensed populations from H-ATLAS, this makes it possible to sample essentially *the complete range of submm galaxy luminosities in the* $z < 6$ *observable Universe*. The extreme star-forming populations have on many occasions driven the development of theoretical descriptions of galaxy evolution, from the discovery of the first hyperluminous galaxy (Rowan-Robinson et al. 1991) to the discovery of submm-luminous galaxies driving the development of the downsizing paradigm. The most extreme systems are those in which the physical processes driving feedback are most apparent. Semi-analytic models diverge in their predictions for the most luminous infrared populations.

7.2.4 Redshift determination of a large sample of strong foreground gravitational lenses

Gravitational lensing is a powerful approach to measuring the stellar mass and dark matter profiles of galaxies. The most accurate measurements of gravitational mass at cosmological redshifts are made through lensing (measuring the mass within the Einstein radius). Moreover, the statistics of gravitational lensing are a strong constraint on galaxy evolution, determining the number and mass evolution of galaxies. Cold Dark Matter (CDM) models predict significant substructure in the haloes of galaxies, and if such structures have no associated star formation, their existence can only be inferred at cosmological distances from gravitational lensing (e.g. Mao & Schneider 1998).

Indeed, the substructure implied by the failure of smooth (unstructured) mass models in around half the known lenses may even exceed the CDM predictions. The gravitational amplification of background objects also allows observations of populations that would otherwise be inaccessibly faint, and since lensing is wavelength-independent, this advantage extends to every observable wavelength. Lensing also conserves surface brightness, so flux magnification implies angular size magnification.

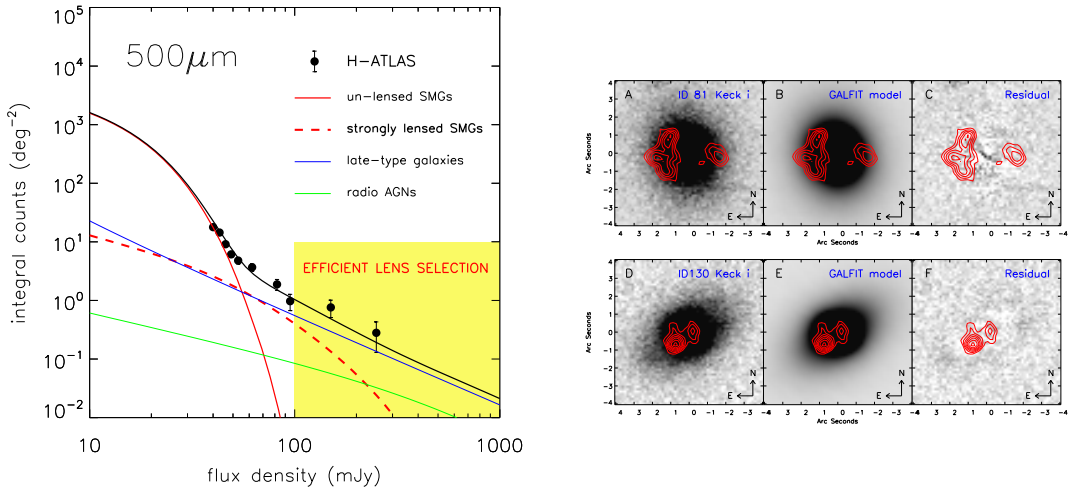

Figure 7.5: Left panel: demonstration of the pioneering lens selection technique comparing H-ATLAS data to a source count model. Galaxies which are sufficiently bright at submm wavelengths are either strong gravitational lenses, late-type local galaxies or radio AGN; the latter two categories are easy to filter out using supplementary data leaving only the lenses. Right panels: optical (i-band) imaging from the Keck telescope of two of our lens candidates (greyscale), compared to submm-wave interferometry from the Sub-Millimetre Array (red contours). There are no significant residuals in the optical image compared to a simple local galaxy model, while the submm morphology is very different. Figures from Negrello et al. (2010).

In practice however, it has proved very difficult to assemble large samples of lenses. The ATLAS team have recently discovered that submm-wave surveys of bright galaxies are ideal for selecting for strong gravitational lenses (Negrello et al. 2010). The negative submm K-correction means that submm sources are generally at redshifts $z \geq 1$ with flux density depending on luminosity but largely independent of redshift. The selection function is therefore both very well-constrained and simple. The steep submm source counts observed at $250-1300\,\mu$m ($\mathrm{d}N/\mathrm{d}S_\nu \propto \nu^{-\beta}$ with $\beta \simeq 3-4$), together with the strong evolution of submm galaxies, give bright submm surveys a high optical depth to gravitational lensing and a strong magnification bias. Models predicted $\sim 35\%$ of bright submm galaxies (e.g. $S_{500\mu\mathrm{m}} > 100\,\mathrm{mJy}$) to be strong gravitational lenses (see Fig.7.5). The other source populations contributing to the source counts are easily distinguished from (lensed and unlensed) proto- spheroidal galaxies. Essentially all conventional radio sources that are detected in the submm are flat- spectrum blazars, already known from low-frequency surveys such as NVSS, FIRST, SUMSS and PMN. The starburst and normal late-type galaxies should be easily identified in the optical; those with $> 100\,\mu$Jy at $500\,\mu$m are at $z \ll 1$ and therefore already in IRAS and AKARI all-sky catalogues. However, high-z dusty galaxies are expected to be very faint in the optical. After removing these other populations, one is left with a sample almost exclusively made of strongly lensed sources, that is, one expects a selection efficiency for such sources close to an

astonishing 100 per cent. For comparison, the Cosmic Lens All Sky Survey (CLASS) found 22 gravitational lens systems amongst over 16000 radio sources.

This was spectacularly confirmed by the demonstration (Negrello et al. 2010) of a near-100% selection efficiency for strong lenses in ATLAS (Fig.7.5). The ATLAS team predict at least ~ 3000, 1600 and 700 strongly lensed proto-spheroids at 250, 350 and 500 μm respectively in the completed ATLAS. This survey will also be able to make indirect constraints on the surface density of (unlensed) high-z dusty galaxies with fluxes $10\times$ lower than the survey limit of $45-53$ mJy at $250-500\,\mu$m (10 is the predicted mean magnification), and deeper than the fundamental blank-field Herschel submm confusion limit of ~ 20 mJy.

The key advantage of this lens selection is that it is sensitive to lensing galaxies at much higher redshifts ($0 < z \lesssim 2$) than other surveys, allowing us to observe directly the build-up of stellar mass and its interplay with dark matter halos over $\sim 70\%$ of the history of the Universe. Fig.7.6 shows the lens redshift histogram for the optically-selected SLACS lenses, the radio-selected CLASS/MG lenses, and the submm-selected lenses from ATLAS and the SCUBA-2 All-Sky Survey (SASSy).

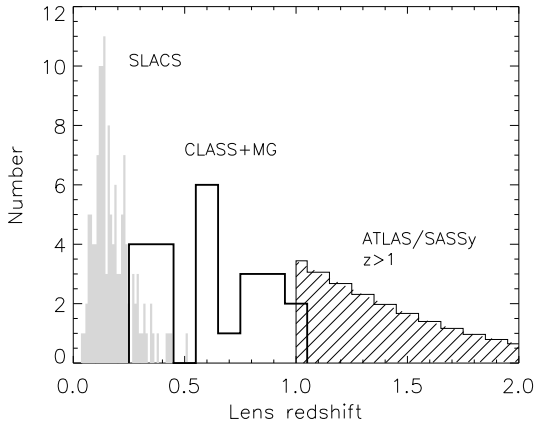

Figure 7.6: Redshift histogram of the known CLASS lenses and the SLACS lenses, combined with the predicted lens histogram of submm-selected lenses.

However, despite the high lens selection efficiency, it is still necessary to conduct multi-wavelength follow-up to prove the systems are lenses. The two submm-selected lenses studied in detail so far are entirely invisible in observed-frame optical imaging and spectroscopy (Negrello et al. 2010), but careful modelling of *Spitzer* lensing galaxies imaging reveals residuals remarkably similar to the submm interferometry of the background sources (Hopwood et al. 2010 arXiv:1011.4940). Is this likely for all submm-selected lenses? Although possible, it is unlikely, given the existence of rest-frame ultraviolet emission lines in $8-10$m-class spectroscopy of least some 850 μm-selected submm galaxies (Chapman et al. 2005a), suggestive of complex dust obscuration morphologies with cavities exposing the ionized gas. 8m-class spectroscopy of the lensing systems will be the

only way to simultaneously extract the redshifts of the lenses and test for the presence of emission lines in the background lensed population.

7.3 Proposed Survey and its Requirements

7.3.1 Baseline Survey Plan

Full Success Level Survey / Main Sample: approximately one-third of entire Herschel-ATLAS galaxies (more than 70,000 expected) in the NGP field with SDSS $r_{\rm AB} \leq 22.4$ mag – 22,000 250 μm detected sources in 150 deg^2. Based on the SDP($\sim$14 deg^2) data the redshift range of this Main Sample is estimated to be $z = 0.3 - 0.5$ (Dye et al. 2010), photometric redshift based on optical-NIR multi-colors). Assuming the FoV of PFS is larger than 1.5 deg^2 and five FoV can be observed per night, the required observing nights is estimated to be 20 nights.

The Main Sample is quite unique, large sample of dusty galaxies with far-IR and submm SEDs beyond $z \sim 0.3$. Not only the NGP, but also H-ATLAS galaxies in the GAMA fields($\delta \simeq 0$deg) may be included as the Main Sample since the depths of the current GAMA survey is $r_{\rm AB} \leq 19.8$ mag (Driver et al. 2009).

Extra Success Level Survey / Secondary Sample: at the time of commisioning of PFS (around 2018 and later), deep, wide-field optical images may be available for the entire ATLAS fields ($sim550$ deg^2). The total number of ATLAS sample is expected to be more than 250,0000 galaxies($\sim$ 500 sources per square degree). A model prediction of their redshift distribution is around $z \sim 1$. The optical magnitude distribution is unknown so far, but from the experience of mid-IR selected dusty galaxy sample obtained from the AKARI deep survey, about half of the entire ATLAS sample is $r_{\rm AB} \leq 24$ mag, hence the optical spectroscopic follow-up is not impossible with 8-m telescope if the throughput of PFS is ≥ 10 parcent. Once this is realized, the proposal science goals will be achieved at $z \sim 1$ violent epoch.

7.3.2 Instrument Requirements

The required specifications of PFS to achieve the science goals described here are summarized as below.

- **Field-of-view:** to survey the entire ATLAS field in reasonable observing nights, more than 1.5 deg^2 is preferable.
- **number of fibers:** more than 500 fibers per square degree, given the surface density of the ATLAS sources.
- **throughput:** the sensitivity is most important key issue for the spectroscopic follow-up for the dusty, red galaxies. Since the throughput of the Keck/DEIMOS is $\sim$40% with more than 200 slits, the degraded throughput (say 10%) of PFS would mean the loss of the advantage in the survey speed over the Keck/DEIMOS.

- wavelength coverage: the baseline coverage (3900-10800A) is sufficient for the active galaxies(AGN and starburst) at z=0.3-0.5, but when one attempt to extend the spectroscopy of $z \sim 1$ sources longer extension (upto 1.3 μm) is preferable to observe [O III], which is likely to be stronger than [O II] in the low-metalicity and intense star-forming environment.

7.4 Synergy with SPICA

SPICA (Space Infrared Telescope for Cosmology and Astrophysics, Nakagawa (2010)) is a space observatory that will provide imaging and spectroscopic capabilities in the 5 to 210 μm wavelength range with 3-m class telescope like *Herschel*, but with unprecedented sensitivity thanks to the cold telescope (<6 K) and advanced instrument suite. SPICA will cover the missing 28 to 60 μm wavelength which is out of the *Herschel* and JWST domains. To reduce the mass of the whole mission, SPICA will be launched at ambient temperature and cooled down on orbit by mechanical coolers on board with an efficient radiative cooling system, a combination of which allows us to have such a large, cooled telescope in space with moderate total weight (3.7t). SPICA is a Japanese-led, international mission with significant contribution from ESA and a European consortium, and Korea. US participations is also being discussed extensively. The target launch year of SPICA is Japanese FY2018, which is well matched to the commission of Subaru/PFS.

SPICA will be between one and two orders of magnitude more sensitive than *Herschel* in the far-infrared spectroscopy, and a few orders of magnitude faster than existing space telescopes in the imaging surveys. Namely, SPICA will be able to carry out blind far-infrared spectroscopic surveys of the violent epoch, which, together with optical diagnostic study with Subaru/PFS, will lead to the first statistically unbiased determination of the co-evolution of star-formation and mass accretion with cosmic time.

Also notable is a imaging survey speed of SPICA: One of the main contributors to a large variation among results from the AKARI and Spitzer in Fig.7.1 is the cosmic variance due to the small field of views of Spitzer/AKARI deep surveys. Similar to the Hershel-ATLAS in the submillimeter, superb sensitivity of the SPICA allows us to survey unprecedentedly large area ($\sim 100\,deg^2$) in the mid and far-infrared, providing us with a large enough area to overcome the cosmic variance. In conclusion, a combination of Subaru/PFS and SPICA is expected to bring a complete understanding of cosmic star formation history and AGN evolution in the violent epoch of the universe.

References

Babbedge, T. S. R. et al., 2006, *MNRAS*, 370, 1159
Balogh, M. et al., 2004, *MNRAS*, 348, 1355
Boyle, B. J., & Terlevich, R. J., 1998, *MNRAS*, 293, L49
Caputi, K. I. et al., 2007, *ApJ*, 660, 97
Chapman, S. C., Blain, A. W., Smail, I., & Ivison, R. J., 2005a, *ApJ*, 622, 772
Chapman, S. C., Ibata, R., Lewis, G. F., Ferguson, A. M. N., Irwin, M., McConnachie, A., & Tanvir, N., 2005b, *ApJL*, 632, L87
Driver, S. P. et al., 2009, Astronomy and Geophysics, 50, 050000
Dunne, L., & Eales, S. A., 2001, *MNRAS*, 327, 697
Dye, S. et al., 2010, *A&A*, 518, L10+

Eales, S. et al., 2010, *PASP*, 122, 499
Elbaz, D. et al., 2007, *A&A*, 468, 33
Farrah, D., Serjeant, S., Efstathiou, A., Rowan-Robinson, M., & Verma, A., 2002, *MNRAS*, 335, 1163
Franceschini, A., Hasinger, G., Miyaji, T., & Malquori, D., 1999, *MNRAS*, 310, L5
Franceschini, A., Rodighiero, G., & Vaccari, M., 2008, *A&A*, 487, 837
Genzel, R. et al., 1998, *ApJ*, 498, 579
Goto, T. et al., 2010, *A&A*, 514, A6+
Granato, G. L., Silva, L., Lapi, A., Shankar, F., De Zotti, G., & Danese, L., 2006, *MNRAS*, 368, L72
Gruppioni, C. et al., 2010, *A&A*, 518, L27+
Hughes, D. H. et al., 1998, *Nature*, 394, 241
Kauffmann, G., White, S. D. M., Heckman, T. M., Ménard, B., Brinchmann, J., Charlot, S., Tremonti, C., & Brinkmann, J., 2004, *MNRAS*, 353, 713
Lagache, G., Abergel, A., Boulanger, F., Désert, F. X., & Puget, J., 1999, *A&A*, 344, 322
Le Floc'h, E. et al., 2005, *ApJ*, 632, 169
Madau, P., Ferguson, H. C., Dickinson, M. E., Giavalisco, M., Steidel, C. C., & Fruchter, A., 1996, *MNRAS*, 283, 1388
Magnelli, B., Elbaz, D., Chary, R. R., Dickinson, M., Le Borgne, D., Frayer, D. T., & Willmer, C. N. A., 2009, *A&A*, 496, 57
Magorrian, J. et al., 1998, *AJ*, 115, 2285
Mao, S., & Schneider, P., 1998, *MNRAS*, 295, 587
Merritt, D., & Ferrarese, L., 2001, *ApJ*, 547, 140
Nakagawa, T., 2010, in Society of Photo-Optical Instrumentation Engineers (SPIE) Conference Series, Vol. 7731, Society of Photo-Optical Instrumentation Engineers (SPIE) Conference Series
Negrello, M. et al., 2010, Science, 330, 800
Pérez-González, P. G. et al., 2005, *ApJ*, 630, 82
Puget, J., Abergel, A., Bernard, J., Boulanger, F., Burton, W. B., Desert, F., & Hartmann, D., 1996, *A&A*, 308, L5+
Rowan-Robinson, M. et al., 1991, *Nature*, 351, 719
Schiminovich, D. et al., 2005, *ApJL*, 619, L47
Serjeant, S. et al., 2010, *A&A*, 518, L7+
Serjeant, S., Farrah, D., Geach, J., Takagi, T., Verma, A., Kaviani, A., & Fox, M., 2003, *MNRAS*, 346, L51
Smail, I., Chapman, S. C., Blain, A. W., & Ivison, R. J., 2004, *ApJ*, 616, 71
Smail, I., Ivison, R. J., & Blain, A. W., 1997, *ApJL*, 490, L5+
Spoon, H. W. W., Marshall, J. A., Houck, J. R., Elitzur, M., Hao, L., Armus, L., Brandl, B. R., & Charmandaris, V., 2007, *ApJL*, 654, L49
Symeonidis, M., Page, M. J., Seymour, N., Dwelly, T., Coppin, K., McHardy, I., Rieke, G. H., & Huynh, M., 2009, *MNRAS*, 397, 1728
Treister, E., Urry, C. M., & Virani, S., 2009, *ApJ*, 696, 110
Vaccari, M. et al., 2010, *A&A*, 518, L20+
van Kampen, E. et al., 2005, *MNRAS*, 359, 469

8 High Redshift Galaxies

Masami Ouchi (Tokyo), Kazuhiro Shimasaku (Tokyo), Yen-Ting Lin (IPMU), et al.

8.1 Summary

We will carry out an unprecedentedly large area deep spectroscopic survey with PFS for Lyman break galaxies (LBGs) and Lyα emitters (LAEs) at $z = 2 - 7$ in the HSC ~ 30 deg^2 deep and ultra deep survey fields. Exploiting the large LBG and LAE samples that can be made by no other existing and planned surveys, we will address four fundamental questions about 1) mass assembly of massive galaxies, 2) chemical/dynamical evolution of star-forming galaxies, 3) galaxy, AGN, and proto-cluster formation in large-scale structures, and 4) neutral-hydrogen fraction evolution and topology of ionized bubble, that are key for understanding galaxy formation, structure formation, and cosmic reionization.

8.2 Science Drivers

8.2.1 Mass assembly of massive galaxies

Galaxy mass assembly process is the major question of galaxy formation. In the hierarchical structure formation models, galaxy merging is a likely process which drives the mass assembly of galaxies in the early stage of galaxy evolution. For $z < 1$, there are many observations of the merger rate (e.g., Bundy et al. 2009; Conselice et al. 2009; de Ravel et al. 2009; Jogee et al. 2009; Bridge et al. 2010; Lin et al. 2010), although the results have not necessarily converged well. On the other hand, observations of galaxy merging beyond $z \sim 1$ are still very limited due to increasing difficulties in identifying close pairs and detecting morphological features of merging (e.g., Ryan et al. 2008; Bluck et al. 2009; Cooke et al. 2010). As well as to mass assembly, galaxy merging is likely to be related to active phenomena such as starburst and AGN. Measuring the merger rate at $z > 1$ is also important in this sense, because such active phenomena are most commonly seen for galaxies at $z > 1$ and they should have played a crucial role in galaxy evolution. Merger rate measurements over a wide redshift range will also constrain galaxy formation models in which the merger rate is one of the key but very poorly constrained parameters (e.g., Hopkins et al. 2010).

Recently, the importance of cold accretion has been emphasized in the models of massive galaxy formation (Keres et al. 2005; Dekel & Birnboim 2006). Dense cold gas with a temperature of $1 - 5 \times 10^4$ K (Goerdt et al. 2010) penetrates the hot gas reservoir of massive dark matter halos,

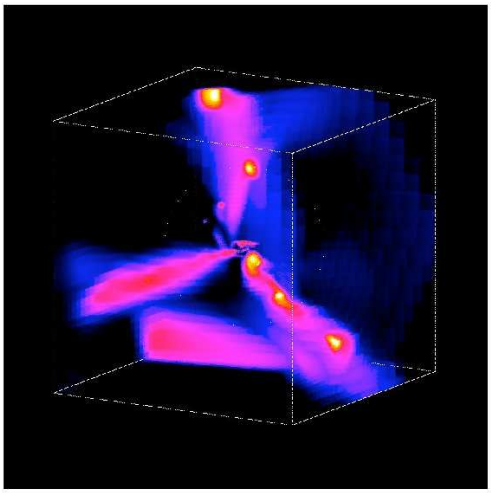

Figure 8.1: Cold accretion predicted by hydrodynamical simulations of Dekel et al. (2009). The colors denote inflow rate per solid angle at the centers of cubic-grid cells. The dotted circle indicates the virial radius of the halo. The size of the box is 320 kpc in a side.

and triggers efficient star-forming activities. Hydrodynamical simulations indicate that only one-third (in mass) of the accreting gas is in clumps which lead to mergers with a mass ratio greater than 1:10, and that the rest of the mass is in the form of smooth flows of cold gas (Figure 8.1; Dekel et al. 2009). Although it is theoretically expected that cold accretion is potentially a key process of mass assembly in the young universe, so far there is no convincing evidence reported observationally. Steidel et al. (2010) claim that there is little evidence of cold accretion based on 89 LBGs at $z \sim 2$ with an Hα line for systemic velocity and UV low-ionization metal absorption lines for cold gas. Figure 8.2 presents the distribution of velocities of metal absorption lines shifted from the systemic velocity. All galaxies have the velocity of metal absorption lines redshifted by $< +200$ kms^{-1} that is predicted by cold accretion models. The velocity is rather blue shifted, which is indicative of outflow. However, Faucher-Giguere & Keres (2010) argue that the absorption lines can be found only in $1-2\%$ of LBGs, due to a very small covering factor of cold accretion streams. We thus need to significantly improve the statistics to the level that can identify a rare signal of cold accretion, if any. A wide-survey will provide a number of bright LBG/LAE pairs for which the cold accretion as well as mergers can be studied.

We will select close pairs of bright LBGs and LAEs from the samples constructed from the HSC Deep and Ultra Deep Survey data, measure their redshifts with PFS with accuracies of < 100 km s^{-1}, and calculate merger fractions up to $z \sim 6$. For lower redshifts ($z \sim 2-5$) where large samples will be available, we calculate merger fractions for different stellar masses and star formation rates.

At a redshift range of $z \simeq 2.1-2.5$ where [Oii], inter-stellar metal, and Lyα lines can be observed at the same time with PFS, we will obtain ~ 2000 LBGs with [OII] lines for systemic velocities

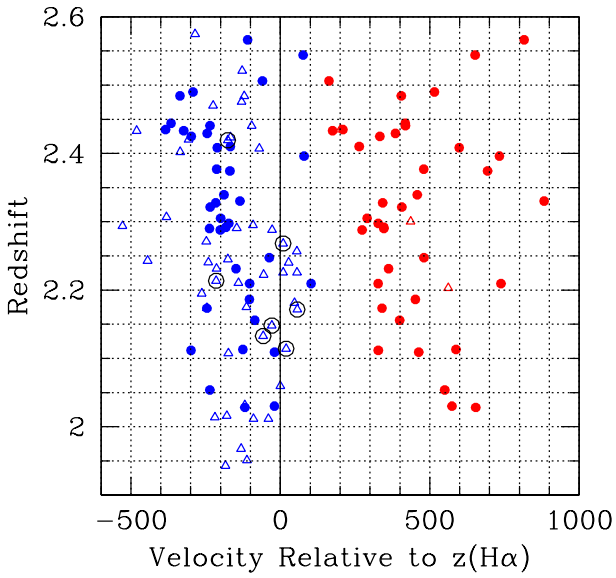

Figure 8.2: Velocities of interstellar absorption lines (blue) and Lyα emission lines (red) relative to the systemic velocities determined with Hα (Steidel et al. 2010).

($v_{\rm [OII]}$) as well as gas velocities of Lyα ($v_{\rm Ly\alpha}$) and UV absorption lines ($v_{\rm abs}$). We will investigate the rare cold-gas inflow signature, and test the cold accretion hypothesis with this sample about 20 times larger than the one of Steidel et al. (2010).

Lyα line profiles obtained by the medium high spectral resolution of $R \sim 3000$ are very useful to constrain models of galaxy inflow and outflow. Tapken et al. (2007) have found that 3 out of 16 high-z galaxy spectra show a double-peaked Lyα profile. They claim that an expanding shell model can explain these double-peaked as well as normal-asymmetric Lyα profiles. However, only a handful number of Lyα profiles are investigated to understand star-formation and feedback associated with outflows and infalls (e.g., Dijkstra et al. 2007). Moreover, it is also suggested that strong Lyα emission lines may be explained by Neufeld's clumpy cloud model (Neufeld 1991). The strong Lyα emission could be produced by the selective, differential dust extinction of UV continuum and Lyα emission. The UV continuum is absorbed through the cores of dusty interstellar (IS) clouds, while Lyα emission might survive by scattering off these same clouds. (e.g., Finkelstein et al. 2008; Kobayashi et al. 2010). However, there is no observational evidence yet to support this model. A clear signature of outflows or infalls can be found with systemic velocities determined by nebular lines, which allows us to investigate the velocity shift of the Lyα line from IS clouds. We will measure a redshift of [OII] line, $z_{\rm [OII]}$, with the IR arm of PFS, and compare it with that of Lyα line, $z_{\rm Ly\alpha}$, from the blue arm of PFS for galaxies at $z = 2.1 - 2.5$. If we find a significant velocity difference between Lyα ($z_{\rm Ly\alpha}$) and [OII] ($z_{\rm [OII]}$), it is unlikely that the Lyα emission undergoes a number of scattering off clumpy IS clouds with random motions as suggested by Neufeld (1991). Outflows and infalls are also investigated in a statistical manner with UV metal absorption lines. We will find galaxy-galaxy or galaxy-AGN close pairs, and make sets of composite spectra of background galaxies/AGN, referring a redshift of foreground galaxies, as a function of angular distance. We will measure average equivalent widths and velocities of UV metal absorption lines for various angular distance, i.e. impact parameter, which is already demonstrated

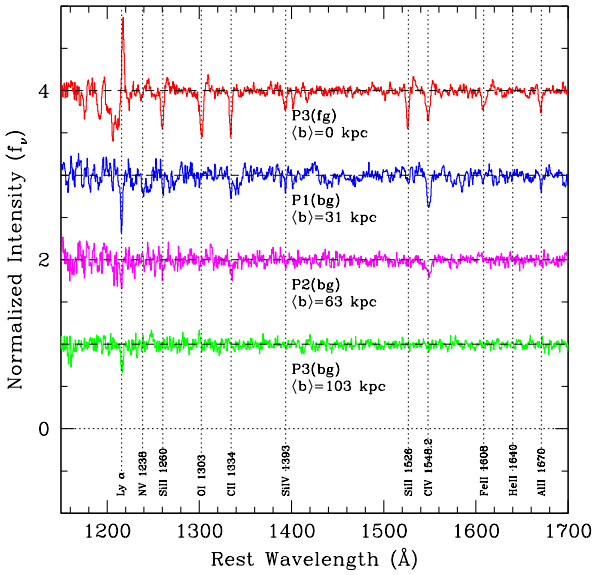

Figure 8.3: Composite spectra of galaxy-galaxy pairs obtained from the sample of Steidel et al. (2010). The top spectrum is the composite of all foreground galaxies that form pairs. The second, third, and forth spectra are composites of all background galaxies whose separation from the foreground galaxies are $< 5''$ ($\langle b \rangle = 31$ kpc), $5'' - 10''$ ($\langle b \rangle = 63$ kpc), and $10'' - 15''$ ($\langle b \rangle = 103$ kpc), respectively, where $\langle b \rangle$ is an average impact parameter.

in Steidel et al. (2010) (Figure 8.3). Our LBG samples are more than an order of magnitude larger than those of Steidel et al. (2010). It will allow us to investigate mass dependence of outflows and infalls with velocities of gas outflow/inflow and geometries of cold and hot gas distributions, assuming a spherical symmetry. We will understand the relation between starbursts and outflows, and to test the star-formation quenching hypothesis for massive galaxies that is necessary to form red-and-dead galaxies like today's ellipticals.

We will also study the mass assembly history of star-forming galaxies by clustering analysis. We use SFR functions from UV LFs, stellar mass functions, and two-point correlation functions (CFs) of LBGs and LAEs over $z \sim 2 - 7$, to reveal star formation and stellar-mass assembly in dark-matter haloes in the early stage of galaxy evolution when the cosmic star formation activity rises with time.

The LBG and LAE samples are constructed from the data to be taken in the HSC Deep and Ultra Deep Surveys over 30 deg^2. Redshifts will then be measured with PFS with accuracies of ~ 100 km s^{-1} for all bright galaxies and for a significant fraction of faint galaxies. The SFR functions are derived from UV luminosity functions after correction for dust extinction, while the masses of dark haloes hosting the galaxies can be inferred from the CFs using the trend inherent in the CDM-based structure formation model that more massive dark haloes are clustered more strongly (e.g., Mo & White 1996). Applying the halo occupation distribution and conditional luminosity function prescriptions (Berlind & Weinberg 2002; Bullock et al. 2002) to the CFs, SFR functions, and stellar mass functions, we derive the mass of hosting dark haloes as a function of the SFR and stellar mass of galaxies. We also derive the average number and spatial distribution of galaxies in single dark haloes.

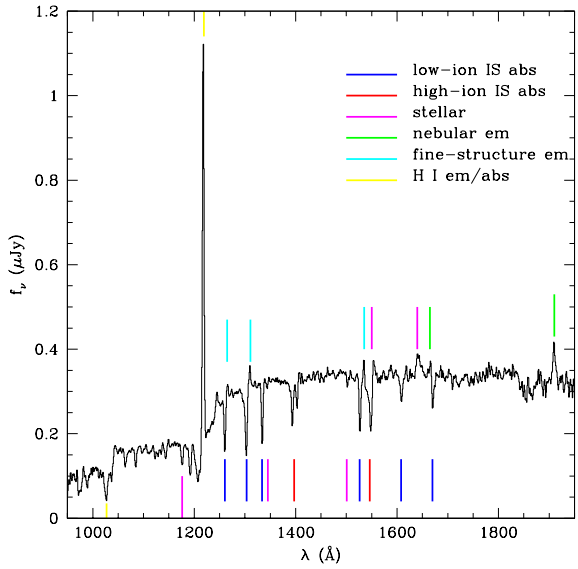

Figure 8.4: The composite rest-frame UV spectrum constructed from 1000 LBGs at $z = 3$ obtained by Shapley et al. (2003). Tick marks indicate the UV emission and absorption features made by stellar photospheric and wind, interstellar low- and high-ionization absorption, nebular emission from H II.

From these analyses we can empirically describe star formation, merging, and cold accretion processes of galaxies in different dark haloes. These results can be used to test galaxy formation models which still have a number of unconstrained parameters in star formation (including its suppression) and merging (e.g., Bower et al. 2010) and help to infer what physical mechanisms dominate in determining galaxy mass assembly in different mass ranges in the early stage of galaxy evolution.

To do these analyses, large samples from wide and deep photometric surveys supplemented with spectroscopic redshifts are essential. Large samples ($N > 10^4$ objects) from cosmological volumes ($> 10^6$ Mpc^3) are required to derive accurate CFs on small scales of less than $\sim 10''$ where the one-halo term dominates and good statistics are needed (Ouchi et al. 2005a), and on large scales where variations due to large-scale structure are expected to be large. Spectroscopic redshifts are necessary to convert angular correlation functions into spatial correlation functions, as well as studying the distribution and kinematics of galaxies in single haloes.

While the relationship between dark haloes and galaxies has been studied well for present-day galaxies (e.g., Zehavi et al. 2004), observations at high redshifts are very limited. In particular, small-scale clustering, i.e., the one-halo term, of LBGs has been detected only at $z \sim 3-5$ (Ouchi et al. 2005a; Kashikawa et al. 2006; Lee et al. 2006; Hildebrandt et al. 2007). There is no study for LAEs due to small sample sizes and survey volumes. Our study will for the first time give a complete census on the connection between dark haloes and two major star-forming galaxy populations (LBGs and LAEs) over a long time span in the early stage of galaxy evolution.

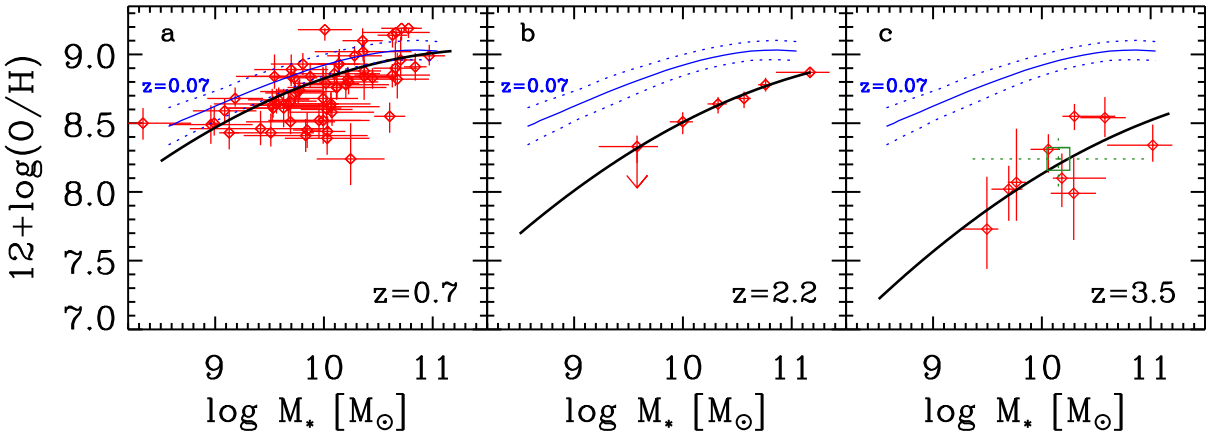

Figure 8.5: Mass-metallicity relation (red circles) obtained at $z = 0.7$ (left; Savaglio et al. 2005) at $z = 2.2$ (center; Erb et al. 2006), and at $z = 3.5$ (right; Maiolino et al. 2008) presented in Maiolino et al. (2008). The local ($z = 0.07$) mass-metallicity relation and its error are shown with a blue line and blue dotted lines, respectively (Kewley & Ellison 2008). The black lines are the best fitting models to the mass-metallicity relations at each redshift. In the right panel, the green square with error bars denotes the average mass and metallicity of the $z = 3.5$ sample.

8.2.2 Chemical and dynamical evolution of intense star-forming galaxies

Unveiling chemical evolution of galaxies is key for understanding their past star-formation activities, because chemical evolution depends on various star-formation parameters including initial mass function (IMF), star-formation history, and gas recycling. To date, mass-metallicity relation is reasonably well determined only at $z < 4$ (Maiolino et al. 2008; cf. Ando et al. 2007) and limited to massive galaxies (Figure 8.5), and no hints of chemical evolution for galaxies at the early galaxy formation stage. Based on composites of our PFS spectra, we will extend the redshift range up to $z \sim 6$ down to a low mass to understand the earlier stage of galaxy formation with the UV metal absorption lines measured with PFS. We will give constraints on metallicity with IS metal absorption lines in UV continuum with 1425 index (Rix et al. 2004), CIV index (Mehlert et al. 2002), and empirical relation of local star-bursts (Heckman et al. 1998; see also Ando et al. 2007). The UV metal absorption lines of these high-z galaxies are too faint to be mostly identified on an individual basis, but in the composite spectra of more than 10,000 LBGs and LAEs. Even with the faintest 10% subsample consisting of, at least, 1,000 LBGs and LAEs, the stacking of spectra will gain a S/N of 30 ($= \sqrt{1000}$), allowing us to obtain a typical spectrum of extremely faint galaxies with the same quality as the one taken with a $\sim$ 250m-diameter aperture telescope. Because our LBG/LAE samples are about $10 - 100$ times larger than the one of Shapley et al. (2003) (Figure 8.4) and Ando et al. (2007), we can investigate the dependence of metalliciy as a function of Lyα luminosity and EW with $10 - 100$ bins, keeping a S/N ratio as high as those of Shapley et al. (2003).

Another important question related to chemical evolution of galaxies is Lyα emission physics. The physical origins of the strong Lyα nature of high-z galaxies are poorly understood. Theoretical models suggest that strong Lyα emission of star-forming galaxies can be produced by hard UV continuum from massive stars, and that galaxies with EW(Lyα) $\gtrsim$ 50Å are either metal poor and/or extremely young galaxies (Schaerer 2003). A problem however is that comparison of LAE

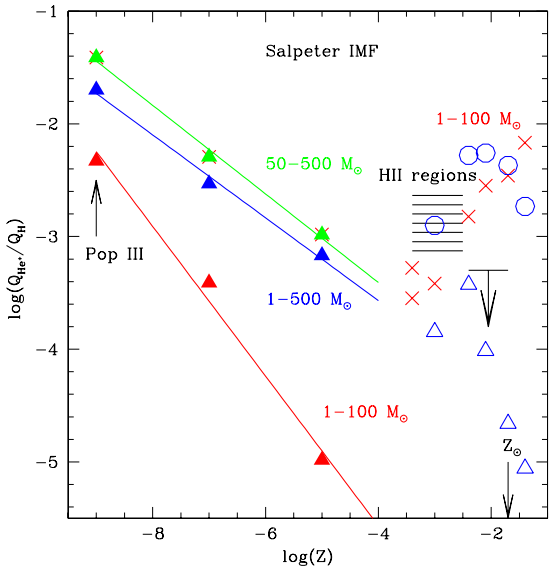

Figure 8.6: Hardness of the ionising flux that is proportional to the flux ratio of HeII to Lyα lines as a function of metallicity predicted by Schaerer (2003). Three IMFs for popIII starbursts are considered.

SEDs with stellar synthesis models cannot constrain not only dust extinction, but also metallicity and age at the same time with a given photometric accuracy, due to strong degeneracy between the two quantities (e.g., Ono et al. 2010a). So far, no metallicity measurements, but only upper limits (Finkelstein et al. 2010), for LAEs have been obtained, but only for LBGs.

If LAEs are a very metal poor population such made of Population III (PopIII) stars, a moderately strong HeIIλ1640 emission with a small velocity dispersion (200-300km s^{-1}) would be found (Schaerer 2003). Ouchi et al. (2008) have reported no detection of HeII emission line in their composite-UV spectra of about 30 LAEs (see also Dawson et al. 2004), and concluded no signature of PopIII stars at the levels of $f_{\rm HeII}/f_{\rm Ly\alpha} = 0.02$ and 0.06 for $\langle z \rangle = 3.13$ and 3.68 LAEs, respectively. On the other hand, Jimenez & Haiman (2006) claim that the composite-UV spectrum of $z \sim 3$ dropout galaxies shows a broad HeIIλ1640 emission possibly originated by massive PopIII stars. Since the signal-to-noise ratio (S/N) is critical in this analysis, we need to increase the number of spectra at least by a factor of 4 (i.e. 120 LAEs) via our PFS program to test the massive PopIII scenario for LAEs with the HeII flux based on the ratio of $f_{\rm HeII}/f_{\rm Ly\alpha}$ down to ~ 0.001, which is low enough to test the PopIII ($Z\odot < 10^{-8}$) scenario with a reasonable choice of IMF (Figure 8.6; Schaerer 2003).

8.2.3 Galaxy, AGN, and proto-cluster formation in large scale structures at the early stage

At low redshifts, galaxy populations in clusters are characterized by the presence of a red sequence with small scatter in galaxy color, indicative of old stellar population with little or no star formation activity, with either synchronized star formation history, or early epoch of star formation (or both; e.g., Stanford et al. 1998). Studies up to $z \sim 1.5$ have repeatedly confirmed the existence of the

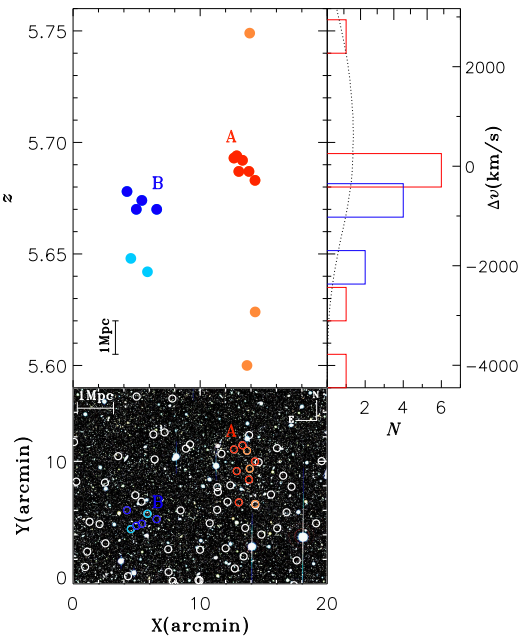

Figure 8.7: Three dimensional map around the proto-clusters (Ouchi et al. 2005b) for the transverse vs. redshift directions (top) and the projection on the sky (bottom). The red and blue circles indicate LAEs associated with the proto-clusters. Black circles plotted on the bottom panel denote the positions of LAEs without spectroscopic redshift. The red and blue histograms correspond to LAEs around each proto-cluster.

red sequence, and the suppression of star formation with respect to lower density environments (e.g., Koyama et al. 2007; Tanaka et al. 2008; Strazzullo et al. 2010).

The color evolution of the red sequence further suggests a formation redshift $\gtrsim 2-3$. Clusters at this redshift range thus hold key to the formation of the majority of (massive) galaxy populations of the local clusters. Hereafter we will refer to overdense, massive ($> 10^{13} M_{\odot}$) galactic systems whose properties are consistent with being progenitors of low-z clusters as "proto-clusters".

As we approach the epoch when the massive cluster galaxies are expected to form, both the existence of the red sequence and the suppression of star formation should break down. A recent study of a $z = 1.62$ cluster reported the finding that the cluster core is populated by many galaxies with high star formation rate (Tran et al. 2010). Hilton et al. (2010) also found evidence of enhanced star formation activity in cluster center, for a system at $z = 1.46$. As there are only a few spectroscopically confirmed clusters at $z > 1.5$, it is not clear whether they are representative. Clearly, a large proto-cluster sample at $z \gtrsim 2$ will be needed to reveal the star formation and mass assembly history of the cluster galaxies.

To date, most of the proto-clusters were discovered by targeted observations of tracers of massive galaxy populations, or as overdense regions within large-scale structures, both requiring extensive supplementing imaging and spectroscopy (Figure 8.7; e.g., Ouchi et al. 2005b; Steidel et al. 2005). A tracer population proved to be highly efficient are high-z radio galaxies (HzRGs; Miley & De Breuck 2008). For example, six out of eight HzRGs observed by Venemans et al. (2007) turned out to be overdense with Lyα emitters at similar redshifts as the HzRGs. These authors estimated that

maybe 75% of powerful HzRGs are hosted in proto-clusters. It is not clear, however, how many proto-clusters contain HzRGs.

Kodama et al. (2007) conducted a near-IR photometric study of proto-clusters at $z = 2 - 3$. It is found that the bright end of the red sequence in $z \sim 2$ proto-clusters is already established, while much less so for the $z \sim 3$ ones. They identified the epoch $z = 2 - 3$ as when the massive galaxies formed through vigorous star formation and merger activities.

Environmental dependence of galaxy formation is also seen in the $z \sim 2$ proto-clusters. For example, both Steidel et al. (2005) and Tanaka et al. (2010) found evidence that the star formation history is accelerated in dense regions, compared to the field at similar redshifts. This is consistent with theoretical expectations, as well as the results found for $z \gtrsim 1.5$ clusters.

With the PFS survey, we expect to significantly increase the number of proto-clusters, thus advancing our knowledge of the formation of most massive galaxies. The most unique aspect of the PFS $z > 2$ survey is that we can *spectroscopically* search for overdensities of LAEs and/or LBGs, which provide a candidate sample of proto-clusters that can be further followed up. Furthermore, it is likely the HSC-deep fields will overlap with the deep fields of LOFAR survey, which would allow us to cross correlate the $z \gtrsim 2$ HzRGs with the LAEs/LBGs. Galaxies surrounding the candidate proto-clusters would then be targeted by the PFS. Therefore, we will have a census of proto-clusters of LAEs/LBGs, and we could compare proto-clusters thus selected with those hosting HzRGs.

As the proto-clusters represent rare peaks in the initial density field, their formation history is expected to vary dramatically; it is thus critical to have a large sample. Together with the need to overcome the cosmic variance (e.g., Overzier et al. 2009), large area (at least ~ 30 deg^2) is needed.

The spectroscopy would allow us to investigate several pressing issues related to proto-clusters, including:

- Is star formation history really accelerated in proto-clusters? Studies in favor or against such a viewpoint both exist in the literature (Steidel et al. 2005; Tanaka et al. 2010; Kuiper et al. 2010; Peter et al. 2007; Overzier et al. 2008). With the large, unbiased sample provided by PFS, we could investigate this issue in a uniform fashion.

- Formation of brightest cluster galaxies (BCGs) in proto-clusters. From deep spectroscopy, we could identify multiple components in the proto-BCGs, thus examining their merger/assembly history (Cooke et al. 2008). Furthermore, we would check the claim that proto-BCGs are often associated with Lymanα blobs (Prescott et al. 2008), and gain insights into the early formation of most massive galaxies.

- Spectroscopic identification of massive, passively evolving population of proto-cluster members. Theoretical models suggest that in early times, central galaxies in massive halos may acquire gas in cold, dense filaments and experience intense star formation, while the star formation in satellite galaxies may be quenched due to environmental effects (Dekel & Birnboim 2006). Many of the HzRGs in proto-clusters, being the central galaxy, are indeed forming

stars vigorously (Stevens et al. 2003); it remains to be seem if the idea of satellite quenching at $z \sim 2$ is valid. Currently there is only one passive galaxy that is spectroscopically confirmed to be companions of HzRGs.

- Are HzRG-selected proto-clusters typical? Do all proto-clusters contain a central radio galaxy? With the HSC and PFS data, we could look for proto-cluster candidates that lack a central radio source, which will not only help us answer these questions, but also provide insights into the ignition of the central engines in the HzRGs. As the PFS deep fields likely contain deep X-ray data, we could stack the proto-clusters and examine the mean X-ray luminosity for proto-clusters with and without a HzRG.

- The rich multi-wavelength data existing in our survey fields, together with the detailed spectroscopic follow up, facilitate the study of AGN content in proto-clusters (e.g., Croft et al. 2005).

- Are the properties of the HzRGs correlated with the proto-clusters? Due to the current sample size, it is not possible to draw definitive conclusions. With the spectroscopic data from PFS, we could examine if any correlation exists between the radio power, stellar mass, or star formation history of HzRGs and the velocity dispersion, spatial distribution of members of the host proto-clusters.

- Characterization of environmental dependence in galaxy formation. Observations show that different galaxy populations (e.g., LAEs, LBGs, distant red galaxies) have different spatial distribution within the proto-clusters, and the spatial segregation is consistent with more massive galaxies being more centrally concentrated (e.g., De Breuck et al. 2004; Overzier et al. 2006; Kodama et al. 2007). There are also suggestions that the differential spatial distribution may be caused by strong ionizing sources, such as QSOs and HzRGs (Kashikawa et al. 2007; Utsumi et al. 2010). We will examine these findings with the large proto-cluster sample offered by PFS; if confirmed, the detailed characterization of such segregation from our data would provide stringent constraints on galaxy formation models.

8.2.4 Cosmic reionization

Understanding physical process of cosmic reionization is one of the major goals in astronomy today. Although the increase of Gunn-Peterson (GP) optical depths may be contiguous from low z to $z > 6$ (Becker et al. 2007), the evolution of GP optical depths clearly show the steep rise at $z \sim 6$ towards high-z (Fan et al. 2006). On the other hand, Dunkley et al. (2009) find that the CMB polarization data of WMAP for Thomson scattering optical depth place the constraints that instantaneous reionization at the late epoch below $z = 8.2$ (6.7) is rejected at the 2σ (3σ) level, and claim that the reionization process would be extended at $z \sim 6 - 11$ (see also Larson et al. 2010 for the latest WMAP7 results). However, physical models would not easily reproduce such a long extended reionization due to the rapid recombination of hydrogen (e.g., Fukugita & Kawasaki 1994; Cen 2003). Observational measurements on neutral hydrogen fraction of inter-galactic medium (IGM) at $z \sim 6 - 11$ are the missing pieces in this cosmological puzzle.

Because QSO GP test can be applied only to IGM with a very small neutral hydrogen fraction, $x_{\rm HI} < 10^{-4} - 10^{-3}$, due to saturation of IGM absorption, the GP test can probe the last stage

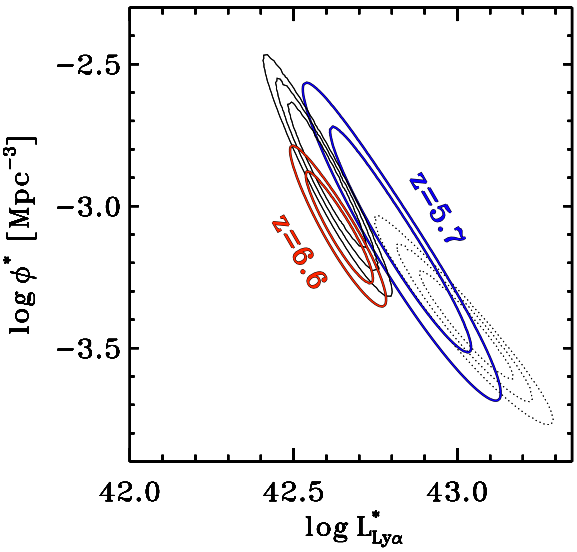

Figure 8.8: Error ellipses of Schechter parameters, $L^*_{\mathrm{Ly}\alpha}$ and ϕ^*, derived from the largest $z = 6.6$ and 5.7 LAE samples (Ouchi et al. 2010, 2008). Red and blue contours represent the fit of $z = 6.6$ and 5.7 LFs, respectively, with the fixed slope of $\alpha = -1.5$ based on a total of 1 deg^2 data of SXDS (and SDF for $z = 6.6$). The inner and outer contours indicate 68% and 90% confidence levels, respectively, which include cosmic variance errors. The error ellipses of the $z = 5.7$ LF are larger than those of our $z = 6.6$ LF. This is because the data of $z = 5.7$ LF have more uncertainties of cosmic variance. Black solid and dotted lines indicate 1, 2, and 3 sigma confidence levels of $z = 6.6$ and $z = 5.7$ LFs with no cosmic variance errors derived solely with the smaller data of SDF (Kashikawa et al. 2006).

of cosmic reionization up to $z \sim 6$. The optical depth measured from the CMB is the integral of Thomson scattering of free electrons along the line of sight, there is no time resolution to constrain reionization history.

An alternative probe is the absorption of Lyα damping wing. The neutral hydrogen of IGM absorbs Lyα emission line of LAEs via Lyα damping wing, and dim Lyα luminosity, which is identified in the evolution of Lyα emitters (e.g., Malhotra & Rhoads 2004; Kashikawa et al. 2006; Iye et al. 2006; Ota et al. 2008). The probe of Lyα damping wing can be applied to gamma ray bursts (GRBs; Totani et al. 2006). Although GRBs do not need detailed models of galaxies and reionization to derive x_{HI} from their spectra, the estimates of a small number of GRBs would include an additional systematic error, up to $\delta x_{\mathrm{HI}} \sim 0.3$, owing to the patchiness of reionization (McQuinn et al. 2008). A large number of widely distributed LAEs will provide complementary estimates of $\delta x_{\mathrm{HI}} \sim 0.3$. Moreover, the observed LAEs will correlate with the inhomogeneous distribution of ionized bubbles that allow Lyα lines escape through the IGM. Thus, LAE distribution gives constraints on the topology of ionized bubbles.

Hu & Cowie (2006) report that no significant change of Lyα luminosity function (LF) from $z = 5.7$ to 6.6, while the study of Kashikawa et al. (2006) claims that Lyα LF evolves from $z = 5.7$ to 6.6. There are two conclusions from these $z = 6.6 - 7.7$ studies, no evolution and a decrease of Lya LF, which do not agree with each other. Recent studies of Ouchi et al. (2010) and Hu et al. (2010) have confirmed that the Lyα LF decreases from $z = 5.7$ to 6.6 (Figure 8.8). However, the amount of decrease is not well constrained. The inferred neutral hydrogen frac-

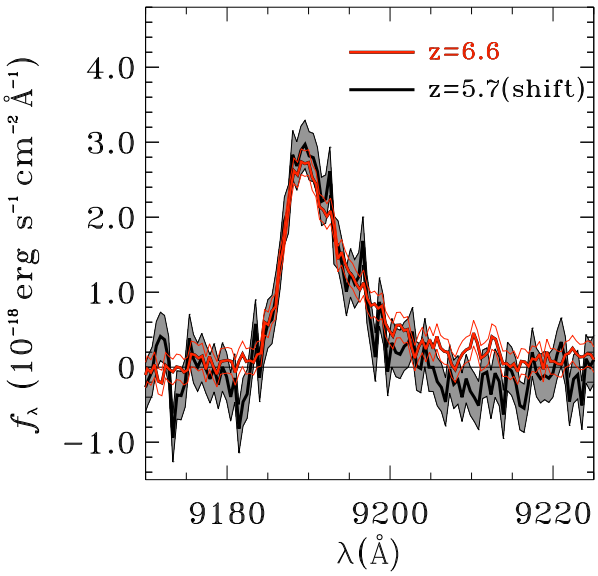

Figure 8.9: Evolution of Lyα line profiles (Ouchi et al. 2010). Red and black thick lines represent composite spectra of LAEs at $z = 6.6$ and 5.7, respectively. For comparison of line shapes, the composite spectrum of the $z = 5.7$ LAEs is redshifted to $z = 6.6$, and scaled by an arbitrary factor. One sigma errors of the composite spectra are shown with thin red lines for $z = 6.6$ LAEs and a gray shade for $z = 5.7$ LAEs.

tion is $x_{\rm HI} = 0.2 \pm 0.2$ whose error is about twice larger than the systematic uncertainties of reionization model dependencies ($\delta x_{\rm HI} = 0.1$; Ouchi et al. 2010). This large statistical error of neutral hydrogen fraction cannot distinguish between more than half ionized and neutral universe at the 2σ confidence level. It is also important to constrain reionization with other independent observational quantities. The stacked spectra of $z = 6.6$ LAEs show no clear signal of evolution from $z = 5.7$ (Figure 8.9; Ouchi et al. 2010; Hu et al. 2010). The average FWHM velocity width does not largely evolve from $z = 5.7$ to 6.6 beyond the measurement errors of 14% (Ouchi et al. 2010). Similarly, the average IGM absorption of Lyα emission can be evaluated with Lyα escape fraction ($f_{\rm esc} = SFR[f_{\rm Ly\alpha}]/SFR$[intrinsic]; Ono et al. 2010b) and Lyα emitting galaxy fraction (Stark et al. 2010a,b). These constraints are important for modeling cosmic reionization and duty-cycle/stochasticity of Lyα emission (Nagamine et al. 2008), because the models cannot predict Lyα fluxes without priori assumptions (e.g., Kobayashi et al. 2010), due to complicated processes underlying Lyα emission and scattering. Since Lyα lines of galaxies residing in ionized bubbles selectively escape from the partially neutral universe, clustering amplitude of observed LAEs would be boosted at the epoch of reionization (EoR; Furlanetto et al. 2006; McQuinn et al. 2007; Lidz et al. 2009; cf. Iliev et al. 2008). Although a clustering signal of $z = 6.6$ LAEs is identified (Figure 8.10), it appears no significant boost of clustering amplitude given by cosmic reionization, which gives an upper limit of $x_{\rm HI} < 0.5$. However, the errors of clustering measurement is large. A moderately large change of clustering in $\Delta b \sim 1 - 2$ cannot be identified in the present data. Moreover, such a poor constraint of clustering does not allow us to identify topology of ionized bubbles (McQuinn et al. 2007).

Studies of galaxies at the EoR, $z \gtrsim 6$, are essential not only for understanding cosmic reionization process but also galaxy formation history. The combination of Subaru and VLT wide-field cameras

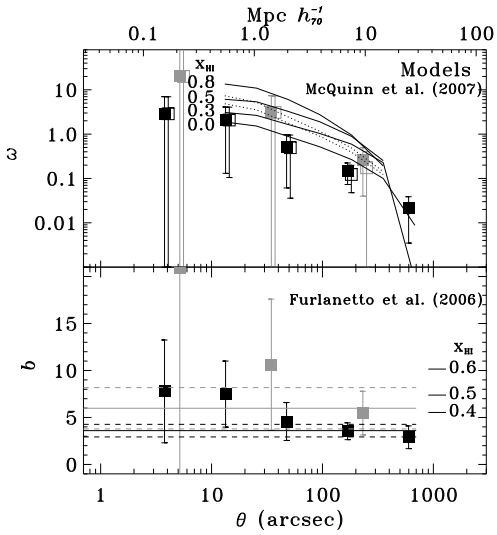

Figure 8.10: Comparison with clustering measurements of SXDS $z = 6.6$ LAEs and reionization models (Ouchi et al. 2010). Top panel presents ACFs, and bottom panels show bias as a function of angular distance. Black and gray filled squares are the estimates for the all ($NB921 < 26.0$) and the bright ($NB921 < 25.5$) LAEs. *Top* : Solid lines are the model predictions of McQuinn et al. (2007) for $z = 6.6$ LAEs whose hosting dark halo mass is $3 \times 10^{10} M_{\odot}$. Neutral fractions of the universe are $x_{\rm HI} = 0.0$, 0.3, 0.5, and 0.8 from bottom to top lines. Dotted lines indicate $z = 6.6$ LAEs with a dark halo mass of $7 \times 10^{10} M_{\odot}$ (bottom) and $1 \times 10^{11} M_{\odot}$ (top) in the case of $x_{\rm HI} = 0.0$. *Bottom* : At the right side of this plot, we present Furlanetto et al.'s (2006) predicted bias values. For clarity, we also plot the best-bias estimate and 1σ ranges for the bright ($NB921 < 25.5$) LAEs with gray solid and dashed lines, respectively.

and the newly-installed HST/WFC3 has identified a definitive decrease of UV-continuum luminosity function (LF) from $z = 6$ to $7 - 8$ (Ouchi et al. 2009; Oesch et al. 2010; Bouwens et al. 2010a; McLure et al. 2010; Castellano et al. 2010; Wilkins et al. 2010a; Bunker et al. 2010; Wilkins et al. 2010b; see also Hickey et al. 2010), which are being confirmed by spectroscopic observations (Lehnert et al. 2010; Fontana et al. 2010; Vanzella et al. 2010). Accordingly the star-formation rates drop roughly by an order of magnitude from its peak of $z = 2 - 3$ to $z = 7$. Because galaxies are thought to be sources of reionization, the decrease of UV LF would indicate that galaxies produce less UV ionizing photons towards high redshifts. The production rate of UV ionizing photons is close to balance with the recombination rate of hydrogen IGM at $z \sim 7 - 8$, and the reionization epoch may be near these redshifts. The other interpretation of the decrease of UV LF is that a moderately high ionizing photon escape fraction, $f_{\rm esc} \gtrsim 0.2$, is required to keep the universe ionized at $z \sim 7$ (e.g., Ouchi et al. 2009; Bunker et al. 2010). The faintest HST/WFC3 sources at $z \simeq 7 - 8$ show a very blue UV continuum slope possibly consistent with extremely young, metal-poor stellar populations, which is also suggestive of large escape fraction of $f_{\rm esc} \gtrsim 0.3$ (Bouwens et al. 2010b; see also Finkelstein et al. 2010), although there are claims that their UV continuum slope measurements include potentially large statistical and systematic uncertainties (Schaerer & de Barros 2010). The contribution from faint galaxies below the current observational limits is an open question. An accurate determination of LF slope, α, is key for estimating the contribution from such faint galaxies. Ouchi et al. (2009) claim that faint galaxies can produce ionizing photons enough for reionization at $z \sim 7$ with the slope steeper than $\alpha \simeq -1.9$. The present studies have obtain $\alpha = -1.9 - -1.7$ (Ouchi et al. 2009; McLure et al. 2010; Oesch et al. 2010; Bouwens et al. 2010a), while the errors of α are large. The faint-end LF is being investigated

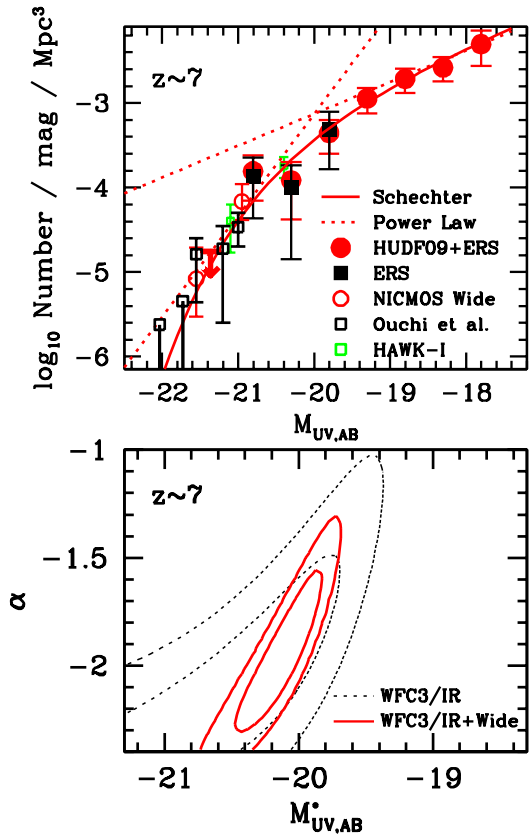

Figure 8.11: (*upper*) *Top* : UV LF at $z \sim 7$ presented in Bouwens et al. (2010a). The red circles, red arrow, and red line present LF determination from deep HST WFC3/IR data. Black open squares, red open circles, and green open squares represent LFs from a wide-area Subaru Suprime-Cam (Ouchi et al. 2009), NICMOS+ISAAC+MOIRCS (Bouwens et al. 2010a), and HAWK-I (Castellano et al. 2010) searches. The black squares denote the $z \sim 7$ LF from the ERS observations (Bouwens et al. 2010a). The dotted red lines show the linear fit of the $z \sim 7$ LF at the bright and faint ends. *Bottom* : 68% and 95% confidence levels on on the characteristic luminosity M^* and slope α solely from the deep HST WFC3/IR results (dotted lines) and from the combination of the HST WFC3/IR and the wide-area survey results (red lines). The inclusion of the bright-end LF from the wide-area search significantly improves the determination of α.

by the HUDF and CANDELS surveys. However, α determination cannot be improved only with deep and small-volume HST surveys, but with measurements of the bright-end luminosity function (Figure 8.11). Our PFS survey will derive the bright-end LF with a good accuracy that allow us to examine with the HST data whether the slope of α is steeper than -1.9.

To address these issues, we will use the data from PFS deep survey. We will conduct an extensive survey that is the largest ever performed in terms of area and number of objects. Our survey field is a large 30 deg^2 area of HSC deep survey fields. The combination of PFS spectra and HSC images will allow us to provide a large statistical sample of $\simeq 10,000$ LAEs at $z = 5.7 - 7.3$ down to $logL(Ly\alpha) \simeq 42.2 - 42.3$ in a large cosmic volume (0.9Gpc$\times$ 0.9Gpc $\times$ 40Mpc in total). With these unprecedentedly large samples, we will obtain measurements of $z = 5.7 - 7.3$ LAEs for constraining the existing and forthcoming cosmological models of cosmic reionization and galaxy formation. We will estimate the neutral hydrogen fraction down to $x_{\rm HI} \simeq 0.1$ at $z \sim 7$, equivalent

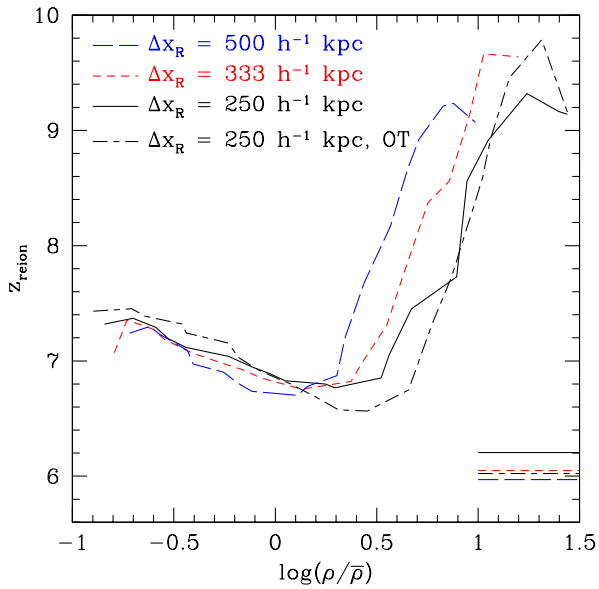

Figure 8.12: The predicted median redshift of reionization as a function of overdensity $\rho/\bar{\rho}$ (curves) and overlap redshift (horizontal lines) for different choices of resolution (Finlator et al. 2009). The black short dashed and long dashed curves represent the median redshifts in the case for 250 h^{-1} kpc with optically thin Eddington tensors.

to the uncertainties of model choices, from luminosity function evolution. The $x_{\rm HI}$ estimate of this accuracy will distinguish between the half (50%) neutral and ionized universe at $z \sim 7$. We will constrain topology of ionized regions at $z \sim 7$ from the LAE distribution and the spatial variance of Lyα profiles from composite spectra of subsamples of LAEs in a mesh of $\sim 20-30 Mpc$ smaller than a typical bubble size. We aim to constrain on reionization models, and to understand which reionization models, inside-out, outside-in, or filament-last, are plausible. Figure 8.12 presents the cosmic reionization model of a combination of radiative transfer and hydrodynamic simulations, and indicates that both overdense regions and voids are ionized earlier than intermediate-density region of filaments, owing to their high recombination rate and low emissivity (Finlator et al. 2009). Figure 8.12 infers that $z \sim 7$ is an important epoch to constrain the reionization process from observations. Our $z \sim 7$ LAE results from the large statistics will also serve as baselines for on-going and future studies of LAEs at $z > 7$ performed with the existing near-infrared imagers of VLT (Willis et al. 2008), Subaru (Tokoku et al. 2008), and VISTA (Nilsson et al. 2007) and the future facilities of JWST, E-ELT, GMT, and TMT.

8.3 Proposed Survey and its Requirements (Tentative Plan)

We propose a deep PFS survey for LBGs and LAEs at $z = 2-7$ to accomplish our four scientific goals shown above. Our target LBGs and LAEs are selected from the HSC deep and ultra-deep survey covering ~ 30 deg^2 area. We will take two sets of 6-hour integration spectra at one pointing of PFS. Based on the sensitivity calculations of Iwata et al., we will reach $f = 4.1 \times 10^{-18}$ erg s^{-1} cm^{-2} at the 5σ detection level, which is the average of the limiting fluxes of v(FWHM) = 200 km s^{-1} and v(FWHM) = 300 km s^{-1}, because the average v(FWHM) of LAEs is $250-260$ km^{-1}

(Ouchi et al. 2010). This detection limit will allow us to identify all of $z = 5.7-7.3$ LAEs found by the HSC surveys Similarly, we will achieve the continuum detection limit of $i'_{\rm AB} = 24.4$ at the 5σ detection level with the spectral resolution of $R \sim 1000$ by pixel binning. We will identify $\sim 30,000$ LBGs and $\sim 8,000$ LAEs at $z \sim 2-6$, and $\sim 10,000$ LAEs at $z = 5.7-7.3$, with their Lyα emission lines, UV metal absorption lines, and/or Lyman and Lyα continuum breaks. For LBGs, most of sources are identified by their Lyα lines, and UV continuum is detected only for bright (< 24.4 mag) sources. To calculate these expected numbers of LBG detections, we assume 30% for a ratio of Lyα emitting LBGs to all faint (≤ 24.4 mag) LBGs (Shapley et al. 2003; Stark et al. 2010b). We will find ~ 100 proto-clusters made of LAEs and LBGs, assuming the number density of proto-clusters given by the previous studies (Ouchi et al. 2005b). This PFS survey requires about 60 nights including the 70% of weather factor and 20% of overhead in case for $\simeq 20\%$ throughput of PFS. If the throughput is only 10%, it will take about 120 nights. Because our target LBGs and LAEs are obtained through the HSC survey planned to be carried out in 2012-2017, our PFS survey can be started after its commissioning in around 2016. We will use the unique large samples of high-z galaxies found by HSC imaging, especially by the unprecedentedly large narrow-band imaging program. Our survey will be the largest spectroscopic program (30 deg^2) focusing on $z > 2$ galaxies, covering more than 100 times wider areas of the sky than the existing deep spectroscopy surveys such as LBG (Steidel et al. 2003), VVDS deep (Le Fèvre et al. 2005), VLT/FORS GOODS-S (Vanzella et al. 2009), and 3D-HST (PI P. van Dokkum). EUCLID program would compete with some of our survey goals, using bright-continuum LBGs down to 24.5 mag at $z < 6$. However, the difference of wavelength coverage and spectral resolution between PFS and EUCLID will be rather complementary, extending the spectral coverage. No other spectroscopic surveys can conduct follow up spectroscopy for these HSC samples, due to the limited capabilities of the wide-area survey. JWST and ELT follow up takes impossibly long time, and Keck/DEIMOS observations will take about ~ 1000 nights for this program. At the time of our PFS survey in 2017-2022, next generation telescopes, such as JWST and ELT, will start their operations that will extend the redshift frontier from $z \sim 7-10$ to $z \sim 10-20$. Our PFS survey results will serve definitive baselines of luminosity functions, correlation functions at $z = 2-7$ that are very important to understand evolution of galaxies and reionization beyond $z > 7$.

Because we will push the faint limits of PFS performance, this survey requires good sensitivities with good sky subtraction. The high throughput (10-20%) is indispensable. Moreover, for good sky subtraction and less smearing of signals, we request a stability of spectrograph ideally as high as Keck/LRIS and DEIMOS.

References

Ando, M., Ohta, K., Iwata, I., Akiyama, M., Aoki, K., & Tamura, N., 2007, *PASJ*, 59, 717
Becker, G. D., Rauch, M., & Sargent, W. L. W., 2007, *ApJ*, 662, 72
Berlind, A. A., & Weinberg, D. H., 2002, *ApJ*, 575, 587
Bluck, A. F. L., Conselice, C. J., Bouwens, R. J., Daddi, E., Dickinson, M., Papovich, C., & Yan, H., 2009, *MNRAS*, 394, L51
Bouwens, R. J. et al., 2010a, ArXiv e-prints, 1006.4360
—, 2010b, *ApJL*, 708, L69
Bower, R. G., Vernon, I., Goldstein, M., Benson, A. J., Lacey, C. G., Baugh, C. M., Cole, S., & Frenk, C. S., 2010, *MNRAS*, 407, 2017
Bridge, C. R., Carlberg, R. G., & Sullivan, M., 2010, *ApJ*, 709, 1067

Bullock, J. S., Wechsler, R. H., & Somerville, R. S., 2002, *MNRAS*, 329, 246
Bundy, K., Fukugita, M., Ellis, R. S., Targett, T. A., Belli, S., & Kodama, T., 2009, *ApJ*, 697, 1369
Bunker, A. J. et al., 2010, *MNRAS*, 409, 855
Castellano, M. et al., 2010, *A&A*, 511, A20+
Cen, R., 2003, *ApJ*, 591, 12
Conselice, C. J., Yang, C., & Bluck, A. F. L., 2009, *MNRAS*, 394, 1956
Cooke, J., Barton, E. J., Bullock, J. S., Stewart, K. R., & Wolfe, A. M., 2008, *ApJL*, 681, L57
Cooke, J., Berrier, J. C., Barton, E. J., Bullock, J. S., & Wolfe, A. M., 2010, *MNRAS*, 403, 1020
Croft, S., Kurk, J., van Breugel, W., Stanford, S. A., de Vries, W., Pentericci, L., & Röttgering, H., 2005, *AJ*, 130, 867
Dawson, S. et al., 2004, *ApJ*, 617, 707
De Breuck, C. et al., 2004, *A&A*, 424, 1
de Ravel, L. et al., 2009, *A&A*, 498, 379
Dekel, A., & Birnboim, Y., 2006, *MNRAS*, 368, 2
Dekel, A. et al., 2009, *Nature*, 457, 451
Dijkstra, M., Lidz, A., & Wyithe, J. S. B., 2007, *MNRAS*, 377, 1175
Dunkley, J. et al., 2009, *ApJS*, 180, 306
Erb, D. K., Shapley, A. E., Pettini, M., Steidel, C. C., Reddy, N. A., & Adelberger, K. L., 2006, *ApJ*, 644, 813
Fan, X. et al., 2006, *AJ*, 132, 117
Faucher-Giguere, C., & Keres, D., 2010, ArXiv e-prints, 1011.1693
Finkelstein, S. L., Papovich, C., Giavalisco, M., Reddy, N. A., Ferguson, H. C., Koekemoer, A. M., & Dickinson, M., 2010, *ApJ*, 719, 1250
Finkelstein, S. L., Rhoads, J. E., Malhotra, S., Grogin, N., & Wang, J., 2008, *ApJ*, 678, 655
Finlator, K., Özel, F., Davé, R., & Oppenheimer, B. D., 2009, *MNRAS*, 400, 1049
Fontana, A. et al., 2010, ArXiv e-prints, 1010.2754
Fukugita, M., & Kawasaki, M., 1994, *MNRAS*, 269, 563
Furlanetto, S. R., Zaldarriaga, M., & Hernquist, L., 2006, *MNRAS*, 365, 1012
Goerdt, T., Dekel, A., Sternberg, A., Ceverino, D., Teyssier, R., & Primack, J. R., 2010, *MNRAS*, 407, 613
Heckman, T. M., Robert, C., Leitherer, C., Garnett, D. R., & van der Rydt, F., 1998, *ApJ*, 503, 646
Hickey, S., Bunker, A., Jarvis, M. J., Chiu, K., & Bonfield, D., 2010, *MNRAS*, 404, 212
Hildebrandt, H., Pielorz, J., Erben, T., Schneider, P., Eifler, T., Simon, P., & Dietrich, J. P., 2007, *A&A*, 462, 865
Hilton, M. et al., 2010, *ApJ*, 718, 133
Hopkins, P. F. et al., 2010, *ApJ*, 724, 915
Hu, E. M., & Cowie, L. L., 2006, *Nature*, 440, 1145
Hu, E. M., Cowie, L. L., Barger, A. J., Capak, P., Kakazu, Y., & Trouille, L., 2010, ArXiv e-prints, 1009.1144
Iliev, I. T., Shapiro, P. R., McDonald, P., Mellema, G., & Pen, U., 2008, *MNRAS*, 391, 63
Iye, M. et al., 2006, *Nature*, 443, 186
Jimenez, R., & Haiman, Z., 2006, *Nature*, 440, 501
Jogee, S. et al., 2009, *ApJ*, 697, 1971
Kashikawa, N., Kitayama, T., Doi, M., Misawa, T., Komiyama, Y., & Ota, K., 2007, *ApJ*, 663, 765
Kashikawa, N. et al., 2006, *ApJ*, 648, 7
Keres, D., Katz, N., Weinberg, D. H., & Dave, R., 2005, *MNRAS*, 363, 2
Kewley, L. J., & Ellison, S. L., 2008, *ApJ*, 681, 1183
Kobayashi, M. A. R., Totani, T., & Nagashima, M., 2010, *ApJ*, 708, 1119
Kodama, T., Tanaka, I., Kajisawa, M., Kurk, J., Venemans, B., De Breuck, C., Vernet, J., & Lidman, C., 2007, *MNRAS*, 377, 1717
Koyama, Y., Kodama, T., Tanaka, M., Shimasaku, K., & Okamura, S., 2007, *MNRAS*, 382, 1719
Kuiper, E. et al., 2010, *MNRAS*, 405, 969
Larson, D. et al., 2010, ArXiv e-prints, 1001.4635
Le Fèvre, O. et al., 2005, *Nature*, 437, 519
Lee, K., Giavalisco, M., Gnedin, O. Y., Somerville, R. S., Ferguson, H. C., Dickinson, M., & Ouchi, M., 2006, *ApJ*, 642, 63
Lehnert, M. D. et al., 2010, *Nature*, 467, 940
Lidz, A., Zahn, O., Furlanetto, S. R., McQuinn, M., Hernquist, L., & Zaldarriaga, M., 2009, *ApJ*, 690, 252
Lin, L. et al., 2010, *ApJ*, 718, 1158
Maiolino, R. et al., 2008, *A&A*, 488, 463

Malhotra, S., & Rhoads, J. E., 2004, *ApJL*, 617, L5
McLure, R. J., Dunlop, J. S., Cirasuolo, M., Koekemoer, A. M., Sabbi, E., Stark, D. P., Targett, T. A., & Ellis, R. S., 2010, *MNRAS*, 403, 960
McQuinn, M., Hernquist, L., Zaldarriaga, M., & Dutta, S., 2007, *MNRAS*, 381, 75
McQuinn, M., Lidz, A., Zaldarriaga, M., Hernquist, L., & Dutta, S., 2008, *MNRAS*, 388, 1101
Mehlert, D. et al., 2002, *A&A*, 393, 809
Miley, G., & De Breuck, C., 2008, A&ARv, 15, 67
Mo, H. J., & White, S. D. M., 1996, *MNRAS*, 282, 347
Nagamine, K., Ouchi, M., Springel, V., & Hernquist, L., 2008, ArXiv e-prints, 0802.0228
Neufeld, D. A., 1991, *ApJL*, 370, L85
Nilsson, K. K., Orsi, A., Lacey, C. G., Baugh, C. M., & Thommes, E., 2007, *A&A*, 474, 385
Oesch, P. A. et al., 2010, *ApJL*, 709, L16
Ono, Y. et al., 2010a, *MNRAS*, 402, 1580
Ono, Y., Ouchi, M., Shimasaku, K., Dunlop, J., Farrah, D., McLure, R., & Okamura, S., 2010b, ArXiv e-prints, 1004.0963
Ota, K. et al., 2008, *ApJ*, 677, 12
Ouchi, M. et al., 2005a, *ApJL*, 635, L117
—, 2009, *ApJ*, 706, 1136
—, 2005b, *ApJL*, 620, L1
—, 2008, *ApJS*, 176, 301
—, 2010, *ApJ*, 723, 869
Overzier, R. A. et al., 2008, *ApJ*, 673, 143
Overzier, R. A., Guo, Q., Kauffmann, G., De Lucia, G., Bouwens, R., & Lemson, G., 2009, *MNRAS*, 394, 577
Overzier, R. A. et al., 2006, *ApJ*, 637, 58
Peter, A. H. G., Shapley, A. E., Law, D. R., Steidel, C. C., Erb, D. K., Reddy, N. A., & Pettini, M., 2007, *ApJ*, 668, 23
Prescott, M. K. M., Kashikawa, N., Dey, A., & Matsuda, Y., 2008, *ApJL*, 678, L77
Rix, S. A., Pettini, M., Leitherer, C., Bresolin, F., Kudritzki, R., & Steidel, C. C., 2004, *ApJ*, 615, 98
Ryan, Jr., R. E., Cohen, S. H., Windhorst, R. A., & Silk, J., 2008, *ApJ*, 678, 751
Savaglio, S. et al., 2005, *ApJ*, 635, 260
Schaerer, D., 2003, *A&A*, 397, 527
Schaerer, D., & de Barros, S., 2010, *A&A*, 515, A73+
Shapley, A. E., Steidel, C. C., Pettini, M., & Adelberger, K. L., 2003, *ApJ*, 588, 65
Stanford, S. A., Eisenhardt, P. R., & Dickinson, M., 1998, *ApJ*, 492, 461
Stark, D. P., Ellis, R. S., Chiu, K., Ouchi, M., & Bunker, A., 2010a, *MNRAS*, 408, 1628
Stark, D. P., Ellis, R. S., & Ouchi, M., 2010b, ArXiv e-prints, 1009.5471
Steidel, C. C., Adelberger, K. L., Shapley, A. E., Erb, D. K., Reddy, N. A., & Pettini, M., 2005, *ApJ*, 626, 44
Steidel, C. C., Adelberger, K. L., Shapley, A. E., Pettini, M., Dickinson, M., & Giavalisco, M., 2003, *ApJ*, 592, 728
Steidel, C. C., Erb, D. K., Shapley, A. E., Pettini, M., Reddy, N., Bogosavljević, M., Rudie, G. C., & Rakic, O., 2010, *ApJ*, 717, 289
Stevens, J. A. et al., 2003, *Nature*, 425, 264
Strazzullo, V. et al., 2010, *A&A*, 524, A17+
Tanaka, M. et al., 2008, *A&A*, 489, 571
Tanaka, M., Finoguenov, A., & Ueda, Y., 2010, *ApJL*, 716, L152
Tapken, C., Appenzeller, I., Noll, S., Richling, S., Heidt, J., Meinköhn, E., & Mehlert, D., 2007, *A&A*, 467, 63
Tokoku, C. et al., 2008, in Astronomical Society of the Pacific Conference Series, Vol. 399, Astronomical Society of the Pacific Conference Series, T. Kodama, T. Yamada, & K. Aoki, ed., pp. 65–+
Totani, T., Kawai, N., Kosugi, G., Aoki, K., Yamada, T., Iye, M., Ohta, K., & Hattori, T., 2006, *PASJ*, 58, 485
Tran, K. et al., 2010, *ApJL*, 719, L126
Utsumi, Y., Goto, T., Kashikawa, N., Miyazaki, S., Komiyama, Y., Furusawa, H., & Overzier, R., 2010, *ApJ*, 721, 1680
Vanzella, E. et al., 2009, *ApJ*, 695, 1163
—, 2010, ArXiv e-prints, 1011.5500
Venemans, B. P. et al., 2007, *A&A*, 461, 823
Wilkins, S. M., Bunker, A. J., Ellis, R. S., Stark, D., Stanway, E. R., Chiu, K., Lorenzoni, S., & Jarvis, M. J., 2010a, *MNRAS*, 403, 938

Wilkins, S. M., Bunker, A. J., Lorenzoni, S., & Caruana, J., 2010b, ArXiv e-prints, 1002.4866
Willis, J. P., Courbin, F., Kneib, J., & Minniti, D., 2008, *MNRAS*, 384, 1039
Zehavi, I. et al., 2004, *ApJ*, 608, 16

9 QSO (AGN) science with PFS

Masatoshi Imanishi (NAOJ), Masayuki Akiyama (Tohoku), Yoichi Itoh (Kobe), Toshihiro Kawaguchi (Tsukuba), Tomoki Morokuma (Tokyo), Tohru Nagao (Ehime), and based on scientific discussion inside the HSC QSO (AGN) team

9.1 Science Goals

The main science driver of QSO (AGN) [1] study using PFS is undoubtedly the follow-up spectroscopy of QSO candidates at $z = 3 - 7$ found through the Subaru Hyper-Suprime-Cam (HSC) survey. The proposed HSC wide survey will cover >1000 deg^2 with g, r, i, z, y filters (Figure 9.1), with the limiting magnitudes of (g, r, i, z, y) = (26.3, 26.0, 26.0, 24.9, 23.8) in AB.

Previous systematic 2dF (Croom et al. 2004) and SDSS (Richards et al. 2009) QSO surveys have found >20,000 and >800,000 QSOs, respectively. However, due to the shallow limiting magnitudes and limited wavelength coverage (z-band is the longest band) of these surveys, it is poorly understood (1) how is the faint end of the QSO luminosity function at $z > 3$, and (2) how many QSOs are present at $z > 6.5$. Thanks to the high sensitivity and the availability of the longest y-band (1 μm or 10,000Å) filter, the proposed Subaru HSC wide survey data will include **many faint (= intrinsically less luminous) QSOs at z > 3**, and **push the QSO redshift barrier from z ∼ 6.4 to z ∼ 7**. Since the number density of bright QSOs has a peak at $z = 2 - 3$ (Richards et al. 2006) (Figure 9.2), the redshift range of $z > 3$ is thought to correspond to the *growing-up phase* of supermassive black holes (SMBHs), and so the understanding of $z > 3$ QSOs in a wide luminosity range is extremely important to understand the evolution of SMBHs and the nature of QSO phenomena in the universe.

By finding many faint QSOs at $z > 3$, we can derive the faint end of the QSO luminosity function, using which the QSO contribution to the cosmic ionizing UV background radiation can be *directly* estimated from observations. Based on numerous faint QSOs at $z > 3$, (1) the clustering properties between QSO-QSO and QSO-galaxy can be investigated in a quantitatively detailed manner, and (2) we can derive the growth history of SMBHs in a wide QSO luminosity range, both of which will help understand the physical origin, triggering mechanism, and life time of QSO phenomena. Additionally, since QSOs are intrinsically much brighter than normal star-forming galaxies, these $z > 3$ QSOs can serve as an excellent probe to study the cosmic chemical evolution history and the physical conditions of the foreground intergalactic medium, through medium to high dispersion spectroscopy with sufficient S/N ratios. Finally, by discovering the most distant (highest-z) bright QSOs at $z > 6.5$, we can constrain the formation theory of SMBHs in the early universe most

[1] Active Galactic Nuclei (AGNs) are objects whose radiative energy is dominated by mass-accreting supermassive blackholes (SMBHs) with masses >$10^6 M_\odot$. QSOs are conventionally defined as luminous AGNs.

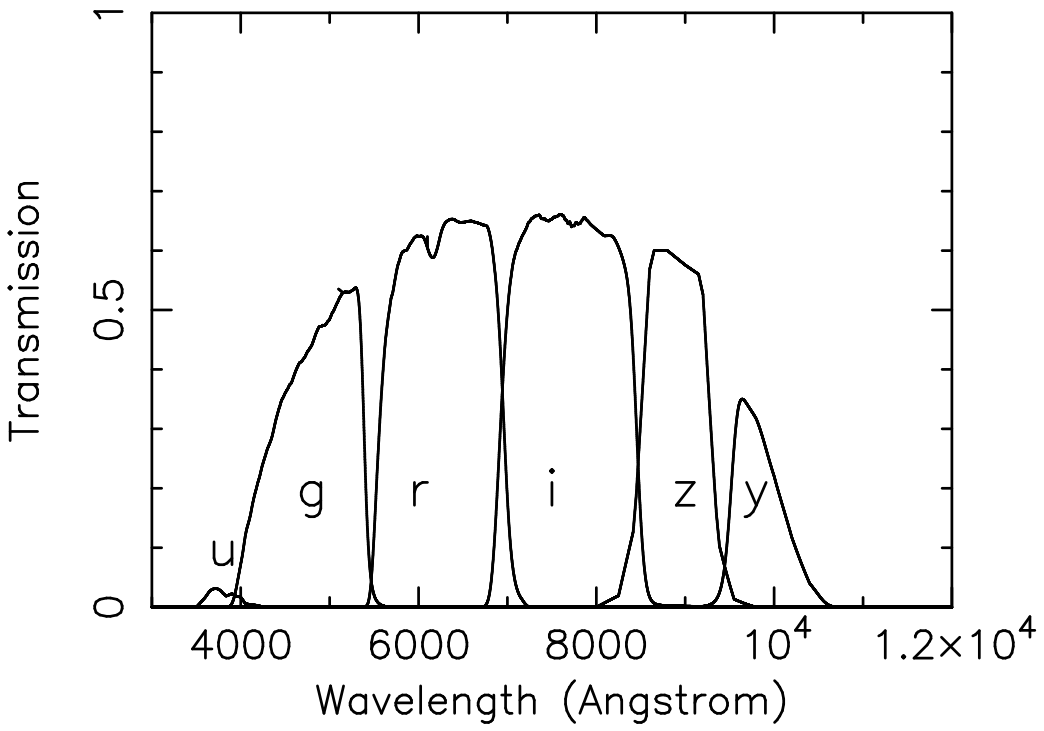

Figure 9.1: HSC filter set (g, r, i, z, y). The abscissa is observed wavelength in Å, and the ordinate is transmission.

strongly. For more details about these HSC-based high-z QSO science cases, please refer to the HSC white paper.

Although so many exciting QSO sciences are possible based on the proposed HSC wide survey, without spectroscopy, the HSC-detected sources are only *candidates* of high-z QSOs. Spectroscopic confirmation as bona-fide high-z QSOs, by disentangling from other contaminants (e.g., Galactic cool stars and normal star-forming galaxies at lower-z), and the redshift identification of these QSOs are at least required to achieve these science goals in a quantitatively convincing manner (to the community outside the HSC team). Unfortunately, the number of HSC-detected QSO candidates is so large (particularly at $z = 3 - 6$) that it is practically impossible to do follow-up spectroscopy of all (or bulk) of them, with currently available spectrographs.

Specifically, based on our *conservative* estimate, the HSC wide survey data are expected to include the following number of QSOs at each redshift.

- $\sim$35 QSOs per 1000 deg^2 at $z > 6.5$ ($y < 23.8$ mag in AB)
- $\sim$350 QSOs per 1000 deg^2 at $z \sim 6$ ($z < 24.2$ mag in AB)
- $\sim$30–650 QSOs per 1 deg^2 at $z = 3 - 5.5$ ($i < 24$ mag in AB)

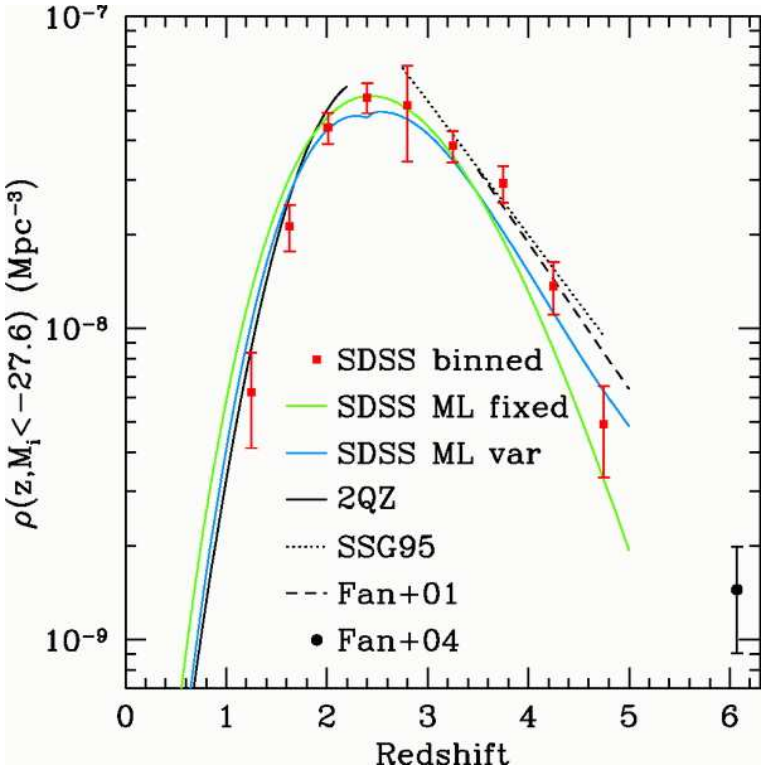

Figure 9.2: Integrated i-band luminosity function of QSOs (with $M_i < -27.6$) as a function of redshift (Richards et al. 2006). The number density of luminous QSOs shows a peak at $z = 2 - 3$, suggesting that the main growing-up phase of SMBHs in the universe is at $z > 3$.

These numbers are for bona-fide QSOs at each redshift, and there are likely to be contaminants by a factor of a few to several. Hence, the number of QSO *candidates* found in the HSC wide survey will be a factor of a few to several larger. Based on these number density estimates, while targeted spectroscopy is feasible for $z > 6.5$ QSO candidates, PFS (2400 fibers per 1.5 deg^2) will play a crucial role for the systematic follow-up spectroscopy of QSO *candidates* at $z = 3 - 6$.

We summarize these PFS-based important science cases below.

1. QSO luminosity function at $z < 6$
2. Clustering properties and environments of QSOs at $z < 6$
3. Evolution of SMBHs at $z < 6$
4. Cosmic chemical evolution at $z < 6$
5. Identification of further QSOs at $z > 6$
6. Ancillary brown dwarf science
7. Optical-variability-selected low-luminosity AGNs (HSC deep field)

Throughout this manuscript, we assume the following PFS parameters.

- spectral resolution: R $\sim$ 3000
- wavelength coverage: 3800–13,000Å(Blue: 3800–6700Å, Red: 6500–10,000Å, NIR: 9800–13,000Å)
- the number of fibers: $\sim$2400
- throughput (in total): 20% at the peak wavelength
- field of view (FOV) : 1.5 deg^2
- fiber size: 1.2" in diameter

For the exposure time calculations, we use the sensitivity table provided by Dr. Iwata (Figure 9.3). The baseline limiting magnitudes we adopt (in AB; S/N = 5; 2Å spectral resolution; 15 min exposure time) are 22.6 mag (blue), 22.2 mag (red), and 21.8 mag (NIR). We assume that (1) PFS spectroscopy of faint QSOs is background-limited, particularly at the long wavelength range of our interest, and (2) the S/N ratio will improve by a factor of $\sqrt{n}$, by binning n spectral elements or with n times longer exposure time. In the optical band, quoted magnitudes are in all cases in AB.

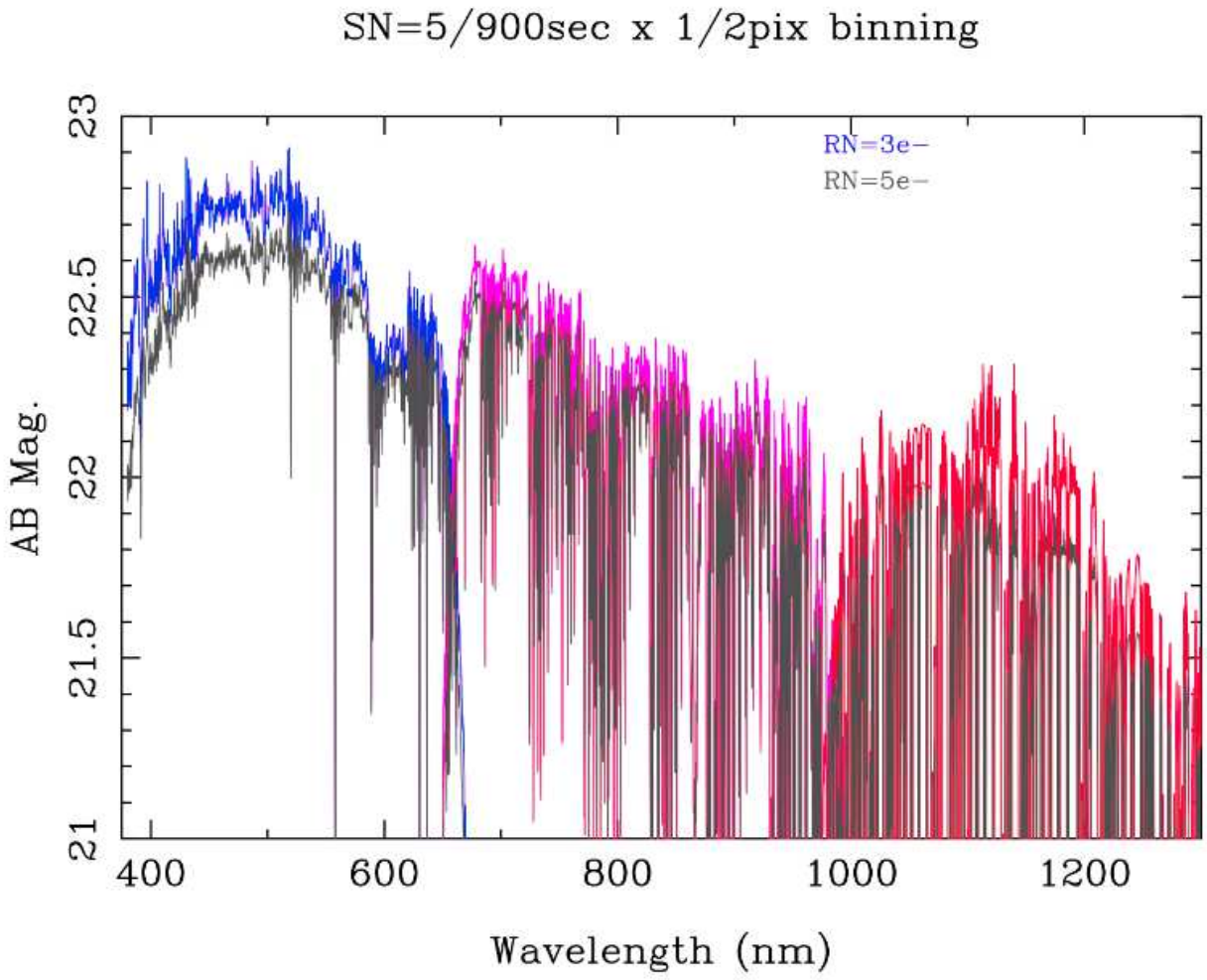

Figure 9.3: Expected PFS sensitivity as a function of observed wavelength, calculated by Dr. Iwata. The abscissa is observed wavelength in Å. The ordinate is the AB magnitude for which S/N =5 will be achieved in 900 sec (15 min) net on-source exposure time, with 2Å spectral resolution (R $\sim$ 4000 at 8000Å).

9.2 QSO Luminosity Function at $z < 6$

Although the SDSS survey has discovered many QSOs at the redshift up to $z \sim 6.4$ (Fan et al. 2003), they are limited to very *bright* QSOs only, particularly at $z > 3$ (Richards et al. 2006). Thus, the faint end of the QSO luminosity function is totally unknown at the important epoch ($z > 3$) to understand the growth of SMBHs (Figure 9.4).

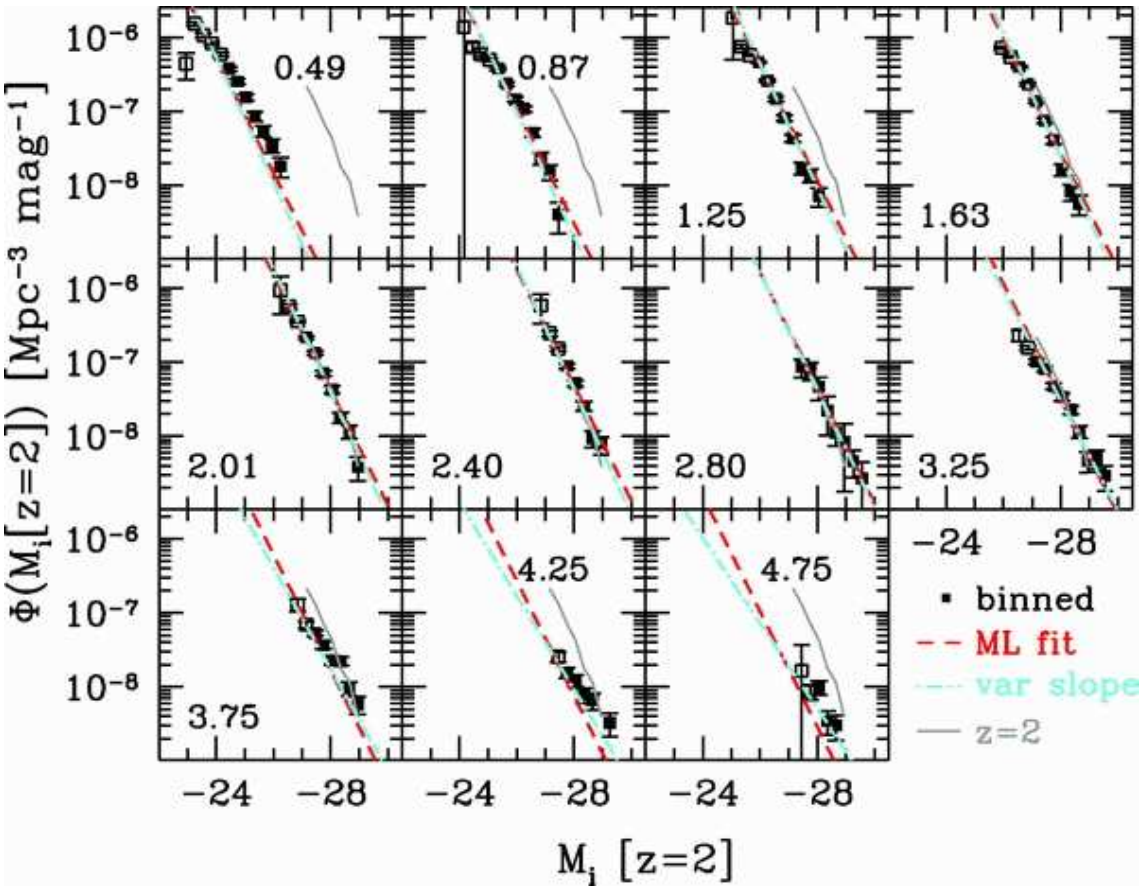

Figure 9.4: QSO luminosity function derived from SDSS survey ($i < 20$ mag) from $z = 0.49$ to 4.75 (Richards et al. 2006). While QSO luminosity function is observationally well constrained to the faint end at $z < 3$, it is not at $z > 3$.

In the proposed HSC wide survey data with >1000 deg^2, many *faint (= intrinsically less luminous)* QSOs at $z > 3$ are expected to be included. The number density of $z > 3$ QSOs with $i < 24$ mag (AB) (= spectroscopic limit for an 8m class telescope) is estimated to be ∼40 per 1 PFS FOV (1.5 deg^2) in a conservative case, or as high as ∼1000 (Casey et al. 2008) (see Figure 9.5). These numbers correspond to 27,000–650,000 QSOs at $z = 3 - 5.5$ in the whole HSC wide survey area. If other contaminants, such as Galactic cool stars and normal star-forming galaxies at lower-z, are taken into account, the number of $z = 3 - 6$ QSO *candidates* will be 50,000–2,000,000. It is practically impossible to do follow-up spectroscopic identification of all (or bulk) of these QSO candidates, using existing spectrographs.

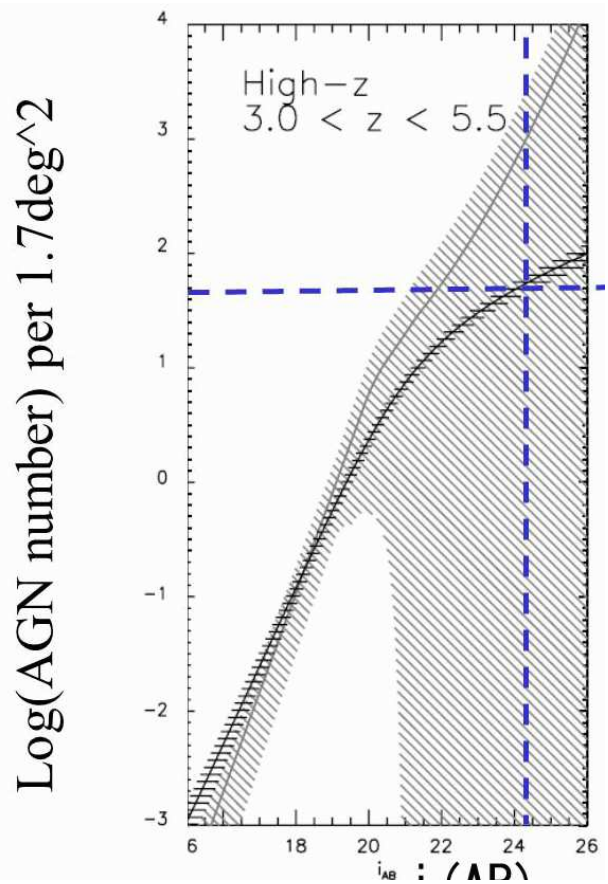

Figure 9.5: Expected number of $z = 3 - 5.5$ QSOs with $i < 24$ mag (practical spectroscopic limit for an 8m class telescope). Adopted from Casey et al. (2008). The ordinate is decimal logarithm of QSO number per 1.7 deg^2 (the size of the COSMOS field). The two lines correspond to luminosity-dependent density evolution model (upper) and pure luminosity evolution model (lower). The expected number of QSOs at $z = 3 - 5.5$ is 40–1000 per PFS FOV (1.5 deg^2).

Targeted follow-up spectroscopy of a small sub-sample (∼100 ?), using Subaru FOCAS or spectrographs at other telescopes, will be conducted to test the reliability of the photometric selection technique, based on HSC g, r, i, z, y colors. Then, QSO luminosity function at $z = 3 - 6$ will be *inferred*, based on the HSC photometric catalog. However, secure spectroscopic identification as true $z = 3 - 6$ QSOs and their redshift identification will be ultimately needed to derive the QSO luminosity function at $z > 3$ in an unarguable manner to the other community in the world. With its high multiplicity (2400 fibers) and wide field of view (FOV $\sim$ 1.5 deg^2), PFS will be only a choice to achieve this spectroscopic purpose, and so play a vital role.

Deriving the accurate QSO luminosity function down to a faint population is closely coupled to understanding the origin of the cosmic ionizing UV radiation. It has been widely known that the universe is re-ionized at $z < 6$ (Gunn & Peterson 1965). The ionizing sources can be star-forming galaxies and/or QSOs. At $z < 3$, QSOs are found to be dominant (Haardt & Madau 1996), but their relative contributions at $z > 3$ are poorly known, simply because the number density of numerous, intrinsically less luminous QSOs is observationally unconstrained. The combination of

HSC and PFS is very powerful to derive the faint end of the QSO luminosity function at $z > 3$. By integrating the obtained QSO luminosity function, we can directly estimate the QSO contribution to the ionizing UV background photons at $z > 3$. Since QSOs have harder UV spectral shapes than star-forming galaxies, if the QSO contribution is important, QSO's high energy UV photons may penetrate into molecular gas of forming galaxies, heat the gas, and thus suppress further star-formation. Thus, understanding the QSO contribution to the cosmic UV background radiation is strongly linked to the subsequent galaxy formation.

The role of PFS for this luminosity function science is just to identify real QSOs at $z = 3 - 6$ and estimate their redshift. Covering the redshifted Lyα (1215Å) emission line and hopefully one more strong emission lines (such as CIV 1549Å) is the minimum requirement (Figure 9.6). The proposed PFS wavelength coverage of 3800–13,000Å is enough to spectroscopically identify QSOs at $z = 2.3 - 6$, by covering both the lines.

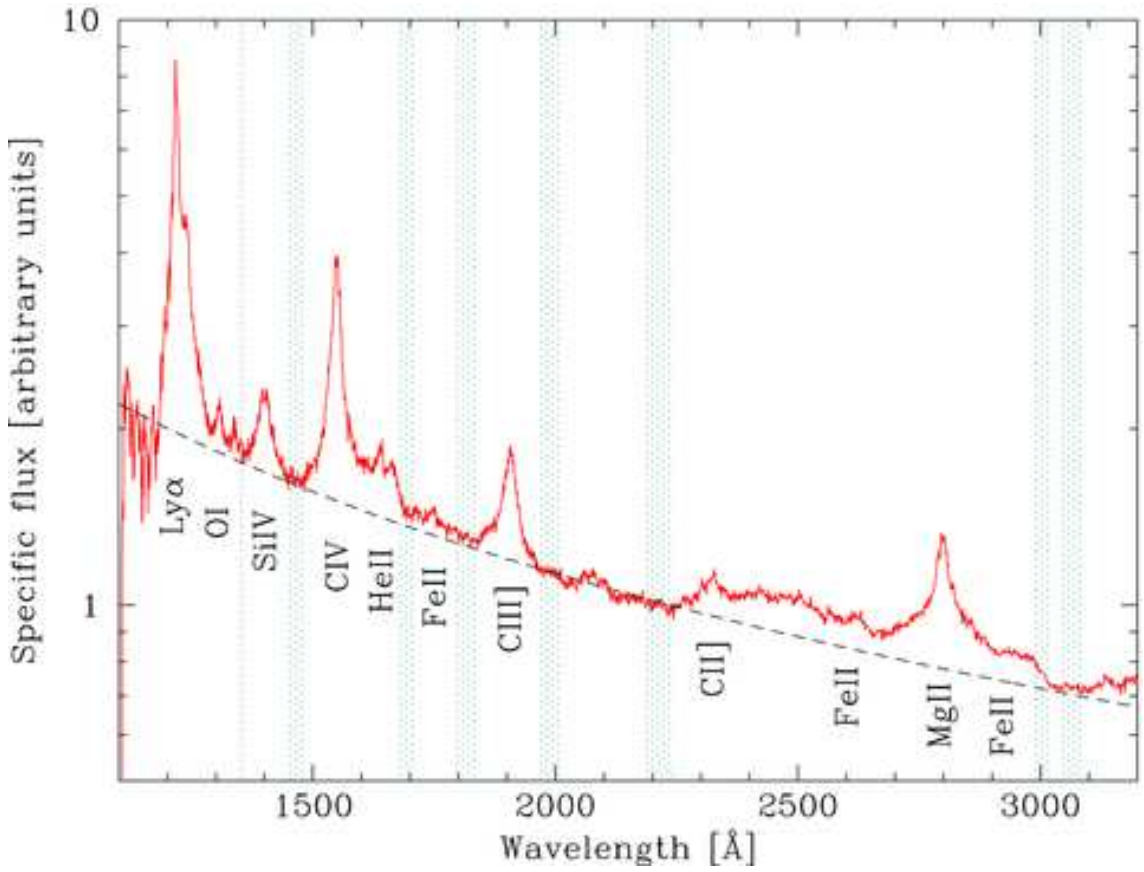

Figure 9.6: Typical QSO spectrum (Decarli et al. 2010). Several strong emission lines are indicated.

Below is the summary of the required PFS specification and survey design for this science.

1. How long exposure per field is needed?

   0.5 hour

The QSO luminosity function at $z > 3$ (Figure 9.4) was derived with the SDSS spectroscopic survey with $i < 20$ mag (AB) (Richards et al. 2006). By pushing the spectroscopic follow-up of QSOs as faint as $i \sim 24$ mag (AB) using PFS (spectroscopic limit of an 8m telescope), we can go ∼4 mag deeper than the current limit, bringing a remarkable progress in our understanding of the faint end of the QSO luminosity function at $z > 3$. In this case, our main interest is the QSO luminosity function at $i = 22 - 24$ mag.

For the redshift identification of QSOs, spectral resolution with R > 500 and S/N > 5 are the minimum requirements. Based on the expected sensitivity table of PFS (Figure 9.3), 0.5 hour (2 × 15 min) exposure is necessary for QSOs with $i \sim 24$ mag .

2. What is the minimum nights to achieve the desired scientific goal?

   4 clear nights

   The luminosity function is basically derivable from a few sources per luminosity bin, albeit large error bars. Dividing the probed luminosity range into narrow luminosity bins and increasing the number of sources per each luminosity bin will improve the accuracy of the luminosity function. We here set luminosity bin as 0.5 mag and minimum number of sources per bin as >25, to reduce the statistical uncertainty to <20%.

   We here adopt the conservative QSO number density, to estimate the minimum number of required nights. The QSO number density is higher in a fainter luminosity bin. Based on the conservative estimate of Casey et al. (2008) and redshift evolution of QSO number density (Richards et al. 2006), the expected number of QSOs in the brightest (= smallest number) luminosity bin ($i \sim 22$ mag) is ∼0.5 and ∼2 at $z = 4 - 5$ and $3 - 4$, respectively, per 1 PFS FOV. To make the minimum QSO number in the smallest number luminosity bin to be >25, we need to cover >50 PFS FOVs. Considering observing overheads, we assume that 16 FOVs with 0.5 hr exposure, or 24 deg^2, can be covered per night. To cover 50 FOVs, we need ∼4 clear nights.

   Note that in the conservative estimate of QSO number density (Figure 9.5), QSO *candidates* at $z = 3 - 5.5$ with $i < 24$ mag is at most ∼200 per PFS FOV (1.5 deg^2). In this case, this program should be combined with other galaxy/star spectroscopic surveys in the HSC wide field.

   However, the number density of QSOs at $z = 3 - 5.5$ with $i < 24$ mag can be as high as ∼1000 (Figure 9.5), and QSO *candidates* per PFS FOV can be ∼2400. In this case, almost all PFS fibers can be effectively used for QSO candidates, and the required FOVs can be reduced to ∼2 FOVs. Only 1 clear night is sufficient.

   In this way, the number of required nights is strongly dependent on the currently-poorly-known number density of the faint QSO population at $z > 3$. Hence, our PFS survey strategy should be updated once we have obtained initial results of the HSC wide survey.

3. What is the impact if the achieved throughput is 10%, rather than 20%?

   If the throughput becomes half and the sensitivity degrades by a factor of $\sqrt{2}$, with the same 0.5 hr exposure time, the faintest bin of the luminosity function constrained from this PFS survey will become brighter by ∼0.4 mag. Even with this, we can make a significant progress in our understanding of the faint end of the QSO luminosity function at $z > 3$.

4. What is the time line for proposed science to get done (e.g. HSC data is enough for target selection, or other datasets are needed? Another spectroscopic follow-up with higher resolution is needed? and so on)

   For target selection, HSC wide survey data are sufficient. However, VIKING (Figure 9.7) near-infrared data are strongly desirable and very important to separate bona-fide QSOs at $z > 3$ and other contamination sources (Galactic cool stars and lower-z galaxies) more efficiently.

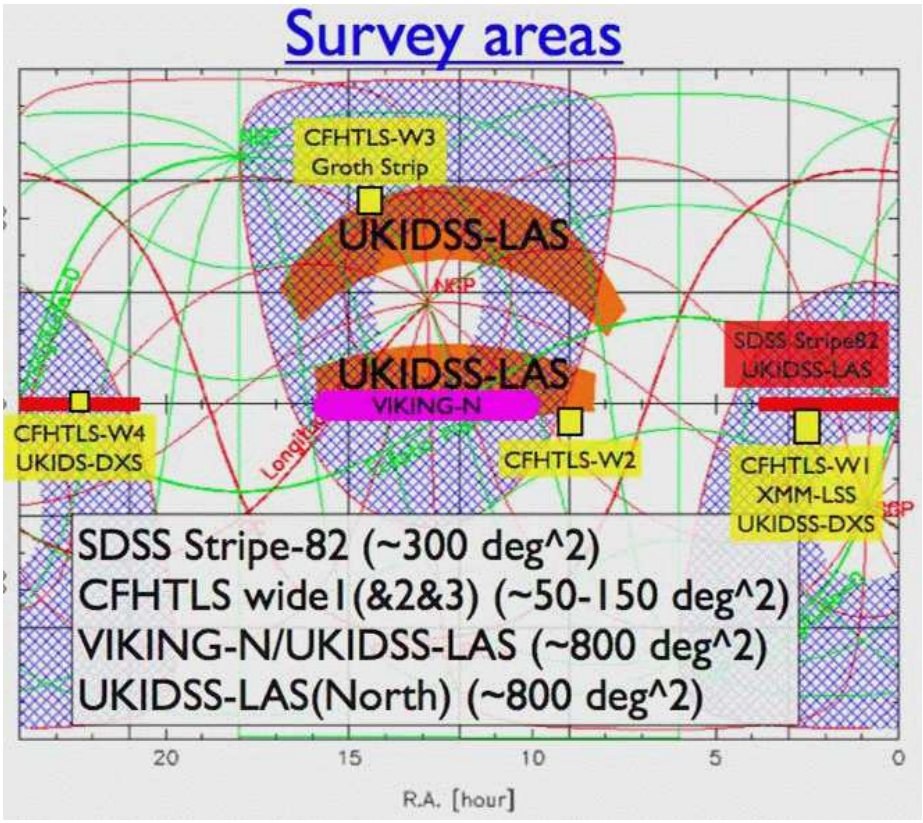

Figure 9.7: Field candidates for HSC wide survey. The VIKING north field is marked with purple.

   For this luminosity function science, the QSO redshift identification is the minimum requirement. PFS spectroscopy is basically enough, and no additional higher resolution spectroscopy is particularly necessary.

5. How unique the proposed science case is, compared to other planned surveys in the world?

   The combination of HSC and PFS is by far the most powerful tool to study faint $z > 3$ QSOs, until LSST and subsequent follow-up spectroscopic survey start operation.

6. What is the most important ingredient of PFS specifications (resolution, the number of fibers, and so on) for achieving the proposed science case?

   Wide wavelength coverage of 3800–13,000Å is important to cover the redshifted Lyα (1215Å) and CIV (1549Å) emission lines in a wide redshift range at $z = 2.3 - 6$. In the conserva-

tive case, the number density of QSO *candidates* is ∼200. A wider PFS FOV will enable simultaneous spectroscopy of more QSO candidates.

9.3 Clustering Properties and Environments of QSOs at $z < 6$

In order to constrain the trigger mechanism of QSOs and understand the importance of QSOs in the context of galaxy formation/evolution within the cold dark matter structure formation scenario, it is crucial to reveal the properties of host halos of QSOs and investigate QSO location in the host halos. Large-scale clustering properties of QSOs (probed through QSO-QSO clustering) provide the information on the mass of their host halos. If QSOs are associated with more massive host halos, QSOs should display stronger clustering. On the other hand, small-scale clustering properties, probed through QSO-galaxy clustering (Kauffmann & Haehnelt 2002) and QSO pairs (Hennawi et al. 2010; Shen et al. 2010), show QSO location inside the host halo. The location can reflect the trigger mechanism of QSOs.

Recent clustering studies of QSOs at $z < 3$ and bright QSOs at $z > 3$ have suggested that (1) the clustering strength is found to increases with redshift, (2) the estimated minimum host halo mass does not strongly depend on redshift, and (3) QSOs inhibit dark halos with masses of $10^{12} - 10^{13} M_{\odot}$ (Croom et al. 2005; Shen et al. 2007, 2009; Coil et al. 2009). Contrary to the expectation that more luminous QSOs (= more massive SMBHs on average) (Ferrarese 2002) show stronger clustering, no strong dependence of the clustering strength on QSO luminosity has so far been observed (Croom et al. 2005; Shen et al. 2009). Investigating the clustering properties of faint QSOs (= generally less massive SMBHs) at the epoch of SMBH growing phase ($z > 3$) will make an important progress in understanding the QSO/galaxy formation scenario and the nature of QSO activity, because at $z > 3$, we can distinguish parameters of various theoretical models more clearly from observations than lower-z (Figure 9.8).

Regarding the location of QSOs inside the host halo, observational study of QSO-galaxy clustering has been performed only at $z < 0.6$ (Padmanabhan et al. 2009). Extending such study to $z > 3$ is again very powerful to understand the origin of QSOs (Kauffmann & Haehnelt 2002) [2].

The HSC wide survey (>1000 deg^2) will find numerous less-luminous QSOs *candidates* at $z > 3$, which are usable for the study of QSO clustering properties at $z > 3$ in unprecedented detail. However, spectroscopic confirmation of these QSO *candidates* as true QSOs at $z = 3 - 6$ is indispensable to study the evolution of QSO-QSO and QSO-galaxy clustering as a function of redshift in an unarguable manner. Because of the large number density of QSO candidates at $z = 3 - 6$, PFS will play a crucial role for this spectroscopic purpose.

Similar to the luminosity function study described in the previous section, covering the redshifted Lyα (1215Å) and CIV (1549Å) emission lines is the minimum requirement for the redshift identification. The proposed PFS spectral coverage with 3800–13,000Å is basically enough for $z = 2.3 - 6$ QSOs.

[2] Although attempts to study the small scale clustering properties of QSOs at $z > 3$, using QSO pairs, have been made, uncertainty is still very large, due to small number statistics (Shen et al. 2010).

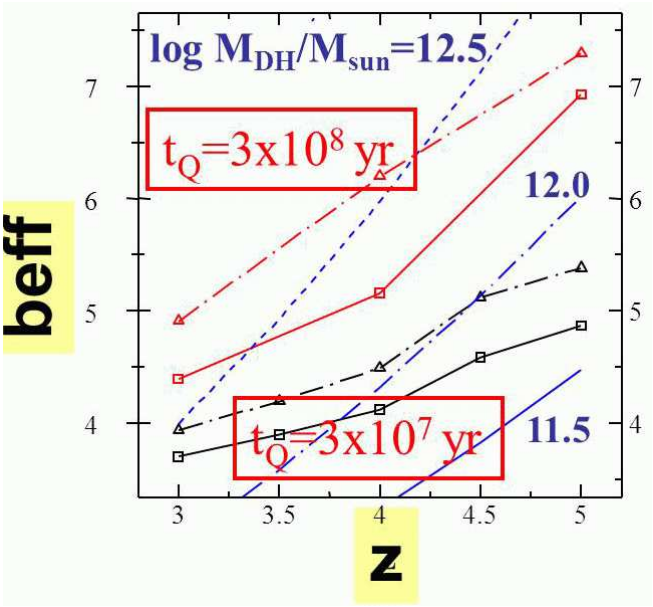

Figure 9.8: Theoretical prediction of QSO clustering properties at $z > 3$, as a function QSO life time and host halo mass, calculated with the model of Enoki et al. (2003). The ordinate is a bias parameter (= clustering strength of QSOs relative to the underlying dark matter).

1. How long exposure per field is needed?

   0.5 hour

   To identify candidate sources as faint as $i \sim 24$ mag, as true QSOs at $z = 3 - 6$ with R > 500 and S/N > 5, 0.5 hr exposure is needed, similar to the QSO luminosity function study (previous section).

2. What is the minimum nights to achieve the desired scientific goal?

   45 clear nights

   To investigate QSO-QSO auto-correlation in a meaningful manner, sample size with >a few 10,000 is at least required (Croom et al. 2005; Shen et al. 2007, 2009). The expected number density of $z = 3 - 5.5$ QSOs with $i < 24$ mag is 40–1000 per PFS FOV (Figure 9.5). This QSO-QSO clustering study generally requires larger number of nights than the studies of the luminosity function (previous section) and SMBH evolution (next section). Based on the conservative estimate of the QSO number density (40 QSOs per PFS 1.5 deg^2 FOV), we require >700 PFS FOVs, or >1000 deg^2, to construct the QSO sample size with >25,000. Considering observing overheads, we assume that 16 FOVs with 0.5 hr exposure, or 24 deg^2, can be covered per night. To cover 700 FOVs, we need ∼45 clear nights.

   In our assumption here, QSO *candidates* at $z = 3 - 5.5$ with $i < 24$ mag is at most ∼200 per PFS FOV. In this case, this program should be combined with other galaxy/star spectroscopic surveys in the HSC wide field. However, the number density of QSOs at $z = 3 - 5.5$ with $i < 24$ mag can be as high as ∼1000 (Figure 9.5), and QSO *candidates* per PFS FOV can be ∼2400. In this case, almost all PFS fibers can be effectively used for QSO candidates, and the required FOVs can be reduced to ∼30 FOVs. Only 2 clear nights are sufficient.

In this way, the number of required nights is strongly dependent on the currently-poorly-known number density of the faint QSO population at $z > 3$. Hence, our PFS survey strategy should be updated once we have obtained initial results of the HSC wide survey.

3. What is the impact if the achieved throughput is 10%, rather than 20%?

   If the throughput becomes half and the sensitivity degrades by a factor of $\sqrt{2}$, with the same 0.5 hr exposure time, the faintest QSOs probed with this PFS survey will become brighter by ∼0.4 mag. In this case, the number density of QSOs can decrease by a factor of ∼1.5, and the required nights will increase by a factor of 1.5.

4. What is the time line for proposed science to get done (e.g. HSC data is enough for target selection, or other datasets are needed? Another spectroscopic follow-up with higher resolution is needed? and so on)

   For target selection, HSC wide survey data are sufficient. However, VIKING near-infrared data are strongly desirable and very important to separate bona-fide QSOs at $z > 3$ and other contamination sources (Galactic cool stars and lower-z galaxies) more efficiently.

   For this QSO clustering science, the QSO redshift identification is the minimum requirement. PFS spectroscopy is basically enough, and no additional higher resolution spectroscopy is particularly necessary.

5. How unique the proposed science case is, compared to other planned surveys in the world?

   The combination of HSC and PFS is by far the most powerful tool to study faint $z > 3$ QSOs, until LSST and subsequent follow-up spectroscopic survey start operation.

6. What is the most important ingredient of PFS specifications (resolution, the number of fibers, and so on) for achieving the proposed science case?

   Wide wavelength coverage of 3800–13,000Å is important to cover the redshifted Lyα (1215Å) and CIV (1549Å) emission lines in a wide redshift range at $z = 2.3 - 6$. In the conservative case, the number density of QSO *candidates* is ∼200. A wider PFS FOV will enable simultaneous spectroscopy of more QSO candidates.

9.4 Evolution of Supermassive Blackholes (SMBHs) at $z < 6$

In the HSC wide survey data, many faint (= intrinsically less luminous) QSOs at $z = 3 - 6$ are expected to be included. This redshift range is extremely interesting to study the evolution of SMBHs, because this range is just beyond the peak of the number density of bright QSOs (Figure 9.2) and thus is thought to correspond to the growing-up phase of SMBHs.

One approach to assess the evolution of SMBHs is to utilize the luminosity function of QSOs, which provides the *average* evolutionary process of QSOs. Recent optical and X-ray observations of QSOs have shown that the number density of faint QSOs peaks at lower redshift than bright QSOs, namely the so-called *downsizing evolution* or luminosity-dependent density evolution is indicated (Figure 9.9) (Ueda et al. 2003; Hasinger et al. 2005; Croom et al. 2009).

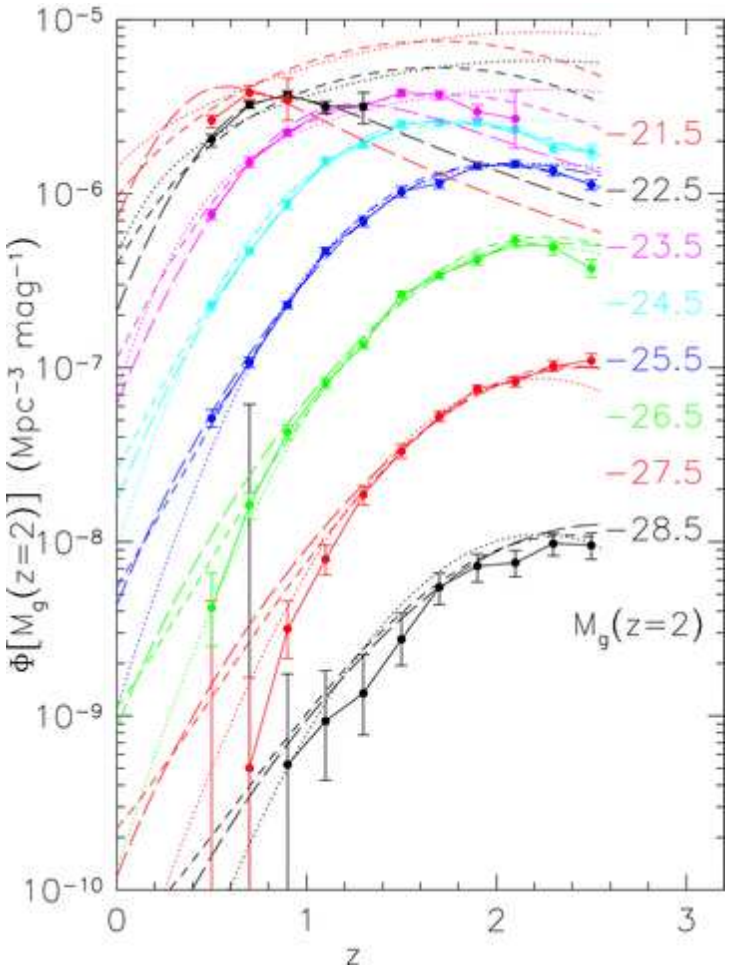

Figure 9.9: Redshift evolution of the space number density of optically-selected QSOs. It is indicated that brighter QSOs show peaks at higher-z in number density than fainter QSOs (Croom et al. 2009).

Based on the redshift evolution of the QSO luminosity function, the average growth history of SMBHs has been discussed (Marconi et al. 2004): massive SMBHs ($> 10^8 M_\odot$) gain their masses at $z \sim 2$, while less-massive ones ($< 10^8 M_\odot$) increase their masses at $z \sim 1$. However, these arguments assume a constant Eddington ratio (L/L_{Edd}) [3] for all QSOs, which is obviously not the case. Thus, the growth curve of SMBHs, estimated above, is still qualitative. In order to reveal the SMBH evolution history quantitatively, we need to determine SMBH masses and accretion rate (L/L_{Edd}) in individual QSOs.

Using SDSS data ($i < 20.1$ mag), SMBH evolution has been investigated out to $z > 4$ only for extreme QSOs with exceptionally large SMBH masses with $>10^{8.7} M_\odot$ (Kelly et al. 2010) (Figure 9.10). In order to understand the cosmological SMBH evolution in a comprehensive manner, it is crucial to prove more *general* QSOs with SMBH masses as small as $\sim 10^8 M_\odot$. Namely, we should go deeper by >2 mag.

[3] The Eddington luminosity (L_{Edd}) is the maximum theoretical luminosity (for isotropic illumination) when particles are accreting spherically onto a SMBH with a given mass. $L_{Edd}/L_\odot = 3.4 \times 10^4 \, M_{SMBH}/M_\odot$.

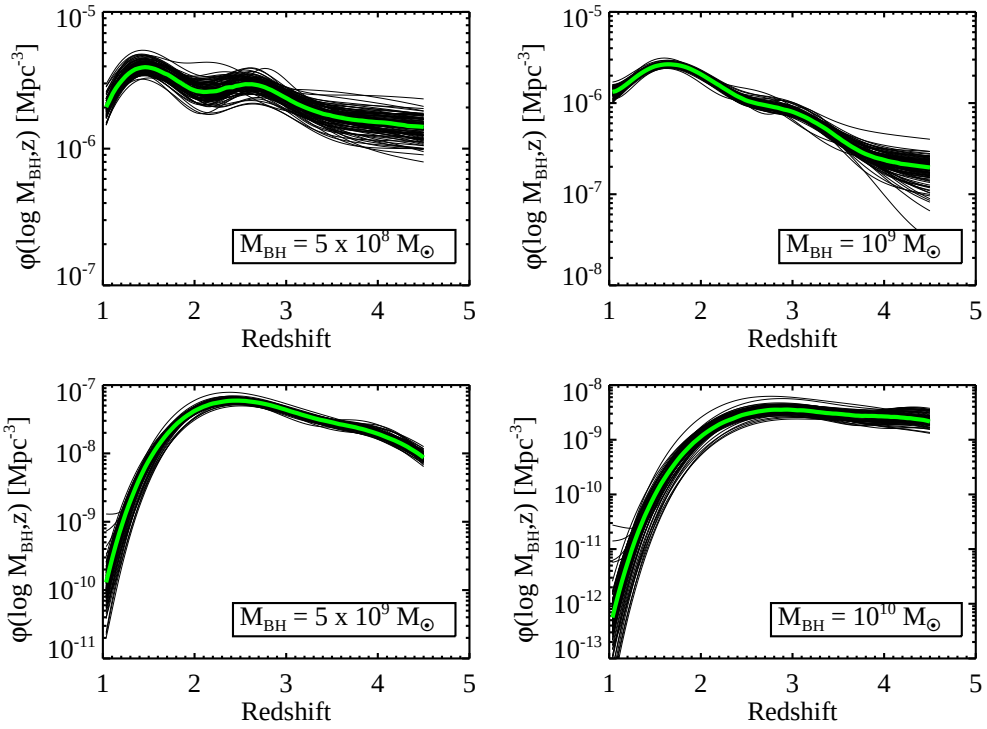

Figure 9.10: Evolution in the number density of SMBHs in QSOs (Kelly et al. 2010). Lower mass SMBHs show peaks at lower-z, suggesting supermassive blackhole downsizing.

Many faint QSOs with SMBH masses of as small as $\sim 10^8 M_\odot$ are expected to be included in the HSC wide survey data. However, again, HSC survey alone will provide only many *candidates* of $z > 3$ QSOs with SMBH masses of $\sim 10^8 M_\odot$. Spectroscopic confirmation as QSOs at $z > 3$ is at least required as a starting point of the study of SMBH evolution at the growing-up phase at $z > 3$. In addition to the redshift identification, we need to estimate SMBH masses of individual QSOs at $z > 3$. The CIV (1549Å) line widths and nearby continuum luminosity will be used for the rough measurements of SMBH masses of QSOs at $z > 3$ (Trump et al. 2009a) [4]. The proposed PFS spectral coverage with 3800–13,000Å is basically enough for $z = 2.3 - 6$ QSOs.

1. How long exposure per field is needed?

   0.5 hour

   For this study, we have to trace the line profile of the CIV (1549Å) emission line, to estimate the SMBH mass of a QSO. Hence, a higher quality spectrum (S/N > 10) is needed than simple redshift identification (previous two sections). Since QSOs usually display broad CIV (1549Å) emission lines with >2000 km s^{-1}, the spectral resolution with R $\sim$ 750 is the minimum requirement, to roughly probe the line profile. We can achieve S/N > 10 for $i = 22.5$ mag QSOs with R $\sim$ 1000 and 0.5 hour exposure. In this case, QSOs with SMBH masses as small as $10^8 M_\odot$ can be probed at $z = 4$.

[4] The MgII (2800Å) line, another (even better) SMBH mass estimator, is covered only for QSOs at $z < 3.5$ with the longest wavelength coverage of PFS (13,000Å or 1.3 μm).

2. What is the minimum nights to achieve the desired scientific goal?

   18 clear nights

   To understand the SMBH evolution as a function of SMBH mass with sufficient precision, 10 sources per mass bin per redshift bin ($\Delta z = 1$ up to $z = 5$) are the minimum requirement. We divide into the following three mass bins: 10^8–$10^{8.7}$M$_\odot$, $10^{8.7}$–$10^{9.3}$M$_\odot$, and $>10^{9.3}$M$_\odot$. The expected number ratio is roughly 100:10:1 (Kelly et al. 2010). Thus, we need >1100 QSOs at each redshift, if we are to include >10 sources in the smallest number bin.

   The number of QSOs at $z = 3-5.5$ with $i < 22.5$ mag is ∼20 per PFS FOV (1.5 deg^2) in the conservative case (Casey et al. 2008). The QSO number density ratio between $z = 3-4$ and $z = 4-5$ is roughly 4:1 (Richards et al. 2006). Namely, we expect ∼4 QSOs with $i < 22.5$ mag at $z = 4-5$ per PFS FOV.

   In order to include >1100 QSOs at $z = 4-5$, we need >275 PFS FOVs or ∼410 deg^2. Assuming that 16 FOVs with 0.5 hr exposure can be covered per night, we need 18 clear nights, as the minimum requirement.

   Similar to the previously discussed sciences, in the conservative estimate, QSO *candidates* at $z = 3-5.5$ with $i < 22.5$ mag is at most ∼60 per PFS FOV. In this case, this program should be combined with other galaxy/star spectroscopic surveys in the HSC wide field.

   However, the number density of QSOs at $z = 3-5.5$ with $i < 22.5$ mag can be as high as ∼100 (Figure 9.5), and QSO *candidates* per PFS FOV can be ∼300. In this case, the required nights will be reduced accordingly.

   In this way, the number of required nights is strongly dependent on the currently-poorly-known number density of the faint QSO population at $z > 3$. Hence, our PFS survey strategy should be updated once we have obtained initial results of the HSC wide survey.

3. What is the impact if the achieved throughput is 10%, rather than 20%?

   If the throughput becomes half, the minimum SMBH mass probed with the PFS spectroscopy is shifted to $>10^8$M$_\odot$. This is not preferable, because we cannot probe the SMBH evolution down to 10^8M$_\odot$ (= general QSO range) at $z > 4$. In this case, we need 1 hr exposure, instead of 0.5 hr.

4. What is the time line for proposed science to get done (e.g. HSC data is enough for target selection, or other datasets are needed? Another spectroscopic follow-up with higher resolution is needed? and so on)

   For target selection, HSC wide survey data are sufficient. However, VIKING near-infrared data are strongly desirable and very important to separate bona-fide QSOs at $z > 3$ and other contaminants more efficiently.

   Subaru/FMOS near-infrared (10,000–17,000 Å or 1.0–1.7 μm) spectroscopy to measure the SMBH masses, based on the redshifted MgII (2800Å) emission lines, for the sub-sample of QSOs at $z = 3.5-6$, may be useful to calibrate the CIV (1549 Å)-based SMBH-mass estimate.

5. How unique the proposed science case is, compared to other planned surveys in the world?

   The combination of HSC and PFS is by far the most powerful tool to study faint $z > 3$ QSOs, until LSST and subsequent follow-up spectroscopic survey start operation.

6. What is the most important ingredient of PFS specifications (resolution, the number of fibers, and so on) for achieving the proposed science case?

   Wide wavelength coverage of 3800–13,000Å is important to cover the redshifted Lyα (1215Å) and CIV (1549Å) mission lines at $z = 2.3 - 6$. Sensitivity is important to probe smaller mass SMBHs. The proposed number of fibers (2400) and spectral resolution (R $\sim$ 3000) are sufficient. A wider PFS FOV will enable simultaneous spectroscopy of more QSO candidates.

9.5 Cosmic Chemical Evolution at $z < 6$

Chemical properties and their redshift evolution give strong constraints on galaxy evolutionary scenarios. The significant positive correlation between the metallicity and the stellar mass of galaxies seen in the local universe (Tremonti et al. 2004; Lee et al. 2006) tells us the past history of the gas inflow and/or outflow of galaxies, as a function of galaxy mass. The natural extension of this powerful study is to investigate the metallicity of galaxies with various properties as a function of redshift. Recently, the mass-metallicity relation of galaxies has been observationally investigated at up to $z \sim 3.5$ (Savaglio et al. 2005; Erb et al. 2006; Maiolino et al. 2008), and the mass-dependent evolution of the mass-metallicity relation in galaxies is now recognized (Figure 9.11). This is interesting since this mass-dependent evolution seems consistent to the so-called downsizing evolution of galaxies (Cowie et al. 1996). However, it is not feasible to extend this research beyond $z \sim 3.5$ since the apparent faintness of galaxies generally makes it very difficult to obtain sufficient-quality, rest-frame optical spectra through near-infrared spectroscopy. Note that star-forming galaxies show no strong emission lines (except for Lyα) in their rest-frame UV spectra.

One approach to overcome this difficulty is focusing on QSOs instead of star-forming galaxies. In addition to the intrinsically higher luminosity of QSOs, various metallic emission lines seen in the rest-frame UV spectra allow us to investigate the chemical evolution at $z > 3.5$. Recent metallicity measurements of QSOs have shown that QSO metallicity is dependent on QSO luminosity, but shows *no redshift evolution* up to $z \sim 6$ (Nagao et al. 2006; Jiang et al. 2007; Juarez et al. 2009; Matsuoka et al. 2009) (Figure 9.12).

Apparently the significant metallicity evolution seen in star-forming galaxies and no metallicity evolution in QSOs seem contradictory to each other. One possible idea to reconcile this apparent contradiction is shown in Figure 9.13 (Juarez et al. 2009; Kawakatu et al. 2003); QSOs we have observed in high-z universe through SDSS are only exceptionally luminous QSOs at each epoch and so we see only well-matured populations. In other words, we have to investigate QSOs with lower luminosity than SDSS QSOs, to study QSO populations in a chemically evolving phase.

In the HSC wide survey data, numerous faint QSOs at $z = 3-6$ should be included. PFS follow-up spectroscopy of these HSC-detected QSO candidates at $z = 3-6$ will simultaneously cover the NV (1240Å), SiIV (1398Å), OIV (1402Å), and CIV (1549Å) emission lines. Their flux ratios can be used for metallicity measurements of QSOs. In this science, we have to detect faint NV (1240Å), SiIV (1398Å), and OIV (1402Å) emission lines, in addition to the bright Lyα (1215Å) and CIV (1549Å) emission lines. Thus, longer exposure time is needed than previously discussed science cases.

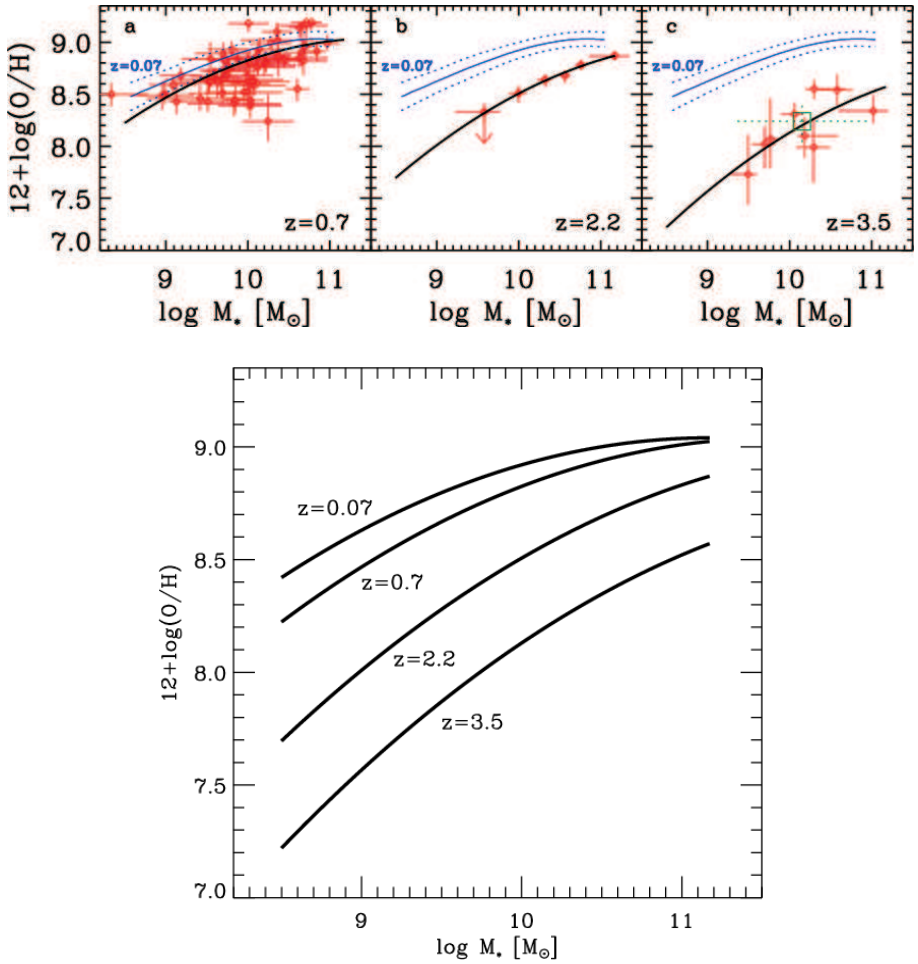

Figure 9.11: Galaxy-mass-dependent evolution of mass-metallicity relation (Maiolino et al. 2008). Less massive galaxies show faster mass-metallicity evolution than massive ones.

Below is the summery of our request for this science.

1. How long exposure per field is needed?

   1 hour

   QSOs with $i \sim 23$ mag correspond to $M_B < -23$ mag at $z = 3-6$, substantially fainter than SDSS QSOs. Thus, a large number of chemically-evolving QSOs are expected to be included. Since the emission line widths of QSOs are >2000 km s^{-1}, we bin spectral elements to R $\sim$ 1000.

   For QSOs at $z = 3-5$, we focus on objects with $i = 22-23$ mag and investigate their spectra at 4900–9300Å. Typically four 900 sec exposures (i.e., 1 hour on-source integration) are requested. This exposure time results in S/N > 10 at 4900–9300Å for QSOs with $i \sim 23$ mag.

   For QSOs at $z \sim 6$, we focus on objects with $z < 22.5$ mag and analyze their spectra at 8000–11,000Å. Four 900 sec exposures result in S/N > 10 at 8000–13,000Å.

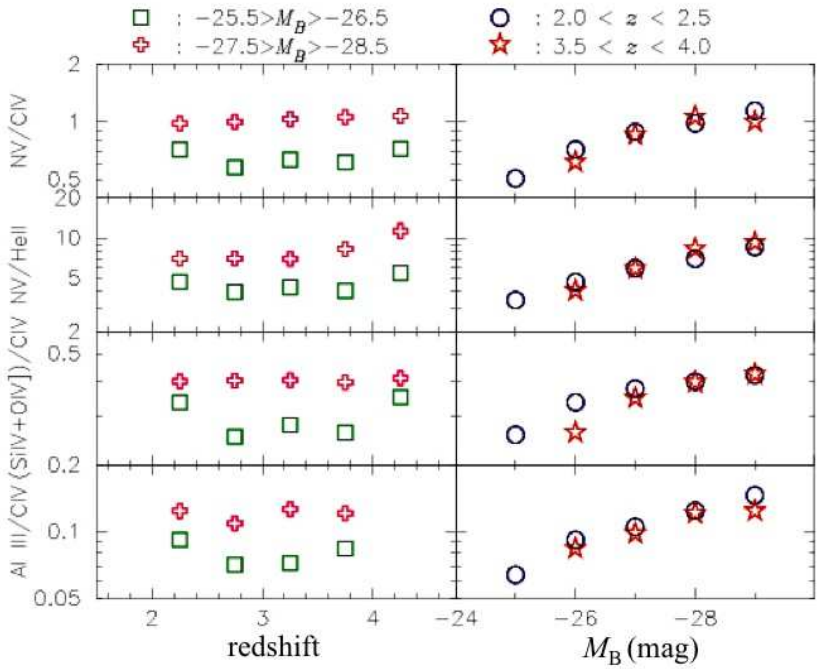

Figure 9.12: Four different methods for metallicity measurement (ordinate) as functions of redshift (left) and QSO B-band (4500Å) absolute magnitude (right), based on SDSS bright QSOs (Nagao et al. 2006). At given QSO luminosity, metallicity shows no redshift dependence, but at given redshift, metallicity increases with increasing QSO luminosity.

Stacking analysis will be useful to improve the S/N ratio of the spectra.

2. What is the minimum nights to achieve the desired scientific goal?

13 clear nights

The number of QSOs at $z = 3 - 5$ with $i < 23$ mag is ∼25 per PFS FOV (1.5 deg^2) in the conservative case (Casey et al. 2008). With 100 FOVs, ∼2500 QSOs at $z = 3 - 5$ with much lower luminosity than SDSS QSOs will be identified. QSOs with various chemical properties can be investigated statistically. Assuming that we can cover 8 FOVs with 1 hr exposure per night, we need 13 clear nights to cover 100 FOVs.

For $z \sim 6$ QSOs with $z < 22.5$ mag, the expected number density is much lower and so must be combined with $z = 3 - 5$ QSOs.

Similar to the previously discussed sciences, in the conservative estimate, QSO *candidates* at $z = 3 - 5.5$ with $i < 23$ mag is at most ∼100 per PFS FOV. In this case, this program must be combined with other galaxy/star spectroscopic surveys in the HSC wide field.

However, the number density of QSOs at $z = 3 - 5.5$ with $i < 23$ mag can be as high as ∼200 (Figure 9.5), and QSO *candidates* per PFS FOV can be ∼600. In this case, the required nights to achieve this science goal will be reduced accordingly.

In this way, the number of required nights is strongly dependent on the currently-poorly-known number density of the faint QSO population at $z > 3$. Hence, our PFS survey strategy should be updated once we have obtained initial results of the HSC wide survey.

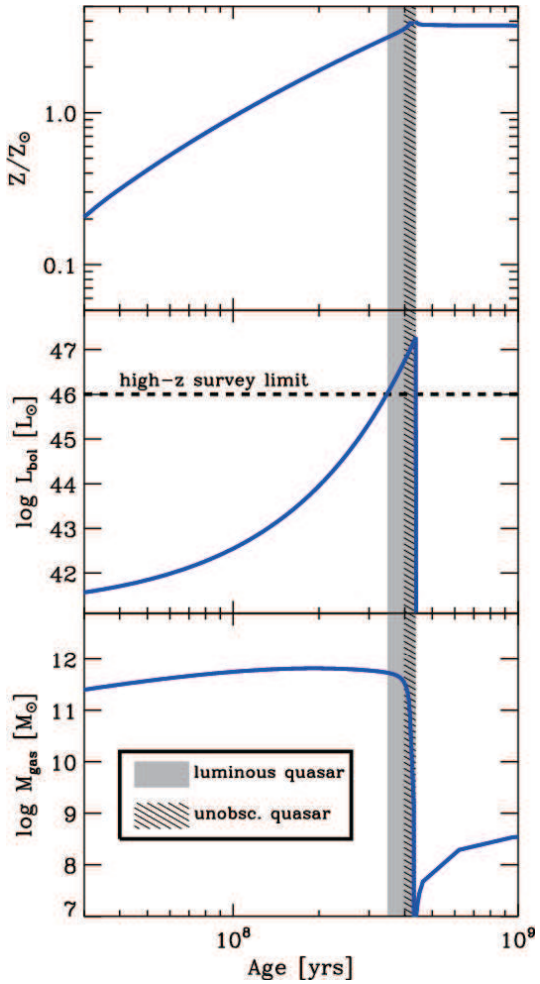

Figure 9.13: Evolution of gas metallicity (top), bolometric QSO luminosity (middle) and total gas mass (bottom) (Juarez et al. 2009). The horizontal dashed line in the middle panel shows the approximate minimum bolometric luminosity detectable at high-z in the SDSS QSO survey. It is evident that bright SDSS QSOs are limited to chemically-matured populations at high-z.

3. What is the impact if the achieved throughput is 10%, rather than 20%?

   High sensitivity is crucial for this study. The reduction of the throughput will seriously affect this science case, because only brighter QSOs can be probed and it becomes difficult to construct a statistically significant sample in various chemically-evolving phases.

   To make a stacking spectrum, *accurate* redshift information of individual QSOs is important. A lower throughput may provide lower S/N spectra and prevent us from applying the stacking analysis.

4. What is the time line for proposed science to get done (e.g. HSC data is enough for target selection, or other datasets are needed? Another spectroscopic follow-up with higher resolution is needed? and so on)

   For target selection, HSC wide survey data are sufficient. However, VIKING near-infrared data are strongly desirable and very important to separate bona-fide QSOs at $z > 3$ and

other contaminants more efficiently.

Near-infrared follow-up spectroscopy at 10,000–22,000Å (1–2.2 μm) is very useful (but not mandatory) to further investigate the chemical evolution of QSOs, because the Fe/Mg abundance ratio can be derived through the measurements of FeII multiplet and MgII (2800Å) emission lines (Figure 9.6). This Fe/Mg abundance ratio is a good probe of star-formation history in the past (Iwamuro et al. 2002).

5. How unique the proposed science case is, compared to other planned surveys in the world?

   The combination of HSC and PFS is by far the most powerful tool to study faint $z > 3$ QSOs, until LSST and subsequent follow-up spectroscopic survey start operation.

6. What is the most important ingredient of PFS specifications (resolution, the number of fibers, and so on) for achieving the proposed science case?

   High sensitivity is critical for this science, because we have to investigate weak NV (1240Å), SiIV (1398Å), OIV (1402Å), and CIV (1549Å) emission lines with sufficient S/N ratios. Wide wavelength coverage of 3800–13,000Å is also important to cover these emission lines in QSOs at up to $z \sim 6$. The proposed number of fibers (2400) and spectral resolution (R $\sim$ 3000) are sufficient. A wider PFS FOV will enable simultaneous spectroscopy of more QSO candidates.

9.6 Identification of Further QSOs at $z > 6$

In this decade, QSOs at $z > 6$ are enthusiastically focused on, because they are crucially important to (1) constrain the formation/evolutionary scenarios of SMBHs in the early universe, (2) prove the physical conditions of the intergalactic medium, including the epoch of the cosmic reionization, (3) provide a landmark of highest-z (proto-)clusters of galaxies, and (4) trace the earliest stage of the cosmic chemical evolution. More detailed descriptions are found in the HSC white paper. For the topic (1), highest-z, brightest QSOs can put the strongest constraints, and will be discovered through targeted spectroscopy using Subaru FOCAS or MOIRCS. However, for the topics (2), (3), (4), finding as many $z > 6$ QSOs as possible is important. As we will describe below, PFS spectroscopic survey will play an important role to increase the number of $z > 6$ QSOs.

9.6.1 QSOs at $z > 6.7$

At $z > 6.7$, the Lyα (1215Å) emission line is redshifted beyond the z-band (9000Å), the conventional longest filter in the optical. QSOs at $z > 6.7$ are extremely faint in all the optical bands, and so are totally undetectable through the conventional optical high-z QSO survey (Fan et al. 2006; Willott et al. 2010b; Jiang et al. 2009). With the advent of the y-band (10,000Å) filter in the HSC survey (Figure 9.1), we can now push the redshift barrier of QSOs from $z \sim 6.4$ (Fan et al. 2003; Willott et al. 2007, 2010a) to $z = 6.7 - 7.3$. Based on the conservative estimate of $z \sim 7$ QSO number density, namely, assuming flat luminosity function at the faint end and a factor of 3 decrease from $z = 6$ to $z = 7$ (Willott et al. 2010b), 35 $z \sim 7$ QSOs should be included in the HSC

wide y-band survey data per 1000 deg^2 ($y = 23.8$ mag in AB). The most important issue is how to *select* the 35 $z \sim 7$ QSOs, from the tremendous number of y-detected objects.

At $z = 6.7 - 7.3$, the Lyα emission is redshifted beyond the z-band, but still shorter than or within the y-band. Thus, $z = 6.7 - 7.3$ QSOs become extremely faint in the z-band, but are moderately bright in the y-band, so that selection based on large (red) $z - y$ colors is the most straightforward way to pick up $z = 6.7 - 7.3$ QSO candidates.

However, Galactic brown dwarfs also display red $z - y$ colors, and their number density is much higher than that of $z = 6.7 - 7.3$ QSOs in the red $z - y$ color sample. It is crucial to remove the contaminations from the numerous Galactic brown dwarfs with reasonable efficiency, if we are to realistically identify $z = 6.7 - 7.3$ QSOs through follow-up spectroscopy in a reasonable telescope time.

While high-z QSOs have sharp spectral gaps at the wavelength of the redshifted Lyα emission lines (Figure 9.14), brown dwarfs display gradually increasing fluxes with increasing wavelength (Figure 9.15). Thus, if we compare the flux just shorter and longer sides of the redshifted Lyα emission, which correspond to z- and y-bands for $z \sim 7$ QSOs, then $z \sim 7$ QSOs should be even redder in $z - y$ colors than brown dwarfs. Hence, the selection efficiency of $z \sim 7$ QSOs increases, if the $z - y$ color becomes redder and redder.

Based on actually-measured $z - y$ colors of brown dwarfs so far detected, we set $z - y > 2.3$ mag to select $z \sim 7$ QSOs, by minimizing contaminations from numerous brown dwarfs (see the HSC QSO/AGN white paper for more details). However, since the limiting magnitudes of HSC wide survey are (i,z,y) = (26.0,24.9,23.8) in AB, the $z - y > 2.3$ mag criterion means that sources close to the y-band detection limit cannot be selected, because $z - y$ color constraints are too weak to practically remove numerous brown dwarfs. Even with this, we will be able to select 7 QSOs at $z \sim 7$ with $y < 22.6$ mag in the 1000 deg^2 HSC wide survey area.

If the VISTA/VIKING north 780 deg^2 field (Figure 9.7) is selected as the HSC wide survey area, deep J-band data (12,500Å or 1.25 μm; $J = 22.0$ mag in AB) will be available. By using the J-band photometric data, we can weaken the $z - y$ color criterion from ∼2.3 mag to ∼1.7 mag for the separation of brown dwarfs, because in the $z - y$ and $y - J$ color plane, the distributions of $z \sim 7$ QSOs and brown dwarfs are different (Figure 9.16). By weakening the $z - y$ color threshold, we can search for $z \sim 7$ QSO candidates from sources as faint as $y = 23.2$ mag, ∼0.5 mag fainter than the case of $z - y > 2.3$ mag color selection alone. By going 0.5 mag deeper, the number density of $z \sim 7$ QSOs increases by a factor of ∼2. If the VISTA/VIKING north 780 deg^2 field is included, then the number of selectable $z \sim 7$ QSOs becomes ∼12 per 1000 deg^2 of the HSC wide survey.

We expect that for the above 7–12 $z \sim 7$ QSOs with sufficient $z - y$ color constraints, the contaminations from brown dwarfs is a factor of less than several, and these QSOs are reasonably selectable, through targeted spectroscopy using Subaru FOCAS. However, as mentioned before, the number of $z \sim 7$ QSOs, included in the HSC wide y-band survey data is ∼35. The remaining 20 $z \sim 7$ QSOs are not readily selectable, unless some serendipity or very lucky situations occur, because the insufficient $z - y$ color constraints (<1.7 mag) makes the brown dwarf's contaminations extremely severe.

PFS spectroscopic survey of y-detected ($y = 22.6 - 23.8$ mag), but z-undetected ($z > 24.9$ mag) sources, if conducted, will help increase the number of $z \sim 7$ QSOs. This PFS spectroscopic survey must be combined with other galaxy/star surveys, because success rate is so low (∼20 per 1000 deg^2).

9.6.2 QSOs at $z = 6 - 6.5$

For QSOs at $z = 6.0 - 6.5$, since the spectral gap at the Lyα emission is redshifted between the i- and z-bands, such QSOs can be selected as red $i - z$ sources (i.e., i-dropout, z-detected). As in the case of $z = 6.7 - 7.3$ QSOs, Galactic brown dwarfs also show red $i - z$ colors (Figure 9.15) and can be major contaminants. However, HSC wide survey employs y-band filter, which can be used to remove the contaminations from numerous brown dwarfs. Brown dwarfs have monotonously increasing fluxes with increasing wavelength until 1.1 μm, and so $z - y$ colors are very red (Figure 9.15), while QSOs at $z = 6.0 - 6.5$ are blue in the $z - y$ colors, because emission at the longer wavelength side of the Lyα emission is probed at z and y.

Specifically, we will employ $i - z > 1.8$ mag and $z - y < 0.5$ mag color selections, to pick up $z = 6.0 - 6.5$ QSOs, by minimizing the numerous brown dwarf contaminations. Given that the limiting magnitudes of the HSC wide survey are (i,z,y) = (26.0,24.9,23.8) in AB, the color selection enables us to pick up sources as faint as z =24.2 mag. Again, adopting the flat luminosity function for faint $z \sim 6$ QSOs (Willott et al. 2010b), we expect to select ∼350 $z \sim 6$ QSOs per 1000 deg^2 of the HSC wide survey.

However, more $z \sim 6 - 6.5$ QSOs should be included in the HSC database as deep as $z = 24.9$ mag. By going 0.7 mag deeper, the number density is expected to increase by a factor of 2–3 (Willott et al. 2010b). PFS spectroscopic survey of z-detected ($z = 24.2 - 24.9$ mag), but i-undetected ($i > 26.0$ mag) sources, if conducted, will identify further $z = 6 - 6.5$ QSOs and help increase the number of such QSOs. This PFS spectroscopic survey must be combined with other galaxy/star surveys, because success rate is so low (1–2 QSOs at $z = 6 - 6.5$ per PFS FOV).

9.6.3 Summary

In summary, PFS survey of z-dropout ($z > 24.9$ mag, $y = 22.6 - 23.8$ mag) and i-dropout ($i > 26.0$ mag, $z = 24.2 - 24.9$ mag) sources will increase the number of $z > 6$ QSOs, which are very important for the science topics (2), (3), and (4), described in the first part of this section.

Below is the summary of the required PFS specification and survey design for this science.

1. How long exposure per field is needed?

   1 hour

   To distinguish between $z \sim 7$ QSOs from brown dwarfs, spectral resolution with R > 500 and S/N > 5 are at least required. To meet these requirements for sources as faint as $y = 23.8$ mag using PFS, we need 1 hr net on-source exposure time. With this exposure, distinction

between $z \sim 6$ QSOs and brown dwarfs will also be possible for sources as faint as $z = 24.9$ mag, if we set R $\sim$ 300 and S/N > 3.

2. What is the minimum nights to achieve the desired scientific goal?

   No minimum nights. 83 clear nights are ideal.

   We do not propose this PFS spectroscopic survey alone, because success rate is so low. Thus, we cannot provide a minimum number of nights. If there are other galaxy/star surveys with 1 hour exposure in the HSC wide field, then we can combine this survey with them. Surveying wider area is better. Ideally, the whole HSC wide 1000 deg^2, or 660 PFS FOVs, is spectroscopically surveyed with PFS. Assuming 8 PFS FOVs can be covered per night, 83 clear nights will be needed.

3. What is the impact if the achieved throughput is 10%, rather than 20%?

   If the throughput becomes half, we need 2 hours net on-source exposure time to achieve the same S/N ratios. Thus, this study becomes more difficult, given that we need a wide area coverage.

4. What is the time line for proposed science to get done (e.g. HSC data is enough for target selection, or other datasets are needed? Another spectroscopic follow-up with higher resolution is needed? and so on)

   Since the total number of strong $z \sim 7$ QSO candidates ($z - y > 2.3$ mag) is expected not to be large (<100), we will first try targeted slit spectroscopy using Subaru FOCAS or MOIRCS, quickly after such candidates are found in the HSC wide survey data. We hope to discover $\sim$10 $z \sim 7$ QSOs within 2–3 years of the HSC survey. This proposed PFS spectroscopic survey should come after such targeted spectroscopy has already discovered several $z \sim 7$ QSOs. If further probable $z \sim 7$ QSOs are found in the low S/N ($\sim$5) PFS spectra, we need subsequent long-exposure, high-sensitivity spectroscopy using Subaru FOCAS or MOIRCS to obtain spectra with higher S/N ratios, in order to derive their redshifts and physical properties (e.g., emission line strengths) with higher quantitative accuracy. Follow-up near-infrared spectroscopy is also planned to estimate their SMBH masses using CIV (1549Å) or MgII (2800Å) emission lines.

5. How unique the proposed science case is, compared to other planned surveys in the world?

   HSC will provide the largest number of $z \sim 7$ QSOs (z-dropout, y-detected), because the y-band limiting magnitude is the deepest among planned survey within next five years (e.g., UKIDSS and VIKING). Thus, the combination of HSC and PFS is most powerful.

6. What is the most important ingredient of PFS specifications (resolution, the number of fibers, and so on) for achieving the proposed science case?

   Sensitivity in the y-band (9500–10,800Å) is the most important factor.

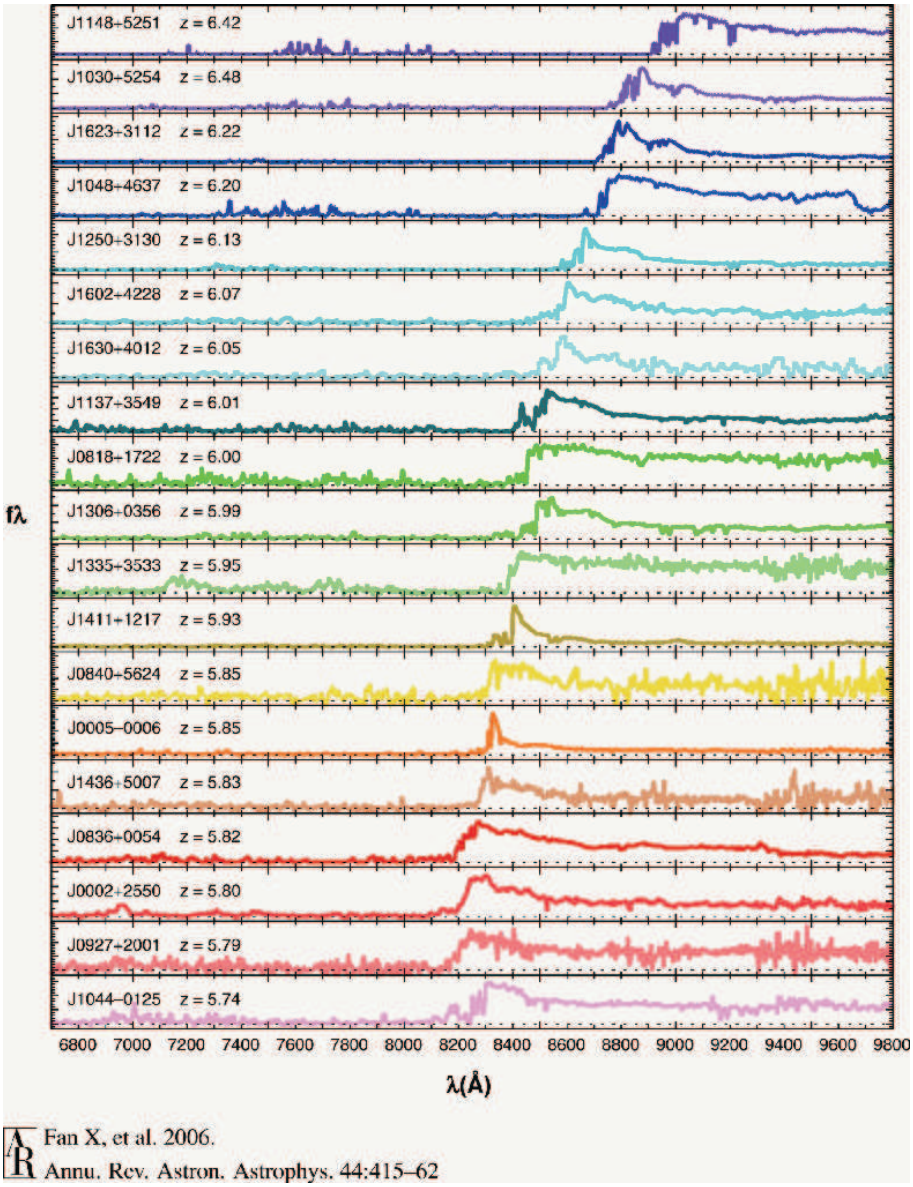

Figure 9.14: Spectra of SDSS-detected QSOs at $z = 5.7-6.42$ (Fan et al. 2006). The abscissa is observed wavelength in Å, and the ordinate is flux in F_λ. As the redshift of QSO increases from the bottom to the top, the spectral gap at the wavelength of the Lyα emission is redshifted to the longer wavelength.

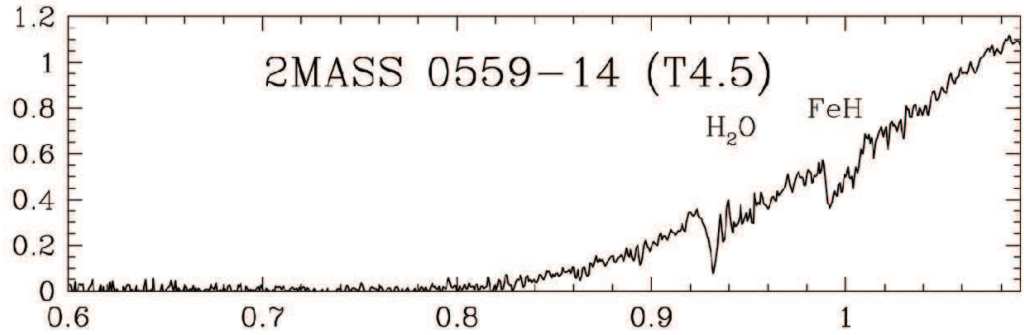

Figure 9.15: Spectrum of a brown dwarf at 0.6–1.1 μm (6,000-11,000Å) (Geballe et al. 2002). The abscissa is observed wavelength in μm, and the ordinate is flux in F_λ. The flux gradually and monotonously increases with increasing wavelength from i-band (0.75μm), through z-band (0.9μm), to y-band (1.0μm).

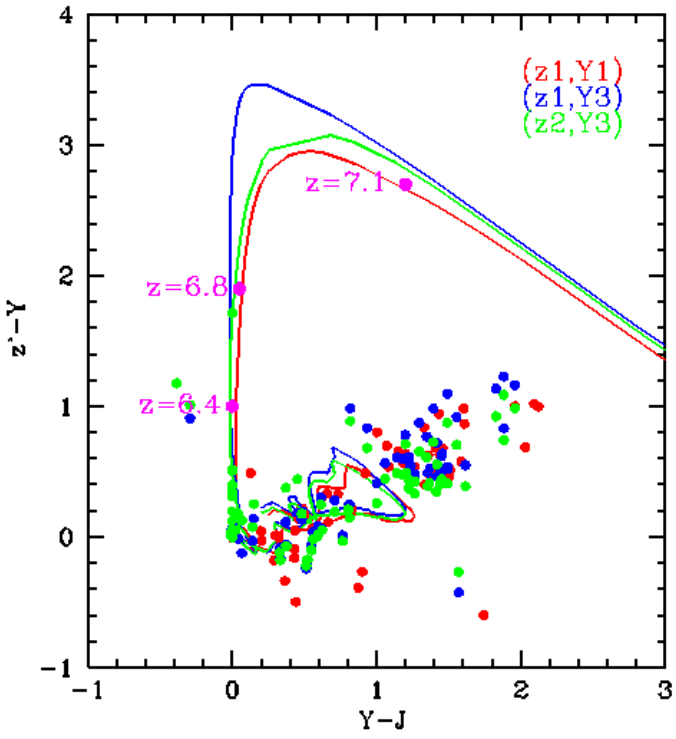

Figure 9.16: Separation between $z > 6.4$ QSOs and brown dwarfs, based on $z-y$ and $y-J$ colors in AB (proposed by N. Kashikawa). Filled circles are brown dwarfs, and solid lines are expected colors of $z > 6.5$ QSOs. The specification of the HSC y-band filter has not yet been finalized, and so three lines are plotted, corresponding to three possibilities. However, the overall behavior does not change significantly. In this figure, y- and Y-bands have the same meaning.

9.7 Ancillary Brown Dwarf Science

A large number of brown dwarfs will be identified as by-products, through PFS spectroscopy of HSC-detected high-z QSO candidates. These brown dwarfs, by themselves, provide important science.

9.7.1 HSC Imaging Survey of Brown Dwarfs

A brown dwarf is an object unable to sustain stable hydrogen burning in its core. It contracts monotonously as it releases gravitational energy into radiation. Its faintness has prevented their discovery in spite of an early prediction of its existence (Hayashi & Nakano 1963). Since GJ 229 B was first identified as a bona-fide brown dwarf (Nakajima et al. 1995), more than 700 brown dwarfs have been discovered by photometric and spectroscopic observations.

A large number of brown dwarfs should be included in the HSC wide survey data with the detection limit of $z = 24.9$ mag and $y = 23.8$ mag. The brown dwarf candidates will be recognized as extremely red objects in the $i - z$ and $z - y$ colors.

9.7.2 Exploring less-massive brown dwarfs

The least-massive brown dwarf discovered to date is UGPS 0722-05 (Lucas et al. 2010). It was discovered by the near-infrared UKIDSS Galactic Plane Survey (GPS) of the UKIRT 3.8m telescope. The follow-up spectroscopy revealed that its spectral type is T10 and the parallax measurements indicated that it is located at 4.1 pc from the Sun. The UKIDSS-GPS is a 7 years program and covers 1800 deg^2 in the near-infrared JHK-bands. The limiting magnitudes are 20.0 mag and 19.0 mag (in Vega) in the J- (1.25μm or 12,500Å) and K-bands (2.2μm or 22,000Å), respectively.

Brown dwarfs and planetary mass objects have red colors, thus they are bright in the near-infrared but faint in the optical. For example, the evolutionary track of Baraffe et al. (2003) indicates that a 5 Gyr-old brown dwarf with the mass of 0.01 $M_\odot$ (or 10 M_J; 10 Jupiter mass) has an effective temperature of 322 K, and M_I (8000Å)=27.06 mag and M_J =22.74 mag. Such an object would have apparent magnitudes of 25.06 mag and 20.74 mag in the I-band and J-band, respectively, if it is located at 4.1 pc from the Sun. These magnitudes are comparable to the limiting magnitude of the HSC survey in the I-band, and that of the UKIDSS-GPS survey in the J-band. Since both surveys have similar areas of the survey region, we conclude that the HSC survey does not have noteworthy advantage to the UKIDSS-GPS survey.

9.7.3 Exploring distant brown dwarfs

We aim at detecting a number of distant brown dwarfs. It enables us to construct the stellar initial mass function (IMF). There are three methods.

1. Star Forming Regions

   Near-infrared imaging and spectroscopic surveys of nearby star forming regions revealed certain populations of brown dwarfs and planetary mass objects (down to $\sim$0.005 $M_\odot$ = 5 M_J) (Oasa et al. 1999). Many astronomers consider that all star forming regions have the same IMF. It has a peak at $\sim$0.3 $M_\odot$ and the number of less massive objects decreases with decreasing mass. Therefore, brown dwarfs are minority. In contrast, some observational results indicate that different star forming regions have different IMFs. Oasa et al. (2006) showed spatial variation of IMFs within one star forming region.

   - advantage:

     Stars belong to one stellar cluster. They have almost the same age and metallicity. Pre-main sequence stars are bright.

   - disadvantage:

     There is ambiguity in the conversion scale from a spectral type to an effective temperature.

     Another ambiguity remains in an evolutionary track. The tracks are very different among different models, especially for 1 Myr old young stars and low mass objects ($<$ 0.5 $M_\odot$).

2. Open cluster

   IMFs of nearby young open clusters are also well investigated. The IMFs are derived down to the brown dwarf regime for the nearby clusters such as the Pleiades.

   - advantage:

     Stars belong to one stellar cluster. They have almost the same age and metallicity.

     Since all stars have the same age and most stars reach the main-sequence phase, the mass-luminosity relation is well established.

   - disadvantage:

     The number of nearby cluster is limited. Many clusters are located far from the Sun, thus cluster members are faint in general. Contamination of background stars often makes a severe problem.

3. Nearby stars

   - advantage:

     Stars are located close to the Sun, thus bright. Most stars are main-sequence stars. Mass-luminosity relation of main-sequence stars is well established.

- disadvantage:

  Knowledge about the duration time of main sequence stars is required, which is necessary for conversion from the observed present-day mass function to the IMF.

  For brown dwarfs, conversion from the luminosity function to the mass function cannot be determined, unless the age of the brown dwarf is known.

  The most comprehensive study of the IMF of nearby stars were provided by the SDSS survey (Bochanski et al. 2010) (Figure 9.17). The SDSS survey covered 6600 deg^2 with the limiting magnitude of $z = 20.4$ mag. In this study, the IMF was derived down to $\sim$0.1 $M_\odot$. The survey also found $\sim$150 brown dwarfs (Chiu et al. 2006). However, the number of brown dwarfs is not sufficient for constructing the IMF in the brown dwarf regime. The limiting magnitude of the HSC survey will be $z = 24.9$ mag, 63 times fainter than that of the SDSS survey. It means that the HSC survey can detect an object located at 8 times farther than that detected by the SDSS survey. The space per unit solid angle with the HSC survey is 512 times larger than that of the SDSS survey. Since the HSC survey will cover 1000 deg^2, it will survey 78 times (1000×512/6600) larger space than the SDSS survey. Thus, the HSC survey will detect 150×78=11,700 brown dwarfs.

  One may wonder whether a brown dwarf detected by such a deep survey is located beyond the disk of the Galaxy. We consider an L4 type brown dwarf as a typical brown dwarf. Its color is z(AB)-K(Vega)=4.66 mag, and its absolute magnitude is 13.03 mag in the K-band. It corresponds to M_z=17.69 mag. A brown dwarf with m_z=24.9 mag is located at 280 pc from the Sun. The scale height of the Galaxy disk is derived to be 325 pc (Bahcall & Soneira 1980) or 250 pc (Mendez & Guzman 1998) for low mass stars. It is well known that massive stars have small scale height of the disk ($\sim$ 70 pc), whereas low-mass stars have large scale height. The HSC survey enables us to investigate the scale height of brown dwarfs.

9.7.4 PFS Spectroscopic Survey of Brown Dwarfs

PFS follow-up spectroscopy of HSC-detected brown dwarf candidates will discover many bona-fide brown dwarfs. Indicators of an effective temperature are absorption bands of TiO (8432Å), CrH (8611Å), and FeH (8692Å) as well as absorption lines of K (7665Å), Rb (7800Å, 7948Å), and Cs (8521Å) for early L type brown dwarfs (Kirkpatrick et al. 1999) (Figure 9.18). The indicators for a late L-type brown dwarf are absorption lines of K (7665Å), Cs (8521Å, 8943Å), and FeH (9896Å), and that for a T-type brown dwarf is a deep absorption band of CH_4 at 1.1 μm (Chiu et al. 2006).

Below, we summarize the requirements for our brown dwarf science.

1. How long exposure per field is needed? What is the minimum nights to achieve the desired scientific goal?

   1 hour and no dedicated night

   We do not request any dedicated night for this science. Instead, we request a few fibers in each observation field. We assume 1 hour (four 900 sec exposure) for each field. The limiting magnitude (10σ) is $z \sim 23$ mag for R $\sim$ 1000 (Figure 9.3), which is enough to

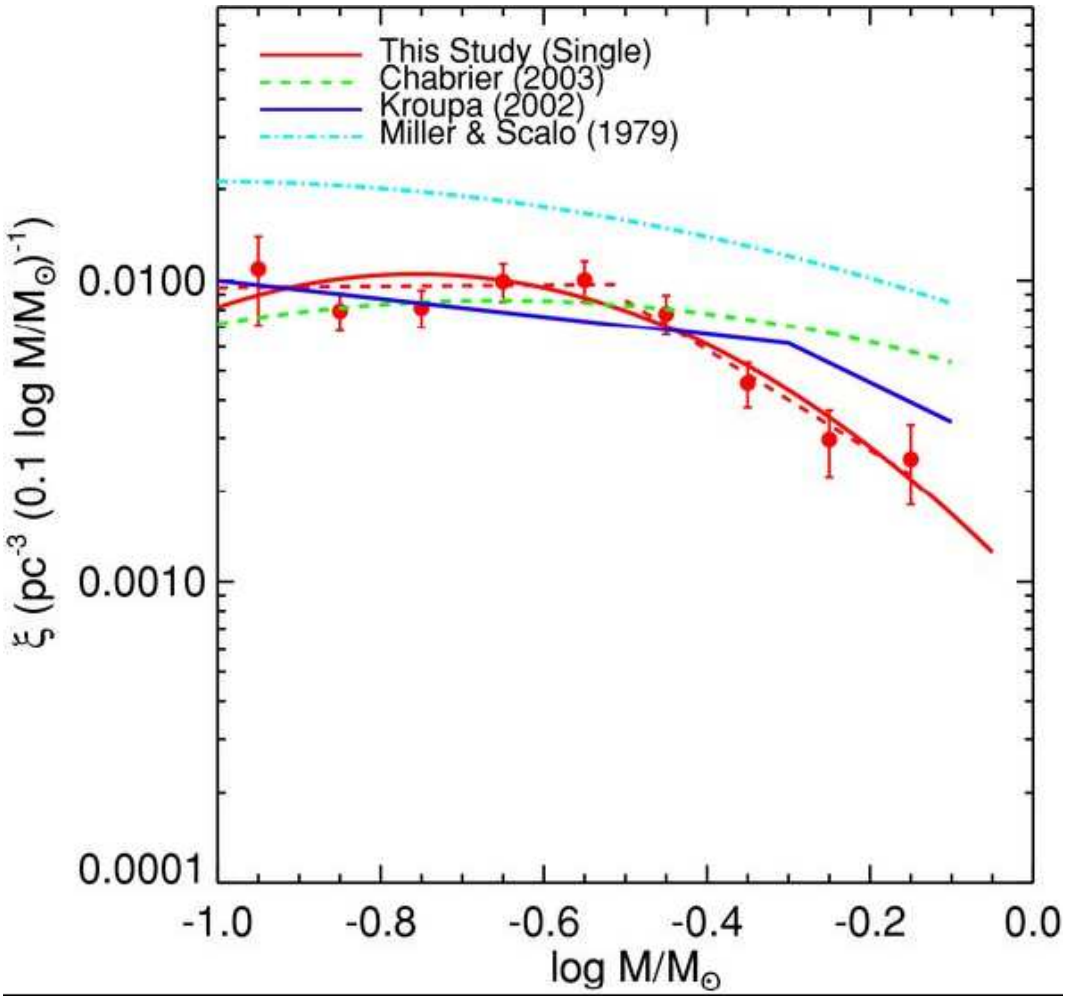

Figure 9.17: Mass functions of nearby stars. Red points with a red line are mass function derived from the SDSS survey (Bochanski et al. 2010). Some efforts have been made for constructing the mass function of nearby brown dwarfs (Reid et al. 1999).

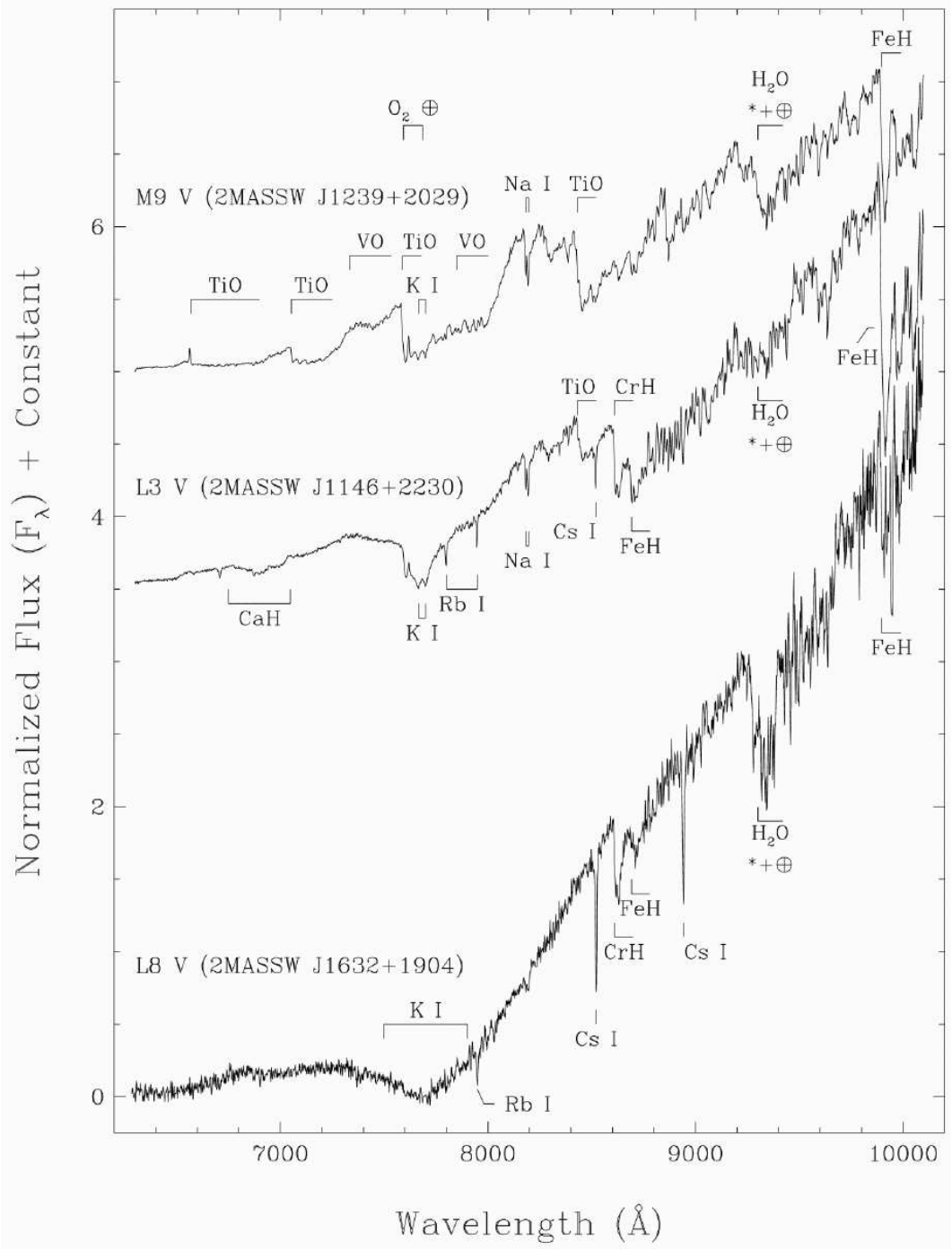

Figure 9.18: Optical spectra of a low-mass star (top) and brown dwarfs (middle and bottom) (Kirkpatrick et al. 1999). The spectral resolution is R $\sim$ 900.

measure the depths of the absorption bands. This limiting magnitude is 2.2 mag deeper than that of the SDSS photometric survey. It means that the PFS survey will search brown dwarfs 2.75 times farther than the SDSS survey. The expected number of brown dwarfs is $\frac{1000\times(2.75)^3}{6600} \times 150 \sim 500$. Assuming PFS FOV with 1.5 deg^2, the HSC wide area of 1000 deg^2 corresponds to 660 FOVs. Assuming 50% success rate, i.e. that we will have one true brown dwarf from two candidates, we need 2 fibers for the brown dwarf science in each field.

2. What is the impact if the achieved throughput is 10%, rather than 20%?

   The S/N ratio decreases by $\sqrt{2}$. The number of the objects observable with PFS is reduced to $(1/2)^{3/4} \sim 0.6 = 300$. The number of brown dwarfs detected by the PFS survey is about twice as that by the SDSS survey.

3. What is the time line for proposed science to get done (e.g. HSC data is enough for target selection, or other datasets are needed? Another spectroscopic follow-up with higher resolution is needed? and so on)

   The HSC data will provide sufficiently large number of brown dwarf candidates. To determine the IMF of brown dwarfs, low-resolution spectroscopy is not sufficient. We need high-resolution optical spectroscopy to determine the surface gravity of the object from the depth and shape of an absorption line, and then determine the mass of the object. It will be carried out with optical high-resolution spectrograph (HDS on Subaru or TMT).

4. How unique is the proposed science case, compared to other planned surveys in the world?

   IMFs of brown dwarfs are now being investigated for star forming regions and open clusters. Only 150 brown dwarfs have been discovered in the solar neighborhood. This number of the field brown dwarf is not sufficient for constructing the IMF of brown dwarfs. Thus, 300–500 brown dwarfs detected through PFS survey is very unique.

5. What is the most important ingredient of PFS specifications (resolution, the number of fibers, and so on) for achieving the proposed science case?

   High sensitivity in the longest optical wavelengths (z- and y-bands).

9.8 Low-Luminosity AGNs Selected by Optical Variability

Fainter QSOs and brown dwarfs will be found in the HSC *deep* fields. However, they will be generally too faint to do follow-up spectroscopy with PFS within reasonable exposure time, and so beyond the main scope of PFS QSO and brown dwarf science. The only exception is low-luminosity AGNs selected by optical variability. They may have moderately high apparent fluxes, but can only be found through multi-epoch observations in the HSC *deep* fields, because it is difficult to select such low-luminosity AGNs by classical color selection due to their faintness compared to host galaxy light. Note that multi-epoch observations are basically not employed in the HSC *wide* field.

Optical variability is one of general properties of (type-1 unobscured) AGNs as well as variability in other wavelengths. This property has been used not only to understand emission mechanisms and

geometry of the central engine through the reverberation mapping but also to select AGNs from huge photometric samples. While many studies have examined optical variability of individual AGNs based on densely-sampled data, recent large and wide-field surveys provided us statistical understanding of UV-optical variability of high-luminosity (high-L) AGNs, i.e., QSOs. However, because of low sensitivities, variability investigation of low-L, Seyfert- and LINER-like [5], AGNs had been limited to nearby objects until 1990s.

Multi-epoch deep imaging data obtained with the Hubble Space Telescope extended variability studies for low-L AGNs to $z \sim 1$ (Sarajedini et al. 2003). They found that about half of them cannot be detected even in very deep X-ray data of ∼1 Ms Chandra or XMM-Newton exposure (Sarajedini et al. 2006; Cohen et al. 2006). Morokuma et al. (2008) significantly increased statistics of such low-L AGNs using multi-epoch Subaru/Suprime-Cam imaging data owing to its wide field-of-view and found that there are clear differences between AGN populations selected by optical variability selection with and without X-ray detection. Some of optical-variability-selected AGNs without X-ray detection have similar properties to those with X-ray detection because whether X-rays from these AGNs are detected or not depends on observation timing as easily imagined. On the other hand, there is a clearly different population in the top-left region of the right panel of brightness and variable component brightness [6] diagrams (Figure 9.19). These have faint variable components ($i_{\rm vari} \sim 25.5$ mag), i.e. faint AGNs, in bright galaxies ($i \sim 21$ mag). Photometric redshifts [7] indicate that most of the host galaxies are early-type galaxies at $z_{\rm ph} \sim 0.5$. Considering the bulge mass-BH mass relation (Wandel et al. 1999), their BH masses are as large as $\sim 10^8 M_\odot$ and the Eddington ratios should be low. The non-detection of X-ray may be consistent with that they are X-ray Bright Optically Normal Galaxies (XBONGs) (Trump et al. 2009b) considering possible time-varying X-ray flux like optical variability and our detection limits in the X-ray and optical. Totani et al. (2005) serendipitously found such faint AGNs using one-month separated Suprime-Cam data and showed similarity of flare-up variability of these AGNs to Sgr A* and possible interpretations of Radiatively Inefficient Accretion Flows (RIAFs) rather than blazar. Maoz et al. (2005) monitored nearby LINERs and detected UV variability of their nuclei indicating existence of low-luminosity AGNs [8]. Taking into account massive BHs and variability behavior of these low-luminosity AGNs, they can be at the ending phases of mass accretion and may be similar populations to LINERs rather than Seyferts. A point which we would like to emphasize is that about 5% of similarly luminous galaxies host such optical-variability-selected AGNs in our time samplings. Although it is difficult to estimate the variability detection completeness because their typical light curves are unknown [9], a significant fraction, comparable to that of local universe, (several tens percent) of luminous galaxies may host such AGNs with low activity. Therefore, it is important to examine properties of these AGNs and what they are in terms of both AGN activity lifetime and massive galaxy formation.

[5] We call high-L, moderate-L, and low-L AGNs as QSOs, Seyferts, and LINERs, respectively.

[6] Defined as differential flux between the maximum and the minimum. It is difficult to measure so-called "variability" because it is difficult to measure AGN components uniformly for all the variable AGNs (some are in cores of very bright galaxies as below).

[7] $z_{\rm ph}$ is calculated without considering AGN components because the contribution from these AGNs to the observed SED is low, as inferred by the goodness of the fit in the $z_{\rm ph}$ estimation process.

[8] On the other hand, Maoz (2007) showed similarity of spectral energy distributions (SEDs) between low-luminosity AGNs (LINERs) and Seyfert nuclei, and indicated no sharp changes of SED in the low luminosity.

[9] For estimating variability detection completeness for such low-luminosity AGNs, nearby AGN monitoring data may be useful (Walsh et al. 2009).

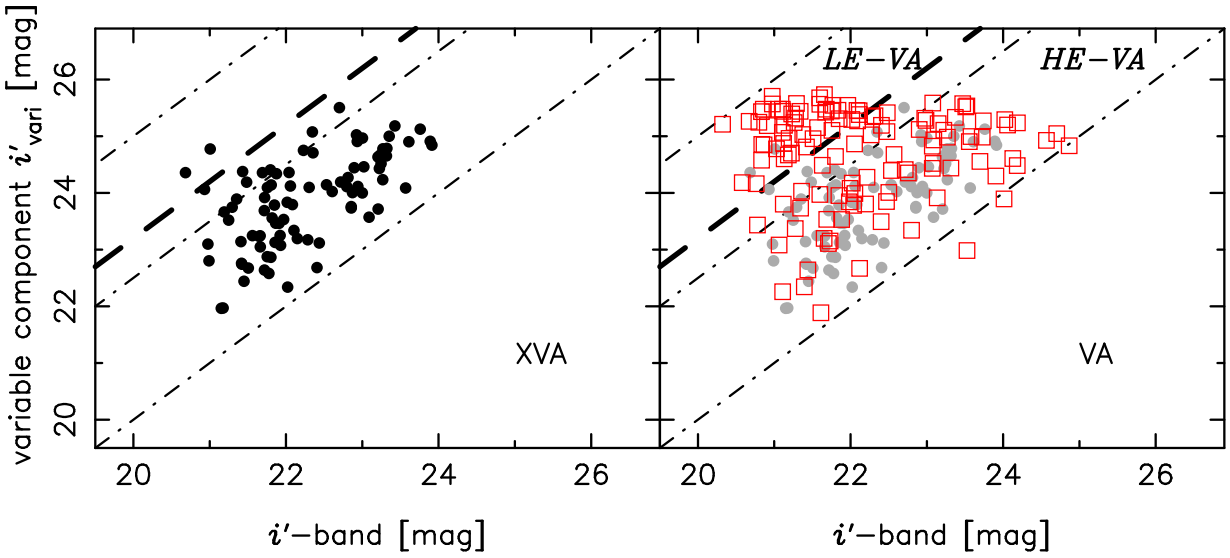

Figure 9.19: Distributions of i-band magnitude (including host components) versus variable component magnitude $i_{\rm vari}$ (defined as differential flux between their maxima and minima) of the X-ray-detected variability-detected AGNs (XVA; filled circles, left panel) and X-ray-non-detected variability-detected AGNs (VA; red open squares, right panel) objects. The XVA objects are also shown in the right panel as gray circles for comparison. We find a concentration in the right panel above a line (notes as "LE-VA") (variable component flux is 0.05 of total flux of host galaxies). Dot-dashed lines are constant flux ratios of 1, 0.1, and 0.01 between i-band and $i_{\rm vari}$. Differences between the panels are not affected by any selection criteria. See Morokuma et al. (2008) for more details.

Identification of its nature by combining with deep spectroscopy, and UV and NIR datasets is now an ongoing project (Morokuma et al. 2011, in prep.) and has been still unknown. Systematic observations with HSC will give us a larger sample of low-L AGNs. In order to understand final stage of AGN activity in massive galaxies and its relation with massive galaxy formation, it is important to know its environmental dependence, which requires at least deep X-ray and deep multi-epoch optical imaging over several tens deg^2 to discuss the distributions and properties of these AGNs as a function of environment. Spectroscopic samples with Subaru/PFS will enable us to know 1) what kind of AGNs they are by emission line diagnostics (with spectra of low-L AGNs, Hβ, [OIII]$\lambda\lambda$4959, 5007, and weak [OIII]$\lambda\lambda$4363) (Nagao et al. 2001) and 2) their environmental dependence (with spectra of low-L AGNs and surrounding galaxies at the same redshifts).

1. How long exposure per field is needed?

   The PFS spectral resolution ($R \sim 3000$) is slightly higher than we need and we can do on-chip binning. In order to detect Hβ and [OIII]$\lambda\lambda$4959, 5007 emission lines expected, we need 2 hours integration per object. We may be able to detect very weak [OIII]λ4363 emission lines by stacking analysis for $\sim$10 low-L AGNs.

2. What is the minimum nights to achieve the desired scientific goal?

   We need >1000 spectra of low-L AGNs and similar number of surrounding galaxies to investigate environmental dependence. One PFS pointing can take $\sim$200 spectra of low-L AGNs. With 10 PFS pointings of 2 hrs exposure, or 3 clear nights, our scientific goal will be achieved.

3. What is the impact if the achieved throughput is 10%, rather than 20%?

If the throughput becomes 10%, we need longer exposure time by a factor of ∼2, both because the redder channel is more important for our case and we can do on-chip binning (namely, readout noise is insignificant).

4. What is the time line for proposed science to get done (e.g. HSC data is enough for target selection, or other datasets are needed? Another spectroscopic follow-up with higher resolution is needed? and so on)

   We at least need data from well-organized HSC observation and deep X-ray observation. If the HSC-deep and ultradeep surveys are done in fields with deep X-ray data, all we need is the HSC data which give us time-domain information.

5. How unique the proposed science case is, compared to other planned surveys in the world?

   It is hard to detect time variability of such low-L AGNs even at low redshifts (except for those in local universe) without 8m-class or space telescopes. This study also requires wide-field coverage and can be done only with Suprime-Cam and HSC before the LSST survey starts operation. We also need 8m-class telescopes for follow-up spectroscopy and even Keck/DEIMOS is not so effective. The combination of HSC and PFS provides unique opportunity for this study.

6. What is the most important ingredient of PFS specifications (resolution, the number of fibers, and so on) for achieving the proposed science case?

   We do not have any critical requirements on the PFS specifications. The fiber density (minimum separation of fibers) can be a problem, but two visits on the same field are enough for our purpose.

9.9 Summary of the Request for PFS Specification and Survey

In summary, **high sensitivity (high throughput) in the z and y-bands**, and **wide wavelength coverage** are the most important for our QSO and brown dwarf study. The proposed spectral resolution with R $\sim$ 3000 and multiplicity (2400) are sufficient. A wide FOV will enable simultaneous spectroscopy of more QSOs and brown dwarfs, and so is important. **The most important thing is that the PFS survey be made in the HSC wide and deep fields.** We can estimate more accurate number density of QSO candidates per PFS FOV, only after the HSC wide survey provides some initial results. If CFHT u-band survey is conducted at the HSC wide area, then selecting QSOs at $z < 3$ becomes more feasible. In the case that the number of $z > 3$ QSO candidates per PFS FOV is substantially smaller than 2400, we can combine PFS follow-up spectroscopy of $z < 3$ QSO candidates as well.

Table 9.1 summarizes the proposed PFS observations for various QSO science cases.

- Through the PFS survey with **0.5 hr** exposure time, we can achieve an important progress in the understanding of the QSO luminosity function, clustering and environments, and SMBH evolution. With minimum **45 clear nights**, all of these scientific topics can be addressed with sufficient quantitative precision. **This 0.5 hr PFS survey can be included in the 1 hr PFS survey (below), if the latter is approved.**

Exposure (hr)	Clear nights	Science
0.5	45	luminosity function, clustering and environments, SMBH evolution
1	83	chemical evolution, $z > 6$ QSOs, brown dwarfs
2	3	variability-selected low-luminosity AGNs

Table 9.1: Summary of PFS observations for QSO science.

- For chemical evolution study and spectroscopic survey of further $z > 6$ QSO and brown dwarf candidates, **1 hr** exposure time is required. If there are other PFS galaxy/star surveys with 1 hour exposure in the HSC wide area, then our survey can be combined. In an ideal case, PFS spectroscopy of the largest possible fraction of the HSC wide field (1000 deg^2 or **83 clear nights**) will discover the largest number of $z > 6$ QSOs and brown dwarfs.
- For variability-selected low-luminosity AGNs with high apparent fluxes, found through the multi-epoch observations in the HSC deep fields, we need only **3 clear nights** with **2 hrs** net on-source exposure time.

References

Bahcall, J. N., & Soneira, R. M., 1980, *ApJS*, 44, 73
Baraffe, I., Chabrier, G., Barman, T. S., Allard, F., & Hauschildt, P. H., 2003, *A&A*, 402, 701
Bochanski, J. J., Hawley, S. L., Covey, K. R., West, A. A., Reid, I. N., Golimowski, D. A., & Ivezić, Ž., 2010, *AJ*, 139, 2679
Casey, C. M. et al., 2008, *ApJS*, 177, 131
Chiu, K., Fan, X., Leggett, S. K., Golimowski, D. A., Zheng, W., Geballe, T. R., Schneider, D. P., & Brinkmann, J., 2006, *AJ*, 131, 2722
Cohen, S. H. et al., 2006, *ApJ*, 639, 731
Coil, A. L. et al., 2009, *ApJ*, 701, 1484
Cowie, L. L., Songaila, A., Hu, E. M., & Cohen, J. G., 1996, *AJ*, 112, 839
Croom, S. M. et al., 2005, *MNRAS*, 356, 415
—, 2009, *MNRAS*, 399, 1755
Croom, S. M., Smith, R. J., Boyle, B. J., Shanks, T., Miller, L., Outram, P. J., & Loaring, N. S., 2004, *MNRAS*, 349, 1397
Decarli, R., Falomo, R., Treves, A., Kotilainen, J. K., Labita, M., & Scarpa, R., 2010, *MNRAS*, 402, 2441
Enoki, M., Nagashima, M., & Gouda, N., 2003, *PASJ*, 55, 133
Erb, D. K., Shapley, A. E., Pettini, M., Steidel, C. C., Reddy, N. A., & Adelberger, K. L., 2006, *ApJ*, 644, 813
Fan, X., Carilli, C. L., & Keating, B., 2006, *ARAA*, 44, 415
Fan, X. et al., 2003, *AJ*, 125, 1649
Ferrarese, L., 2002, *ApJ*, 578, 90
Geballe, T. R. et al., 2002, *ApJ*, 564, 466
Gunn, J. E., & Peterson, B. A., 1965, *ApJ*, 142, 1633
Haardt, F., & Madau, P., 1996, *ApJ*, 461, 20
Hasinger, G., Miyaji, T., & Schmidt, M., 2005, *A&A*, 441, 417
Hayashi, C., & Nakano, T., 1963, Progress of Theoretical Physics, 30, 460
Hennawi, J. F. et al., 2010, *ApJ*, 719, 1672
Iwamuro, F., Motohara, K., Maihara, T., Kimura, M., Yoshii, Y., & Doi, M., 2002, *ApJ*, 565, 63
Jiang, L. et al., 2009, *AJ*, 138, 305
Jiang, L., Fan, X., Vestergaard, M., Kurk, J. D., Walter, F., Kelly, B. C., & Strauss, M. A., 2007, *AJ*, 134, 1150

Juarez, Y., Maiolino, R., Mujica, R., Pedani, M., Marinoni, S., Nagao, T., Marconi, A., & Oliva, E., 2009, *A&A*, 494, L25
Kauffmann, G., & Haehnelt, M. G., 2002, *MNRAS*, 332, 529
Kawakatu, N., Umemura, M., & Mori, M., 2003, *ApJ*, 583, 85
Kelly, B. C., Vestergaard, M., Fan, X., Hopkins, P., Hernquist, L., & Siemiginowska, A., 2010, *ApJ*, 719, 1315
Kirkpatrick, J. D. et al., 1999, *ApJ*, 519, 802
Lee, H., Skillman, E. D., Cannon, J. M., Jackson, D. C., Gehrz, R. D., Polomski, E. F., & Woodward, C. E., 2006, *ApJ*, 647, 970
Lucas, P. W. et al., 2010, *MNRAS*, 408, L56
Maiolino, R. et al., 2008, *A&A*, 488, 463
Maoz, D., 2007, *MNRAS*, 377, 1696
Maoz, D., Nagar, N. M., Falcke, H., & Wilson, A. S., 2005, *ApJ*, 625, 699
Marconi, A., Risaliti, G., Gilli, R., Hunt, L. K., Maiolino, R., & Salvati, M., 2004, *MNRAS*, 351, 169
Matsuoka, K., Nagao, T., Maiolino, R., Marconi, A., & Taniguchi, Y., 2009, *A&A*, 503, 721
Mendez, R. A., & Guzman, R., 1998, *A&A*, 333, 106
Morokuma, T. et al., 2008, *ApJ*, 676, 121
Nagao, T., Marconi, A., & Maiolino, R., 2006, *A&A*, 447, 157
Nagao, T., Murayama, T., & Taniguchi, Y., 2001, *ApJ*, 549, 155
Nakajima, T., Oppenheimer, B. R., Kulkarni, S. R., Golimowski, D. A., Matthews, K., & Durrance, S. T., 1995, *Nature*, 378, 463
Oasa, Y. et al., 2006, *AJ*, 131, 1608
Oasa, Y., Tamura, M., & Sugitani, K., 1999, *ApJ*, 526, 336
Padmanabhan, N., White, M., Norberg, P., & Porciani, C., 2009, *MNRAS*, 397, 1862
Reid, I. N. et al., 1999, *ApJ*, 521, 613
Richards, G. T. et al., 2009, *ApJS*, 180, 67
—, 2006, *AJ*, 131, 2766
Sarajedini, V. L., Gilliland, R. L., & Kasm, C., 2003, *ApJ*, 599, 173
Sarajedini, V. L. et al., 2006, *ApJS*, 166, 69
Savaglio, S. et al., 2005, *ApJ*, 635, 260
Shen, Y. et al., 2010, *ApJ*, 719, 1693
—, 2007, *AJ*, 133, 2222
—, 2009, *ApJ*, 697, 1656
Totani, T., Sumi, T., Kosugi, G., Yasuda, N., Doi, M., & Oda, T., 2005, *ApJL*, 621, L9
Tremonti, C. A. et al., 2004, *ApJ*, 613, 898
Trump, J. R. et al., 2009a, *ApJ*, 700, 49
—, 2009b, *ApJ*, 706, 797
Ueda, Y., Akiyama, M., Ohta, K., & Miyaji, T., 2003, *ApJ*, 598, 886
Walsh, J. L. et al., 2009, *ApJS*, 185, 156
Wandel, A., Peterson, B. M., & Malkan, M. A., 1999, *ApJ*, 526, 579
Willott, C. J. et al., 2010a, *AJ*, 140, 546
—, 2007, *AJ*, 134, 2435
—, 2010b, *AJ*, 139, 906

10 Quasar Absorption Lines

Nao Suzuki

10.1 A Brief History of the Studies of the Quasar Absorption Lines

The observations of the quasar absorption line systems enabled us to explore the physical state of the high redshift universe (Rauch 1998). Gunn & Peterson (1965) predicted in its note that the amount of the neutral hydrogen gas can be measured in the form of intergalactic medium (IGM) which is known as Gunn-Peterson trough (effect) today. Although the integalactic origin of the Lyα Forest had been observationally established in early 1980s (Sargent et al. 1980; Weymann et al. 1981), it was not until 90s that the cosmological computer simulations (Miralda-Escude & Ostriker 1992; Cen & Ostriker 1993) revealed that the identify of the Lyα forest. The primordial mass fluctuation forms filamentous structure in the universe (Figure 10.1(a)), and the powerful light source, quasars, backlight the foreground IGM and the primordial fluctuation manifests as the Lyα Forest (Figure 10.1(b)).

With the avent of the Hubble Space Telescope (HST) and the large telescopes (Keck, VLT, Subaru, Gemini), the observations of the Lyα forest have flourished and branched into many areas of studies. The Sloan Digital Sky Survey data revolutionized the way we study the Lyα forest. We highlight the IGM studies in the last decade and foresee expectations from the PFS on Subaru in the following sections.

Extracting Cosmological Parameters from the IGM: Schramm & Turner (1998) titled their paper with "Big-Bang Nucleosynthesis enters the Precision Era" which has rung the bell of the arrival of the "precision cosmology" era. The measurement of primordianl deuterium abundance in the IGM reported the baryon density of the universe is $\Omega_b \sim 0.04$ within 10% precision for the first time (Tytler et al. 1996; Burles & Tytler 1998). Today, the observation of the cosmic microwave background (CMB) by WMAP satellite is leading the precise measurement on the cosmological parameters (Spergel et al. 2003, 2007; Komatsu et al. 2009, 2010). However, the Lyα forest has two majour advantages over the CMB or other observations and can play a complimentary role (Tegmark et al. 2004) to the future CMB (Planck) experiments and other observation.

First, the Lyα forest probes the small scale structure (< 30 Mpc/h) which other probes such as CMB or galaxy clustering does not reach. From the SDSS Lyα Forest data (McDonald et al. 2006) measured the power spectrum of the scale of 5-30 (Mpc/h) which has led Seljak et al. (2006) to probe the power spectrum amplitude σ_8, slope n_s and the spectral running index dn/dlnk as well as the upper limit of the neutrino mass ($\sum m_\nu < 0.17$ eV) by combining CMB, galaxy clustering and Type Ia supernova (SNe Ia) data. The power spectrum slope and spectral running index is

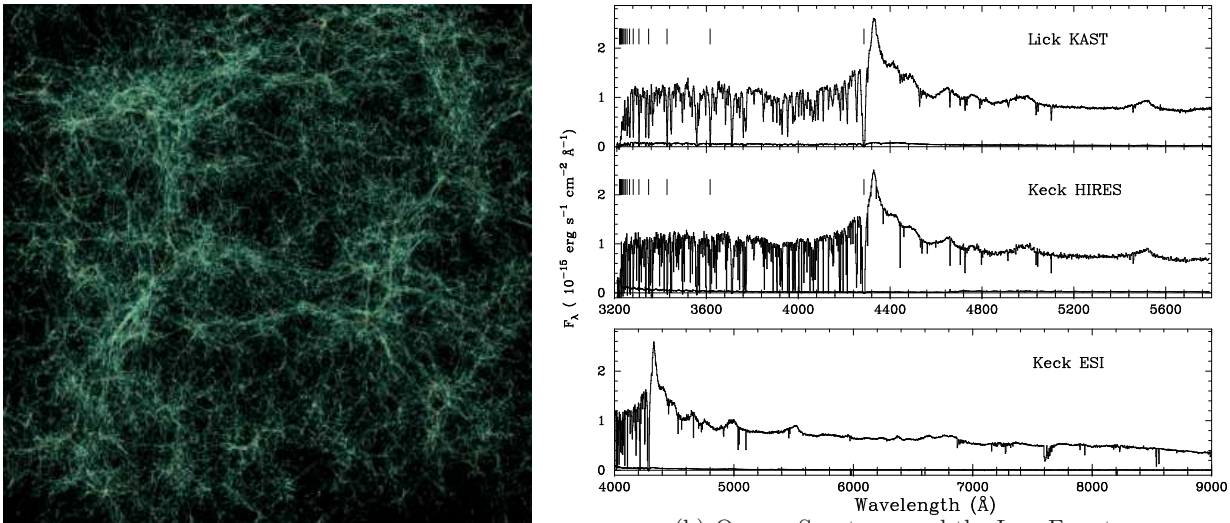

(a) Lyα Forest Simulation

(b) Quasar Spectrum and the Lyα Forest

Figure 10.1: Left : Hydro-Simulation of the Lyα Forest. The primordial flucuation creates the moderatly non-linear filament structure at z=2.0 and observed as the Lyα forest. Right: An example of high S/N quasar spectra at z=2.52. The emission line at 4275 Åis the Lyα emission from the quasar and we see the Lyα Forest due to neutral hydrogen of the foreground IGM in the blueward of the Lyα emission line. In the redward, we do not see as many line as the blue side but the sharp lines are metal lines from the IGM.

of our great interest to investigate the inflation scinario and test the ΛCDM concordance model. Neutrino mass (m_ν) manifests in the amplitude of the small scale structure (Croft et al. 1999), and the upper limit is given by the Lyα Forest (Seljak et al. 2006). More recently, Thomas et al. (2010) reports the upper limit of $\sum m_\nu \leq 0.28$ (eV) from the combined analysis of CMB, SNe Ia and the 7×10^5 luminous red galaxies (LRGs) from the SDSS DR7 data, but we note that the constraint from the Lyα Forest is tighter than that of LRGs. We expect the ongoing SDSSIII/BOSS data will further tightens the constraint and the PFS/Subaru will place stringent constraint.

The second advantage of the Lyα Forest as a cosmological probe is that it provides us with a window of investigating high redshift universe over a wide range of redshifts ($2.2 < z < 5$) which no other observations can reach with proper statistics. A quasar spectrum at $z \sim 3$ contains a few hundred Mpc of the Lyα Forest in a line of sight. With a sufficient number of quasars, we can study the tomography of the Lyα Forest and impose a geometrical test (McDonald 2003).

The Lyα forest has a potential to measure the nature of the dark energy at $2.2 < z < 3.5$ for the first time in history which may bring us a breakthrough to answer if the dark energy is changing in time (dynamical) or not (static). We will discuss the strategy of observing the Lyα Forest with PSF/Subaru in the following sections.

Ionization History of the Universe: The Lyα forest probes the ionization history of the universe, and it turned out that the universe is highly ionized at $z < 4$ and the fraction of the neutral fraction is $\sim 10^{-5}$ with with the temperature of $T > 10^4$ K (Hu et al. 1995; Bahcall et al. 1996; Kirkman & Tytler 1997a,b). However, we know from the CMB experiments, the universe was completely neutral after the recombination had happened at z $\sim$ 1090 (Spergel et al. 2003), and the neutral hydrogen gets ionized by the energetic UV photons from the star forming galaxies. We

did not know when the reionzation had happened until a handful number of quasar observations at $z > 4.5$ showed the optical depth of the IGM quickly evolves at $z > 5$ and indicated that the reionization had happened $z_{reion} \sim 6$ (Becker et al. 2001; Djorgovski et al. 2001; Fan et al. 2002). WMAP observation independently finds $z_{reion} \sim 10$ (Komatsu et al. 2010) from Thomson scattering measurement. Now, the epoch and structure of ionization background is of a great interest for 21 cm cosmology (Furlanetto et al. 2006), and we will discuss how we can study $z > 5$ universe with PFS/Subaru in the science goal section.

HeII is reionized around z $\sim$ 3, and there are hints of observations (Heap et al. 2000; Theuns et al. 2002; Bernardi et al. 2003) which suggests HeII reionization but nothing is definitive yet. Finding HeII reionization epoch is important for the studies of the IGM because it implies the universe becomes transparent to the high energetic photons below HeII reionization redshift, and we expect the increase of temperature and degree of ionization.

Chemical Enrichment of the Universe: One of the unique aspects of the quasar absorption lines is that we can measure the chemical abundance from the metal absorption lines Sargent et al. (1988); Petitjean & Bergeron (1994). Although the Lyα Forest is a moderately non-linear system, we often find highly evolved, non-linear systems in the line of sight also known as the Lyman Limit System (LLS : $17.3 < \log(\mathrm{NHI}) < 20.3$) or the Damped Lyman α System (DLA : $\log(\mathrm{NHI}) > 20.3$, Wolfe et al. 2005). The LLS/DLA system shields the UV photons from outside world and keeps the system neutral which makes the translation of element abundance easy. MgII (λ2800) and C IV (λ1450) are often well measured (Misawa et al. 2002; Ménard & Chelouche 2009) because they are strong and easily identified from its doublet structures. IGM can trace the chemical evolution and enrichment of the universe for a wide range of redshifts (z $<$ 5). One of the applications is that we can deduce when SNe Ia is turned on by measuring the ratio between Fe and α element such as Si or Mg (Kobayashi & Nomoto 2009).

10.2 Key Science Goals

We aim to conduct precise measurements of distances at 2.2 $<$ z $<$ 3.5 from the Lyα Forest and place constraints on the equation of the state of the dark energy $w(z)$.

After a decade of the discovery of the dark energy (Perlmutter et al. 1998; Riess et al. 1998), the existence of dark energy is well established by independent observations and our focus is now on the nature of the dark energy. Namely, if the equation of state, w, is exactly -1 or not and if it changes with time (dynamic) or not (static). It is very important for PFS/Subaru to establish its scientific identity among other big projects in 2015-20, and we will need a careful strategic plan for unique and distinguished sciences. In this subsection, we briefly foresee ongoing and near future surveys and attempt to optimize the PFS/Subaru survey strategies.

We use the following model to describe the observed universe:

$$\frac{H^2(z)}{H_0^2} = \Omega_m(1+z)^3 + \Omega_\Lambda \exp[\int 3(1+w(z))\mathrm{dln}(1+z)] + \Omega_k(1+z)^2, \tag{10.1}$$

where the equation of state w(z) is parameterized by w_0 and w_a (Linder 2003) as follows:

$$w(z) = w_0 + w_a \frac{z}{1+z}. \tag{10.2}$$

For a ΛCDM, w_0=-1 and $w_a = 0$, and our task in this decade is to test if $w_0 \neq -1$ and if $w_a \neq 0$ with high precision measurement.

We note that SNe Ia cosmology measures is the luminosity distance, $d_L(z)$. For a flat universe, $\Omega_k = 0$,

$$d_L(z) = (1+z) \int \frac{cdz}{H(z)}$$

and the angular diameter distance, $D_a(z)$ which is related to d_L by

$$D_a = \frac{d_L}{(1+z)^2}. \tag{10.3}$$

Dark Energy Today: SNe Ia observations give pristine measurement of dark energy in the redshift range of $0 < z < 1.4$ (Astier et al. 2006; Riess et al. 2007; Kessler et al. 2009; Kowalski et al. 2008). The observations of Baryon Accoustic Oscillation (BAO) from LRGs pins down the distance measurements of redshifts at z=0.25 and z=0.3 from SDSS(DR7) and 2dFGS (Percival et al. 2010). CMB (WMAP7) experiments measures the geometry of the last scattering surface at z $\sim$ 1090 (Komatsu et al. 2010). By combining observations from $\sim$ 700 SNe Ia, BAO and CMB, Amanullah et al. (2010) place a constraint on w for a flat universe with:

$$w = -1.009^{+0.050}_{-0.055}(stat, 68\%CL),$$

and the figure of merit, FoM, which is defined as the inverse of the area of 95% CL on w_0-w_a plane $(1/\sigma(w0)\sigma(w_a))$ (Albrecht et al. 2006) is an order of unity. And we note that we do not have any observational constraints for dark energy at z > 1.5 (Rubin et al. 2009; Amanullah et al. 2010).

Dark Energy in 2015: Plack Satellite on CMB experiemnt will be released in 2012, and we have a high expectation of getting tight constraints on cosmological parameters. For SNe Ia studies, the final results from the SDSSII SN survey (Frieman et al. 2008) 3-year data ($\sim$ 500 SNe Ia) and the SNLS (Astier et al. 2006) 5-year data ($\sim$ 500 SNe Ia) will be released. More importantly SNLS and SDSSII/SN plan to perform a joint calibration analysis which can potentially reduce/eliminate the sources of systematic errors. Carnegie Supernova Project (CSP, Freedman et al. 2009) and CfA Supernova Survey will attempt to standardize the SNe Ia with IR data. The Dark Energy Survey (DES) plants to start its 5 year survey from 2011 and expect to have a few thousand SNe Ia up to z $\sim$ 1. Ongoing HST Multi-Cycle Treasurery Program will have 20-40 SNe in redshift $1.0 < z < 1.6$. The Hyper-SuprimeCam deep survey will also populate 100 SNe Ia at $z > 1.0$. Thus, we expect to have a few thousand SNe Ia will be on the Hubble Diagram in the redshift rante of $0 < z < 1.5$ by 2015. Ongoing SDSSIII/BOSS LRG survey will have a constraint on cosmological distance at z=0.7. The BOSS Lyα Forest team may be able to detect the signature of BAO at z $\sim$ 2.5 for the first time in history.

The scenary of the dark energy study is very different from what we have today in 2015. Therefore, it is essential to design PFS/Subaru survey based on the forecasts from other surveys.

10.2.1 Probing Dark Energy in $2.2 < z < 3.5$ with BAO

McDonald & Eisenstein (2007) explored the possibility of detecting the BAO features from the Lyα Forest in $2 < z < 4$ from WFMOS-like experiment. They showed that with a high enough density of quasars ($\sim$ 40 quasars/deg^2), both H(z) and Da(z) can be measured in a high precision ($\sim$ 1.4%) for 2000 deg^2 survey with S/N $\sim$ 1.8/Å at g=23.

Slosar et al. (2009) has used N-body simulation (3000^3 particles in a 1500 Mpc/h box) with Fluctuating Gunn-Peterson Approximation (Croft et al. 1998) to model the Lyα Forest and generated 180,000 mock quasar line of sight spectra. They demonstrated that they can recover radial and transverse correlation from the Lyα forest which the linear theory predicts and showed the detection of BAO signal. They formulate the two-point correlation function of the flux fluctuation around its mean flux as $\xi(r)_{ff}$ and the underlying mass density fluctuation as $\xi(r)_{\delta\delta}$, and relate these two terms by:

$$\xi_{ff}(r) = B(r)\xi_{\delta\delta}(r) + A(r),$$

where A(r) and B(r) terms can be found through the simulation or theoretical models. B(r) term serves as a bias and it is constant at a large scale. Figure 10.2 shows how the correlation function manifests in real space, redshift space from the simulations and the theoritical prediction. The top panel is in mass and the bottom panel is in flux. In practice, we observe the flux correlation and through B(r) term, we can translate into mass correlation, however we can directly find BAO signal from the flux correlation as shown in Figure 10.3.

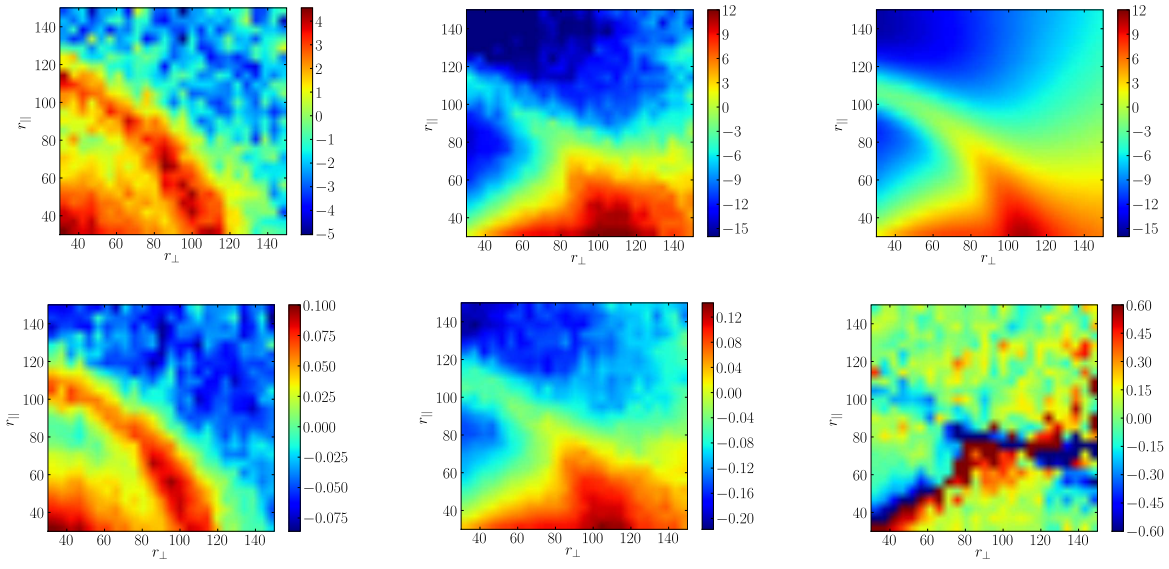

Figure 10.2: Taken from Slosar et al. (2009) with author's permission : The correlation functions, multiplied by r^2 for easier visualization, as a function of $r_\perp$ and $r_{||}$ in h^{-1}Mpc. (Top) Correlation functions for matter over-density in real space, redshift space and the theoretical predictions for linear theory. (Bottom) The correlation function in real and redshift space for the flux fluctuations, $\delta_F = F/\bar{F} - 1$, and (bottom right) the relative difference between the flux and (appropriately scaled) dark matter correlation functions in redshift space $(\xi_{ff} - b^2\xi_{\delta\delta})/\xi_{ff}$. The features in this plot follow the crossing of ξ_{ff} through zero, where the quantity we plot diverges. Note that each panel has a very different color scale.

One of the potential sources of the systematic uncertainites from the Lyα Forest BAO measurement is that the UV background. One may concern that the optical depth fuctuations which manifests as the Lyα Forest may not reflect the underlying mass fluctuations as assume but represents the fluctuations of the UV background sources such as quasars and star forming galaxies. They have tested the effect of fluctuating photo-ionizatino rate with extreme cases, yet they recovered the BAO signal.

White et al. (2010) simulated the Lyα Forest with higher resolution (4000^3 particles in a 70 Mpc/h box) and showed that the BAO can be found from the flux fluctuations. They have tested with more realistic models of the UV background fluctuations and the potential temperature change due to the HeII reionizatino around $z \sim 3$. Although the BAO signal weakens with the UV background fluctuation and the temperature change, the BAO signal still survives in the measurement.

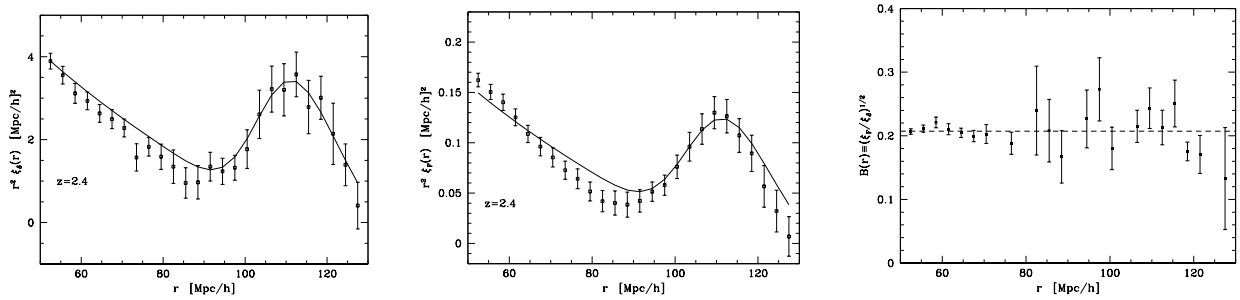

(a) ξ_δ: Mass Correlation Function (b) ξ_F: Flux Correlation Function (c) $B(r)^2 \equiv \xi_F/\xi_\delta$

Figure 10.3: Taken from White et al. (2010) with author's permission: Real space correlation function from the mock spectra is multiplied by r^2 for (a) Mass and (b) Flux. BAO signal is clearly seen with high significane. Right panel (c) shows the flux bias ξ_F/ξ_δ which exibits scale-independence.

10.3 Proposed Survey and its Requirements

In this survey requirement section, we followed the prescription laid out by McDonald & Eisenstein (2007) and estimate our errors on the measurement of dark energy. The critical element of the survey design is the number density of the Lyα Forest. We used the proposed PFS/SuMiRe configuration with assumption of the throuput of 20% and obtained the following forecast.

Table 10.1: PFS Survey Forecast for the BAO measurement from the Lyα Forest at z=2.64

mag g(AB)	exptime (min)	nights	n_{quasar} (deg^{-2})	n_{fiber}	$\delta H/H$	$\delta D_a/D_a$	FoM_1	FoM_2	N_{total}
21.0	10	21	8.8	32	0.049	0.091	TBD	TBD	17600
22.0	20	41	22.5	81	0.021	0.035	TBD	TBD	45000
23.0	48	99	45.0	162	0.015	0.021	TBD	TBD	90000
24.0	120	246	76.6	276	0.013	0.017	TBD	TBD	153200

Table 10.1 has the following columns:

- **mag** : Limiting magnitude with which we can have S/N$\sim$ 2 at the continuum level in g-band.
- **exptime** : Exposure time per pointing needed to achive the limiting magnitude above.
- **nights** : Net nights needed to complete 2000 deg^2 survey with the given exposure time. We do not include weather factor here. The telescope pointings will have overlaps, for simplicity, we assumed 1.6 deg^2 square as an effective area per pointing. Thus, 2000/1.6=1234 pointings in total is assumed in this calculation.
- $\mathbf{n}_{\rm quasar}$: The number density of a quasar per deg^2 with the given magnitude limit based on the luminosity function (Jiang et al. 2009, Richards et al. 2006) with a concordance ΛCDM model (Ω_k=0, Ω_m=0.26, h=0.72).
- $\mathbf{n}_{\rm fiber}$: The number of fibers needed to allocate to achieve the quasar number density above. Just from the *ugriz* photometry information, the success rate of allocating quasar is about 50% for the ongoing SDSSIII/BOSS survey because the stellar objects crosses on the locus of quasars on the color vs. color diagram and we cannot distinguish them in advance. We note that with variability information, we can increase the success rate.
- $\delta\mathbf{H/H}$: Estimated fractional error on H(z) (equation 10.1) at the end of the 2000 deg^2 survery at z=2.64.
- $\delta\mathbf{D}_a/\mathbf{D}_a$: Same as above but with Da(z) (equation 10.3).
- $\mathbf{FoM}_1$: Figure of Merit (FoM), $1/\sigma(w_0)\sigma(w_a)$ with 95% CL (**?**) calculated from the Lyα Forest BAO forecast with the existing data from WMAP7 for CMB (Komatsu et al. 2010), SDSS DR7 + 2dFGRs for BAO (Percival et al. 2010) and UNION2 compilation for SNe Ia (Amanullah et al. 2010).
- $\mathbf{FoM}_2$: Calculated from the Lyα Forest BAO forecast with the expected data from Planck for CMB, SDSSIII/BOSS for BAO, forecast from majour surveys of SNe Ia and LRG BAO constraint from PFS/Subaru.
- $\mathbf{N}_{Total}$: The expected total number of quasar spectra obtrained after the 2000 deg^2 survey. We note tht number of quasars is doubled every magnitude since the slope of the luminosity function is steep.

If the throughput becomes 10%, we simply need to double the exposure time. On the blue side, the effect of the sky counts are negligible. Instead, the faint objects are limited by the readout noise.

10.3.1 Future Prospects

PFS/SuMiRe will have a unique capability of producing high quality spectra in the era of JWST, TMT, LSST, and WFIRST. The Lyα Forest provides us with a unique opportunity to probe high-z (z>2) universe and gives us insights on the nature of dark energy and we should be able to answer if the dark energy is static or dynamic with PFS.

References

Albrecht, A. et al., 2006, ArXiv Astrophysics e-prints, arXiv:astro-ph/0609591
Amanullah, R. et al., 2010, *ApJ*, 716, 712
Astier, P. et al., 2006, *A&A*, 447, 31
Bahcall, J. N. et al., 1996, *ApJ*, 457, 19
Becker, R. H. et al., 2001, *AJ*, 122, 2850
Bernardi, M. et al., 2003, *AJ*, 125, 32
Burles, S., & Tytler, D., 1998, *ApJ*, 499, 699
Cen, R., & Ostriker, J. P., 1993, *ApJ*, 417, 404
Croft, R. A. C., Hu, W., & Davé, R., 1999, Physical Review Letters, 83, 1092
Croft, R. A. C., Weinberg, D. H., Katz, N., & Hernquist, L., 1998, *ApJ*, 495, 44
Djorgovski, S. G., Castro, S., Stern, D., & Mahabal, A. A., 2001, *ApJL*, 560, L5
Fan, X., Narayanan, V. K., Strauss, M. A., White, R. L., Becker, R. H., Pentericci, L., & Rix, H., 2002, *AJ*, 123, 1247
Freedman, W. L. et al., 2009, ArXiv e-prints, 0907.4524
Frieman, J. A. et al., 2008, *AJ*, 135, 338
Furlanetto, S. R., Oh, S. P., & Briggs, F. H., 2006, *Phys. Rep.*, 433, 181
Gunn, J. E., & Peterson, B. A., 1965, *ApJ*, 142, 1633
Heap, S. R., Williger, G. M., Smette, A., Hubeny, I., Sahu, M. S., Jenkins, E. B., Tripp, T. M., & Winkler, J. N., 2000, *ApJ*, 534, 69
Hu, E. M., Kim, T., Cowie, L. L., Songaila, A., & Rauch, M., 1995, *AJ*, 110, 1526
Kessler, R. et al., 2009, *ApJS*, 185, 32
Kirkman, D., & Tytler, D., 1997a, *ApJ*, 484, 672
—, 1997b, *ApJL*, 489, L123
Kobayashi, C., & Nomoto, K., 2009, *ApJ*, 707, 1466
Komatsu, E. et al., 2009, *ApJS*, 180, 330
—, 2010, ArXiv e-prints, 1001.4538
Kowalski, M. et al., 2008, *ApJ*, 686, 749
Linder, E. V., 2003, Physical Review Letters, 90, 091301
McDonald, P., 2003, *ApJ*, 585, 34
McDonald, P., & Eisenstein, D. J., 2007, *Phys. Rev. D*, 76, 063009
McDonald, P. et al., 2006, *ApJS*, 163, 80
Ménard, B., & Chelouche, D., 2009, *MNRAS*, 393, 808
Miralda-Escude, J., & Ostriker, J. P., 1992, *ApJ*, 392, 15
Misawa, T., Tytler, D., Iye, M., Storrie-Lombardi, L. J., Suzuki, N., & Wolfe, A. M., 2002, *AJ*, 123, 1847
Percival, W. J. et al., 2010, *MNRAS*, 401, 2148
Perlmutter, S. et al., 1998, *Nature*, 391, 51
Petitjean, P., & Bergeron, J., 1994, *A&A*, 283, 759
Rauch, M., 1998, *ARAA*, 36, 267
Riess, A. G. et al., 1998, *AJ*, 116, 1009
—, 2007, *ApJ*, 659, 98
Rubin, D. et al., 2009, *ApJ*, 695, 391
Sargent, W., Young, P., Boksenberg, A., & Tytler, D., 1980, *ApJS*, 42, 41
Sargent, W. L. W., Boksenberg, A., & Steidel, C. C., 1988, *ApJS*, 68, 539
Schramm, D. N., & Turner, M. S., 1998, Reviews of Modern Physics, 70, 303
Seljak, U., Slosar, A., & McDonald, P., 2006, *JCAP*, 10, 14
Slosar, A., Ho, S., White, M., & Louis, T., 2009, *JCAP*, 10, 19
Spergel, D. N. et al., 2007, *ApJS*, 170, 377
—, 2003, *ApJS*, 148, 175
Tegmark, M. et al., 2004, *Phys. Rev. D*, 69, 103501
Theuns, T., Bernardi, M., Frieman, J., Hewett, P., Schaye, J., Sheth, R. K., & Subbarao, M., 2002, *ApJL*, 574, L111
Thomas, S. A., Abdalla, F. B., & Lahav, O., 2010, Physical Review Letters, 105, 031301
Tytler, D., Fan, X.-M., & Burles, S., 1996, *Nature*, 381, 207
Weymann, R. J., Carswell, R. F., & Smith, M. G., 1981, *ARAA*, 19, 41
White, M., Pope, A., Carlson, J., Heitmann, K., Habib, S., Fasel, P., Daniel, D., & Lukic, Z., 2010, *ApJ*, 713, 383

Wolfe, A. M., Gawiser, E., & Prochaska, J. X., 2005, *ARAA*, 43, 861

11 Star Formation History

Yoichi Itoh (Kobe University)

11.1 Science Goals

A star is born in a molecular cloud. It evolves as its photosphere contracts on the Hayashi track. Objects on the Hayashi track and the successive Henyey track are called pre-main sequence stars (PMSs). PMSs harbor characteristic circumstellar structures. A protostar is the youngest stellar object surrounded by a spherical envelope. Due to scattering and absorption of dust in the envelope, a protostar is faint in the optical wavelengths. A classical T Tauri star (CTTS) has a proto-planetary disk. Mass accretion from the disk and outflow phenomena produce prominent emission line features such as Hα lines and several forbidden lines. CTTSs are identified by strong Hα emission lines from the boundary layer and infrared excess from the circumstellar disk. Age of CTTSs is estimated to be $\sim$ 1 Myr. As an object evolves, it is called a weak-line T Tauri star (WTTS). Dust grains in the circumstellar disk aggregate into planetesimals, so that the circumstellar disk is optically thin. Small amount of the mass accretion makes weak emission lines. WTTSs are defined as objects with the Hα emission less than 10 Å in its equivalent width. Age of weak-line T Tauri stars is estimated to be $\sim$ 10 Myr.

More evolved PMSs but do not reached at zero-age main sequence (ZAMS) are called post T Tauri stars (PTTSs). In the PTTS phase, planets are formed around the star by collisions of planetesimals. However, only a couple of PTTSs have been detected. This scarcity is caused by two characteristics of the PTTSs. One is a featureless spectrum of the PTTSs. They do not show Hα emission, Ca H&K emissions, nor continuum excesses in the optical and infrared wavelengths. Another is spatial distribution of the PTTSs. With the upper limit of the proper motion of T Tauri stars in Taurus (3 km/s; Frink et al. 1997), we consider that an object moves as large as 12° during 10^7 yrs. PTTSs may be located far from the parent molecular cloud.

These PMSs show Li in aborption. ^{7}Li is fragile and burns at 2×10^6 K. Core of young PMSs has too low temperature to destroy the Li element. D'Antona & Mazzitelli (1994) calculated that the lithium depletes at 10^7 yr and 6×10^7 yr for a 1.3 $M_\odot$ star and a 0.1 $M_\odot$ star, respectively. Thus, presence of Li in its photosphere provides a strong evidence of youth. However, the Li absorption line at 6708Å is rather shallow line. High- or medium-resolution spectra with high S/N (> 50) are required for the Li detection (e.g. Martin et al. 1994).

The fact that the WTTSs are 10 times older than the CTTSs implies that the number of the WTTSs is 10 times larger than that of CTTSs in a star forming region. However, survey of Hα emission line stars in the Taurus molecular cloud indicated that the number of WTTSs is the same

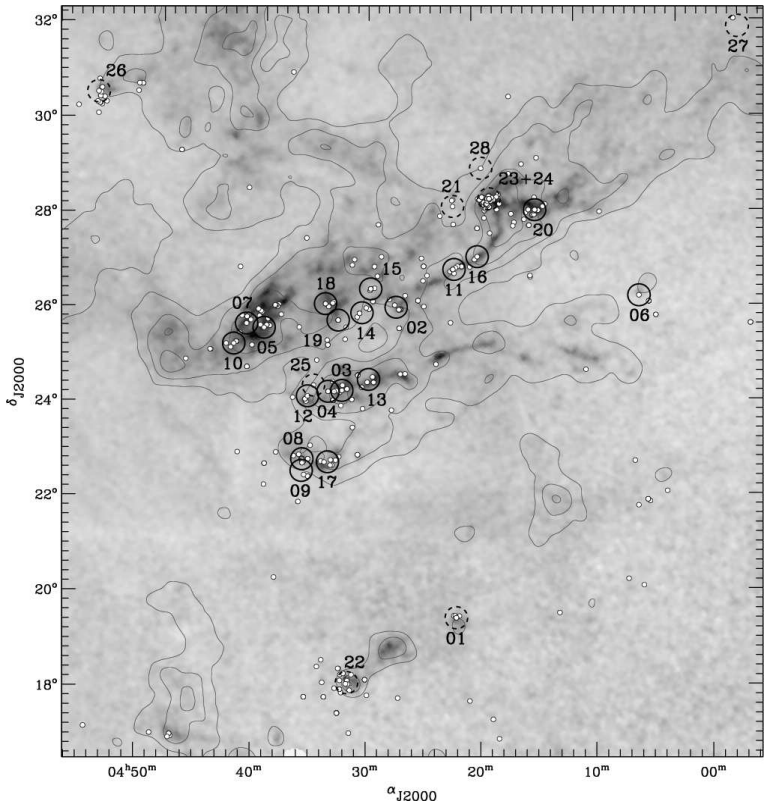

Figure 11.1: Map of the Taurus molecular cloud (Güdel et al. 2007). The grayscale map is an extinction map of Dobashi et al. (2005). Contours show the CO emission (Dame et al. 1987). The large circles show the observed fields of the XMM-Newton survey. The diameter of each field is 0.5 degree. Small white dots are the positions of solar mass T Tauri stars.

order of magnitude to that of CTTSs. Palla & Stahler (2002) interpreted this fact as the star formation being active within recent 10 Myr.

Extensive searches for old TTSs (WTTSs and PTTSs) have been conducted in the X-ray wavelengths. Since old TTSs are rapid rotators, they show strong X-ray emission due to the enhanced corona. The first survey was carried out by Walter (1986). He observed 14 square degree of 3 star forming regions with the Einstein Observatory. He found 16 new PMSs. Wider and deeper survey was conducted by the ROSAT satellite. Neuhaeuser et al. (1995) observed 1000 square degree of the Taurus molecular cloud. They detected 43 known WTTSs and 382 objects whose nature were unknown. Among them, 154 sources have optical counterparts brighter than $V = 16$ mag. Recently, Güdel et al. (2007) observed 28 regions of the Taurus molecular cloud by the XMM-Newton satellite (Fig. 11.1). Each field has 30 arcmin diameter, and the total observed field is 5 square degree. They detected 85% and 98% of known CTTSs and WTTSs in the observed area, respectively. They detected 2347 X-ray sources in total. Those may be old TTSs.

However, field close binary system as well as late type dwarfs also exhibit X-ray emission. Neuhaeuser et al. (1995) identified 64 objects as WTTSs by the follow-up optical spectroscopy. By extrapolating this result, they claimed that in the Taurus star forming region, there are ∼600 WTTSs. Since the number of the WTTSs are about 10 times larger than that of CTTSs in the same region, this

estimate is consistent with the age ratio of WTTSs and CTTSs. Magazzu et al. (1997) carried out optical spectroscopy of 115 ROSAT sources in the Taurus molecular cloud (Fig. 11.2). They are bright in optical ($V < 16$ mag). In the medium resolution ($\lambda/\Delta\lambda \sim 2000$ to 8000) spectra, they found Li 6708Å absorption line from 30 objects. They also the spectral types of the PMSs with uncertainty of 1 subclass, based on Ca 6718Å line, Fe 6495Å line, and TiO bands in the I-band.

Nevertheless, any follow-up observation do not yet conducted for the most X-ray sources. Their nature are still unidentified. They may be PTTSs. Featureless spectra and sparse distribution of PTTSs prevent us from discovering such old populations. This missing population can be found only with a wide field spectrograph. With the PFS survey proposed here, we will investigate history of star formation in a molecular cloud.

11.2 Proposed Survey and its Requirements

X-ray survey is an effective tool for detecting relatively old PMSs. Such objects do not show any continuum excess (e.g. infrared excess) except X-ray excess. They also do not exhibit any line signatures (e.g. Hα emission, Ca H&K line emission) except the Li absorption line. Several attempts were made by optical spectroscopy for revealing the population of such old, thus inactive PMSs. However, their targets are flux limited. In most cases, the targets are brighter than 16 mag at the V-band. With such shallow limiting magnitude, one cannot detect less-massive objects and more evolved objects. With the limiting magnitude of $V \sim 16$ mag and an average visual extinction of the WTTSs in the Taurus molecular cloud of 2 mag, the previous optical spectroscopy could detect 3 Myr old 0.1 $M_\odot$ stars or 0.6 $M_\odot$ ZAMS. In contrast, low-mass ($M < 0.5M_\odot$), more evolved ($> 10^7$ yr) stars were missed from the previous optical spectroscopy. Note that Li survives for long time in less-massive objects. We will observe the optical counterparts of the X-ray sources detected by the XMM-Newton satellite or future X-ray missions.

We will search PTTSs in 5 star forming regions; Taurus, ρ Oph, Serpens, Orion, and Perseus. First we search optical counterparts of the X-ray sources by R-band imaging observations. We will use Hyper Suprime Cam. Integration time is expected to be only a few minutes. Then, we will conduct medium resolution ($R \sim 2,500$) optical spectroscopy. Since the objects are expected to be low-mass objects, they have intrinsically red color. The wavelengths are 6000Å to 9000Å. We will search the Li absorption line at 6708Å. The spectral types of the objects are determined with several absorption line signatures (Ca 6718Å, Fe 6495Å) as well as TiO absorption bands in the I-band. Since the Li line is shallow, we need high S/N ratio. With 900 sec integration, a spectrum with S/N=50 will be obtained for $R = 19$ mag objects. It corresponds to 0.1 $M_\odot$ ZAMS in the Taurus molecular cloud. Thus, by this observations we will first complete the age census of low-mass PMSs down to ZAMS.

1. What is the minimum nights to achieve the desired scientific goal?

   We will search PTTSs in 5 star forming regions; Taurus, ρ Oph, Serpens, Orion, and Perseus. 7 Fields will be investigate in each region. Assuming the same number density of old TTS candidates as that of the Taurus molecular cloud, we expect 250 candidates in each field. Integration time for each field is only 900 sec. Thus we request 2 half nights (15 min $\times$ 7 fields $\times$ 5 regions = 8.75 hour).

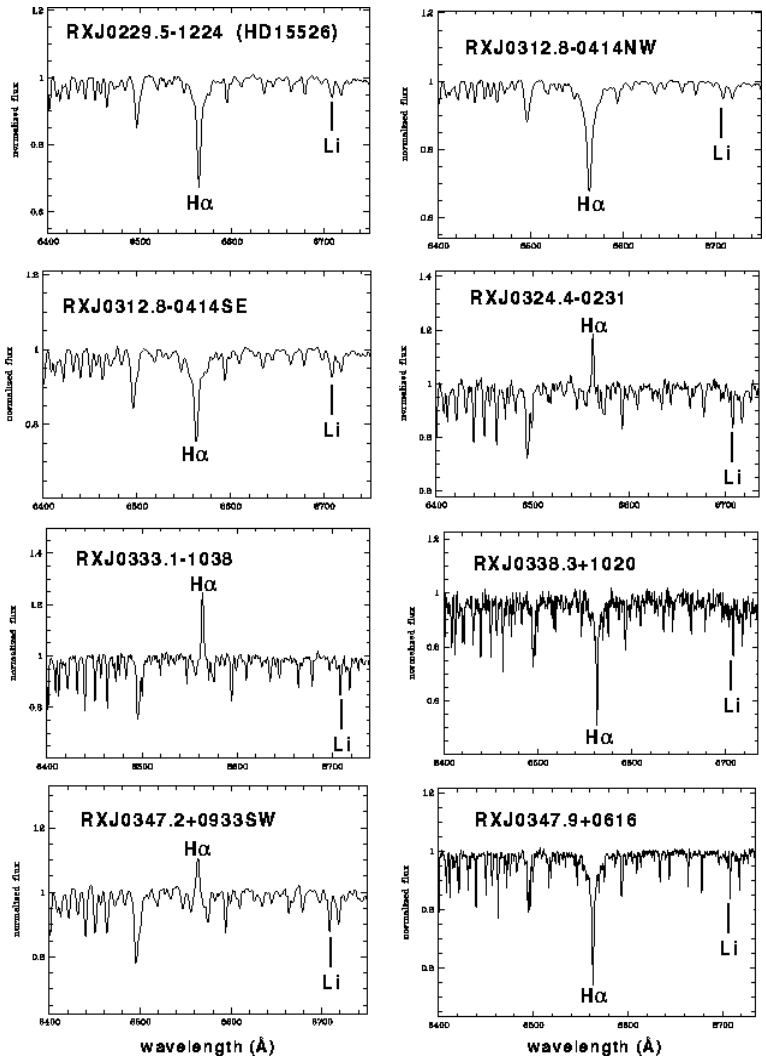

Figure 11.2: Example of optical spectra of X-ray selected PMSs. Li absorption line at 6708Å is a strong indicator of youth. Objects with the Li absorption line and the Hα emission line are WTTSs, while those with the Li absorption line and the Hα absorption line are PTTSs (Magazzu et al. 1997).

2. What is the impact if the achieved throughput is 10%, rather than 20%?

   We requrest 4 full nights in this case.

3. What is the time line for proposed science to get done (e.g. HSC data is enough for target selection, or other datasets are needed? Another spectroscopic follow-up with higher resolution is needed? and so on)

   HSC imaging data is enough.

4. How unique is the proposed science case, compared to other planned surveys in the world?

   Many surveys aim at detecting low-mass TTSs, i.e. constructing the initial mass function at low mass end. No survey is proposed for searching widely separated PTTSs.

5. What is the most important ingredient of PFS specifications (resolution, the number of fibers, and so on) for achieving the proposed science case?

   Current design is sufficient.

References

Dame, T. M. et al., 1987, *ApJ*, 322, 706
D'Antona, F., & Mazzitelli, I., 1994, *ApJS*, 90, 467
Dobashi, K., Uehara, H., Kandori, R., Sakurai, T., Kaiden, M., Umemoto, T., & Sato, F., 2005, *PASJ*, 57, 1
Frink, S., Röser, S., Neuhäuser, R., & Sterzik, M. F., 1997, *A&A*, 325, 613
Güdel, M. et al., 2007, *A&A*, 468, 353
Magazzu, A., Martin, E. L., Sterzik, M. F., Neuhauser, R., Covino, E., & Alcala, J. M., 1997, *A&AS*, 124, 449
Martin, E. L., Rebolo, R., Magazzu, A., & Pavlenko, Y. V., 1994, *A&A*, 282, 503
Neuhaeuser, R., Sterzik, M. F., Schmitt, J. H. M. M., Wichmann, R., & Krautter, J., 1995, *A&A*, 295, L5
Palla, F., & Stahler, S. W., 2002, *ApJ*, 581, 1194
Walter, F. M., 1986, *ApJ*, 306, 573